5-2014

Modeling, Analysis, and Control of a Mobile Robot for *In Vivo* Fluoroscopy of Human Joints during Natural Movements

Matthew A. Young
University of Tennessee - Knoxville, myoung41@utk.edu

To the Graduate Council:

I am submitting herewith a dissertation written by Matthew A. Young entitled "Modeling, Analysis, and Control of a Mobile Robot for *In Vivo* Fluoroscopy of Human Joints during Natural Movements." I have examined the final electronic copy of this dissertation for form and content and recommend that it be accepted in partial fulfillment of the requirements for the degree of Doctor of Philosophy, with a major in Mechanical Engineering.

William R. Hamel, Major Professor

We have read this dissertation and recommend its acceptance:

Gary V. Smith, Xiaopeng Zhao, Seddik M. Djouadi

Accepted for the Council:

Carolyn R. Hodges

Vice Provost and Dean of the Graduate School

(Original signatures are on file with official student records.)

Modeling, Analysis, and Control of a Mobile Robot for *In Vivo* Fluoroscopy of Human Joints during Natural Movements

A Dissertation Presented for the

Doctor of Philosophy

Degree

The University of Tennessee, Knoxville

Matthew A. Young

May 2014

DEDICATION

This dissertation is dedicated to the glory of God.

ACKNOWLEDGEMENTS

I would like to thank my advisor, Dr. Hamel for his continual encouragement and guidance. I would like to express my appreciation to my committee; Dr. Smith, Dr. Zhao and Dr. Djouadi, for being so flexible with your schedules and providing guidance and direction throughout the project. Andrzej Nycz provided a strong, stable platform, for which I am immensely grateful. So much of my practical understanding of mechatronics and control was gained through our many conversations. I would also like to thank Tian Qiu for innumerable discussions regarding the theoretical, technical aspect of control systems and structures. I appreciate the hard work and support of the entire BioRobotics Lab at the University of Tennessee. Thank you for help!

My completion of this project could not have been accomplished without the support of our church family. I am especially grateful to George Taylor, who rented his house to our family; and to Carol Cochran, who was always willing to watch the children. I will always remember your kindness and generosity. I would like to thank my parents for instilling in me a desire to learn and a work ethic to pursue my calling. I would like to thank my children for being so understanding in my frequent evening absences, and your encouragement to me as I was "working on my doctorate."

Finally, I would like to thank my wife, Janna. From the beginning, this was a joint project. I'm sure that you worked two hours holding down the fort for every hour I was away. It was often your encouragement and support that kept me going when things got tough. I look forward to seeing what new challenges we will tackle together.

ABSTRACT

In this dissertation, the modeling, analysis and control of a multi-degree of freedom (mdof) robotic fluoroscope was investigated. A prototype robotic fluoroscope exists, and consists of a 3 dof mobile platform with two 2 dof Cartesian manipulators mounted symmetrically on opposite sides of the platform. One Cartesian manipulator positions the x-ray generator and the other Cartesian manipulator positions the x-ray imaging device. The robotic fluoroscope is used to x-ray skeletal joints of interest of human subjects performing natural movement activities. In order to collect the data, the Cartesian manipulators must keep the x-ray generation and imaging devices accurately aligned while dynamically tracking the desired skeletal joint of interest. In addition to the joint tracking, this also requires the robotic platform to move along with the subject, allowing the manipulators to operate within their ranges of motion.

A comprehensive dynamic model of the robotic fluoroscope prototype was created, incorporating the dynamic coupling of the system. Empirical data collected from an RGB-D camera were used to create a human kinematic model that can be used to simulate the joint of interest target dynamics. This model was incorporated into a computer simulation that was validated by comparing the simulation results with actual prototype experiments using the same human kinematic model inputs. The computer simulation was used in a comprehensive dynamic analysis of the prototype and in the development and evaluation of sensing, control, and signal processing approaches that optimize the subject and joint tracking performance characteristics.

The modeling and simulation results were used to develop real-time control strategies, including decoupling techniques that reduce tracking error on the prototype. For a normal walking activity, the joint tracking error was less than 20 mm, and the subject tracking error was less than 140 mm.

TABLE OF CONTENTS

LIST OF TABLES

LIST OF FIGURES

LIST OF ABBREVIATIONS

FPGA: Field Programmable Gate Array. Often used when prototyping equipment needs extremely high processing speeds, FPGA equipment can be reconfigured at the hardware level. The FPGA employed by the **TFS** has a clock speed of 40 MHz.

IMAQ: Standard National Instruments drivers and software for Image Acquisition devices.

Joint Tracking: Use of the TP to position the fluoroscope components of the TFS.

MIMO: Multiple-Input-Multiple-Output System

MIWD: Motor-In-Wheel-Drive. A consolidated drive wheel that encompasses forward motion and steering in one unit. The current TFS is equipped with two MIWDs. Each is comprised of a motor for steering the wheel, a motor for driving the wheel. An encoder reports the rotation of the driving motor and a potentiometer is used to measure the rotation of the steering motor. For steering, the wheel pivots about a line that intersects with the axis of rotation of the driving wheel.

ROI: Region of Interest: An image area that encompasses the skeletal joint of interest for a particular TFS clinical experiment.

Subject Tracking: Use of the torso or other human body features to control the relative position of the TFS mobile platform and the human subject.

TFS: Tracking Fluoroscope System. A mobile robot with an integral x-ray fluoroscope that can x-ray human skeletal joints of interest while a human subject performs natural movements like walking and climbing/descending stairs.

TITO: Two-Input-Two-Output System

TP: Target Point: A particular point in the ROI that is used as a control target during TFS joint tracking.

CHAPTER 1. RESEARCH MOTIVATION AND MOBILE FLUOROSCOPY

Advances in many engineering disciplines have produced a flurry of robotic research in the twentieth century. Better materials and manufacturing techniques have created cheaper, stronger and more compact motors. Improved electronics has allowed these motors to be used with higher power efficiency and with greater flexibility. Advancements in digital controls have allowed these motors to be utilized with increasing accuracy, effectiveness and safety. Modern production methods have produced environments that favor industrial robotic applications. These developments are contributing to more robots performing more diverse tasks in industry. For instance, even with a severe economic slump, companies from North America sold more robots in 2011 than ever before[1].

While the use of robotics in medical fields has risen dramatically in the last decade, very little research has been done to examine the advantages and contributions that a robotic fluoroscope device could provide. The few cases of robotics and fluoroscopy merging are for applications like surgical navigation and assistance. The concept of a mobile robot fluoroscope is unique to the research performed by the BioRobotics Lab at the University of Tennessee [2]. This research has primarily focused on providing accurate, stable fluoroscopic videos that can be used for in vivo analysis of skeletal joints. With such fluoroscopic videos and additional three-dimensional geometrical information, such as total joint implant CAD models and CT data, in vivo force analyses of common human movements can be calculated. An example of this could be examining three dimensional force vectors that result within the knee joint of a human who is walking normally. The novelty of the mobile robot fluoroscope is its ability to take images while the human subject is performing natural movements. Without the use of robotics, this type of data is difficult to collect and is often of an inadequate quality.

The result of our past research was the creation and implementation of a Tracking Fluoroscope System, or TFS. The TFS is able to obtain fluoroscopic video of skeletal joints by virtue of two separate real-time control functions: 1) the mobile platform tracks the human subject's body (torso) movement, and 2) separate actuated mechanisms track the skeletal joint of interest which moves relative to the body motion. The TFS achieves these control functions through inputs from two laser scanners, six sonar rangefinders, two firewire digital cameras, four custom radiation detectors, and the fluoroscope image frames. Control of the robot is applied by two independent driving wheels (the mobile platform) and four linear actuators (the centerline of the fluoroscope). The integral fluoroscope is based on a modified General Electric fluoroscopic stenoscope. The TFS is tetherless and wireless being powered completely from onboard batteries, and utilizing WiFi data communications with the operator control station.

In its present form, the TFS is a fully functional prototype that is being used to further refine its design and performance, and to perform actual clinical trials for total joint implant manufacturers. Results from this phase of testing and evaluation will be used in the continued development of future TFS versions. One of the areas that clearly needs additional research is the dynamic control of the overall machine such that tighter tracking of the skeletal joint of interest can be achieved, particularly in the more complex activities like stair climbing and descent. This research is will explore the improved dynamic control of the TFS through detailed modeling and simulation of the machine and exploration of advanced control methods.

In vivo kinematic analysis is the study of motion inside a living organism. This type of analysis yields, among other data, information about how human skeletal joints work; providing essential data for improving current total joint replacement devices and surgical procedures, and generating new concepts for future artificial joints. Current in vivo skeletal data collection techniques are limited to:

- External markers that are used to estimate internal features,
- 2-D x-ray images that are overlaid with 3-D joint information [3],
- X-ray images of implanted pins [4].

While research is working to increase the accuracy of external marker interpolation, the basic understanding of bone motion is built from x-ray data [5]. This data have typically been collected using a conventional fluoroscope, in which x-ray transmission is used to image density variations in body tissue, resulting in a real-time video images of internal tissue features [6]. As pre-operative and post-operative analysis techniques have improved, there is a need for the collection of better quality data that can include a wider range of subject motions than can be achieved with conventional static fluoroscopes. This need can be addressed through robotic concepts. Some robots have been designed to use fluoroscopic images to aid in surgeries [7-9], but to the best of our knowledge there is no work in the use of a Wheeled Mobile Manipulator to obtain in vivo skeletal data.

In 2005,[10] discussed the first concept of such a robot. It was proposed to dynamically position the x-ray source and image intensifier used in a conventional fluoroscope unit two-dof Cartesian manipulators mounted to a mobile platform. The robot, coined the Tracking Fluoroscope System, would be automated – the system would use the motion of the patient for tracking the joint of interest, would be tetherless – operating completely on battery power, and would be a wheeled mobile robot. Since the x-ray components would move relative to the robot platform, it would have the general form of a mobile manipulator. A patent on the concept was applied for the same year [11].

CHAPTER 2. MOBILE ROBOTICS

Wheeled Mobile Robots are translated and rotated with the use of wheels. In 1989, [17] discussed the basics of WMRs. The basic kinematics of the system were analyzed, with a fair amount of attention given to slippage (when a wheel turns too fast with relation to the ground) and skidding (when a wheel turns too slow with relation to the ground). These terms are the opposite of rolling, and the necessary constraints that guarantee rolling were derived for two-wheeled robots. One of the assumptions made was that the wheels have no thickness. The forward and inverse kinematic equations were solved with forces known and velocities unknown. This is computationally simpler than using velocities to solve for forces, but highly impractical, since it is typically easier to know angular and linear velocities, while frictional forces at the wheel surface are seldom known.

By 1996, wheel mobile robots had become a diverse enough group to allow for a sub-classification of WMRs into five categories of kinematic models, [18]. Omnidirectional WMRs represent the least restrictive, because can move in any direction parallel to the floor. They have no kinematic constraints imposed by the wheels. By way of contrast, another category contains robots that have no fixed wheels, and at least two wheels that can be oriented. A large percentage of WMRs, including the platform of the TFS are in this category. The only velocity profile that any fixed point on the robot can have is one that is perpendicular to the Instantaneous Center of Rotation, which is determined by the intersection of vectors that are perpendicular to the orientation of the steering wheels.

WMRs designed to function on flat or nearly flat surfaces are three dof. For steering robots, the degrees of freedom are the translational motion of the wheels, and the angle of the wheels relative to the platform. For these robots, the wheels remain roughly parallel to each other and move with roughly the same velocity. For differential drive robots, the wheels remain fixed and the ability to rotate the robot comes from moving the wheels at different velocities. The TFS is not in either of these classes. The two driving wheels have independent velocities. This allows the platform to rotate about any point in the plane of the floor. This increased flexibility in the motion of the robot has its costs, however. The platform has four dof, making it redundant. Also, it is not feasible that the wheels can instantly rotate to an arbitrary required position. This means that there is always some slip, hopefully negligible, associated with the motion.

Although slippage occurs with almost all wheeled motion, it is often possible to ignore the effects of slip. This assumption becomes less likely to be valid when robots begin moving in two dimensions. Adding feedback also accentuates the effect of slip, as does allowing the wheels to spin and rotate independently.

[19] dealt with slip in multi-dof WMRs. Five possible wheel configurations, including the layout of the TFS, are discussed. The source and importance of wheel slip is discussed, specifically in how it relates to the actuation of the robot. Borenstein claimed that *all* multi-dof robotic wheeled platforms will produce slip or backlash unless a source of compliance has been designed into the structure. This slip is caused by the inability of the physical system to instantaneously align every steering wheel with the true instantaneous center of rotation. Rubber manufacturing techniques and compression characteristics practically ensures that any slip that does occur to introduce an error that builds over time. In the case of the TFS, this can be dismissed for two reasons. First, the TFS tracks a human directly. This means that the position of the robot to the ground is not as important as the relative position of the robot to the human. Second, it is possible to use sensors to

independently measure the position of the TFS relative to the ground. The equipped laser scanners or IMUs could resolve the motion due to slip.

The literature for wheeled mobile manipulators is as vast as their applications, and much research activity has been spent in trying to understand and control them in a general, overreaching sense. The majority of the research can be divided into broad categories. There has been much attention to modeling, using a kinematic approach, a dynamic approach, or an iterative, adaptive approach. A kinematic approach does not take into account the inertias and forces of the system. A dynamic approach attempts to approximate the constants of the system, to create a better control model. Iterative approaches adjust control constants to create a better estimation of the total system. There have been several papers on the stability and tip-over concerns for WMMs [20-26]. One key concept is that of holonomic constraints. The term holonomic has many implications, and can therefore be described in many different ways. We will define a holonomic constraint by stating that there exists some function, *f*, such that the constraint can be written as

$$0 = f(x_1, x_2, \dots, x_i, t) \quad (1)$$

This definition specifically stipulates that the function f is not dependent on the partial derivatives of any of the variables. This stipulation forces a holonomic constraint to be independent on a particular path. Practically in robotics, a system is holonomic if it is possible to *instantly* move the end effector in any direction contained in its total degrees of freedom. Most mobile manipulators incorporate a holonomic manipulator and a non-holonomic platform. For instance, [27] consider the holonomic portions of nonholonomic systems (i.e. the constraint that the rolling surface of a wheel must contact the ground at all times). This demonstrates that the factors that cause slip are leading factors in the result of mobile platforms being non-holonomic. [28] examined nonholonomic solutions (defining the equations using the Lagrangian) and dynamic models, including slip with a nonlinear model for tire friction, using Newtonian formulation. For other common terms and considerations of wheeled mobile manipulators, [29] serves as a good survey.

[30] first recognized the full value in placing a manipulator on a wheeled robot. Inspiration for this idea came from examining the way that humans position our bodies to keep our arms in positions that are highly configurable. Applying this to robotics allows a criterion that can be used to generate a trajectory for the platform that is related, in general, to the manipulator, but separable from the actual actuation of the manipulator.

The quest to create a truly holonomic wheeled robot has been elusive. The term omnidirectional robot refers directly to this quest. A terrestrial robot is classified as omnidirectional if it is capable of traversing along a vector contained in the plane of the floor at any point in time. This is surprisingly difficult to accomplish ideally, but this research builds a foundation for TFS motion, since it is desired to track along an arbitrary curvilinear path, [31, 32].

In particular, [33] had results that might be useful in controlling the TFS. Qualifications were given to allow conventional redundant manipulator control techniques to be used on mobile manipulators. The importance of this work hinges on the idea of allowing a non-holonomic platform to be modeled as an omnidirectional platform.

The objective of mobile robot control is typically to generate and actualize some type of trajectory or path. A path consists of a group of coordinates that a point on the system is attempting to pass

through. A trajectory is a path that also has a dependence on time. Once a trajectory is generated, it is possible to orchestrate task planning. For real time systems, this process is highly integrated. At each new evaluation, a new trajectory is generated, and a new task plan must be initiated. For example, [34] used event-based kinematic redundancy allocation to design a decoupled force/position control scheme, which is in turn used to generate an integrated task planning and control approach. In this case, the kinematic redundancy of the mobile manipulator system is resolved by utilizing the degrees of freedom to add additional control parameters. The orientation of the cart was considered as a revolute joint. Several controls were considered. The most effective was an adaptive gains approach for the manipulator and the platform. Kalman filtering was also utilized in integrating a range finder to locate the orientation of the cart.

The TFS generates two paths from two distinct sources. The Subject Tracking uses two range finding lasers to determine the parallel and perpendicular standoff distance between and the angle of the subject's torso and the mobile platform. The Joint Tracking is accomplished using visual servoing that determines the centerline of the fluoroscope with respect to the joint feature of interest.

Visual servoing is a very large research area with extensive publications. [35] provides a basic understanding of video servoing. Some research has been done using visual servoing applications to control mobile manipulators. For examples, see [36-39].

Other sensors could be employed by the TFS to facilitate other control schemes. In 2009, Microsoft introduced a relatively inexpensive range sensor. The Kinect is part of the Xbox 360 game console, and the sensor outputs a color video stream and a 3D range map. In addition, the Kinect has algorithms that find 20 data points that correspond to body parts of a human. These data points can be delivered at a loop rate of around 30 Hz, although the system runs only on a Windows platform, which is notoriously unreliable for real time applications. A 3D range scanner could possibly eliminate the need for the 2D laser range scanners, while providing additional information about the orientation of the TFS with respect to the room. The Kinect has been used in many robotic control problems [40-43].

Another type of sensor that could be helpful for the TFS is Inertial Measurement Units (IMUs). MEMS based IMUs have been used to control flying Unmanned Air Vehicles [44-46]. These devices sense orientation and acceleration, and might be useful for determining the position of the TFS with respect to the ground [47-49].

As with any robot that has possible physical interactions with humans, a great deal of care must be taken to ensure the safety and comfort of the human. The necessary control loops and communication protocol are set down in [50, 51].

CHAPTER 3. MOBILE FLUOROSCOPE ROBOT CONCEPT

A successful Tracking Fluoroscope System will have three major design criteria:

3.1 PSEUDO-OMNIDIRECTIONAL PLATFORM.

An omnidirectional terrestrial mobile robot can translate in any direction along the plane of the ground and rotate along any axis normal to the plane in the ground at any time. In other words, there are no constraints that prohibit the robot from traveling in any new direction. Most wheeled mobile robots are not modeled as omnidirectional because they can only traverse in the direction of the wheels, thus they have constraints that prohibit motion along the axis of each wheel. As mentioned above, the TFS has two Motor-In-Wheel-Drives (MIWDs) that allow it to move in any direction, but time must be allowed for the MIWDs to align correspondingly. At any point in time, the platform has constraints along the vector that runs through the axis of each driving wheel. If a system can align the wheels fast enough, it will behave as if there are no constraints, so a system that is not truly omnidirectional might behave like one if the response of the wheel alignment is "much faster" than the desired changes in velocity vectors. The term psuedo-omnidirectional is meant to convey that the robotic system is capable of curvilinear motion; however the system need not comply with all the freedoms necessary to invoke the term omnidirectional.

The pseudo-omnidirectional nature of the TFS gives the system the ability to track a subject who walks along a curvilinear course. There are many human kinematic questions about the way joints behave during common actions such as pivoting and turning. While the TFS need not track fast athletic motions, it would be helpful if the system was capable of following significant but smooth changes in direction. The proposed dissertation will shed light on what can be reasonably mean by "significant smooth changes in direction".

An extended version of the TFS will also be considered that adds an additional two MIWDs, so that the system would be controlled by four independent driving motors. While the added complexity of the motors does not add additional motion degrees of freedom to the system, the additional thrust would possibly allow the system to respond with better dynamics to a greater range of subject movements. The assets and risks associated with this design should be carefully considered. In particular, it needs to be determined that additional forward thrust of the wheels would increase the response time, since all four wheels must be aligned correctly to allow the TFS to rotate and translate about the correct point.

The TFS is a medical x-ray diagnostic device that can only be operated under radiation control and exposure conditions, usually achieved by shielded lab rooms. As is the case with most medical equipment, the design of the platform does not need to include the ability to handle rough terrain or outdoor conditions. The robot design can assume that the floor will be a flat, smooth surface, contributing only small disturbances injected into the system. Additionally, design can assume that the floor is reasonably hard, as medical locations will not contain floors that are covered in carpet and other soft textures.

Figure 1 MIWD

3.2 FOUR DOF AXES ACCOMPLISH ROI TRACKING

The principal novelty of the TFS is the ability for the fluoroscope device to capture images of a moving target point (TP) with a Region of Interest (ROI). The TFS accomplishes this by actuating the x-ray generator, or source, and the image intensifier that views and records the x-ray image along vertical and horizontal axes. This actuation is accomplished by four linear servo actuators. The two vertical actuators are each composed of a servo motor coupled to a ball drive. An encoder on the motor provides feedback to the system, and a precision gear head and coupler reduce backlash. The two horizontal actuators are linear electric motors with a linear encoder for feedback. The system, therefore, has four independently controlled actuators.

State fluoroscope licensing regulations mandate that all of the radiation produced by the source must be captured by the intensifier. Conventional fluoroscope units have a rigid and fixed mechanical link between the source and the image intensifier, that assures adherence with this regulation. Since the TFS requires independent dynamic motion of the source and intensifier, two independent safety controls are implemented to assure adherence. One system is a real-time watchdog of the horizontal and vertical encoder counts between the source and intensifier servo drives. If the system drifts out of alignment, the x-ray generator and all systems capable of motion

are disabled immediately. The other independent system uses x-ray detectors along the perimeter of the intensifier. If radiation is detected by any of the four sensors, this means that all of the x-rays are not contained in the intensifier area and the x-ray generator is disabled immediately.

3.3 SELF-CONTAINMENT

Medical devices are often standalone, self-contained systems. Self-contained systems are easier to transport and less complicated to install/operate. In keeping with typical medical configurations, the original specifications of the TFS required it to operate with wireless communication, have self-contained power supplies, and without tethers. These specifications still provide significant design parameters for the system.

The TFS is powered by two 12 VDC batteries linked in series, to create a 24VDC system. The MIWDs, sonar sensors, emergency stop buttons and many of the auxiliary electrical components are powered by the 24 VDC directly. A square-wave power inverter converts 24 VDC to 110 VAC, providing power to the Axis motors, onboard computers, laser scanner, x-ray equipment, router and the PLC controlling the safety loop. The combined system can draw around 800 amps from the battery pack during peak usages. Typical battery life is around 30 minutes for continuous testing.

In addition to physical self-containment, the TFS needs to be able to follow the TP automatically. While the TFS is not an autonomous system, the control loops of the system are closed directly by feedback of the subject. Feedback of the subject comes from two main measurements:

1. The Cartesian manipulator is controlled by image processing techniques that identify the location of a TP within each x-ray video frame created by the fluoroscope unit. This allows the x-ray image to affect the tracking of the joint directly. Effective dynamic control, therefore, occurs when the TP remains in the physical center of the image intensifier regardless of the subject's actual movement.
2. The platform utilizes two 2D laser range scanners that measure the profile of a subject's chest from a known location on the platform. This information is used for Subject Tracking. The laser feedback is essentially relative distance and orientation information between the subject and the platform, allowing the system to TFS to track the subject's motion without reference to position in the room itself. This is a far more effective and direct method than measuring the platform and subject from a room-fixed sensor system.

The control loops are closed using a Dell PC employing the Labview RealTime operating system. The computer communicates to the axis and wheel hardware using standard PCI-slot boards. Communication to the axes and MIWD is accomplished using Field Programmable Gate Array technology. The FPGA board has eight analog input channels and eight analog output channels and uses standard -10 to 10 Volt signals. It also has 96 digital TTL input/output ports that are configured to accept, among other I/O, the raw encoder outputs.

The onboard Dell also uses a forty-eight channel industrial digital Input/Output board, made by National Instruments. When configured as outputs, the channels function as a traditional relay, opening and closing a channel-channel isolated circuit. Inputs are compared with a supplied reference voltage, se each channel can be based on 5V, 12V or 24V logic.

A black and white camera and the x-ray detection equipment communicate to the onboard computer using an IEEE 1394 (firewire) framegrabber. A National Instruments driver communicates with the Labview software using canned IMAQ algorithms. The two laser scanners communicate using TCP/IP protocol over Cat 5 Ethernet cable. The wireless router located on the TFS serves as a hub for all TCP/IP communication on the TFS platform.

The operator of the TFS has supervisory control of the axes and wheels and can perform manual motion control, home the axes and other supervisory functions. The operator also has the ability to monitor the video feed from the TFS, begin data recording, and enable x-ray functionality. X-rays are only generated when all safety loops are intact, functionality in enabled and a remote deadman switch is depressed. During trials involving human subjects, the remote is operated by a Radiation Technician certified by the Registry of Radiologic Technologists (ARRT).

CHAPTER 4. APPROACH

4.1 DEFINITION OF THE TFS MODEL

Figure 2 shows the TFS as a dynamic robot being driven by the kinematics of a human subject. The robot has five rigid bodies: a mobile platform, two bodies that move in the horizontal direction, and two bodies that move in the vertical direction. The human subject is described by a Torso, a Femur and a Tibia section. The input to the system is given through the kinematic motion of the human. For the Simulation phase and a portion of the experimental phase of the research, this input is created from profiles of pre-recorded human movements. For the remaining portion of the experimental phase, the input is a live human subject.

The masses of the five rigid bodies that compose the robot portion of the system are recorded in Table 1. The total mass of the system was measured by placing scales under each of four wheels and summing the readings. The weight of the vertical axes was measured by setting a scale under the load and releasing the vertical brakes. The weight of the horizontal axes was estimated using SolidWorks.

Table 1 Mass of Robot Links

Link	Symbol	Mass (kg)
Platform	m_p	695
Right Horizontal	m_{RX}	20
Left Horizontal	m_{LX}	20
Right Vertical	m_{RZ}	30
Left Vertical	m_{LZ}	27
Total	$\boldsymbol{m_T}$	*792*

.

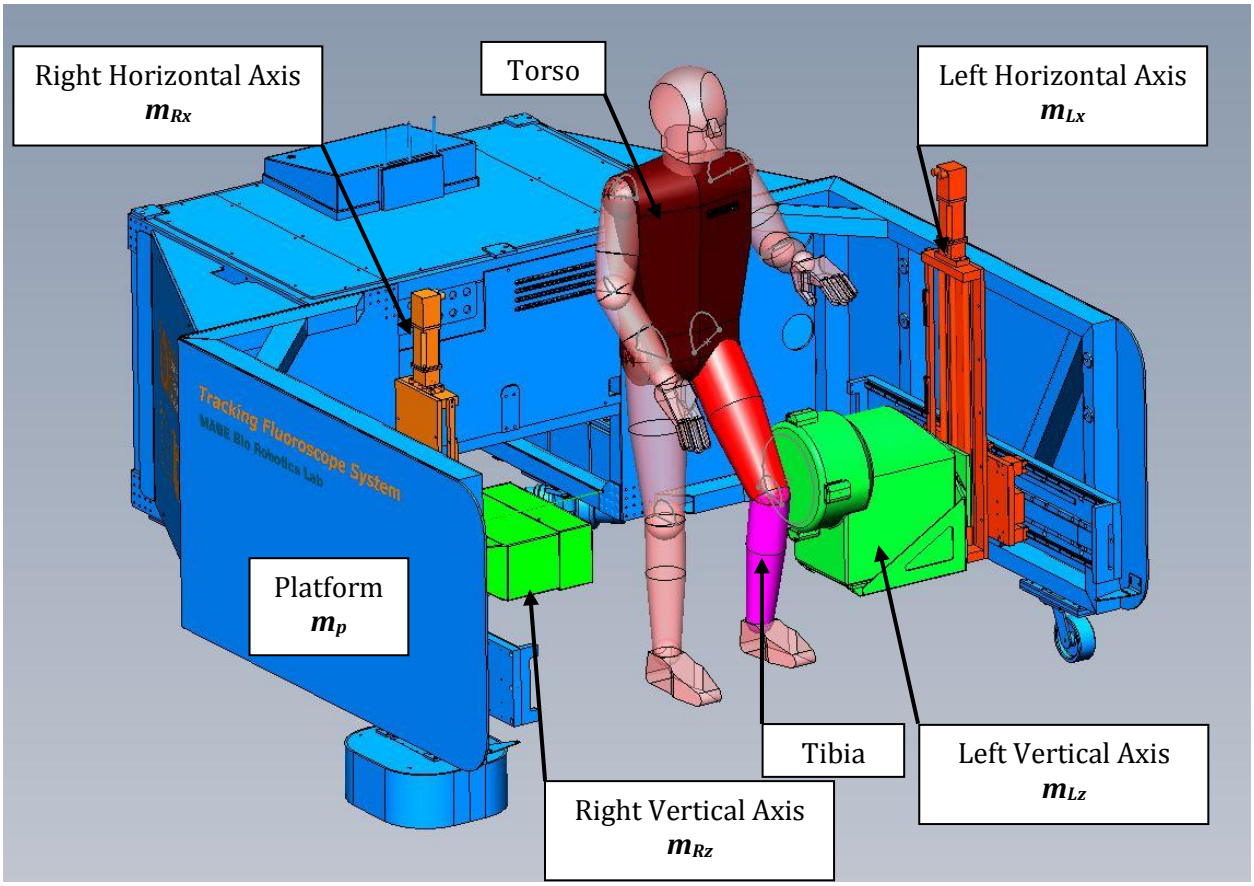

Figure 2 Rigid Body Model of TFS

The robot has eight actuator channels.

- Two MIWDs with turning and driving motors (4 DOF total),
- Two linear motors for the horizontal axes,
- Two rotary servo motors driving a ball screw for vertical axes.

There are 13 sensor channels:

- Encoders from all four axes,
- Encoders from both MIWD driving motors
- Potentiometers from both MIWD turning motors,
- Video feedback of the distance of the Joint of Interest from the center of the camera (x-ray or external camera) in 2 directions, and
- Laser Range Scan of Subject Torso providing two translational and one rotational input of the torso.

To date, the TFS has only been used to analyze motions that occur in a straight line. For the majority of this work, the two driving wheels will be considered to remain parallel to each other and parallel to the motion of the horizontal axes. The two wheels are identical motors and will be actuated using the same command signal. The feedback of the left driving encoder will be used. The necessary actuator and sensor channels for linear motion are listed below.

Actuator channels for linear motion:

- MIWD wheels aligned for linear motion
- Right Horizontal Axis
- Right Vertical Axis
- Left Horizontal Axis
- Left Vertical Axis

Sensor channels for linear motion:

- Left MIWD encoder
- Right Horizontal encoder
- Right Vertical encoder
- Left Horizontal encoder
- Left Vertical encoder
- Laser feedback location of horizontal Torso location
- Camera feedback location of horizontal and vertical Joint of Interest location

Table 2 defines the channels for TFS linear motion and Figure 3 provided a combined block diagram of the system.

Table 2 TFS Linear Channel Definition

	Channel	Mass	Force	Encoder Feedback	State
Platform	1	m_p	f_p	Left Wheel	x_p
Horizontal Right Axis	2	$m_{Ra} = m_{RaH} + m_{RaV}$	f_{RaH}	Right Horizontal	$x_{Ra/p}$
Vertical Right Axis	3	m_{RaV}	f_{RaV}	Right Vertical	$z_{Ra/p}$
Horizontal Left Axis	4	$m_{La} = m_{LaH} + m_{LaV}$	f_{LaH}	Left Horizontal	$x_{La/p}$
Vertical Left Axis	5	m_{LaV}	f_{LaV}	Left Vertical	$z_{La/p}$

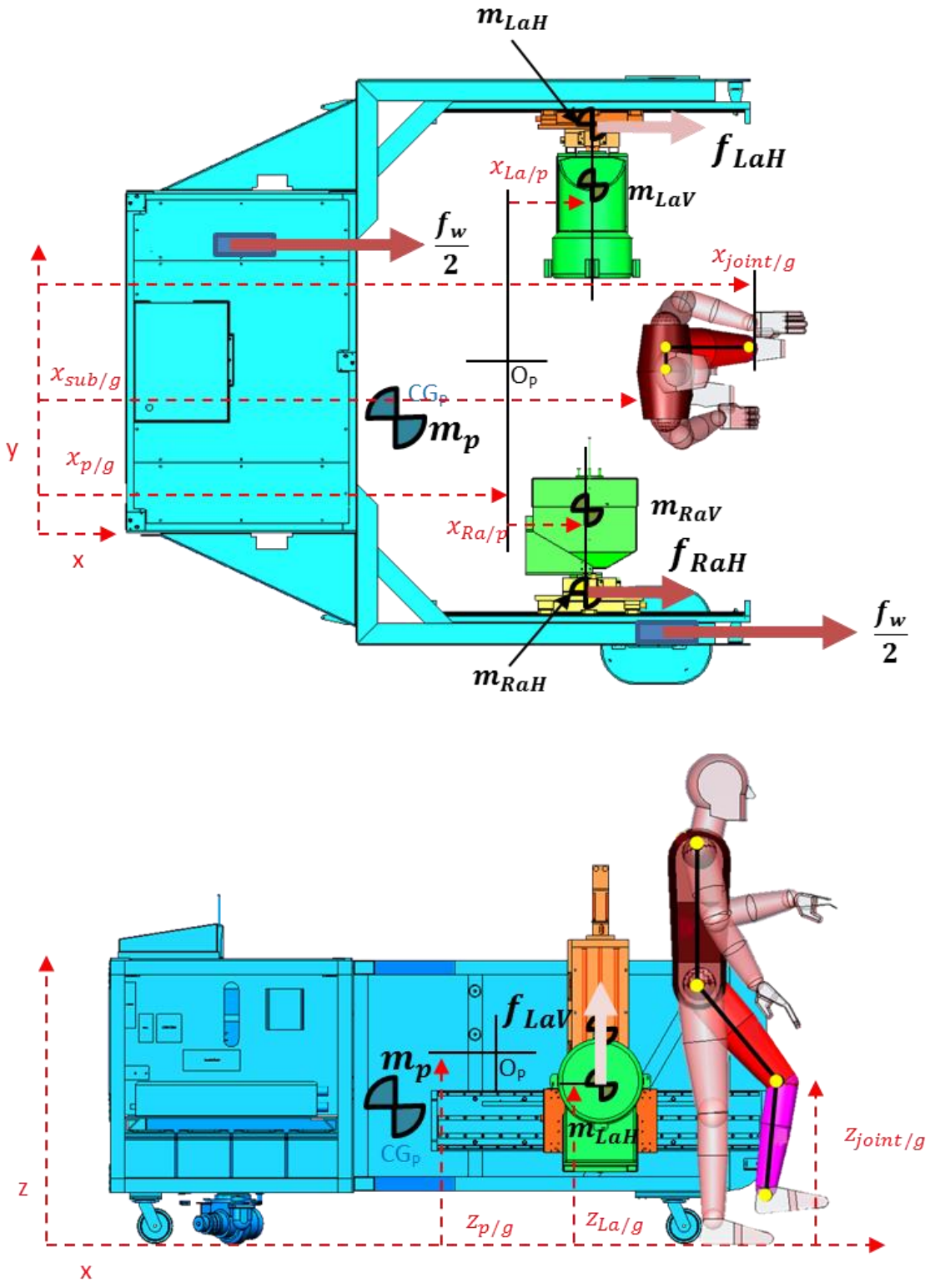

Figure 3 TFS Linear Block Diagram

The depicted configuration provides the most significant cross-coupling effects, which must be accounted for before curvilinear motion can be achieved.

There are five steps associated with developing empirical models of each actuator channel.

- Isolate the channel by locking all other actuator channels,
- Record an open loop response from a known input at a known sampling rate,
- Record closed position loop response from a known input at a known sampling rate and known gains,
- Develop a model using the equations of motion of the system and MATLAB System Identification tools to estimate model parameters,
- Validate the model by applying other inputs and compare the actual and modeled outputs

The obvious choice for a basic model is a linear, second order system. If the modeled system does not respond like the actual system, more complicated models including nonlinear friction affects must be used.

4.2 Supervisory Control Architecture

The TFS has several independent supervisory control loops. A thorough explanation of the TFS system architecture was done by [52]. Figure 4, modified from [52], shows the major systems. One of primary importance is the safety control system. The safety system uses a Mitsubishi FX PLC, which is independent of other control computers, to monitor the environment of the TFS and disable the x-ray equipment and all drives if any of the following faults are detected from:

- A sensing bumper, indicating that the bumper has been depressed,
- The sonar sensors, indicating an obstacle in the path of the TFS,
- An Emergency switch, indicating that a E-Stop has been depressed,
- The control computer, indicating that the computer has become unresponsive,
- The remote control relays, indicating a remote E-Stop condition.

The sensing system is responsible for collecting data from the laser scanners and cameras, processing the data and transmitting the needed control information to the main control unit, synchronizing the data and storing recorded images. The Main Control Unit issues commands to the drives and provides supervisory drive information to the operator. The Main Control Unit must be capable of manual, operator-controlled drive movements as well as automatic responses to the sensing information.

All research to date has used a primary onboard computer for the main control unit and offloaded the sensing system responsibilities to a secondary onboard computer. The computational complexities were too great for a single computer. Both computers used National Instruments Real Time for the operating system. Figure 5 shows concurrent loops and the communication structure of the standard TFS system. Double arrows represent TCP-IP communication. In order to make the system faster and more deterministic, it is desirable to install one PC that is capable of handling all

the onboard computation. The TCP/IP communication loop between the Control RT PC and the Processing RT PC has undesirable delays.

The newly implemented structure is shown in Figure 6. In addition to the elimination of the communication loop, the new structure includes a different method of controlling the wheels and axes. To date, the axes were controlled using drive amplifiers that have a built-in feedback control loop. The drives have an input of velocity, and use a modified PI controller with feed-forward. This scheme is not acceptable for decoupling schemes, because the system is fundamentally coupled on the mass-acceleration/ force level, not the velocity level. The proposed structure eliminates the drive control loop, executing a single PD control with feedforward from the decoupling control. Figure 7 compares the two structures.

During the tuning of the original PI controller, it was necessary to make the K_p term a function of error magnitude. For errors less than 10 mm, the proportional gain was scaled down, allowing for smooth motions when the tracking is acceptable. For error above 10 mm, the proportional gain was a constant. The new control scheme no longer needs this non-linearity for stability. Implementation of the new scheme and structure was accomplished using FPGA PCIe boards made by National Instruments and mounted on a custom PC from Dell. The FPGA monitors the encoders of all drives and sends an analog signal proportional to the desired drive current. The FPGA clock is 40 MHz, and communication to and from the control computer to the FPGA occurs on an average of 50 kHz. Any delay caused by the communication to the FPGA is considered negligible.

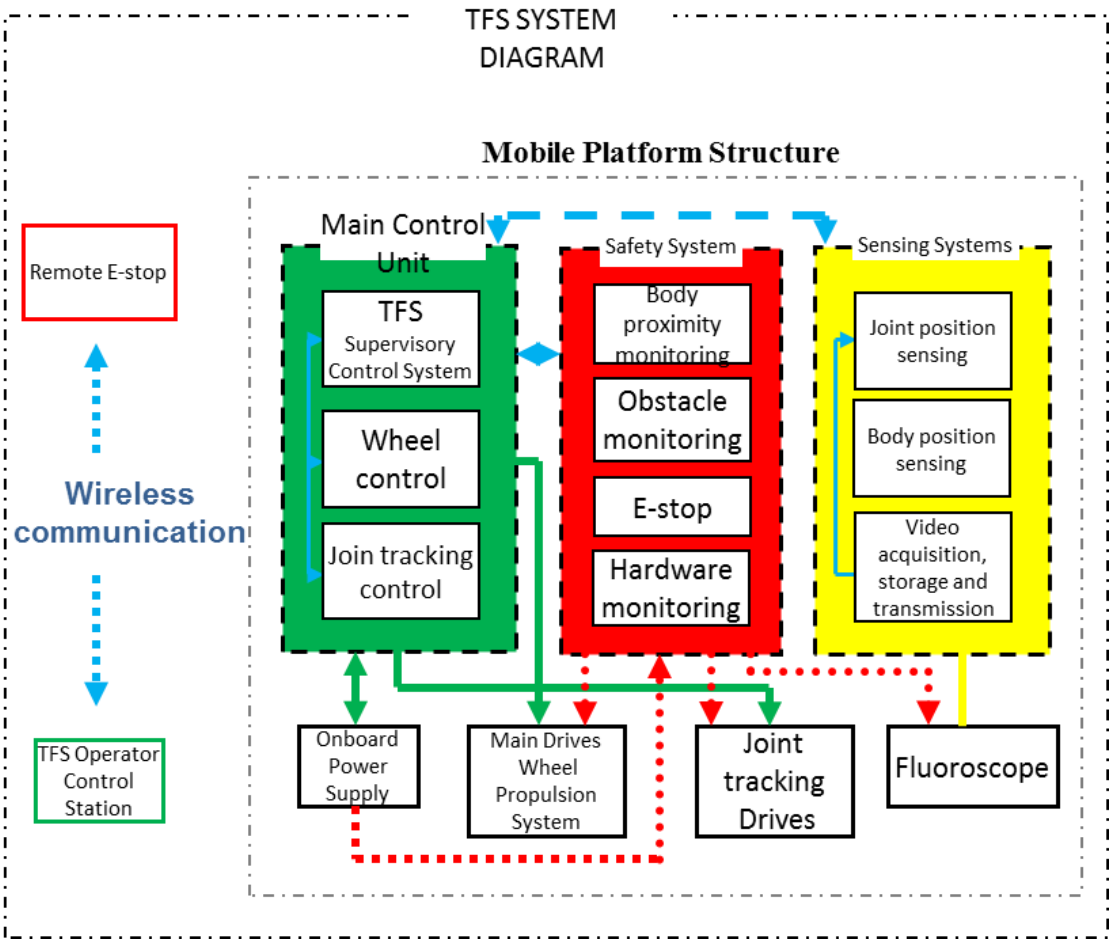

Figure 4 TFS System Diagram

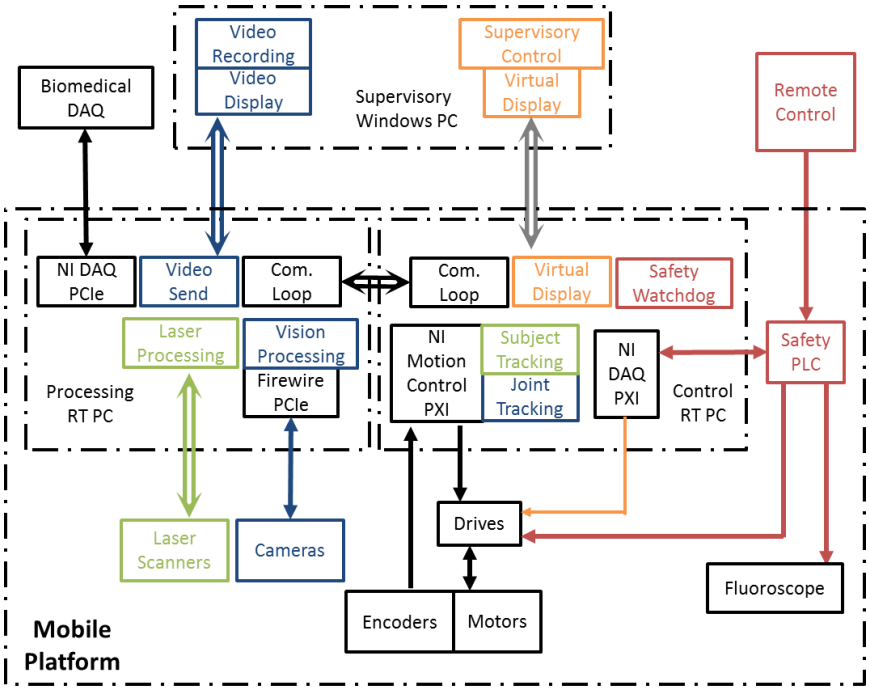

Figure 5 Former TFS Communication Structure and Loop Scheme

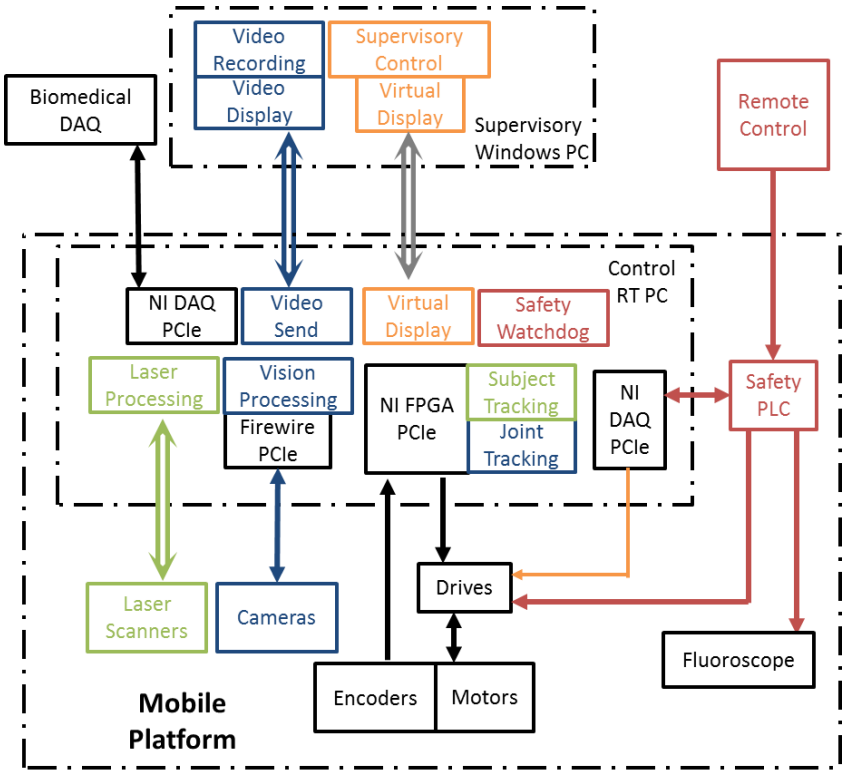

Figure 6 Current TFS Communication Structure and Loop Scheme

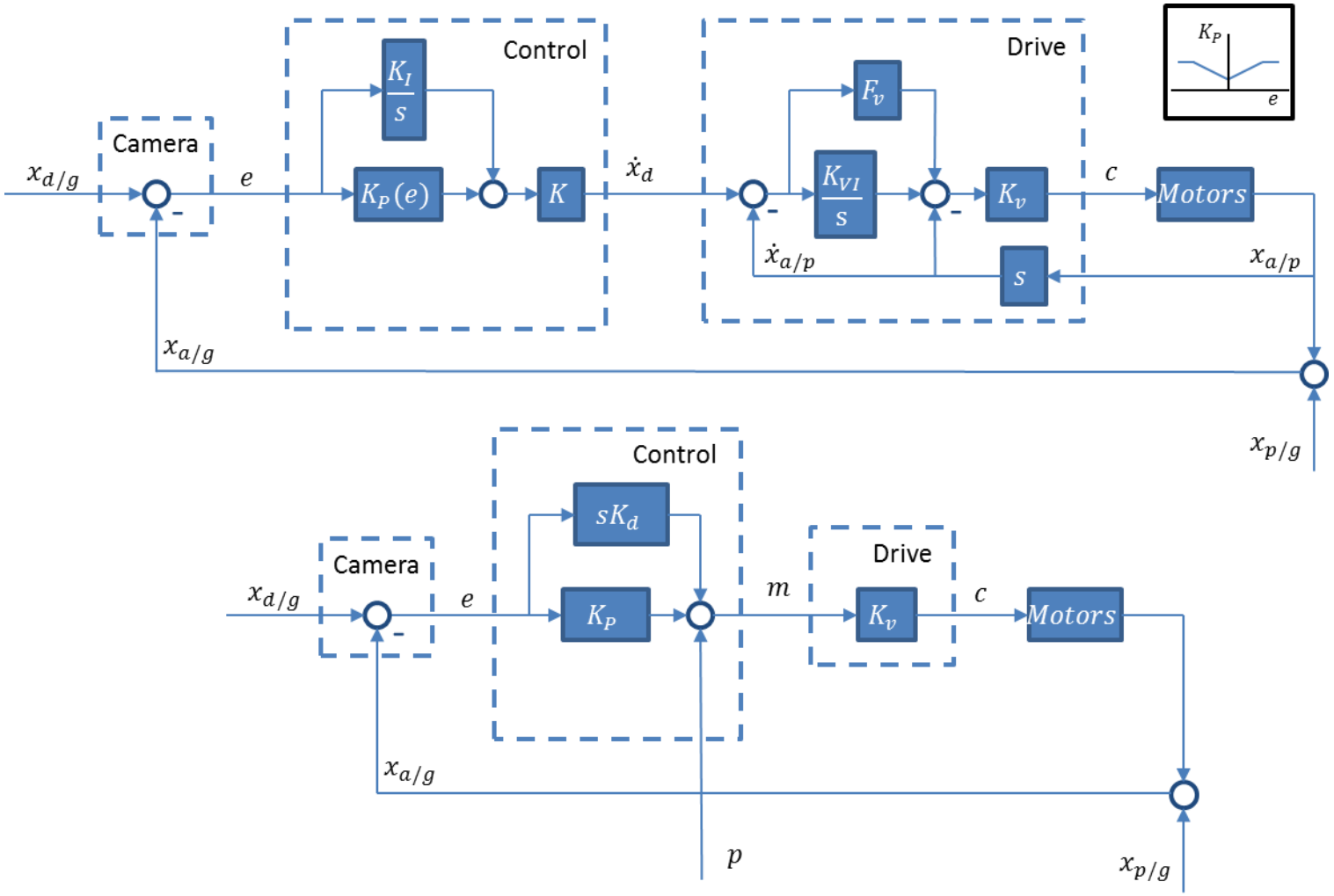

Figure 7 Former and Current Control Structure of Horizontal Axes

Each motor on the TFS is driven by a power amplifier. The MIWD units are composed of 24VDC brushless motors. The axis motors are driven by three phase 110 VAC. The amplifiers are each driven by the control computer which generates an analog voltage in the range of -10V to 10V. The current output for each amplifier is proportional to the input voltage. As in most mechatronic systems, the response time of the electrical circuit portion of the amplifier-motor system is fast enough to neglect. Throughout this work the input to each amplifier will have units of Volts, and the output from the motor will be x_i with units of millimeters. The motor will provide f_i Newtons of force, where $f_i = C_i u_i$ and C_i has the units of Newtons per Volt, as shown in Figure 8. The details of each system will be provided in the corresponding sections below.

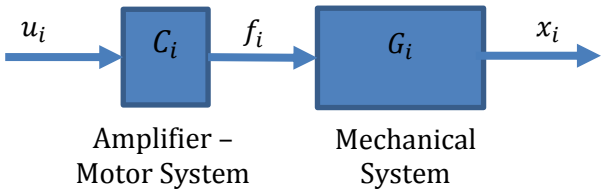

Figure 8 Transfer Function Definition

4.3 Simulation

The purpose of simulating human motion to the TFS is to create a set of repeatable inputs similar to the types of input a real human would produce. Repeatability is important when comparing two different control schemes. Realistic inputs are important to ensure the control strategies will work for the frequency content of real data and to provide benchmarks for the control strategy.

This research used two types of input simulation: well-established, analytical inputs and kinematically-accurate, empirical inputs. Step and ramp inputs are useful for gaining insight into the system. Responses to ramp and step inputs are well established. For instance, step inputs excite high frequencies in the system. This can be useful in discovering un-modeled system behavior. Confidence in the accuracy of a proposed model is established by comparing actual results against the expected results of known inputs.

Once the accuracy of the model is established, a control law can be designed to optimize the response based on the actual input to the model. To simulate the human input, a Microsoft Kinect was used to empirically capture humans performing five natural activities, described in Table 3.

These activities are the types of motion the TFS is required track. The goal is to use the collected data to simulate the sensors located on the TFS. By analyzing the Kinect data, it can be improved to better represent the content of human motion, both in terms of frequency content and amplitude. Figure 10 shows the process of converting the raw Kinect data into a simulated sensor reading on the TFS.

Table 3 Natural Human Motion Description

Activity	Initial Position	Motion	Final Position
Chair Rise	Sitting position with the back straight and knees at a right angle to the back.	Person begins standing up	Standing position with the legs fully extended
Gait	Standing with back straight and the leg of interest slightly ahead of the other leg	Person begins walking	Standing straight up with legs fully extended
Deep Knee Bend	Standing position with the leg of interest fully extended	Person slowly squats down keeping the back straight and flexing the knee of interest until full knee flexion is achieved	Squatting position with the knee of the leg of interest in fully flexion
Step Up	Standing with back straight on a level surface right below a series of steps	Person walks up the steps	Standing position with both legs fully extended
Step Down	Standing with back straight on a level surface right above a series of steps	Person walks down the steps	Standing position with both legs fully extended
Curvilinear Walk	Standing with back straight and the leg of interest slightly ahead of the other leg	Person walks following the back described by Figure 9	Standing position with both legs fully extended

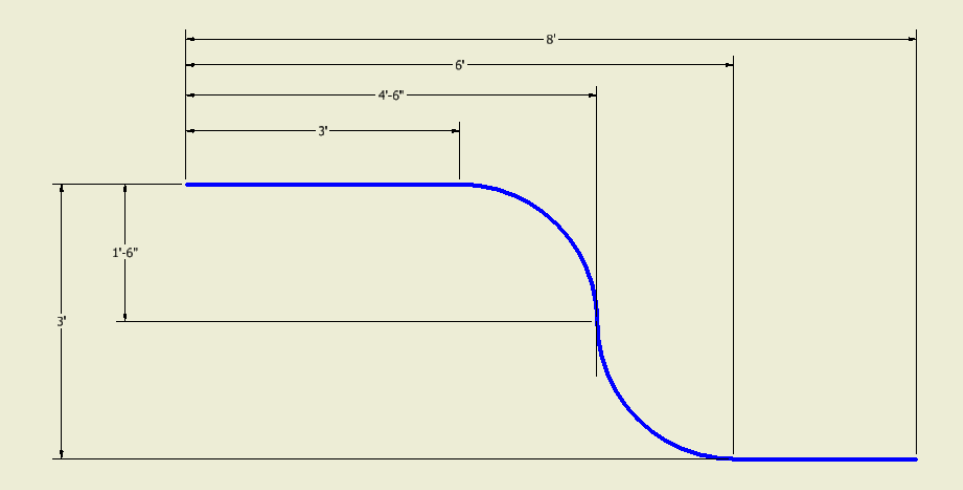

Figure 9 Curvilinear Path

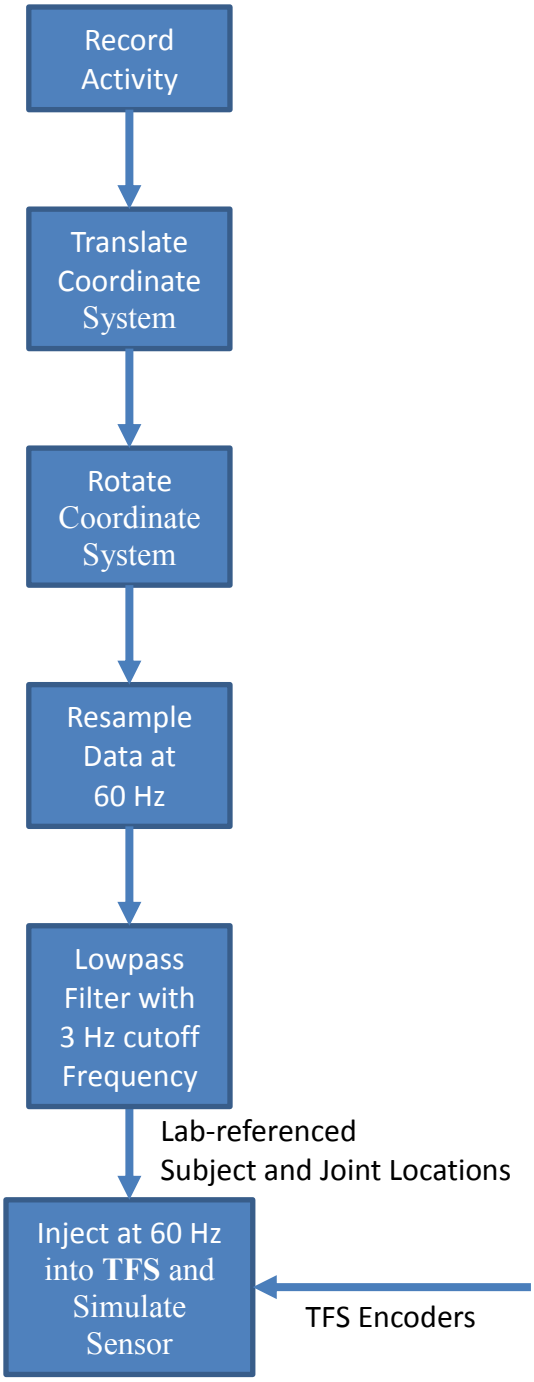

Figure 10 Kinect Dataflow

RECORDED DATA

The Microsoft Kinect is a RGB-D camera, providing color data and depth information of each pixel. In addition to this information, the Kinect has a built-in skeleton generator, shown in Figure 11. The generator outputs 20 anatomical points defined from a coordinate space described in Figure 12, which was modified from [53]. The provided points are recorded in millimeters with a millisecond timestamp. Table 4 shows a partial list of the raw Kinect skeletal data. The skeletal algorithm is proprietary, but the basic concept is to take a point cloud corresponding to a human and fit the anatomical points on the cloud. The algorithm uses background data to calculate a floor plane to aid in the translation of pixels to mm. Assumptions regarding the orientation of the human and the stationary nature of the background are other key elements of the algorithm. The Kinect records skeleton data at roughly 15 frames per second. [54] The data are transferred using USB protocol, and is recorded in LabView using the freeware Microsoft SDK Kinect Driver and the Kinesthesia Toolkit for LabView developed by [55]. The data are stored as a 61 x n text array, where the first column is time and n is the number of recorded frames. For the protection of the human subject and in accordance with the Internal Review Board of the University of Tennessee, only the skeletal time-stamped data provided by the Kinect is saved.

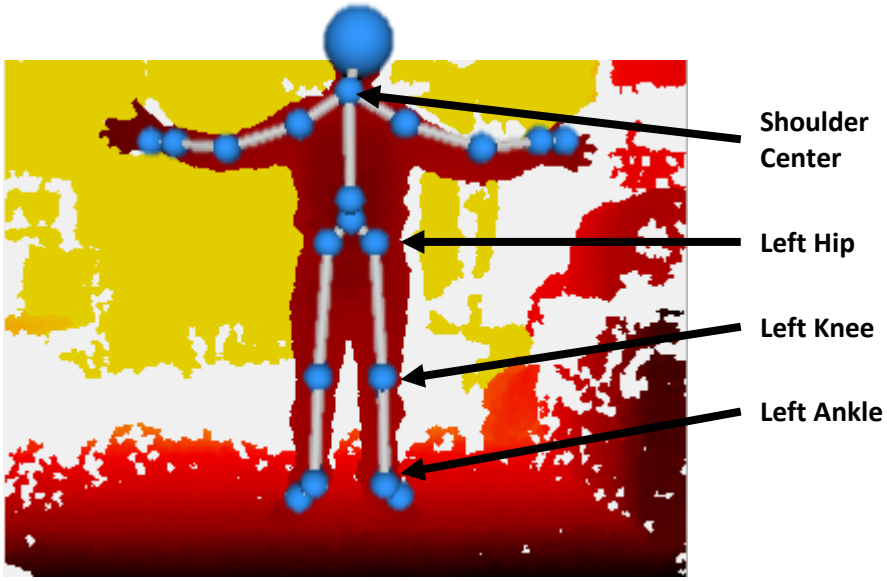

Figure 11 Twenty-point Kinect Skeleton Data

Figure 12 Kinect Coordinate System

Table 4 Partial Table of Raw Kinect Skeleton Data

Time	Hip_X	Hip_Y	Hip_Z	Torso_X	Torso_Y	Torso_Z	Neck_X	Neck_Y	Neck_Z
0	-1079	602	3700	-1087	672	3769	-1115	1092	3783
64	-1079	603	3699	-1087	673	3768	-1114	1093	3780
132	-1077	602	3698	-1086	672	3767	-1112	1091	3777
200	-1077	603	3698	-1086	673	3766	-1111	1089	3775
264	-1076	602	3698	-1085	672	3767	-1111	1088	3774
332	-1073	602	3699	-1084	672	3766	-1108	1086	3770
400	-1073	602	3699	-1084	672	3766	-1104	1084	3769
464	-1072	604	3700	-1082	673	3767	-1104	1085	3770
532	-1072	604	3700	-1082	673	3767	-1106	1084	3770

Coordinate System redefinition according to platform orientation

In order to simulate a sensor input, it is desirable to translate the native Kinect coordinate system into a new coordinate system that is aligned from the human activity. This is because the mobile platform is always positioned with respect to the person based on the type of activity and the joint of interest. The origin of all Kinect data is taken to be the initial hip position. A simple transformation can be achieved by subtracting the desired initial position from all values recorded by the Kinect. The coordinate axes are then defined from the origin and two other points, which vary according to the activity recorded. Figure 13 through Figure 16 show how a coordinate system is generated from all activities. While all analysis to date has used an x-ray image that comes from a medial-lateral (sideways) perspective, hip information is typically extracted from an

x-ray image that is generated from an anterior-posterior (front to back) perspective. In this position, the human faces the side of the TFS, and the platform moves perpendicularly to the horizontal axes, as shown in Figure 17. The recorded Kinect data can be used to simulate this orientation by performing a final rotation that achieves a ninety-degree rotation about the z-axis. Figure 18 shows this coordinate system for a walk activity.

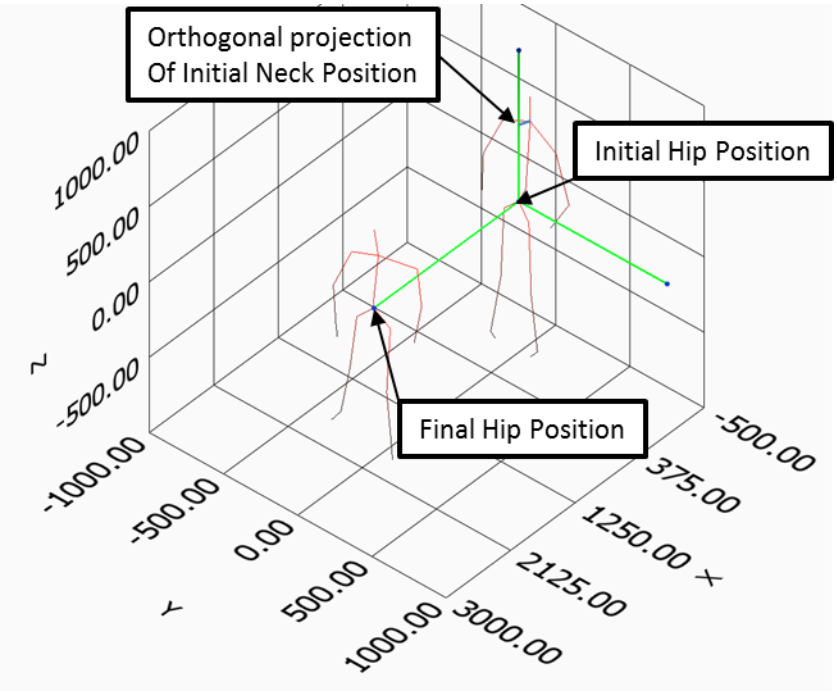

Figure 13 World Frame from Walk Kinect Data

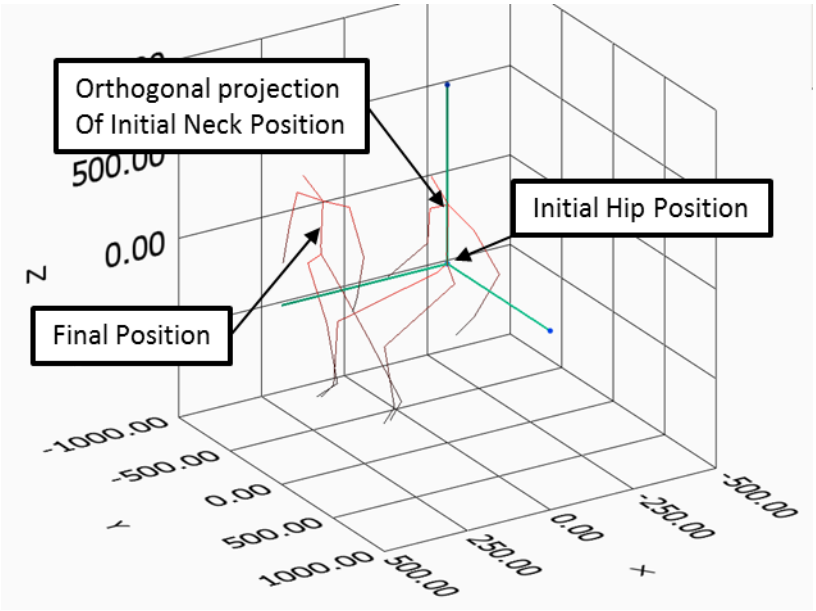

Figure 14 World Frame from Chair Rise Kinect Data

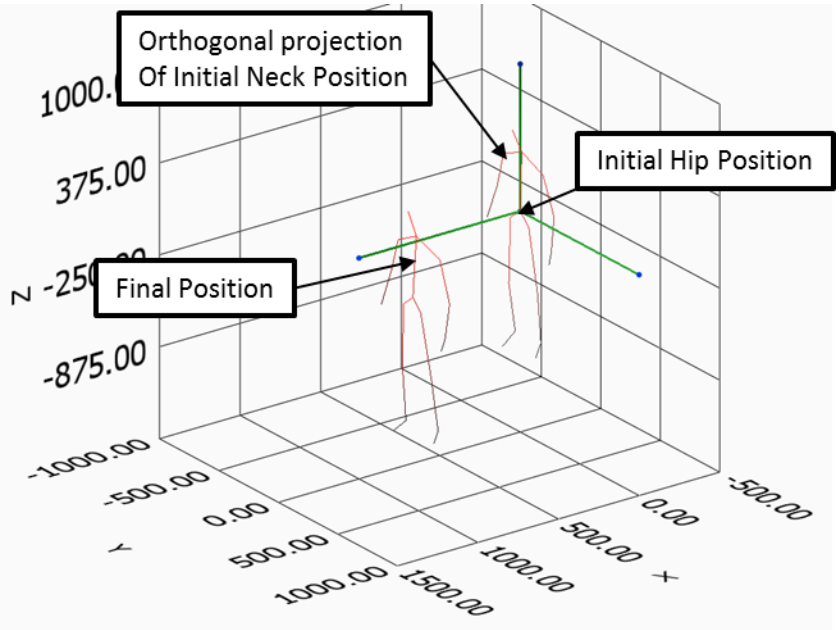

Figure 15 World Frame from Step Down Kinect Data

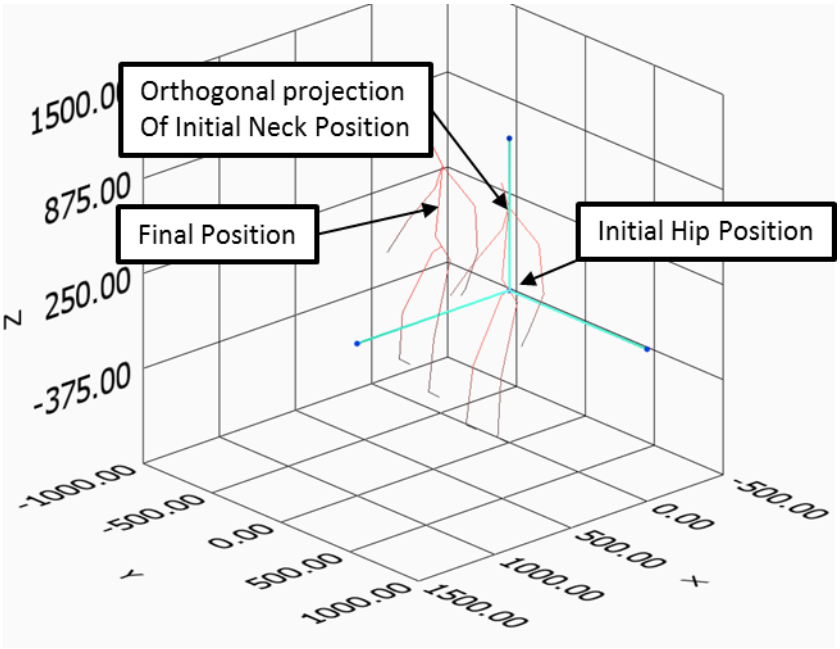

Figure 16 World Frame from Step Up Kinect Data

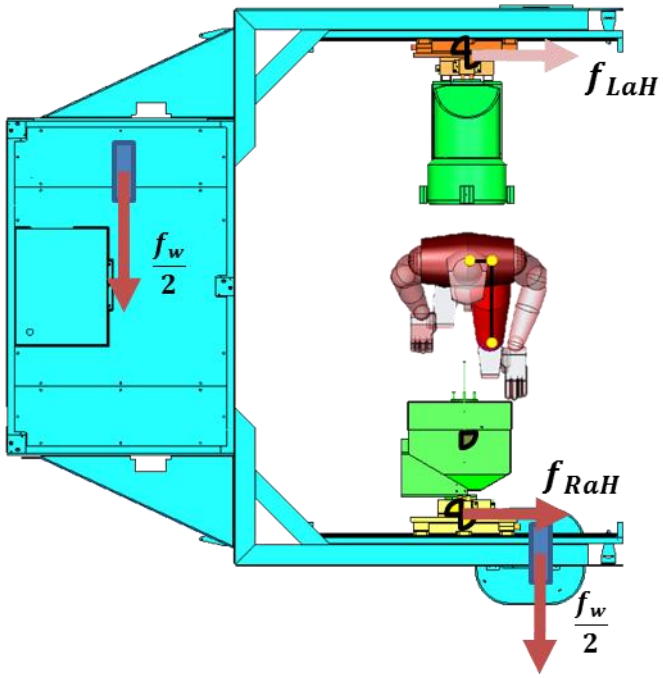

Figure 17 TFS Configuration for Hip Tracking

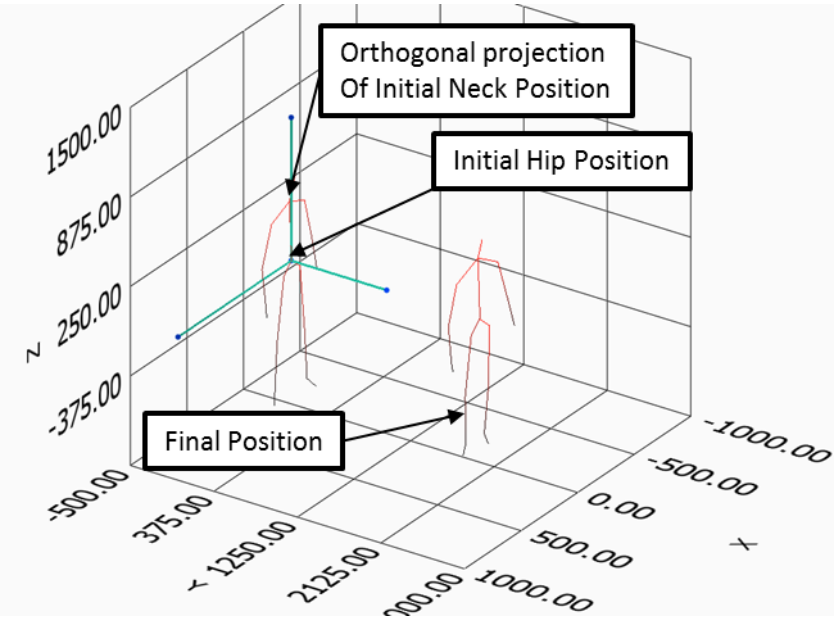

Figure 18 World Frame from Walk Kinect Data for Hips

RESAMPLE AND FILTER

All camera systems onboard the TFS currently run at 60 Hz. In order to simulate the camera input, the data must be resampled to approximate this sampling time of the control system. A one dimensional spline interpolation is performed on each coordinate of each point. In other words, each coordinate system is considered independent for the resample and filter process. The initial and final boundary conditions for the spline algorithm dictate that the derivative of the resulting spline is zero at the boundaries.

Although quite sufficient for gaming applications, the skeletal algorithm employed by the Kinect is inherently noisy. A first order, low pass filter is needed to remove the noise from the data.

The applied filter is a simple Butterworth filter that removes all frequencies greater than 3 Hz. The importance of the simulation is not accuracy of the joint with respect to time, rather accuracy of the frequency content and amplitudes of the expected input. Sharp motions in the Kinect data are caused by algorithm malfunctions and slow sampling, not by actual human motion. These artificial disturbances should be removed from the simulated input.

ONBOARD SENSOR INCLUSION AND INJECTION

After a data set has been created, transformed, resampled and filtered, it is ready to be injected into the TFS. The TFS utilizes two laser rangefinders to determine the location of the human subject. [52] shows the details of the laser processing algorithms. The result is a distance in millimeters from the chest of the human subject to a laser origin located on the back of the TFS cart. A fixed distance from the laser origin to the desired platform origin is defined in Figure 19. Platform control is using the laser is achieved by driving the parameter $x_{s/p}$ to zero.

$$x_{s/p} = x_{s/laser} - d_{laser/p} \quad (2)$$

To use the Kinect data, the center shoulder point is taken to be $x_{s/g}$, and the equation becomes

$$x_{s/p} = x_{s/g} - x_{p/g} \quad (3)$$

where

$$x_{p/g} = x_{w/g} + d_{w/p} \quad (4)$$

is found from the encoder of the left MIWD.

To control the axes, it is desired to have the TP located in the center of the image. This means that the horizontal and vertical distances from center, $x_{j/a}$ and $y_{j/a}$, should be zero, as shown in Figure 20. To use the Kinect data the joint of interest (hip, knee or ankle) is taken to be the point $(x_{j/g}, y_{j/g})$. The equations now become

$$x_{j/a} = x_{j/g} - x_{p/g} - x_{a/p} \quad (5)$$
$$y_{j/a} = y_{j/g} - d_{p/g} - y_{a/p} \quad (6)$$

where $x_{a/p}$ is the encoder reading of the horizontal axis, $y_{a/p}$ is the encoder reading of the vertical axis, $x_{p/g}$ is the encoder reading of the left MIWD, and $d_{p/g}$ is a constant distance.

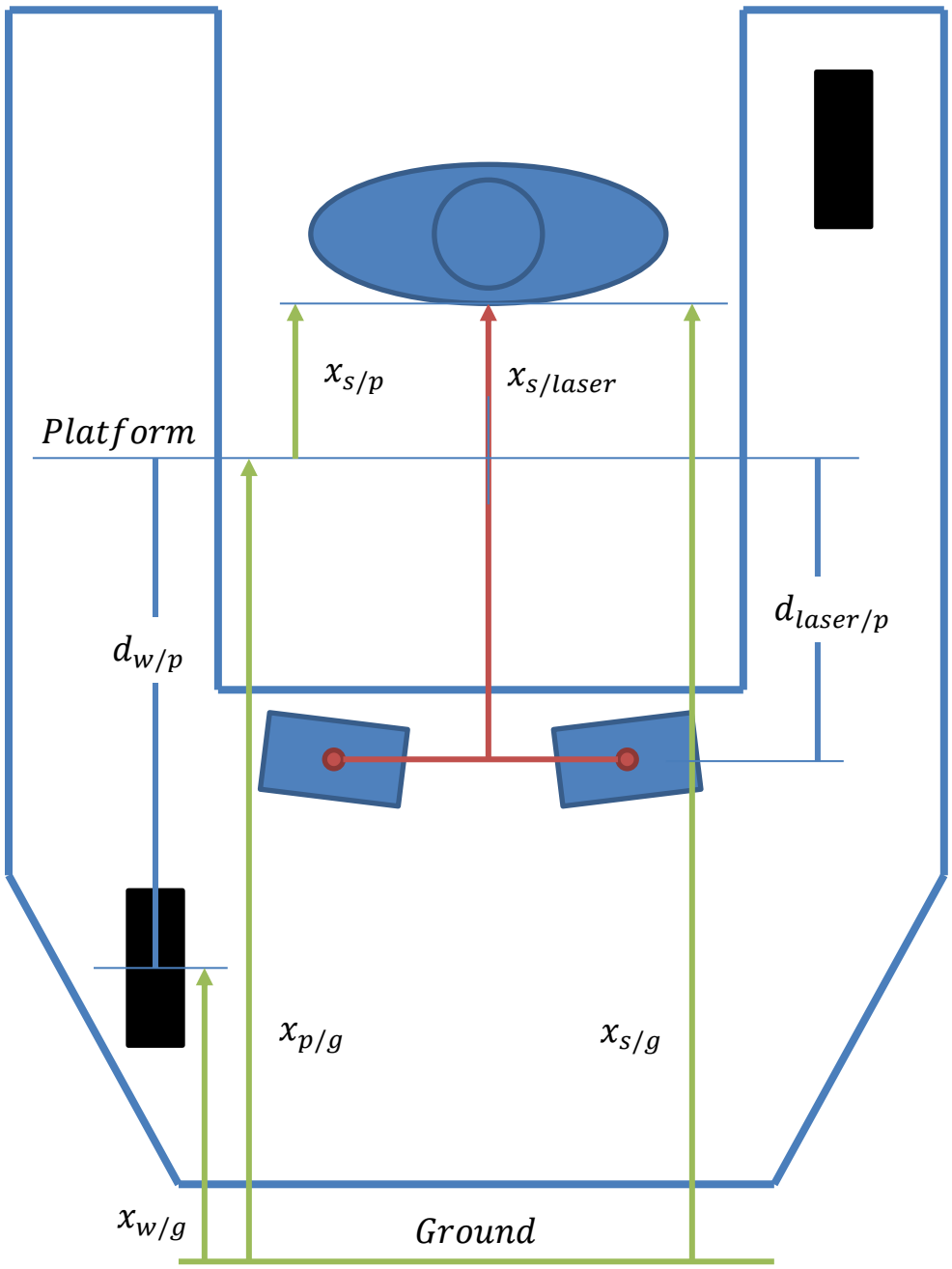

Figure 19 Platform and Laser Coordinate System

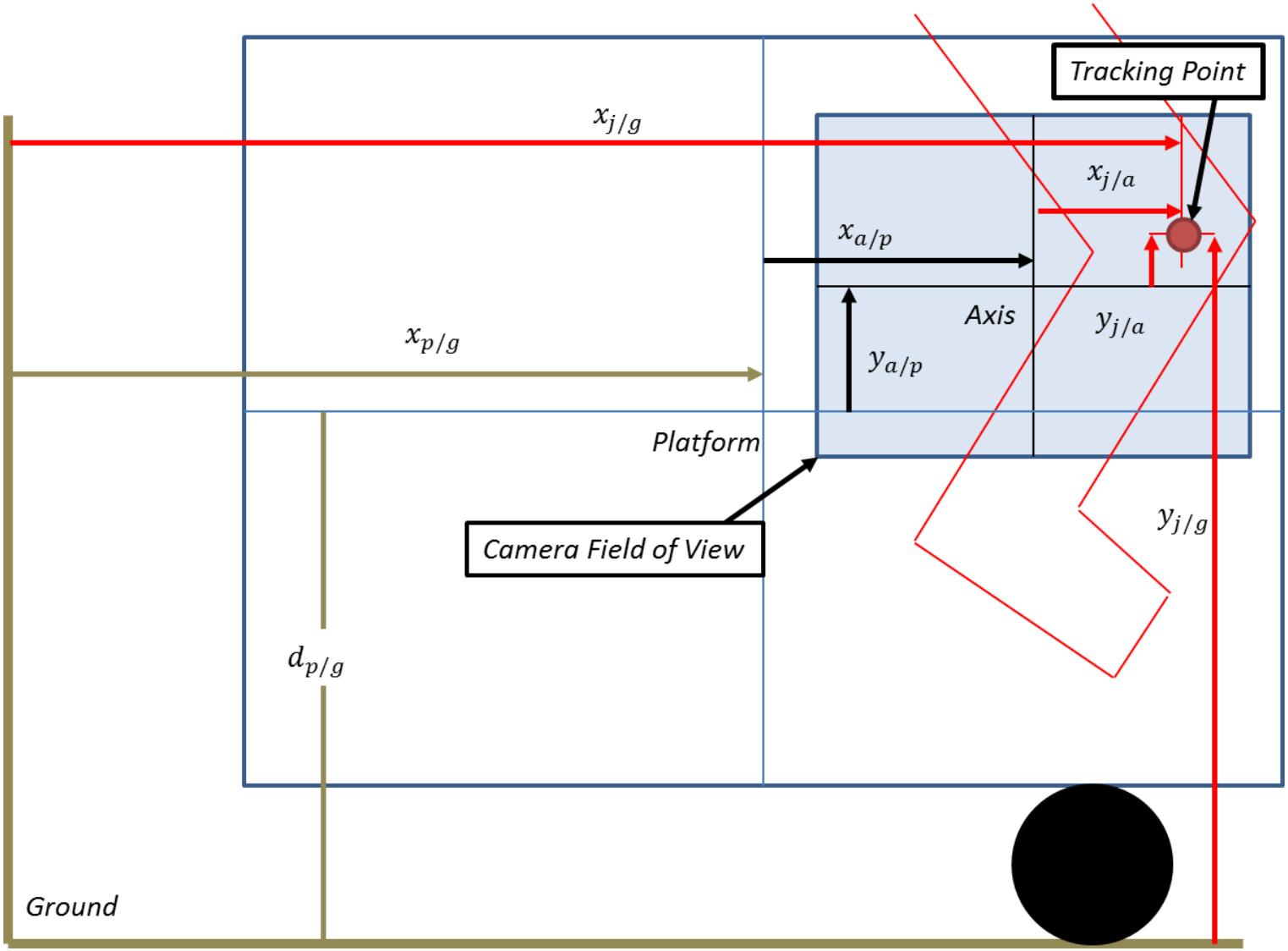

Figure 20 Axis and Camera Coordinate System

STATIONARY TRACKING OF KNEES AND ANKLES

There are times when it is useful to operate only the horizontal and vertical axes. This is important when computing the system characteristics of the uncoupled axes and when tuning the axes. To accomplish this, a modification to the simulation was made. When a subject walks, the recording of the joint of interest is with respect to the ground. The subject might travel several meters, while the horizontal axes only has around 800mm of total travel. The location of the joint of interest is taken with respect to the center of the shoulder. The shoulder was chosen as a reference point because currently the TFS is configured so that the lasers are tracking the human subject's chest. Figure 21 and Figure 22 demonstrate the importance of changing the reference of the data for axes operation without the platform. In each figure, the raw data are displayed in blue, and the resampled, filtered data are displayed in red.

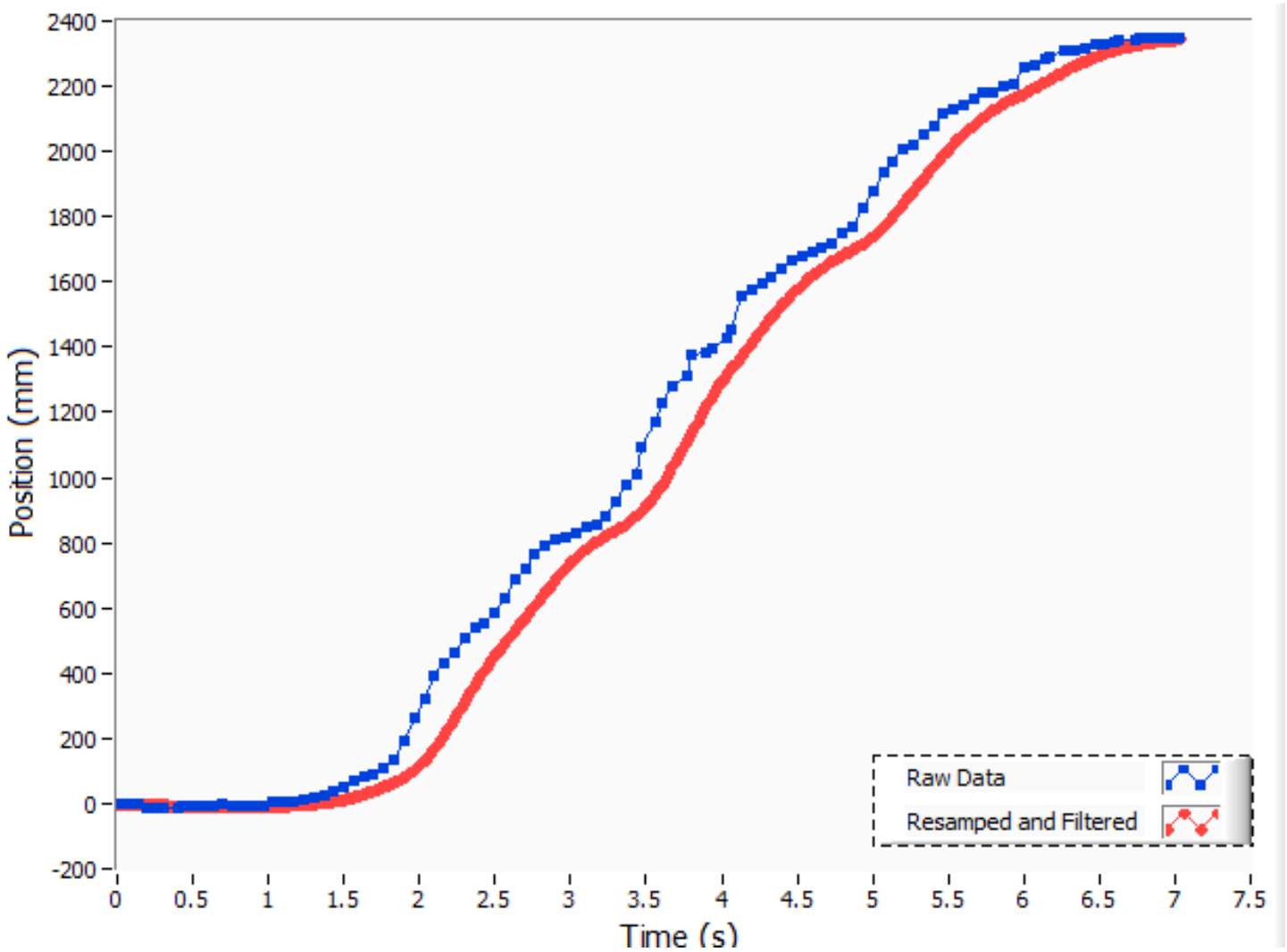

Figure 21 Raw and Filtered Knee Motion Relative to the Lab.

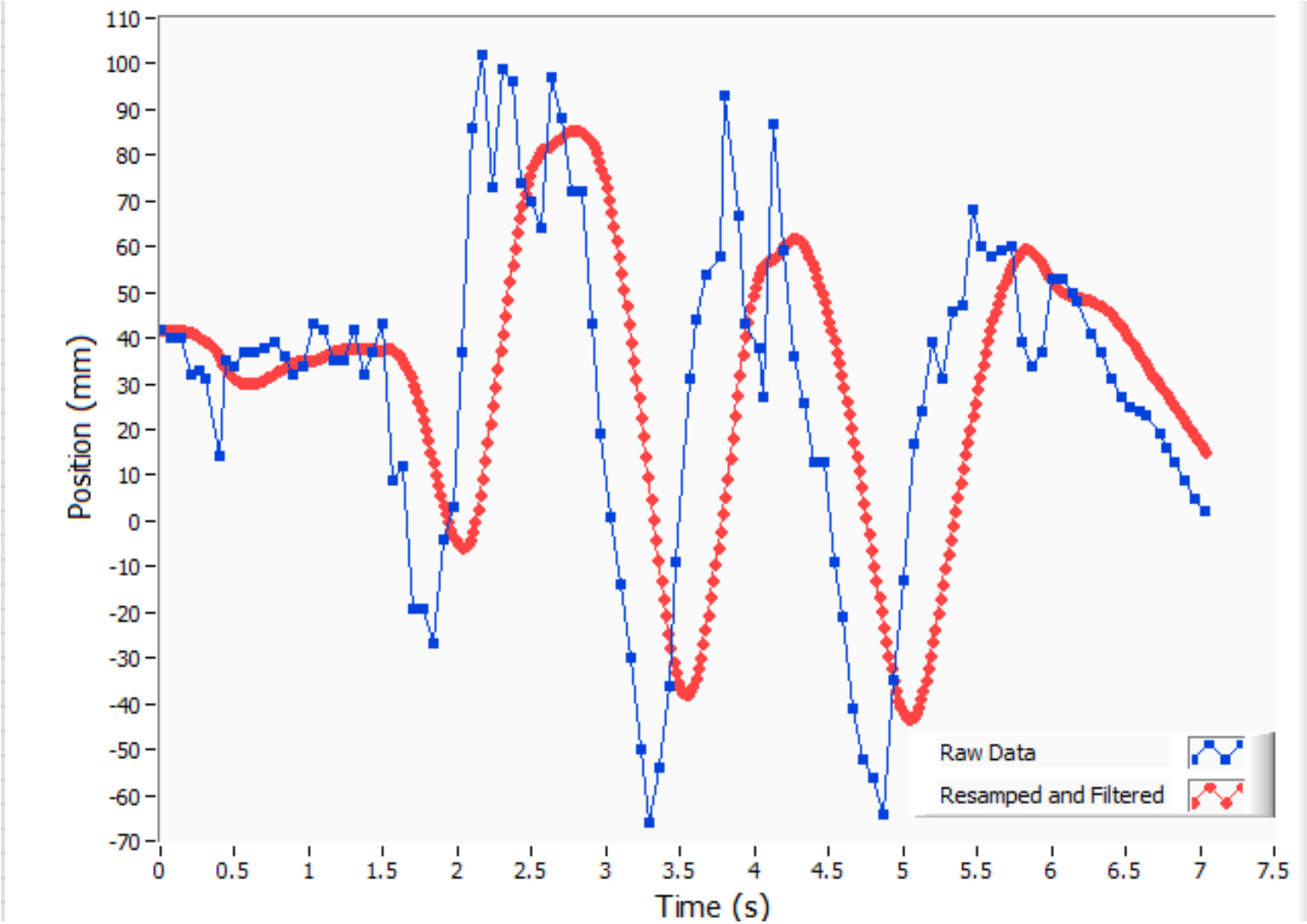

Figure 22 Raw and Filtered Horizontal Knee Motion Relative to the Shoulder.

KINECT LIMITATIONS AND DATA COLLECTION

One of the chief advantages of using the Kinect to capture human activities is the freedom to choose almost any activity desired. The activities chosen for this were restricted to the types of activities of current interest to the biomedical clinical community. Any limitations to the activities are due to the collection nature of the Kinect sensor or algorithm assumptions from the skeleton generator. The IR-driven depth camera and RGB color camera are both 640 x 480 pixels. The Kinect has a depth range of about 800 mm to 4000 mm. All activities must be within this window. The skeleton generator requires that the human must be roughly perpendicular to the system and that most of the body is in the field of view of the sensor. Experimentally, the maximum distance that the Kinect could detect a human is about one meter, while the minimum distance needed was about 0.2 m. This gives the Kinect a working distance of about 0.8 meters. All human activities must be constrained within this distance.

To demonstrate the flexibility of the Kinect sensor, data were collected from humans of different sizes. [56] states that 59.3 inches is the fifth percentile of women over the age of twenty, while the mean height is 63.8 inches. For men over the age of twenty, the mean height was found to be 69.3 inches, while 74.1 inches is the 95^{th} percentile. Data were collected from three subjects. One was 60 inches tall, one was 66 inches tall, and one was 76 inches tall. The Kinect was able to record all activities for all three subjects.

CHAPTER 5. TRANSLATION OF THE MOBILE PLATFORM

5.1 TRANSLATIONAL PLATFORM MODELING

MODEL DEFINITION

The platform is modeled as a mass acted on by the external forces of the MIWD's. The translational equation of motion is

$$m_t \ddot{x}_p + b_p \dot{x}_p = f_w = C_p u_w \tag{7}$$

Where m_t is the mass of the total platform and $b_p$is the friction in the system and f_w is the force of the wheels, provided by the MIWD's. In the Laplace domain, the transfer function becomes

$$\frac{X_p}{U_w} = \left(\frac{C_p/m_t}{s^2 + sb_p/m_t} \right) = \frac{C}{s^2 + sb} \tag{8}$$

where $C = C_p/m_t$ and $b = b_p/m_t$.

To isolate the MIWD driving channel, the horizontal and vertical axes were locked in a known position. Both wheels were turned parallel to each other and parallel to the chassis. Each wheel was sent the same command signal. Since the platform is a rigid body, and the wheels are operating parallel to each other, the model can contain both wheels as one large MIWD. The full model of the combined MIWD driving system is shown in Figure 23.

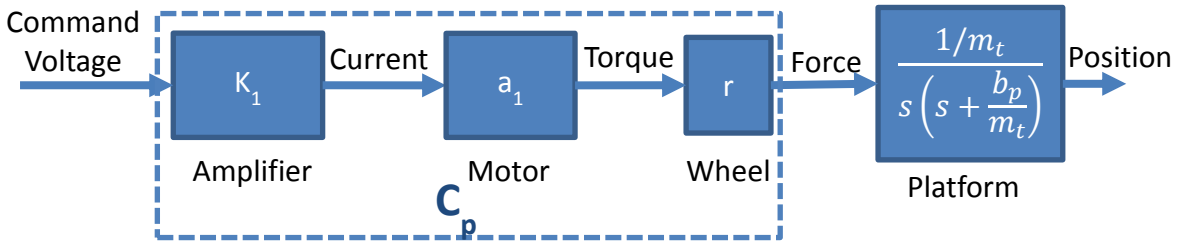

Figure 23 TFS Translation Platform Block Diagram

Again,

$$C = \frac{C_p}{m_t} = \frac{K_1 a_1 r}{m_t} \quad (9)$$

The Wheel component introduces two complications. The first problem results from slip. The time domain equation for the wheel component is:

$$F(t) = r * T(t) \quad (10)$$

This equation is only valid for the no slip condition that occurs when the torque of the motor is less than the torque produced by the static friction between the tire and the ground.

$$f = \mu N = \mu m_t g \quad (11)$$

$$T < fr = \mu m_t g r \quad (12)$$

Figure 24 shows a reduced free body diagram of the torque applied by the MIWD motor and the resulting frictional force acting on the wheel. The total kinetic energy of a translating wheel system is:

$$KE = \frac{1}{2} m \dot{x}^2 + \frac{1}{2} I \dot{\theta}^2 \quad (13)$$

where x is linear motion, m is the mass, θ is the rotation of the wheel, and I is the inertial component of all the wheels. Recognizing that the angular position of the wheel is related to the translational motion of the platform, $r\theta = x$, (13) becomes

$$KE = \frac{1}{2}\left(m + \frac{I}{r^2}\right)\dot{x}^2 \quad (14)$$

In the case of the TFS, the wheels can be assumed to be a cylinder that is 150mm in diameter and 25mm in thickness and is composed of a hard, polyurethane rubber, with a density of around 1.3 g/cm^3 [57]. The equivalent mass of the inertia of four wheels can be estimated:

$$\frac{I}{r^2} = 4\left(\frac{1}{2}\frac{m r^2}{r^2}\right) = 2\pi\rho r^2 h \approx 1.14\ kg \quad (15)$$

The mass of the platform is almost 800 kg, so $\frac{I}{r^2} \ll m$, and can be neglected. Following the work of [58], we can assume that there is no slip, and that the wheels are massless.

The second problem is found in the radius of the wheel. In an ideal system, a wheel has a constant radius. In real systems, however, the rubber that composes the tire of the wheel is compressed by the weight of the platform. If this weight shifts, the compression of the tire changes. This means that is it difficult to use the ideal diameter of the wheel to determine the value *r*. In fact, *r* might be a function of time, and not a constant. This will be handled by considering the radius to be a constant, and the changes to be a disturbance:

$$r(t) = r_0 + d_r(t) \qquad (16)$$

Since the amount of disturbance due to the weight shifting is not known, it will be lumped will all other disturbances in the model. This leads to the final transfer function model shown in Figure 25, where C and b are defined in (8) and (9).

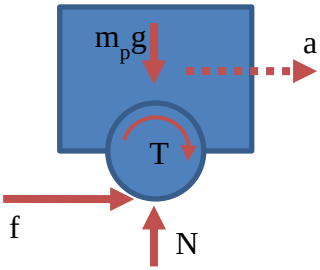

Figure 24 Conversion of Torque to Acceleration with? static friction

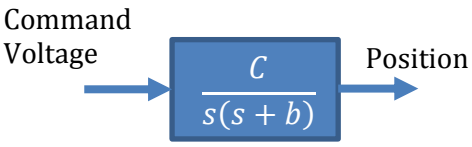

Figure 25 Condensed Platform Block Diagram

PARAMETER ESTIMATION

It is not necessary to determine all the independent values from Figure 23 (such as the compressed radius of the tire). Only the overall constants, C and b need to be estimated. This is accomplished by applying a known command voltage to the amplifiers and recording the position response of the platform. The recorded data are comprised of input, output and sample time and is imported into the MATLAB platform. The MATLAB System Identification Toolbox will adjust estimated values of b and C using a Least Squares-based cost function. Figure 26 shows a step input of 4 Volts applied to the MIWD. The corresponding platform position recorded by the TFS is contrasted with the approximated model. The data were recorded with a sample time of 1ms. The maximum deviance between the model and the actual is about 50 mm, and the least squared loss function has a recorded cost of 279.3.

The modeled transfer function is:

$$G_{pOL} = \frac{57.59}{s^2 + 1.888s} \quad \textbf{(17)}$$

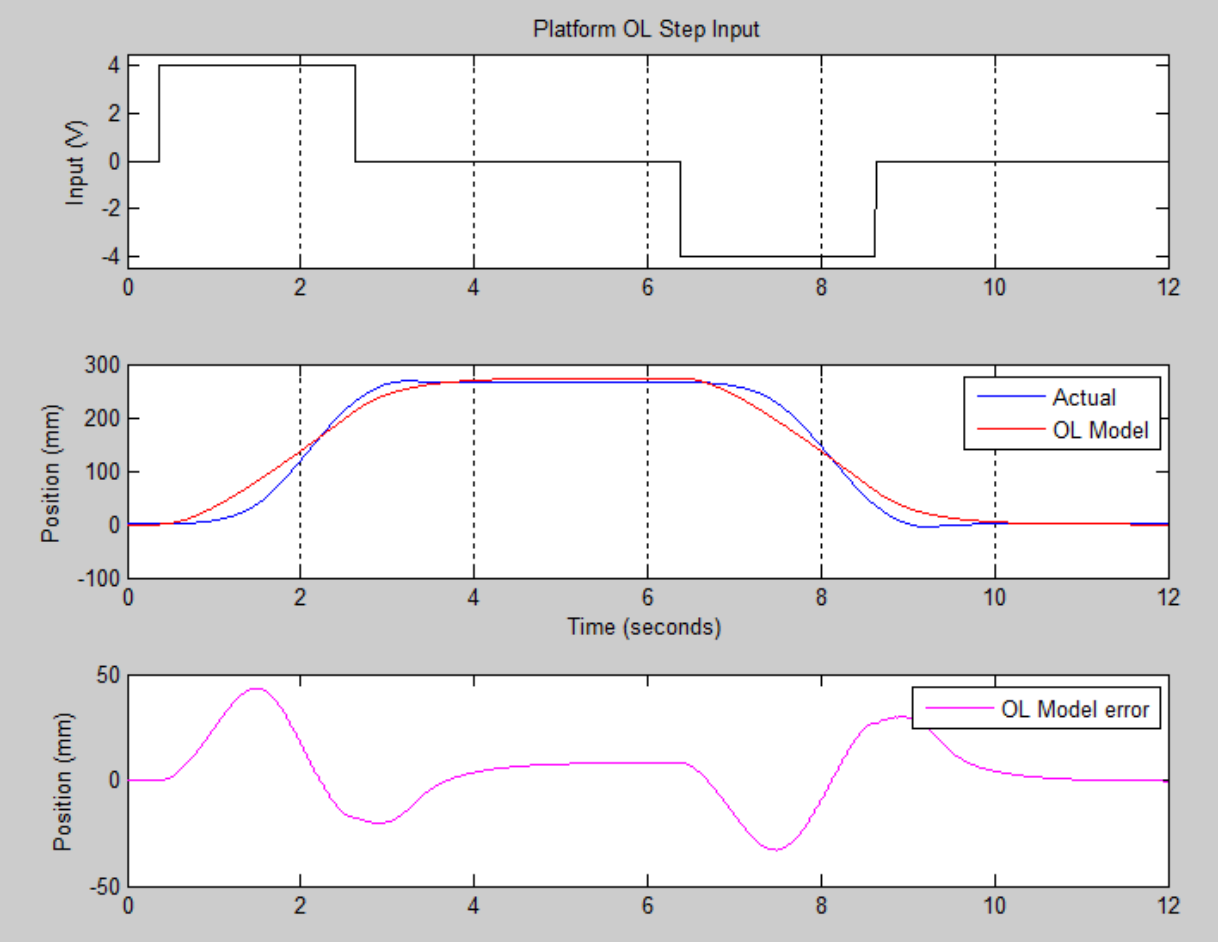

Figure 26 Platform Open Loop Step Response

A closed loop with a proportional gain was then used to get a better estimate of the system. As with all real systems, there is a maximum torque that the MIWD can input. The amplifier is limited to an input of ten volts, which corresponds to a maximum continuous current of 25 Amps. The motor has a maximum output of 120 Watts. By using a nonlinear element, the saturation function, this can be accounted for in the model. Initial saturation is set at 10V for the high value and -10V for the low value.

Figure 28 shows the response of the system with five different values of *K* to a step input of 200 mm and the corresponding control effort. The saturation of the input, which corresponds to the maximum power of the drives, limits the maximum acceleration of the system. For this reason, increasing *K* above one has little impact on the response. Lowering *K* reduces overshoot, but the response time is slower. For *K* values below 0.01, the system has a steady state error that cannot be neglected.

This new data can be used to redefine the parameters of the system. A new modeling technique with Matlab was employed to handle the nonlinearities introduced by the saturation of the drives. A greybox nonlinear model was initialized that used the following code as the governing nonlinear state variables.

```
0  function [dx, y] = WheelNL(t, x, xd, b, C, varargin)
1  m = 792; %kg
2  k = 1;
3  u = k*(xd - x(1)); % Definition of input
4  % Saturation of input
5  if u > 10
6      u = 10;
7  elseif u < -10
8      u = -10;
9  end
10 % Output Equation
11 y = x(1);
12
13 %State equations
14 dx = [x(2);              ... % x(2) = velocity
15    1/m*(-b*x(2) + C*u) ... % EOM for CL P control
16    ];
```

Line 3 defines a P-Control input. Lines 4 through 9 limit the maximum input to the state. Using a K value of one, new values for b and C were estimated. This modified the open loop transfer function:

$$G_{pCL} = \frac{85.94}{s^2 + 1.515s} \tag{18}$$

This new model is a much better fit, having a least squares loss function of 13.9 and a maximum deviance from the actual response of 11mm. Figure 29 shows the desired position set points and the actual and modeled response of the platform.

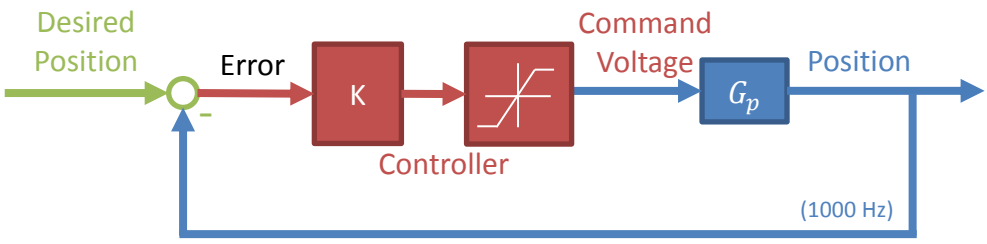

Figure 27 Position Feedback Control System of Platform

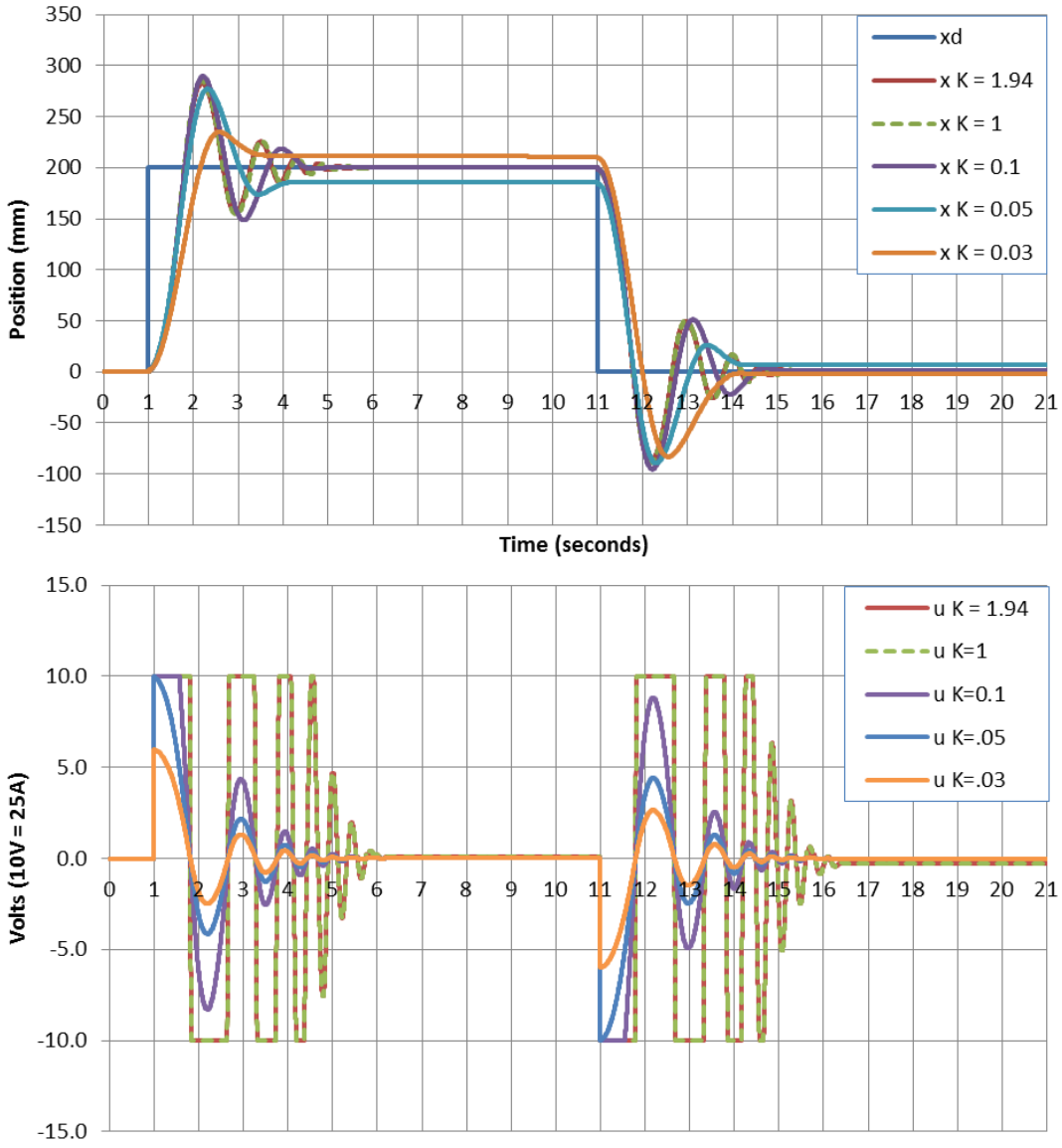

Figure 28 Platform Closed Loop Step Response with Various K

The closed loop data were then used in Simulink to compare the two transfer functions. Figure 30 shows the block diagram used to compare the two transfer functions. Figure 31 shows the response. The closed loop model performs better than the open loop model.

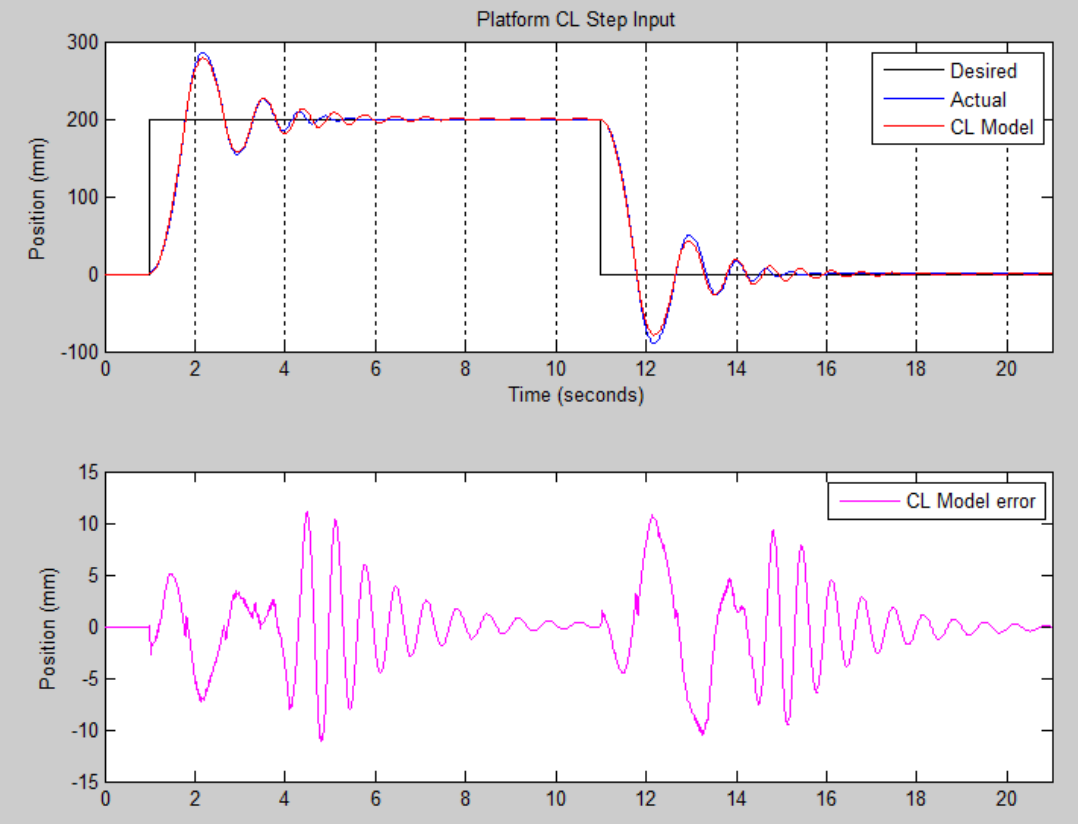

Figure 29 Platform Closed Loop Step Response

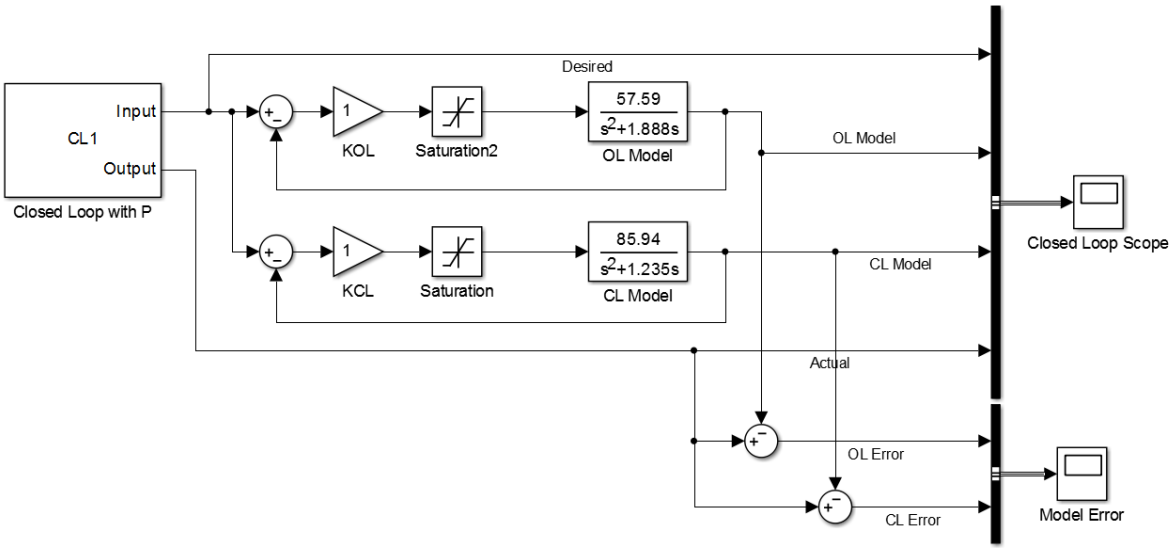

Figure 30 Platform CL P Control Simulink

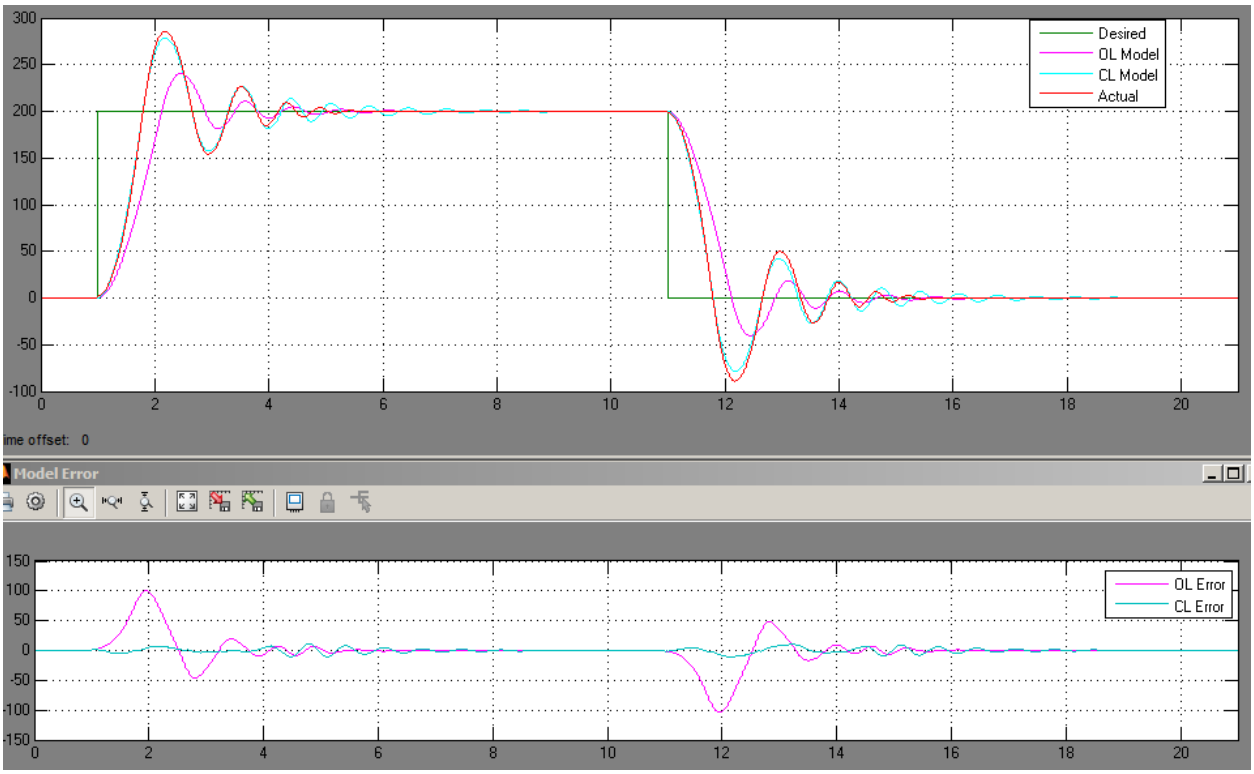

Figure 31 Platform Closed Loop P Control Modeled Response

5.2 Translational Platform Control

The previous system tests and resulting models provide the insight needed to apply control. A closer look at the control effort in Figure 28 shows that a proportional control scheme provides a faster response at the cost of a severe overshoot and oscillations. Adding a derivate term to the control will decrease the overshoot [59]. The new PD control scheme was designed in Labview and is shown in Figure 32.

Increasing the derivative term effectively adds damping to the system. Figure 33 shows several iterations in the tuning process.

The advantage of adding derivative action to the system can be seen in Figure 34. Response to disturbances is the same, while overshoot, settling time and control effort are reduced. A tuned PC controller was found to be:

$$K_{plat}(s) = 0.2 + 0.02s \quad (19)$$

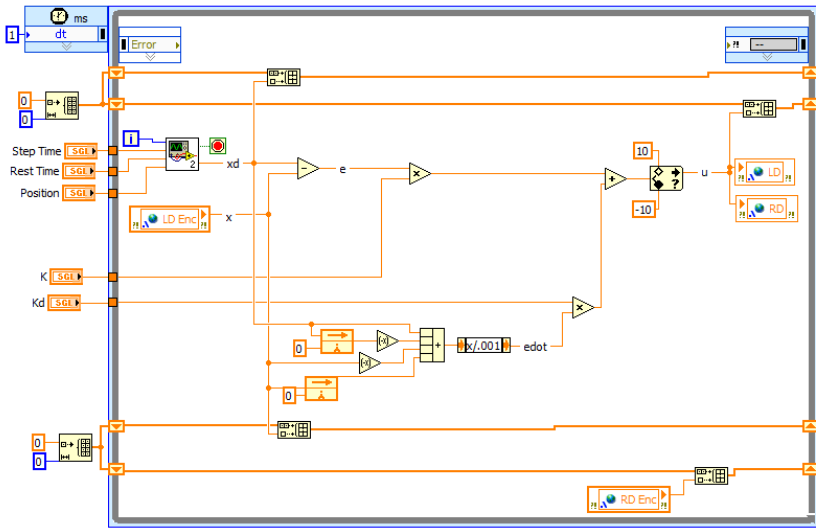

Figure 32 Platform PD Control in Labview

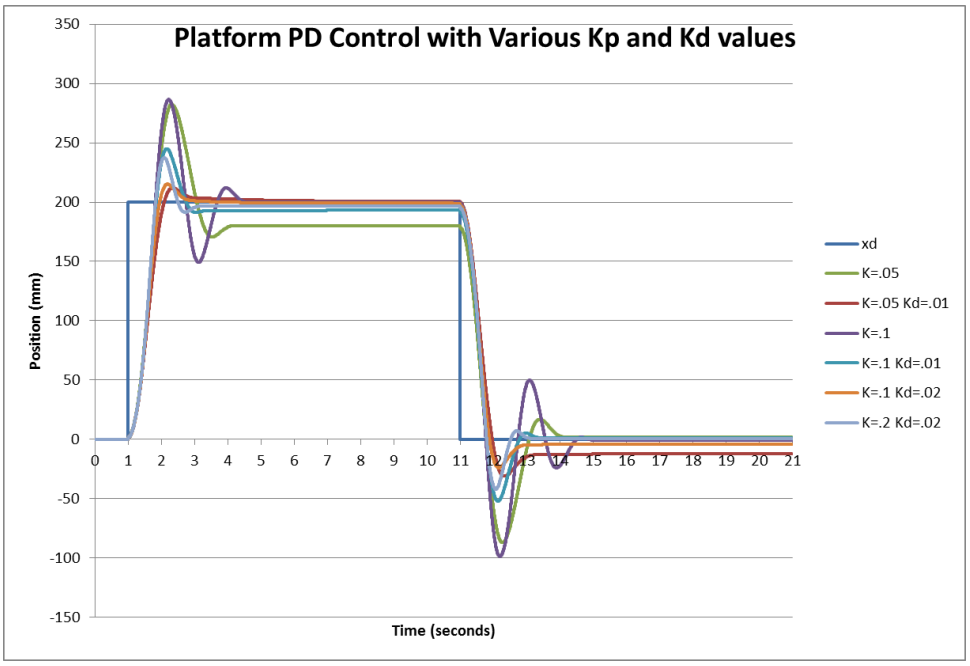

Figure 33 Platform PD Control with Various Kp and Kd Values

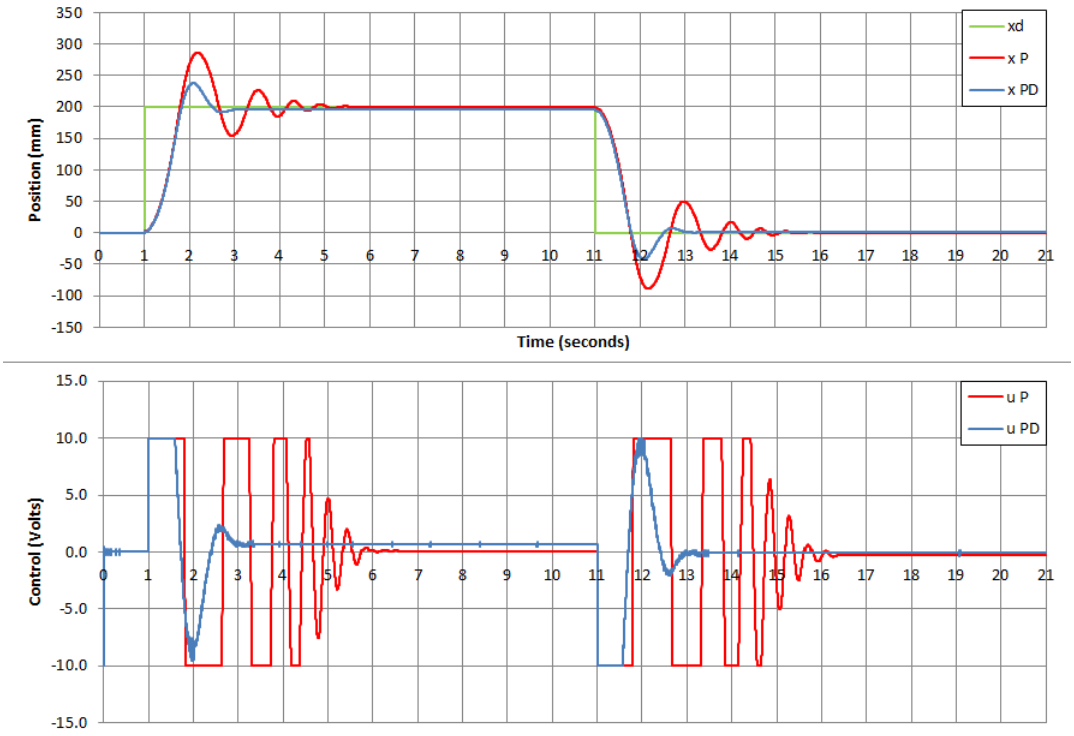

Figure 34 Platform Step Response with P and PD Control

As a final examination of the model, the response to a step input using the tuned PD controller was recorded and imported to Simulink, shown in Figure 35. The models derived from open loop and proportional closed loop were compared with the new data. Figure 36 shows that the closed loop model again performed well, with about 10mm deviation from the actual data.

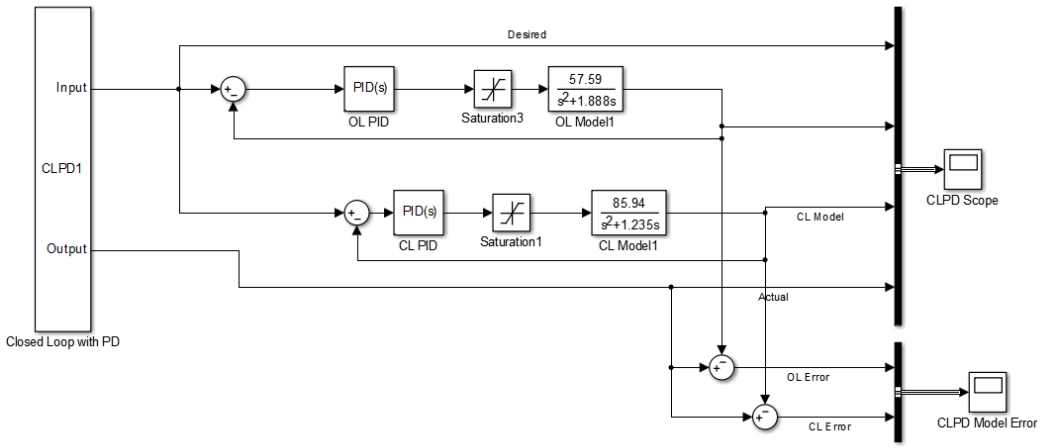

Figure 35 Platform PD Control Simulink

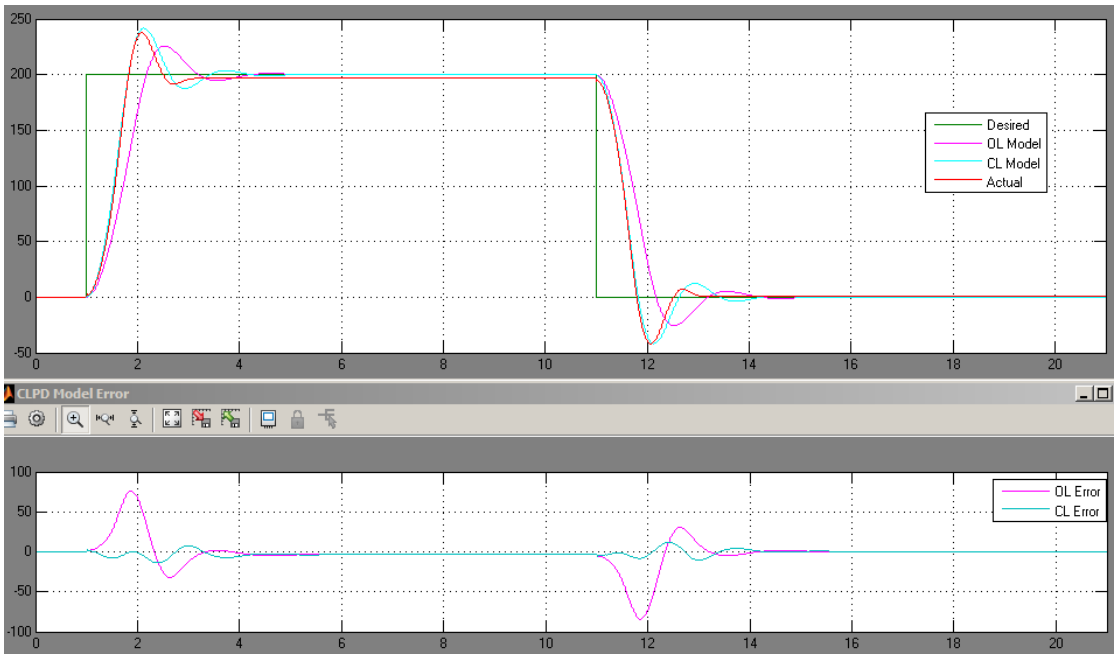

Figure 36 Platform PD Control Modeled Response

5.3 Translational Platform Simulation

The final test of a control structure is a simulation with real input data. A walking motion was recorded by a 76in tall person for 5.23 seconds. The motion was inputted into the TFS control system at a rate of 40 Hz, and the response of the system is shown in Figure 37.

The motion of the torso of the subject can be broken into five regions:

- Rest,
- Acceleration,
- Constant Velocity,
- Deceleration, and
- Rest

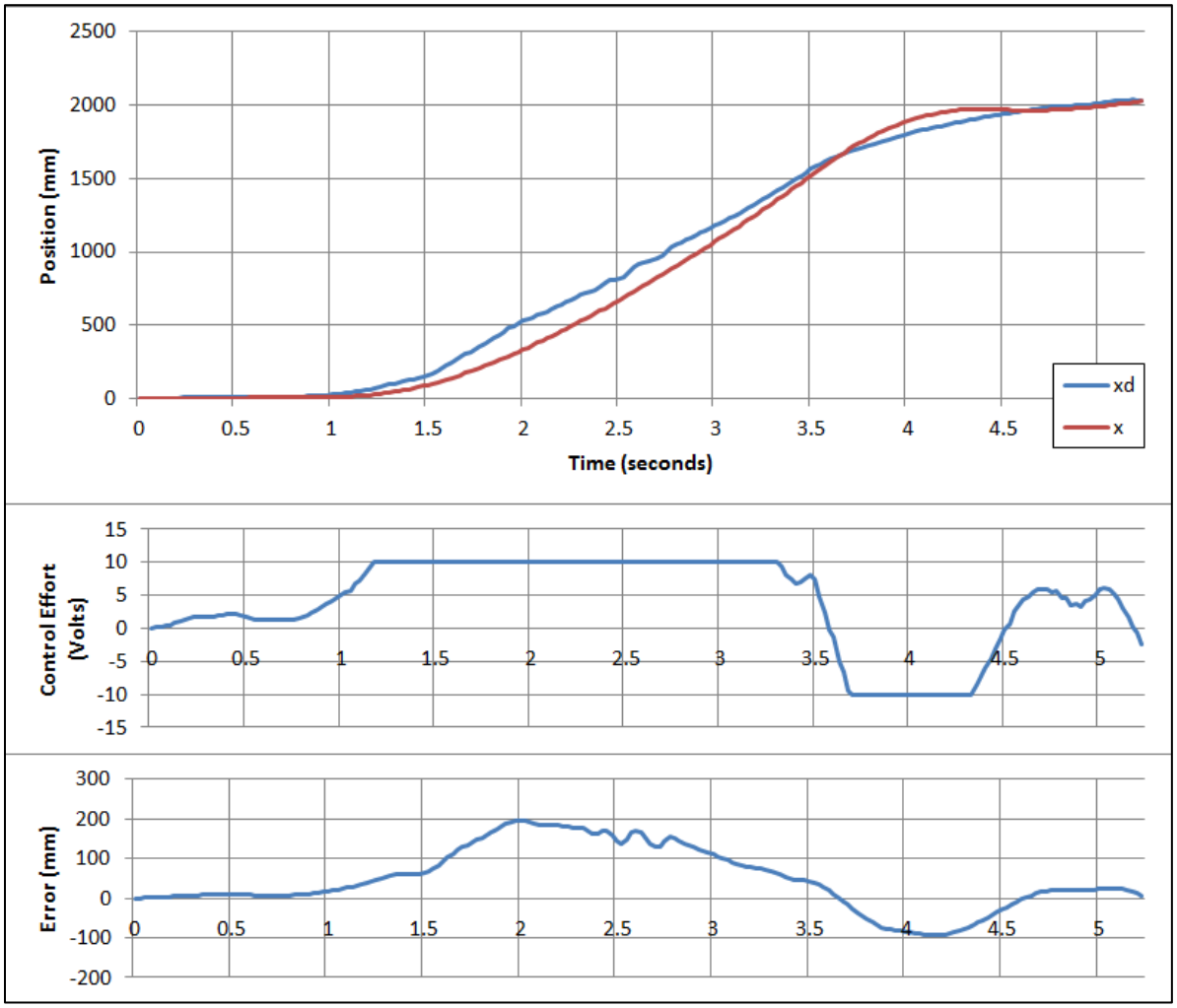

Figure 37 Platform Simulation Results

For the first second, the torso was stationary. The torso then underwent an acceleration of about $1\ m/s^2$ for about a second. For about 1.5 seconds, the torso continued at a roughly constant velocity of $1\ m/s$. The deceleration of the torso was slower than the initial acceleration, averaging $-0.7\ m/s$^2, until coming to a stop just after 5 seconds.

The control effort was saturated almost as soon as the subject began walking. This indicates that the drives are not capable of keeping up with the acceleration exhibited by the human. No control strategy can compensate for the lack of power. The maximum tracking error was 200 mm, which occurred at two seconds. After that point, the platform was traveling at a higher velocity than the torso. At 3.7 seconds the platform passed the torso, and the error became negative. Almost immediately the drive was saturated in the negative direction, indicating the maximum deceleration of the platform. During this phase, the platform overshot the torso by 100 mm, and came to rest with the human. The control of the system is satisfactory. The tracking error was bounded by 200 mm, and the response of the platform was smooth.

CHAPTER 6. HORIZONTAL FLUOROSCOPE AXES

6.1 HORIZONTAL AXIS MODELING

MODEL DEFINITION

The horizontal axes are modeled as a concentrated mass acted on by the external force of the linear motor. The equation of motion is

$$m_a\ddot{x}_a + b_a\dot{x}_a = f_a = C_a u_a \quad (20)$$

Where m_a is the total mass of each axis that can move in a horizontal direction. The friction of the system is denoted b_a andd f_a is the force of linear motor that acts on the mass. In Laplace domain, the transfer function becomes

$$\frac{X_a}{U_a} = \left(\frac{C_a/m_a}{s^2 + sb_a/m_a}\right) = \frac{C}{s^2 + sb} \quad (21)$$

Where $C = C_a/m_a$ and $b = b_a/m_a$.

To isolate the left horizontal axis, the brakes for each MIWD and vertical axes were engaged. The right horizontal axis was clamped to the platform. Traditional rotary electric motors produce torque by applying alternating current to an electromagnet. The change in magnetic field caused by the electromagnet induces a torque to a permanent magnet that is physically attached to the rotating shaft. The electromagnet is known as a stator, and the permanent magnet called a rotor. In linear motors, strips of permanent magnets make up a stationary magnet track, and the electromagnet (coil assembly) is suspended by linear bearings just above the magnet track. The electromagnetic principles used to drive linear motors are the same as rotary motors, but current is directly proportional to the force of the motor, instead of the torque.

Figure 39 compares the structure of linear and rotary motors. The model of one horizontal motor is shown in Figure 38.

This leads to the final transfer function model for the horizontal axes shown in Figure 40 where C and b are defined in (20).

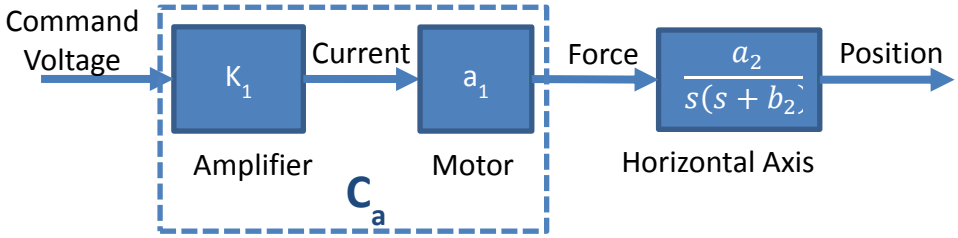

Figure 38 Horizontal Axis Block Diagram

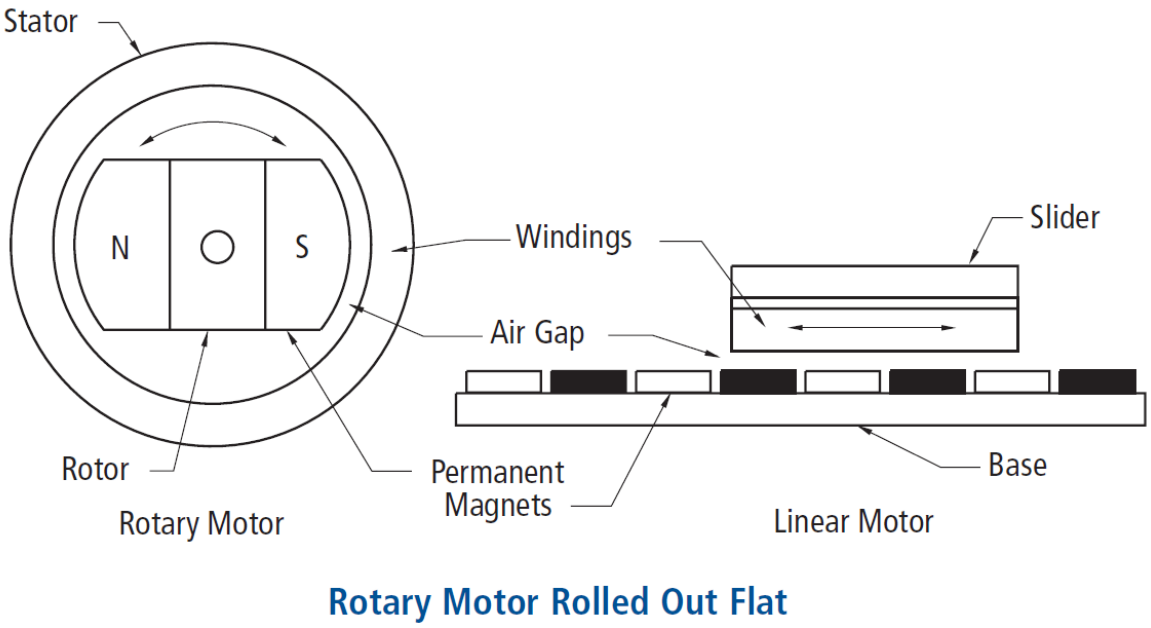

Figure 39 Rotary vs. Linear Motor [60]

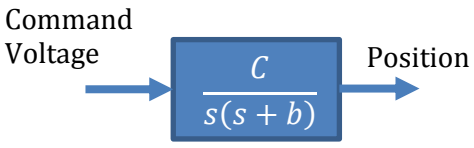

Figure 40 Condensed Horizontal Axis Block Diagram

PARAMETER ESTIMATION

The procedure for determining the parameters of the horizontal axes initially followed the same steps as the platform. An open loop controller was designed. First the Left Horizontal Axis was considered. An step input of 1.5 Volts was applied to the system for 0.375 seconds, then a step back to zero Volts was applied. The system was allowed to settle for 2.25 seconds, then a step of -1.5 Volts was applied for 0.375 seconds, and then the input was returned to zero. The sampling time of the system was 1 KHz. A second run was implemented that was the reverse of the first run. The data, shown in Figure 41, are not symmetrical. A positive voltage causes less motion than a negative voltage. The open loop data were evaluated by MATLAB's System Identification Toolbox, but the resulting model was a poor estimation of the system. It was concluded that there is additional friction that opposes positive velocity. The system model was expanded to allow the frictional term to have two values. When the commanded input is positive, $b = b_{pos}$. When the commanded input is negative, $b = b_{neg}$. The frictional term is then defined as:

$$b(u) = b_{ave} + \text{sign}(u) * b_{diff} \quad \textbf{(22)}$$

where $b_{ave} = \frac{b_{pos}+b_{neg}}{2}$ and $b_{diff} = \frac{b_{pos}-b_{neg}}{2}$

Estimations for C, b_{pos} and b_{neg} produce a much more accurate model for the open loop system. A friction model following [61] was then developed to account for Coulomb and Stribeck effects. The new equation for friction becomes:

$$f = b_1(\tanh(s_1\dot{x}) - \tanh(s_2\dot{x})) + b_2(\tanh(s_3\dot{x})) + b_3\dot{x} + b_4\dot{x}\text{sign}(u) \quad \textbf{(23)}$$

The hyperbolic tangent function, shown in Figure 42, goes to one as the argument goes to infinity and to negative one as the argument goes to negative infinity. It is useful as a continuous and continuously differentiable switching function. The friction force has four parameters for friction coefficients and three parameters for switching these effects on and off. Considering the gain, C, to be an additional parameter, there are now eight parameters to be solved.

Figure 43 compares the measured response with the three models. While the advanced model is more accurate than the other two, the simple bidirectional model is a good approximation of the system.

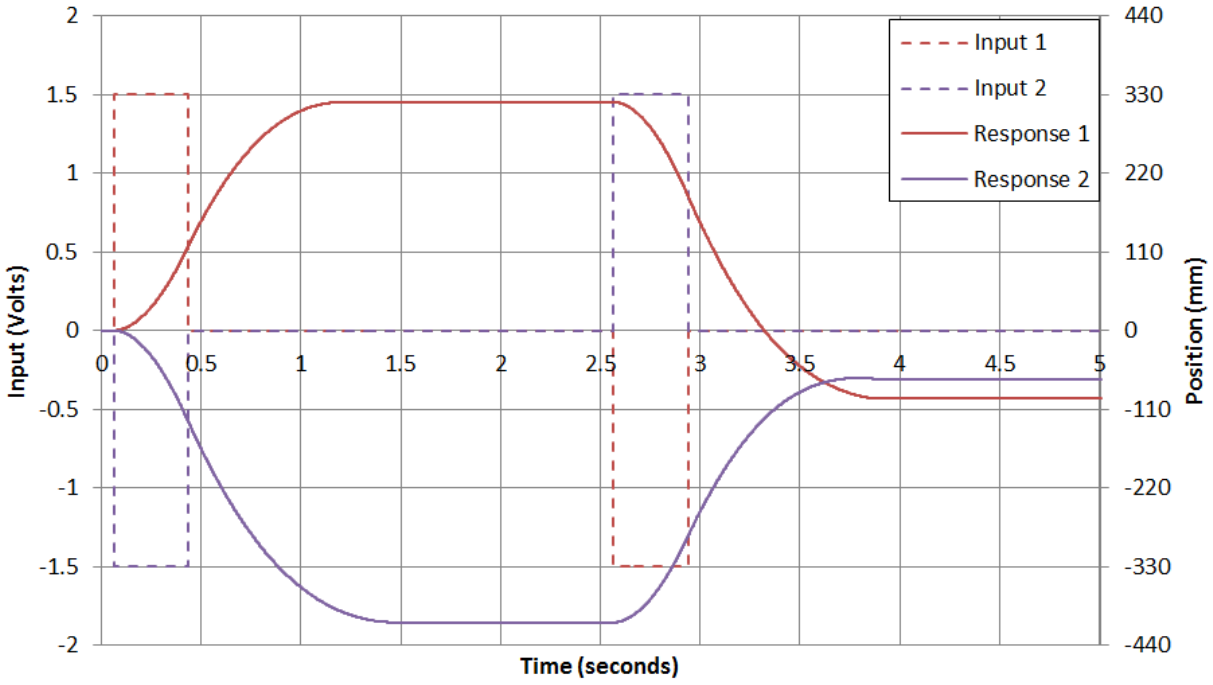

Figure 41 Left Horizontal Axis Open Loop Response

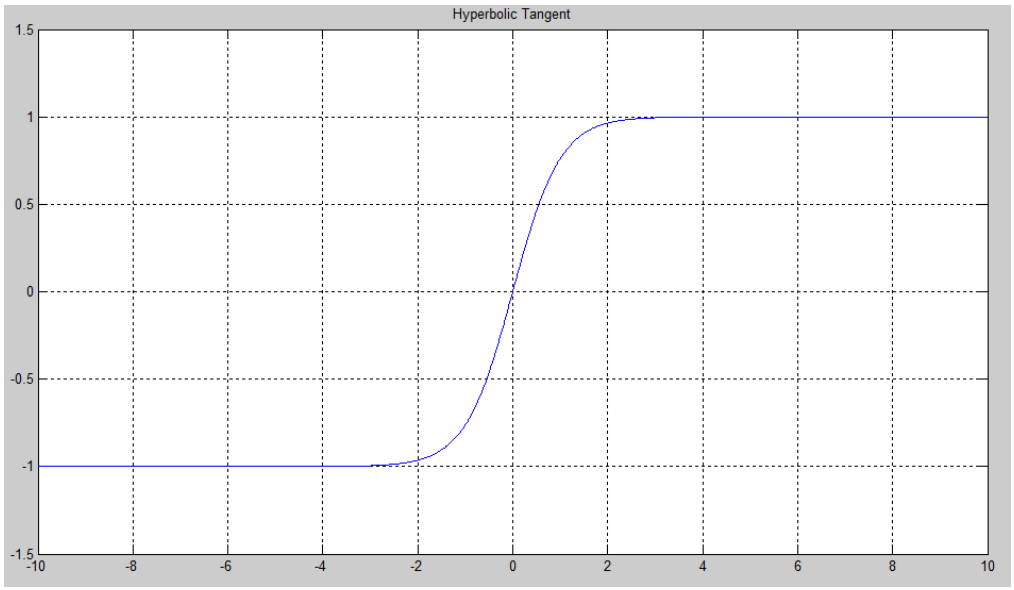

Figure 42 Hyperbolic Tangent

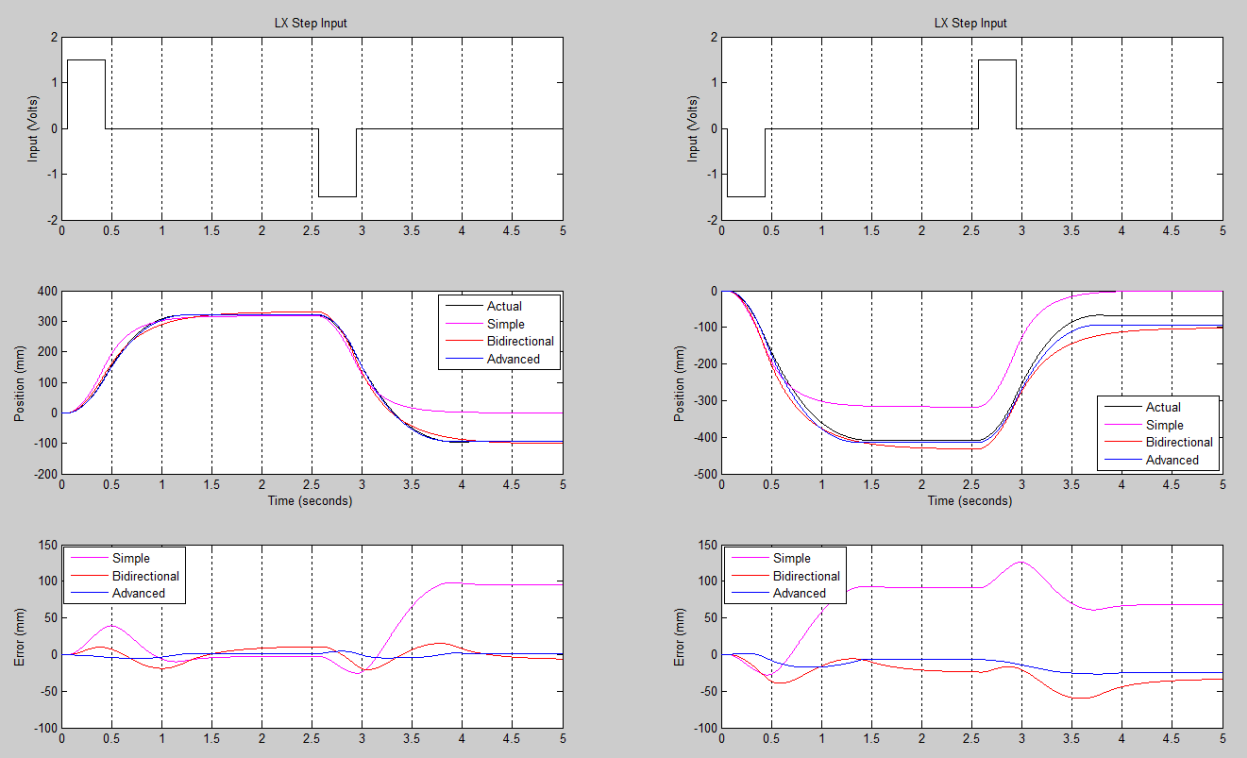

Figure 43 Left Horizontal Axis Model Response

Table 5 Horizontal Axis Coefficient Values

	C	b_{pos}	b_{neg}
Simple	2335	4.14	4.14
Bidirectional	1856	3.76	1.79
Advanced	1620	1.44	0.33

Rewriting (23) to separate the viscous friction from the Coulomb and Stribeck effects,

$$f = f_{effects} + f_{viscous} \quad (24)$$

$$f_{effects} = 118(\tanh(3340\dot{x}) - \tanh(21300\dot{x})) + 63.5(\tanh(22000\dot{x})) \quad (25)$$

For velocities above 0.01 m/s and below -0.01 m/s this is becomes

$$f_{effects} \approx 63.5\ sign(\dot{x}) \qquad (26)$$

This means that these effects are nearly a constant, and give further validity to neglecting the Coulomb and Stribeck effects.

The difference between the two horizontal axes is very slight. The right side carries the x-ray emitter, while the left side carries the x-ray collector/imaging device. There is only about a three kg difference in weight, and the load has a similar inertia. Each axis was subjected to the same control loop and the response was recorded in Figure 44. For a 100 mm step input, the maximum deviation between the response of the axes was less than 2.5 mm. The model constants found for the left side will be accurate enough to estimate the right side.

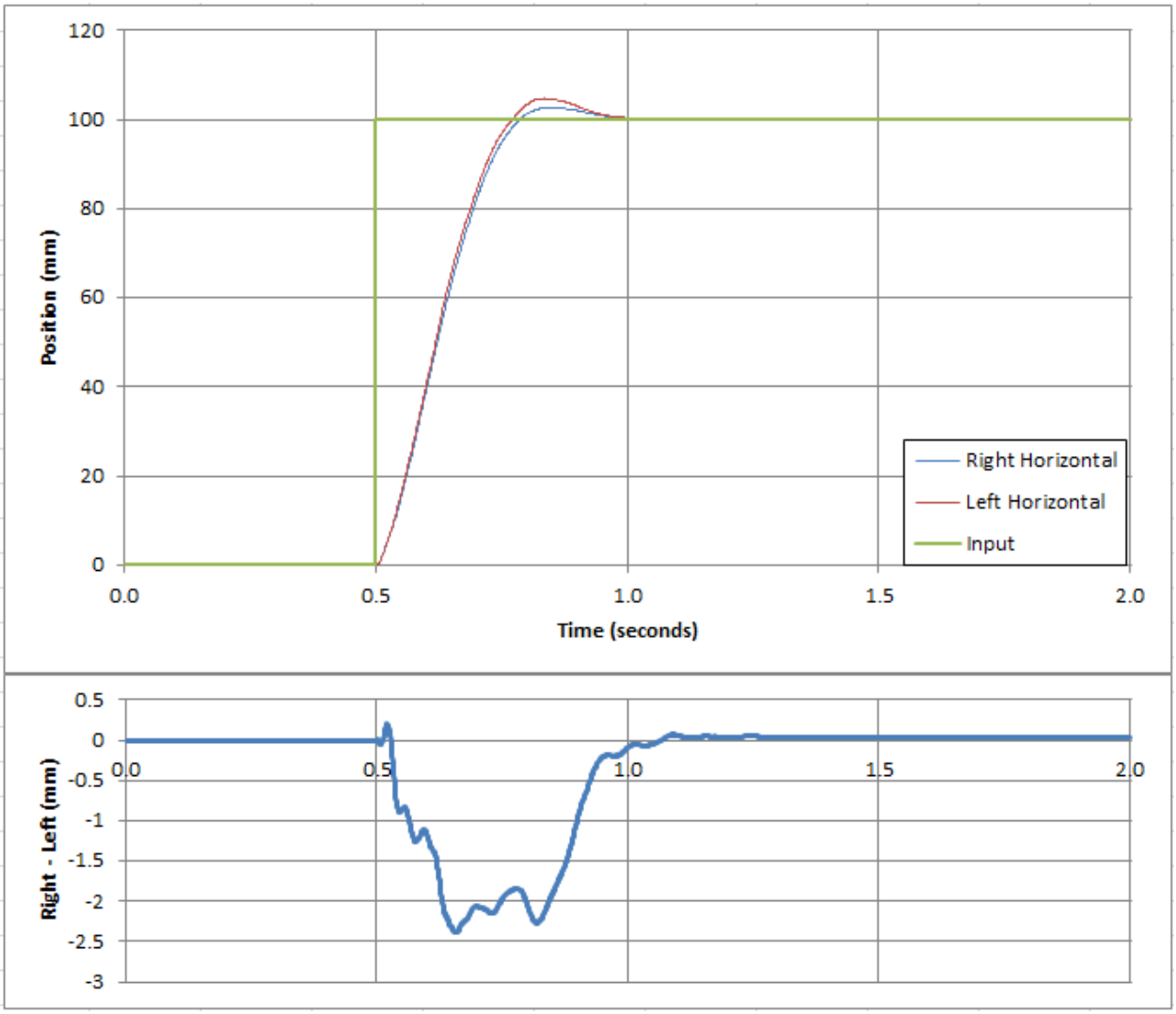

Figure 44 Right and Left Horizontal Axes Compared

6.2 Horizontal Axis Control

With a clear understanding of the dynamic nature of the horizontal axes, a control scheme can be designed. As with the platform, a minimum tracking error is desired, so a PD controller was implemented. Analyzing the collected Kinect data reveals that a 20mm step is very likely for a sampling rate of 60 Hz for certain parts of normal activities. This gives a useful metric to design the controller. It is desired that the axes respond to a 20mm step as fast as possible, but without overshoot. Setting $K_d = 0$, K_p is increased until there is no improvement. This occurs when the control output becomes saturated. Additional gain is no longer beneficial. Once the maximum rise time is established, K_d is increased until the system is critically damped. In this system, the derivative term is calculated, rather than measured. The derivative term is therefore sensitive to noise, which can result in chatter-type motion resulting from the drives trying to respond to the noise. For a given sampling rate, there is a maximum allowable K_d. If too much chatter is introduced in the system, it is necessary to decrease K_d until the chatter level is acceptable, then decrease K_p until the response is critically damped. Using the model in Simulink for initial gain selection, fine tuning the control parameters on the system, a tuned PD controller for both horizontal axes was found to be:

$$K_{aH}(s) = 0.1 + 0.01(s) \quad (27)$$

Figure 45 and Figure 46 give a summary of the tuning process.

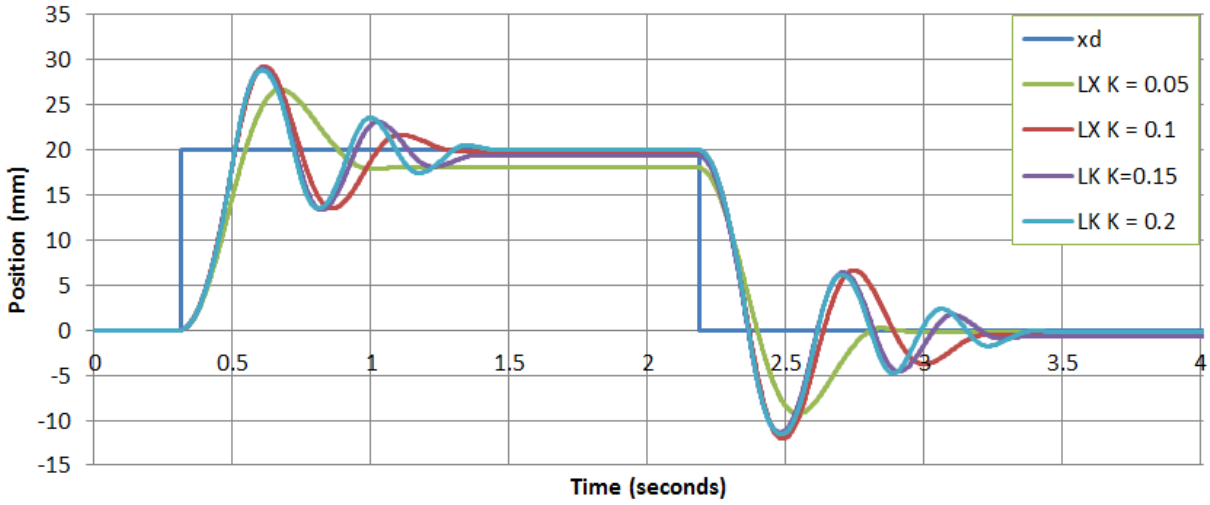

Figure 45 Horizontal Axis K_p Tuning

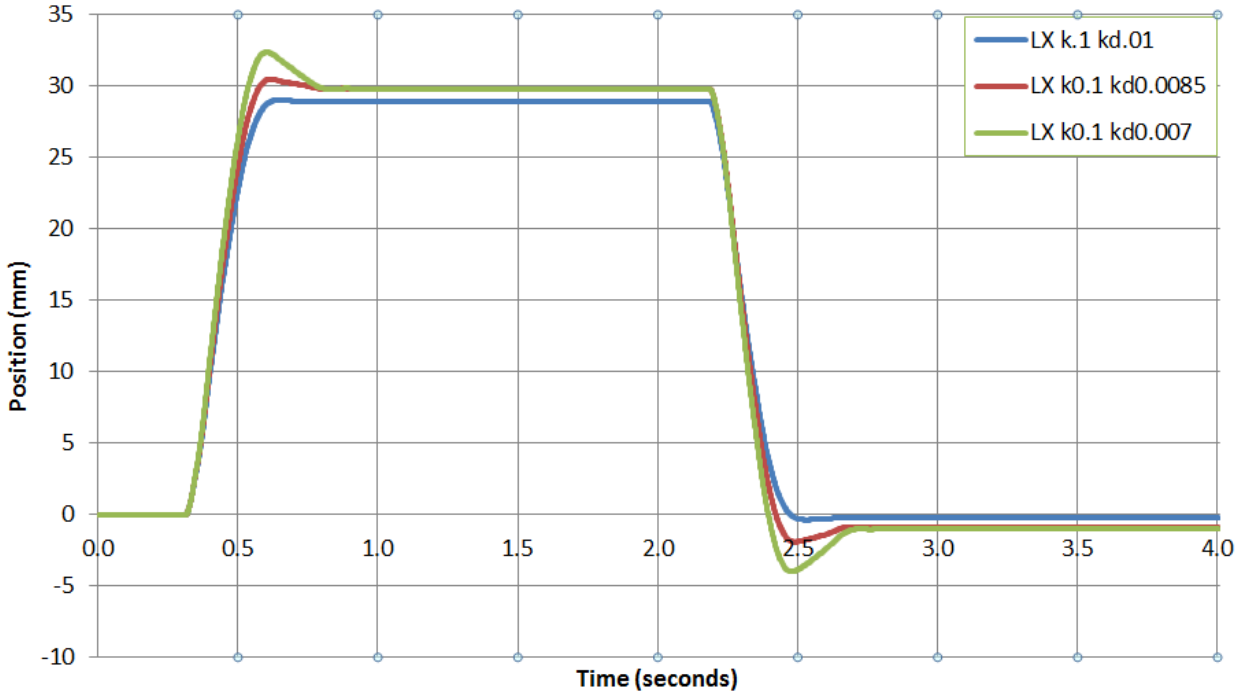

Figure 46 Horizontal Axis K_d Tuning

6.3 Horizontal Axis Simulation

As discussed in Chapter 4, the Kinect data can be configured to simulate the motion of the knee relative to the chest. This is useful for providing a baseline of axis tracking control to measure against the fully- coupled system. Figure 47 shows the motion of the right knee with respect to the chest in the x direction, as defined by Figure 13. The data were collected from three humans walking at a moderate pace. The walking activity was used because it provides the greatest challenge for the horizontal axes and platform.

Figure 48 shows the response of the actual TFS to the simulated input. For this test, the platform was left in a locked position, and the Kinect data for the left knee were injected as a desired location for the left axis. The tracking error is bounded by 20 mm, and the response was smooth.

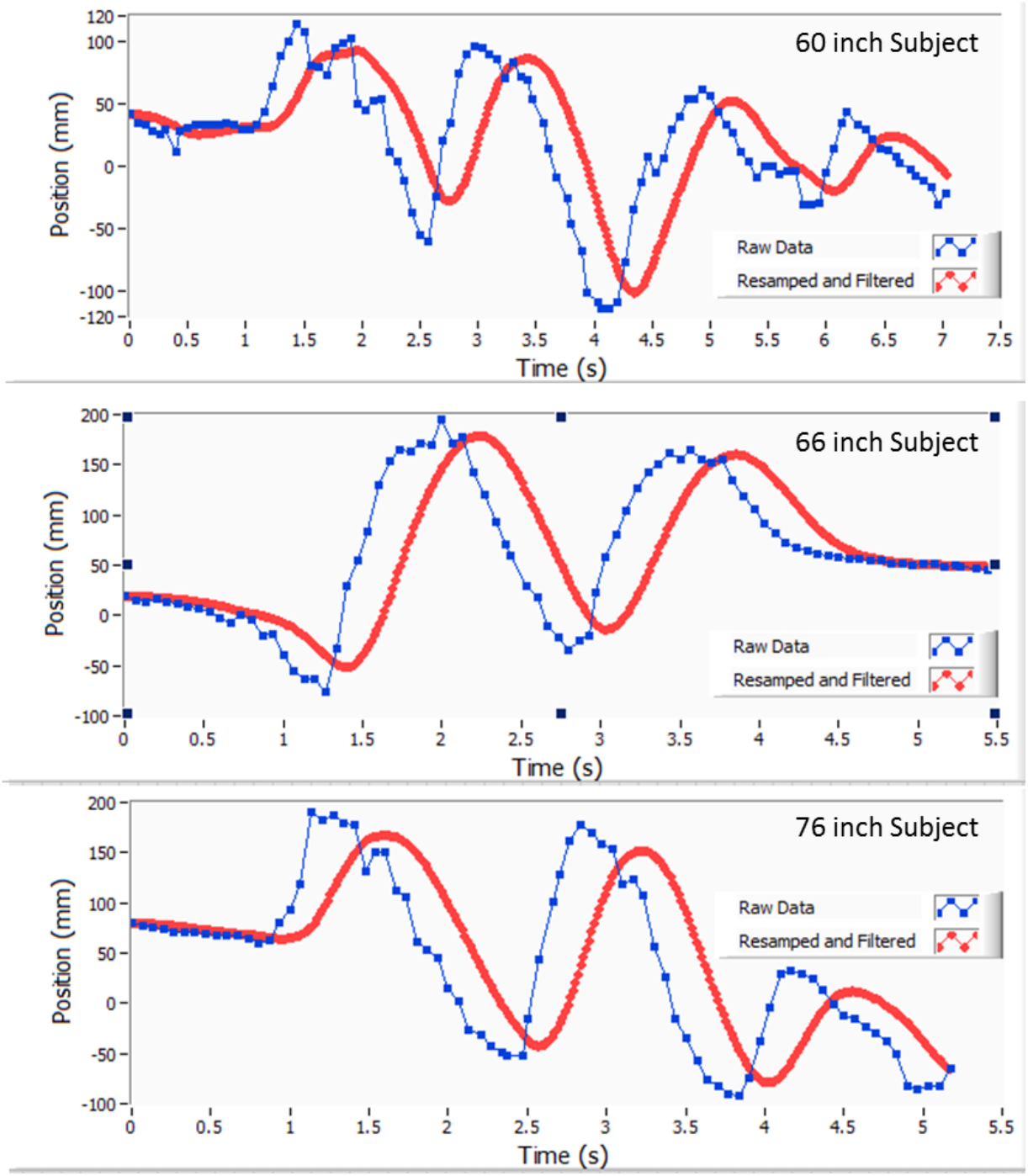

Figure 47 Knee Data from Kinect for Horizontal Axis Only Tracking

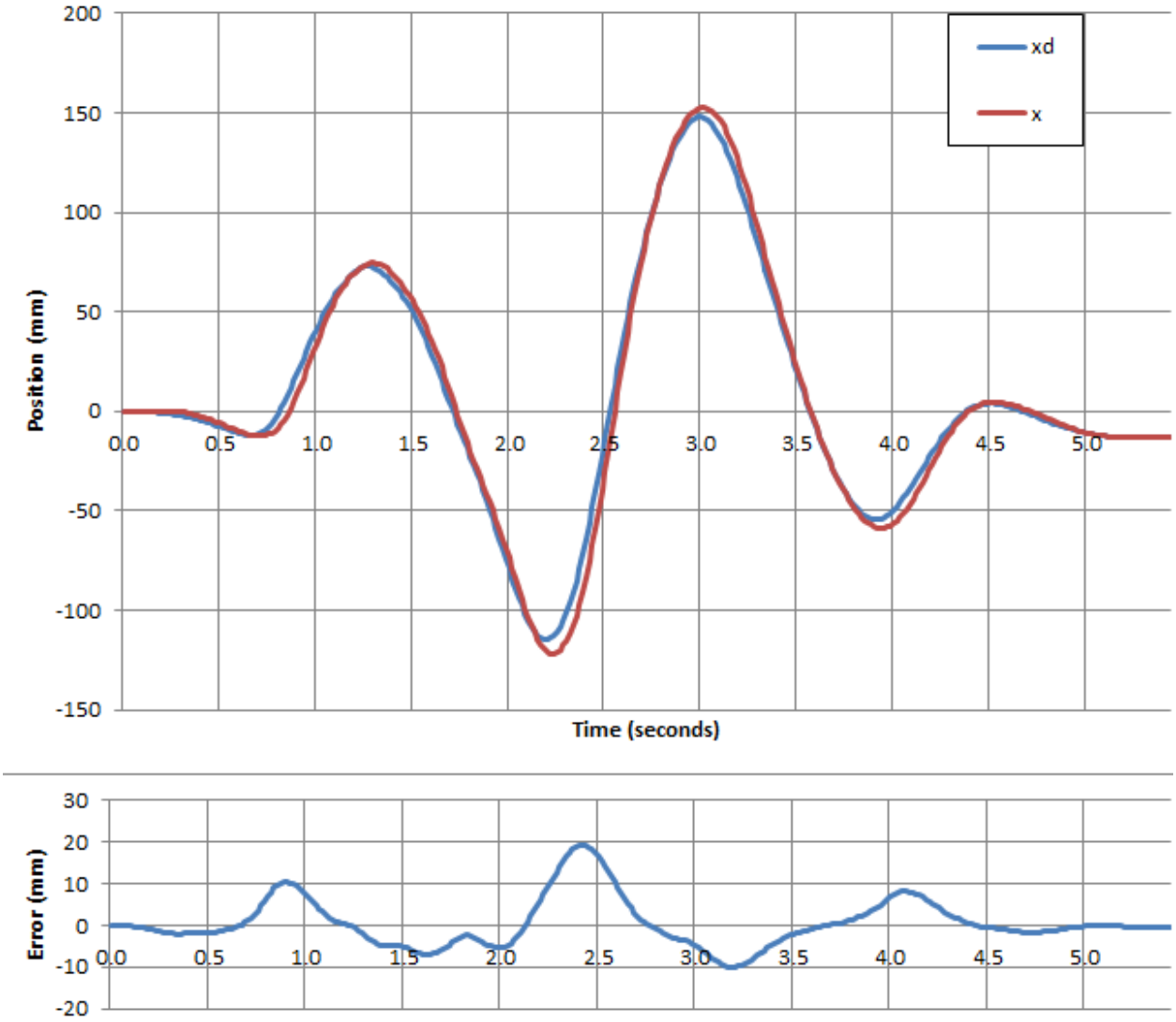

Figure 48 Simulation, Response and Error on the Uncoupled Left Horizontal Axis

CHAPTER 7. VERTICAL FLUOROSCOPE AXES

7.1 VERTICAL AXIS MODELING

MODEL DEFINITION

The vertical axes are modeled as a concentrated mass acted on by the external force of a rotary motor connected to a linear screw drive. The equation of motion is

$$m_{av}g + m_{av}\ddot{x}_{av} + b_{av}\dot{x}_{av} = f_{av} = C_{av}u_{av} + C_{av}u_g \quad (28)$$

where m_{av} is the total mass of each axis that can move in a vertical direction. The friction of the system is denoted b_{av} andd f_{av} is the force that the motor applies to the mass. The control effort needed to compensate for gravity can be found and treated as a separate control source. To do this, let u_g be set so that $\ddot{x}_{av} = 0$. This implies that $m_{av}g = C_{av}u_g$, and the equation of motion reduces to

$$m_{av}\ddot{x}_{av} + b_{av}\dot{x}_{av} = f_{av} = C_{av}u_{av} \quad (29)$$

To discover the necessary value for u_g, a simple position P controller was implemented on the left vertical axis. The axis began with the brake engaged at an origin. As the brake was release, the drive was enabled. The axis was allowed to come to an equilibrium position, and the output was recorded. To check the gravity compensation, a controller was designed that only applied a constant force. The drive was enabled and the axis was pushed by hand up and down. The value of the gravity compensation input was adjusted until the effort to raise and lower the axis was equal.

Table 6 Gravity Compensation Terms

	LZ	RZ
u_g	0.72 V	0.76 V

Although not necessary for control, this compensation provides a means to estimate the gain of the system.

$$m_{av}g = C_{av}u_g \quad (30)$$

$$C_{av} = \frac{27\ kg * 9.81\frac{m}{s^2}}{0.72\ V} = 368\ N/V \quad (31)$$

$$C_{av} = \frac{30\ kg * 9.81 \frac{m}{s^2}}{0.76\ V} = 387\ N/V \quad (32)$$

Notice that the two values do not perfectly agree. This might mean the weight of the axes was not measured accurately, that inertial effects of the load placement are not negligible, or that the motor characteristics are slightly different. For the rest of this work, the effect of gravity will be assumed to be perfectly compensated by u_g, which will be added to all control outputs. The saturation limits of the vertical drives are -10V and 10V. Since $u_g$is always being applied in the positive direction, the saturation limits in the model are adjusted so that the maximum control effort in the model is $10 - u_g$ V and the minimum control effort is $-(10 + u_g)$ V.

In Laplace domain, the transfer function becomes

$$\frac{X_{av}}{U_{av}} = \left(\frac{C_{av}/m_{av}}{s^2 + sb_{av}/m_{av}}\right) = \frac{C}{s^2 + sb} \quad (33)$$

Where $C = C_{av}/m_{av}$ and $b = b_{av}/m_{av}$.

The rotary motors are Kollmorgen Goldline Series attached to a linear slide with an Acme screw that has a one half inch lead. This means that one rotation of the motor causes the linear slide to translate one half of an inch, or 12.5 mm. A review of the kinematics behind Acme screw can be found by [62]. The resulting torques are:

$$T_{raise} = f_{av}\frac{\mu \sec(\beta) + \tan(\alpha)}{1 - \mu \sec(\beta)\tan(\alpha)} \quad (34)$$

$$T_{lower} = f_{av}\frac{\mu \sec(\beta) + \tan(\alpha)}{1 + \mu \sec(\beta)\tan(\alpha)} \quad (35)$$

where μ is the coefficient of friction between the screw and the nut, $\beta = 14.5^o$ (for all Acme thread), and α is the lead angle and is defined as:

$$\alpha = \tan^{-1}\left(\frac{pitch}{diameter}\right) \quad (36)$$

PARAMETER ESTIMATION

Because of the Acme thread, it first appeared as if the vertical axes would need bidirectional friction components. A model assumes a constant b was created to establish the starting point of bidirectional friction values. An open loop input of a one Volt step was applied to the system for 0.375 seconds and the response was sampled at 1 kHz. This set was used to estimate the parameters. Another step of 1.5 Volts was recorded to compare the system. To isolate the left vertical axis, the brakes for each MIWD and the brake on the right vertical axis were engaged. The horizontal axes were clamped to the platform. The results of the modeling iteration are seen in

Figure 49 Left Vertical Axes Model Figure 49. A linear model performed exceptionally well, and will be used as the system model. A comparison between the response of the left and right vertical axes Figure 50 reveals that they have virtually the same response to the same input. The final transfer function for the left and right vertical axes is:

$$G_{avOL} = \frac{3043}{s(s + 28.2)} \quad (37)$$

A general comparison between the horizontal axes and the vertical axes reveals that the vertical axes has a damping term that is much higher. This is expected, as power screws such as Acme thread have inherently high frictional forces. The vertical response of the system is therefore hampered by the use of the Acme lead screw.

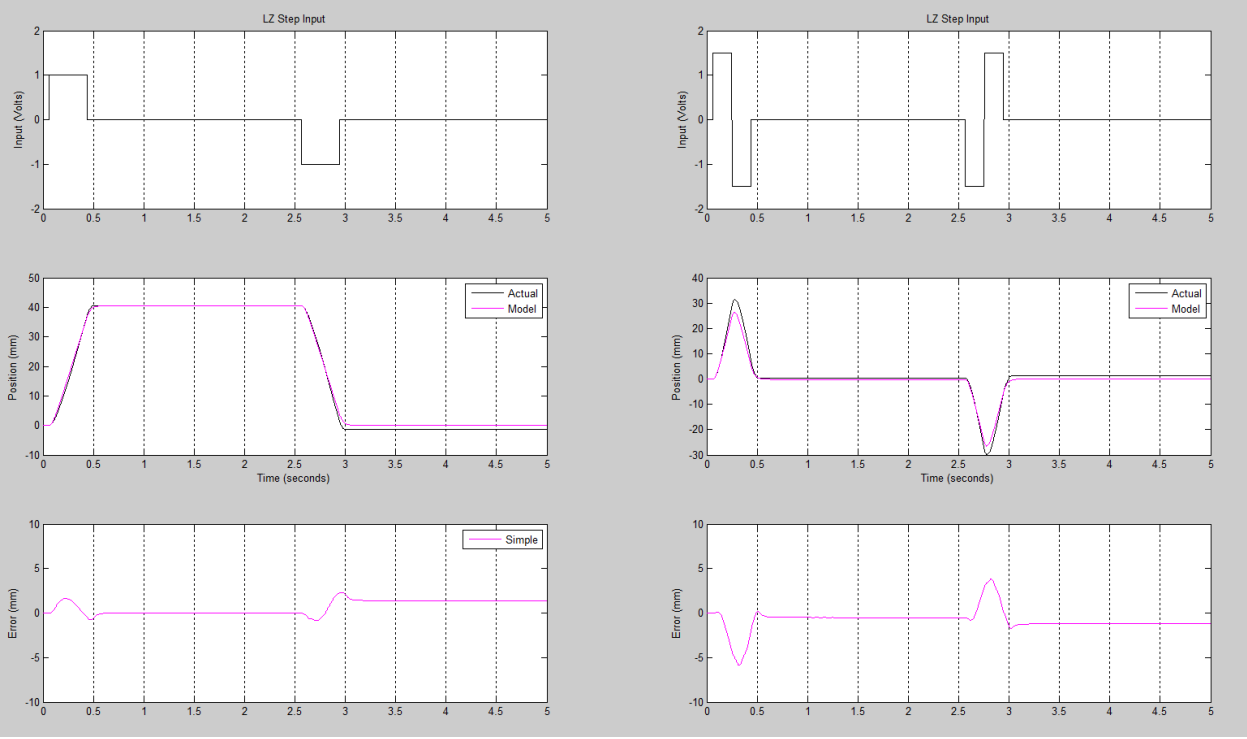

Figure 49 Left Vertical Axes Model

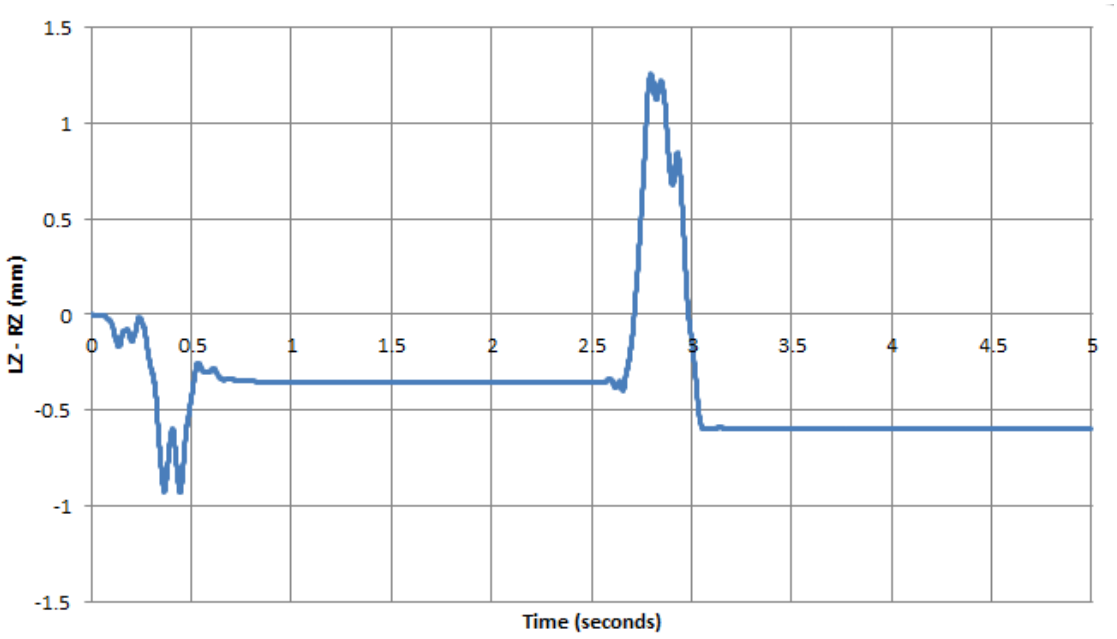

Figure 50 Right and Left Vertical Axes Compared

7.2 Vertical Axis Control

The vertical axes have the same tracking requirements as the horizontal axes, so again a PD controller was implemented. Analyzing the collected Kinect data reveals that a 20mm vertical step is very likely for a sampling rate of 60 Hz for certain parts of normal activities. This gives a useful metric to design the controller. It is desired that the axes respond to a 20mm step as fast as possible, but without overshoot. Setting $K_d = 0$, K_p can be increased until there is no improvement. Once the maximum rise time is established, K_d is increased until the system is approximately critically damped. Using the model in Simulink for initial gain selection and fine tuning the control parameters on the system, a tuned PD controller for both vertical axes was found to be:

$$K_{aV}(s) = 0.4 + 0.02s \quad (38)$$

Figure 51 and Figure 52 give a summary of the tuning process.

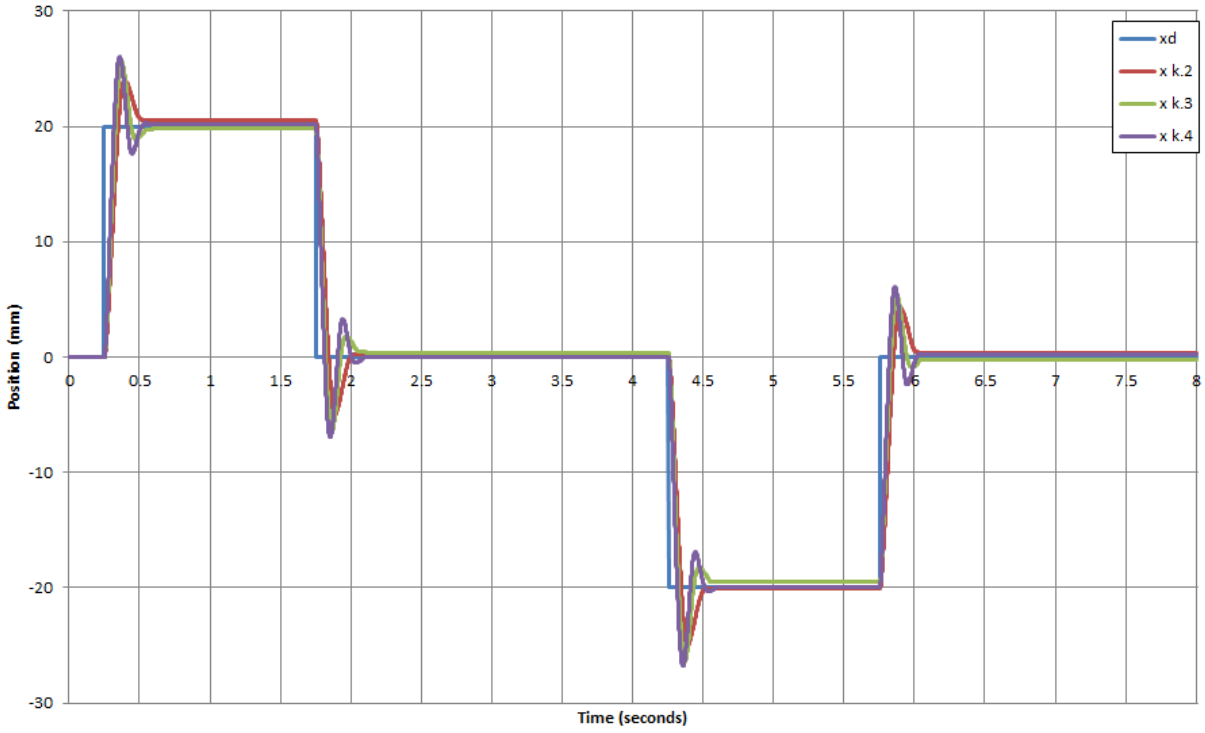

Figure 51 Vertical Axis K_p Tuning

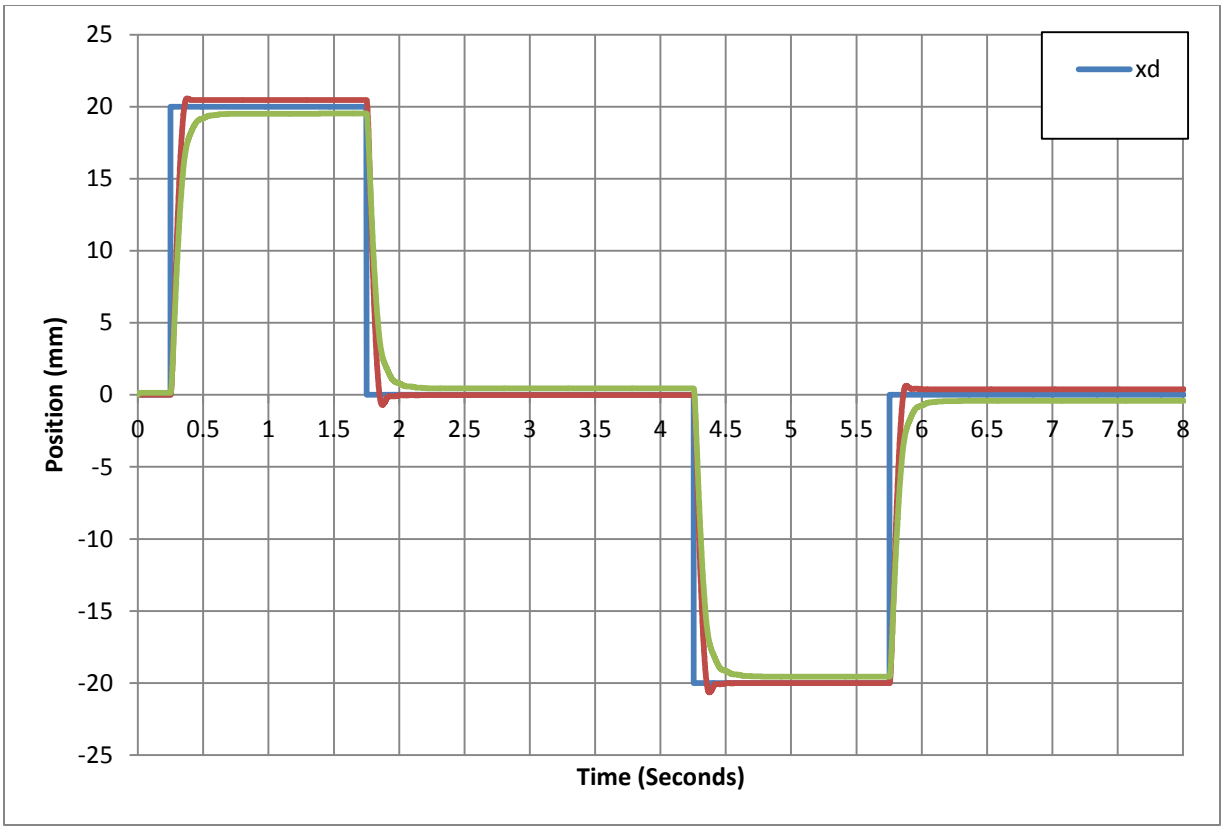

Figure 52 Vertical Axis K_d Tuning

7.3 Vertical Axis Simulation

To simulate the vertical axis, a walking motion was recorded by a 66 inch tall person for 5.4 seconds. The motion was injected into the vertical axis at a rate of 60 Hz, and the response is shown in Figure 54. The error was bounded by 3 mm. Past control efforts on walking activities have produced a maximum tracking error of 40 mm. [52]

One reason for the small tracking error is the magnitude of vertical motion during walking activities. The total vertical motion was only around 60 mm. For this reason, a step up and step down activity were each applied to the vertical axis. Figure 54 shows the response. The maximum error is less than 10 mm, and the maximum control effort was less than 40% of the axis capability.

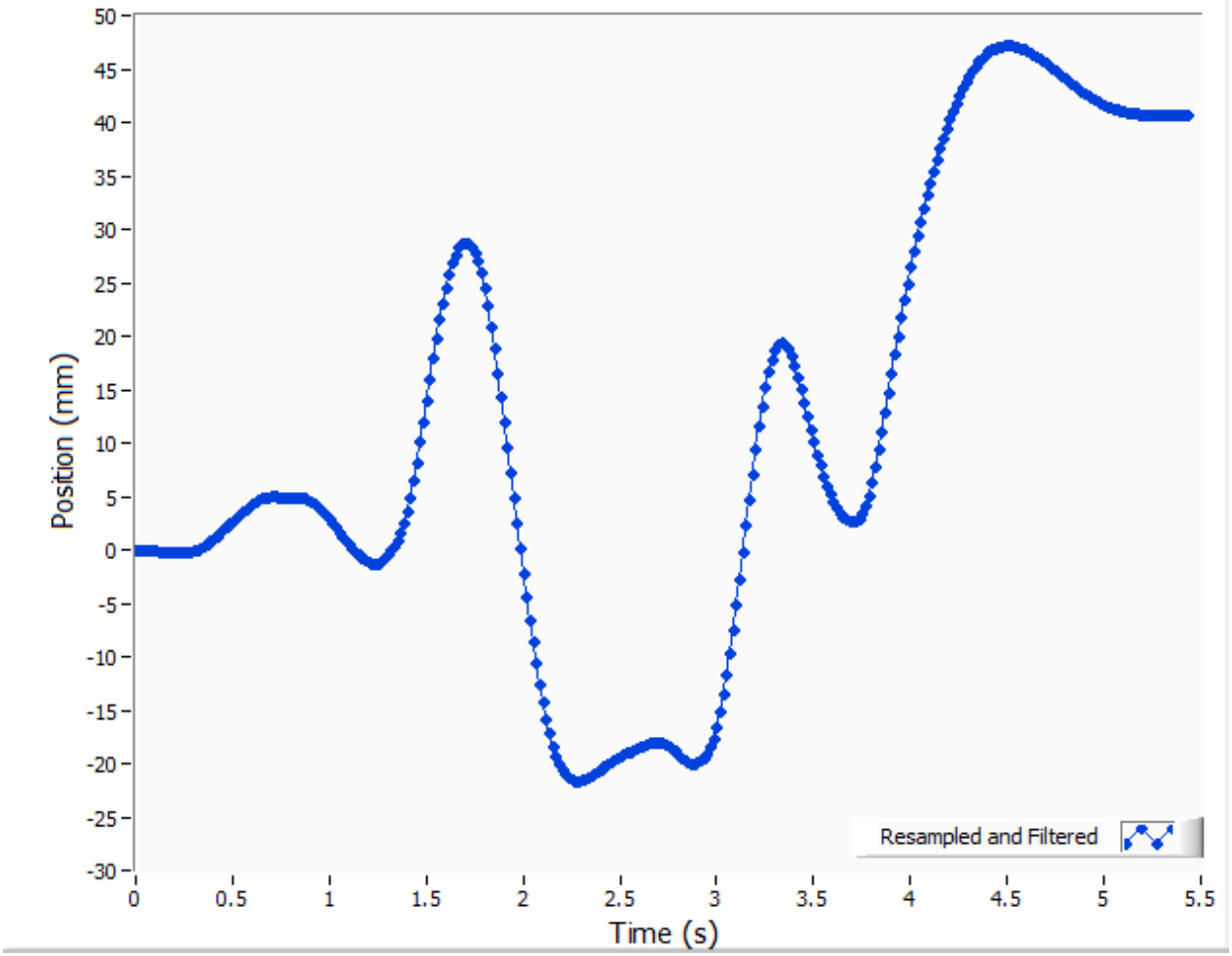

Figure 53 Knee Data from Kinect for Vertical Axis Tracking

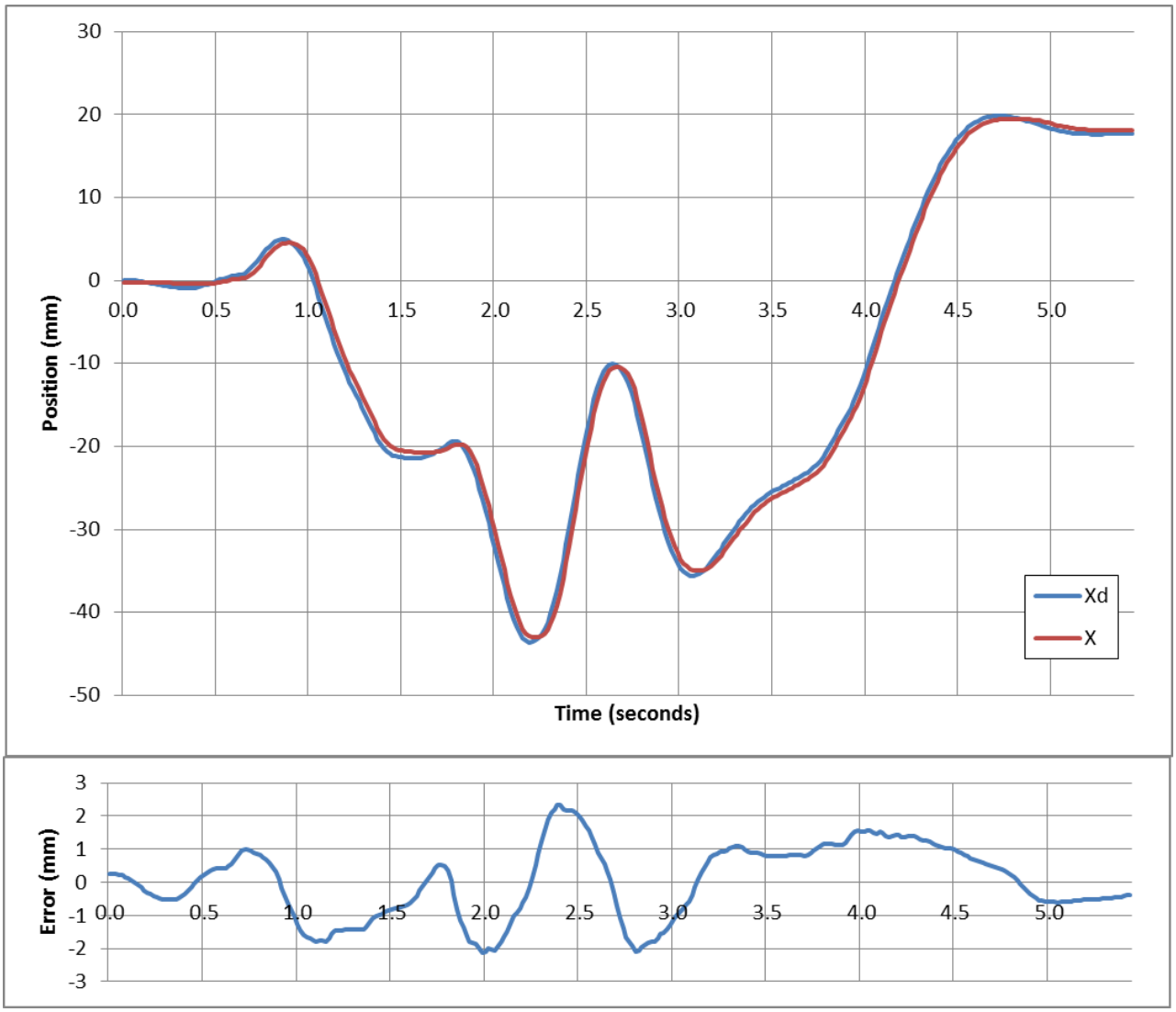

Figure 54 Simulation, Response and Error on the Uncoupled Left Vertical Axis

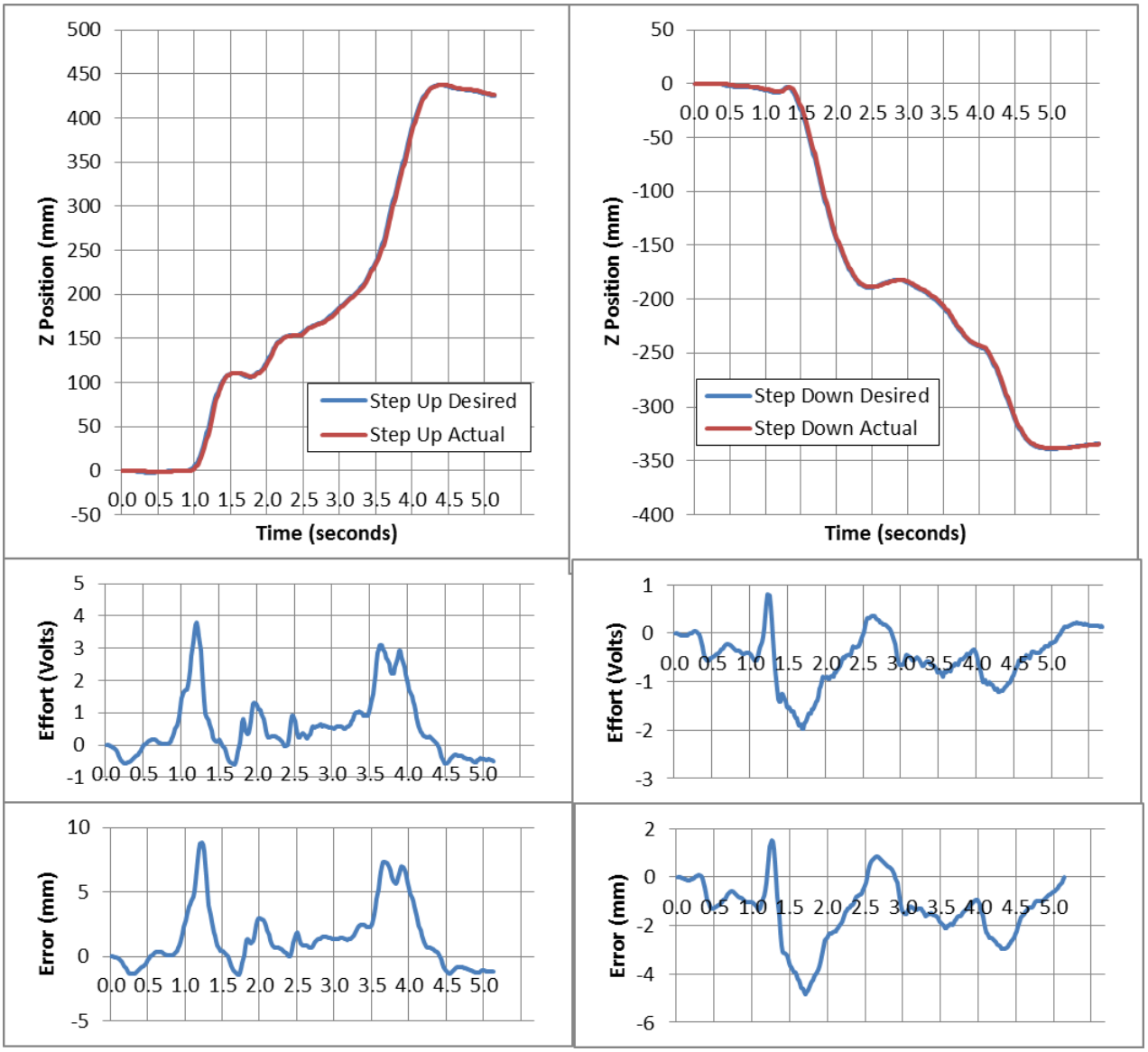

Figure 55 Step Up and Step Down Response, Effort and Error

For the step up activity, the initial position of the knee is with the leg slightly in front of the body. After 1 second, the knee lifts up about 100 mm and rests on the first step. At this point, the subject puts weight on this leg and swings the other leg to the top step. At 2.5 seconds the other leg is planted on the top step and the leg of interest begins to rise, coming to rest on the top step after 5 seconds at 420 mm higher than the initial position.

The step down activity is the opposite of the step up activity. The subject leads off with the leg of interest, descending from the top step to the middle step rapidly. After the leg is planted on the middle step, the opposite leg swings through to the bottom of the steps, and the leg of interest follows, coming to rest after 5 seconds.

The control effort for the vertical axes was never above 4 Volts for any activity tested. This is only forty percent of the maximum control effort. Likewise, the error was bounded for all activities by 10 mm.

CHAPTER 8. DYNAMIC COUPLING

8.1 MODELING

When multiple channels are physically connected, there is a potential for interaction between the channels. Often these interactions are negligible, but the motivation for the treatment of this dynamic coupling in the TFS has two sources:

1. Large tracking errors were recorded by initial control strategies, which were believed to be related to the coupling of the system. The combined manipulator weight on the TFS is 57 kg, while the total platform weighs 792 kg. This means that over seven percent of the mass of the system is moved when the horizontal axes are actuated.

2. Occlusion of the joint of interest during fluoroscopy is common and unavoidable. A small field of view is highly desirable to limit x-ray exposure to the subject. In order to keep the joint in the field of view an estimated joint position must be calculated during the occlusion. This estimation will be more accurate if a human gait model is built *from the ground*, while the platform is controlled by the position of the subject from the platform. In order to calculate the subject location from the ground, an accurate model of the interaction between the platform and the axes is needed.

The coupling of multiple channels can be modeled by examining the combined block diagram and solving the equations of motion. This section will be broken into two parts. First, a simplified Two-Input-Two-Output structure will be considered. Then, an expanded Multiple-Input-Multiple-Out structure will be derived and implemented.

TWO-INPUT-TWO-OUTPUT (TITO) SYSTEMS

A mass connected to a motor has the general equation

$$m\ddot{x} + b\dot{x} = f \tag{39}$$

Where m is the mass of the system, b is the damping of the system, including motor damping and Coulomb friction, f is the force applied to the system, and x is the position of the mass.

Consider this system in Figure 56. Assume the manipulator on the left is fixed to the platform and the manipulator on the right moves only along the x axis. Let the mass of the platform be m_p and the mass of the right manipulator be m_a. The external forced F_a and F_p act on the axis and platform respectively. Equations of motion can be derived from the free body diagrams in Figure 57.

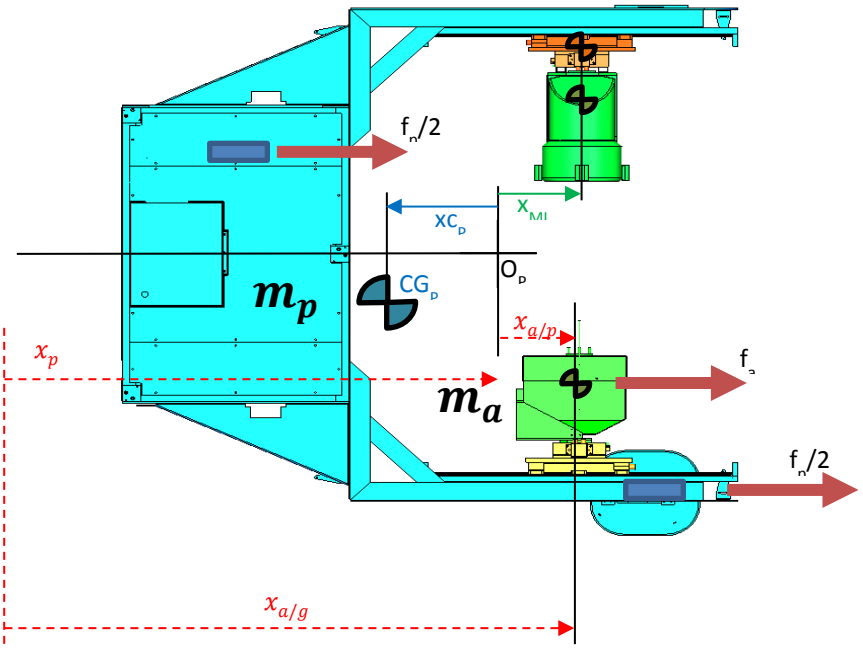

Figure 56 Reduced TFS System

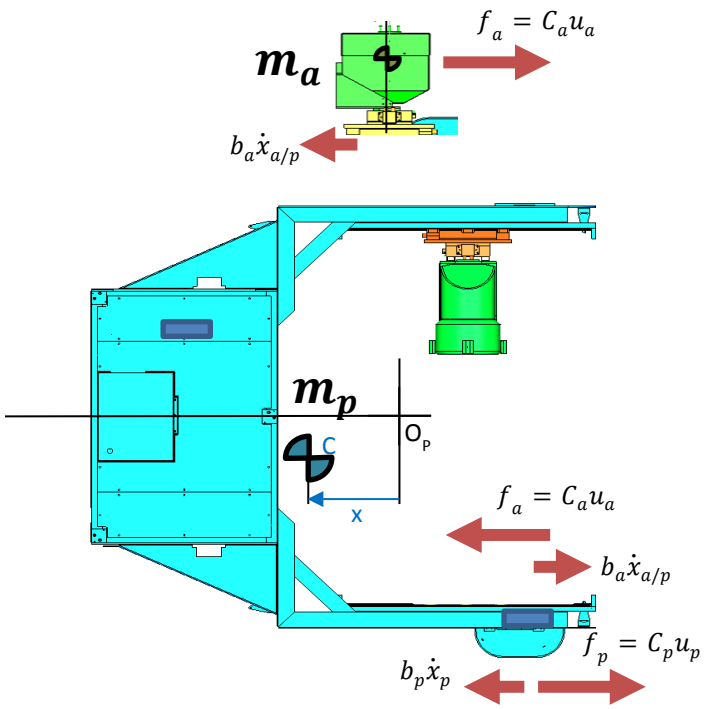

Figure 57 FBD of Reduced TFS System

$$m_a\ddot{x}_{a/g} + b_a\dot{x}_{a/p} = C_a u_a \quad (40)$$

$$m_p\,\ddot{x}_p + b_p\dot{x}_p = C_p u_p - C_a u_a + b_a\dot{x}_{a/p} \quad (41)$$

Where u_i is an input to the system. Notice the platform acceleration and velocity are both measured relative to the ground. The axis acceleration is measured relative to the ground, but the axis velocity is measured relative to the platform. Using (42) as the definition of the position of the axis relative to the ground, (40) can be re-written.

$$x_p + x_{a/p} = x_{a/g} \quad (42)$$

$$m_a\ddot{x}_{a/p} + b_a\dot{x}_{a/p} = C_a u_a - m_a\ddot{x}_p \quad (43)$$

This system is linearly time invariant, so a set of state variables can be chosen such that $\dot{x} = Ax + Bu$ and $y = Cx + Du$. Choosing state variables $x_1 = x_p$, $x_2 = \dot{x}_p$, $x_3 = x_{a/p}$ and $x_1 = \dot{x}_{a/p}$ and input variables $u_p = u_1$ and $u_a = u_2$, let $\zeta = \frac{m_a}{m_p}$

$$\dot{x} = \begin{bmatrix} 1 & 0 & 0 & 0 \\ 0 & 1/m_p & 0 & 0 \\ 0 & 0 & 1 & 0 \\ 0 & 0 & 0 & 1/m_a \end{bmatrix} \left(\begin{bmatrix} 0 & 1 & 0 & 0 \\ 0 & -b_p & 0 & b_a \\ 0 & 0 & 0 & 1 \\ 0 & \zeta b_p & 0 & -(1+\zeta)b_a \end{bmatrix} x + \begin{bmatrix} 0 & 0 \\ C_p & -C_a \\ 0 & 0 \\ -\zeta C_p & (1+\zeta)C_a \end{bmatrix} u \right) \quad (44)$$

$$y = \begin{bmatrix} 1 & 0 & 0 & 0 \\ 0 & 0 & 1 & 0 \end{bmatrix} x + \begin{bmatrix} 0 & 0 \\ 0 & 0 \end{bmatrix} u \quad (45)$$

The interaction of the two channels happens dynamically in the off-diagonal terms and statically in the $(1 + \zeta)$ terms.

To derive the transfer functions for the system, it is convenient to convert (41) and (43) to Laplace domain. While it follows from (45) that $y_1 = x_1$ and $y_2 = x_3$, the Laplace formulation is done with respect to $\dot{x}_1 = x_2$ and $\dot{x}_3 = x_4$ to make the solution easier to follow.

$$(m_p s + b_p)X_2 = b_a X_4 - C_a U_2 + C_p U_1 \quad (46)$$

$$(m_a s + b_a(1+\zeta))X_4 = \zeta b_p X_2 + C_a(1+\zeta)U_2 - \zeta C_p U_4 \quad (47)$$

Let eight constants be set such that the equations become:

$$c_1 X_2 = c_2 X_4 + c_3 U_1 + c_4 U_2 \quad (48)$$

$$c_5 X_4 = c_6 X_2 + c_7 U_1 + c_8 U_2 \quad (49)$$

So that:

$$X_2 = \frac{c_2c_7 + c_3c_5}{c_1c_5 - c_2c_6}U_1 + \frac{c_2c_8 + c_4c_5}{c_1c_5 - c_2c_6}U_2 \quad (50)$$

$$X_4 = \frac{c_6c_3 + c_7c_1}{c_1c_5 - c_2c_6}U_1 + \frac{c_6c_4 + c_8c_1}{c_1c_5 - c_2c_6}U_2 \quad (51)$$

Replacing the constants gives:

$$X_4 = \frac{-\zeta b_p C_a + C_a(m_p s + b_p)}{den}U_2 + \frac{\zeta b_p C_p - \zeta C_p(m_p s + b_p)}{den}U_1 \quad (52)$$

$$X_4 = \frac{C_a(m_p s + (1-\zeta)b_p)}{den}U_2 - \frac{\zeta C_p m_p s}{den}U_1 \quad (53)$$

$$X_2 = \frac{b_a C_a(1+\zeta) - C_a(m_a s + b_a(1+\zeta))}{den}U_2 + \frac{-b_a\zeta C_p - \zeta C_p(m_a s + b_a(1+\zeta))}{den}U_1 \quad (54)$$

$$X_2 = \frac{-C_a m_a s}{den}U_2 + \frac{-\zeta C_p(m_a s + b_a(2+\zeta))}{den}U_1 \quad (55)$$

$$den = m_p^2\left(\zeta s^2 + \frac{1}{m_p}\left((1+\zeta)b_a + b_p\right)s + \frac{b_a b_p}{m_p^2}\right) \quad (56)$$

Recognizing that

$$X_2 = sX_1 = sY_1 \quad (57)$$

$$X_4 = sX_3 = sY_2 \quad (58)$$

The transfer function from *u* to *y*, *G*, can now be formed such that:

$$G = \begin{bmatrix} G_{11} & G_{12} \\ G_{21} & G_{22} \end{bmatrix} \quad (59)$$

$$G_{11} = \frac{Y_1}{U_1} = \frac{-\zeta C_p\left(m_a s + b_a(2+\zeta)\right)}{m_p^2\left(\zeta s^3 + \frac{1}{m_p}\left((1+\zeta)b_a + b_p\right)s^2 + \frac{b_a b_p}{m_p^2}s\right)} \quad (60)$$

$$G_{12} = \frac{Y_1}{U_2} = \frac{-C_a m_a s}{m_p^2\left(\zeta s^3 + \frac{1}{m_p}\left((1+\zeta)b_a + b_p\right)s^2 + \frac{b_a b_p}{m_p^2}s\right)} \quad (61)$$

$$G_{21} = \frac{Y_2}{U_1} = \frac{-\zeta C_p m_p s}{m_p^2\left(\zeta s^3 + \frac{1}{m_p}\left((1+\zeta)b_a + b_p\right)s^2 + \frac{b_a b_p}{m_p^2}s\right)} \quad (62)$$

$$G_{22} = \frac{Y_2}{U_2} = \frac{C_a\left(m_p s + (1-\zeta)b_p\right)}{m_p^2\left(\zeta s^3 + \frac{1}{m_p}\left((1+\zeta)b_a + b_p\right)s^2 + \frac{b_a b_p}{m_p^2}s\right)} \quad (63)$$

This is equivalent to expanding (41) and (43) in block diagram form as shown in Figure 58.

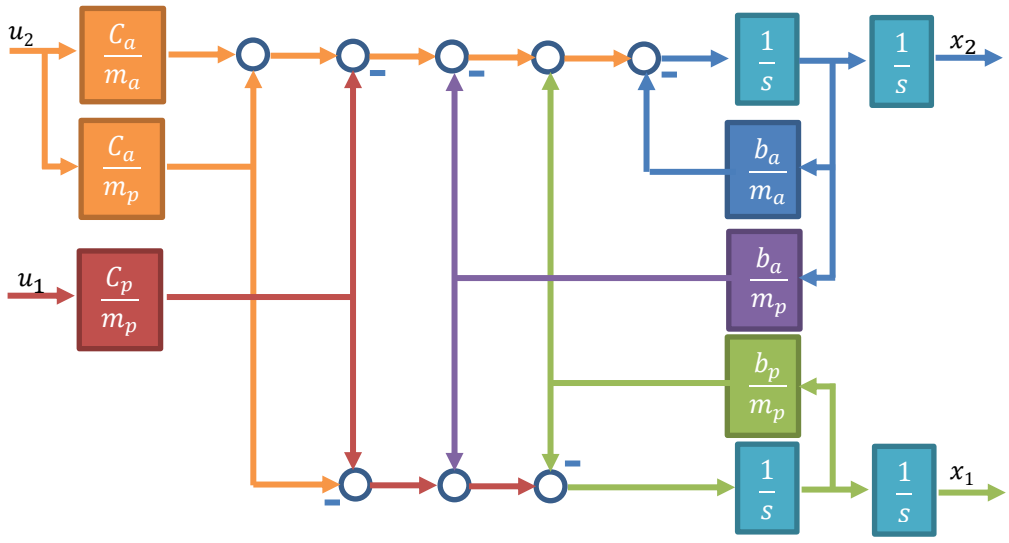

Figure 58 Block Diagram of Cross Coupling of Reduced TFS System

Using the results from Chapter five and the linear approximation, (Table 5), from Chapter six, the transfer function becomes:

$$G(s) = \begin{bmatrix} \dfrac{91.7s + 379.8}{s^3 + 6.04s^2 + 6.70s} & \dfrac{-91.7s}{s^3 + 6.04s^2 + 6.70s} \\ \dfrac{-157.3s}{s^3 + 6.04s^2 + 6.70s} & \dfrac{2491s + 3775}{s^3 + 6.04s^2 + 6.70s} \end{bmatrix} \quad \textbf{(64)}$$

Although a nonlinear model that accounts for bidirectional friction in the horizontal axes is more accurate than a linear model, it will be shown that the linear model is still affective in creating the decoupling control. A linear model will be used in the full system model.

Multiple-Input-Multiple-Output (MIMO) Systems

Now consider the full five channel system necessary for linear movements shown in Figure 3.

To create a five by five transfer function that represents the plant, the coupling from each channel must be found. The procedure to determine the effect of dynamic coupling is as follows:

- Force three channels to be fixed,
- Apply a step input of 100mm (Closed Loop) to one of the free channels and,
- Measure the response of the other free channel.

Figure 59 through Figure 63 show the magnitude of response in each of the twenty tests needed to evaluate all coupling in the system. The coupling is considered negligible if the response to a channel was less than 2% (2 mm) of the input.

Table 7 presents the coupling in a compact form.

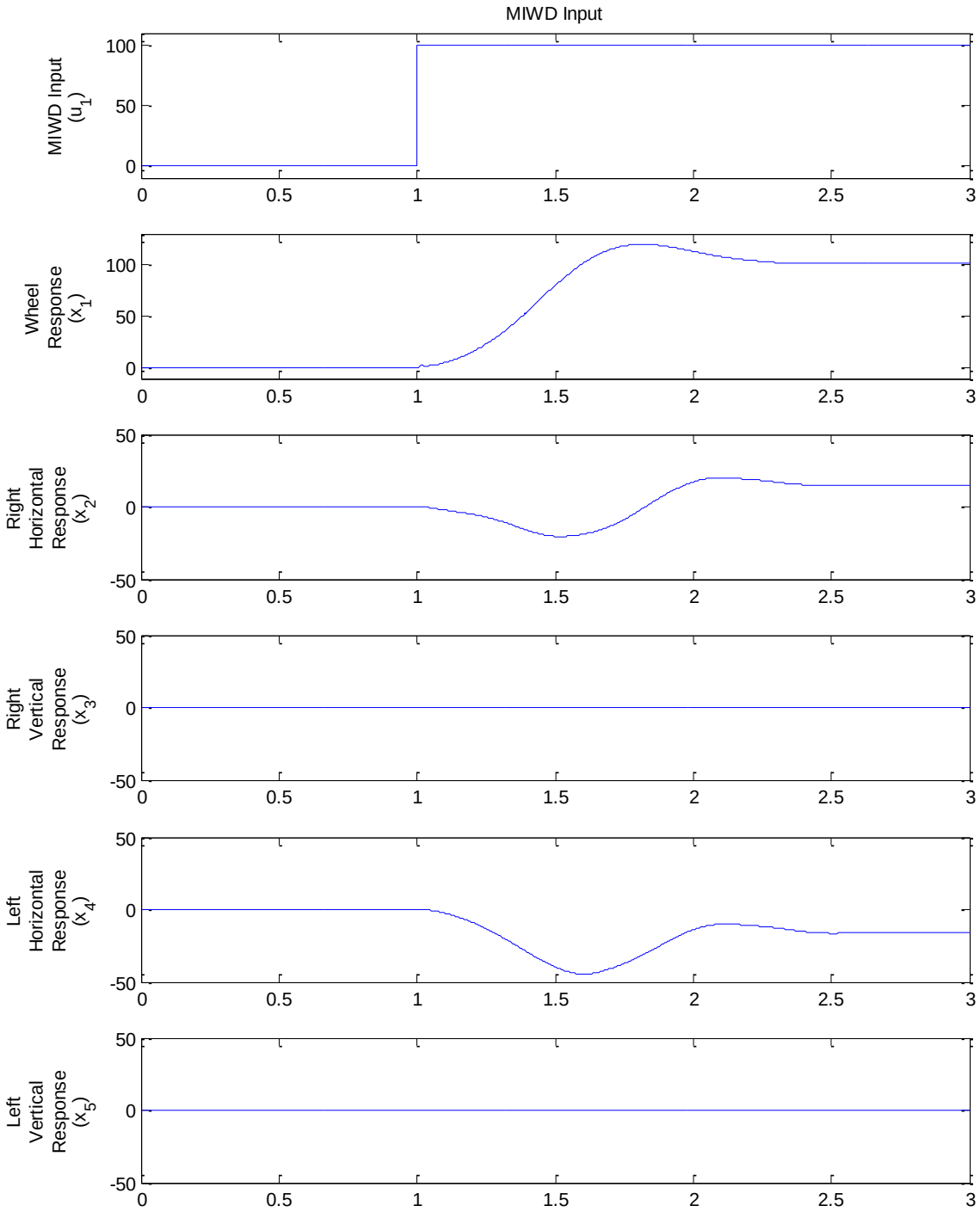

Figure 59 Coupling Interaction caused by MIWD Input

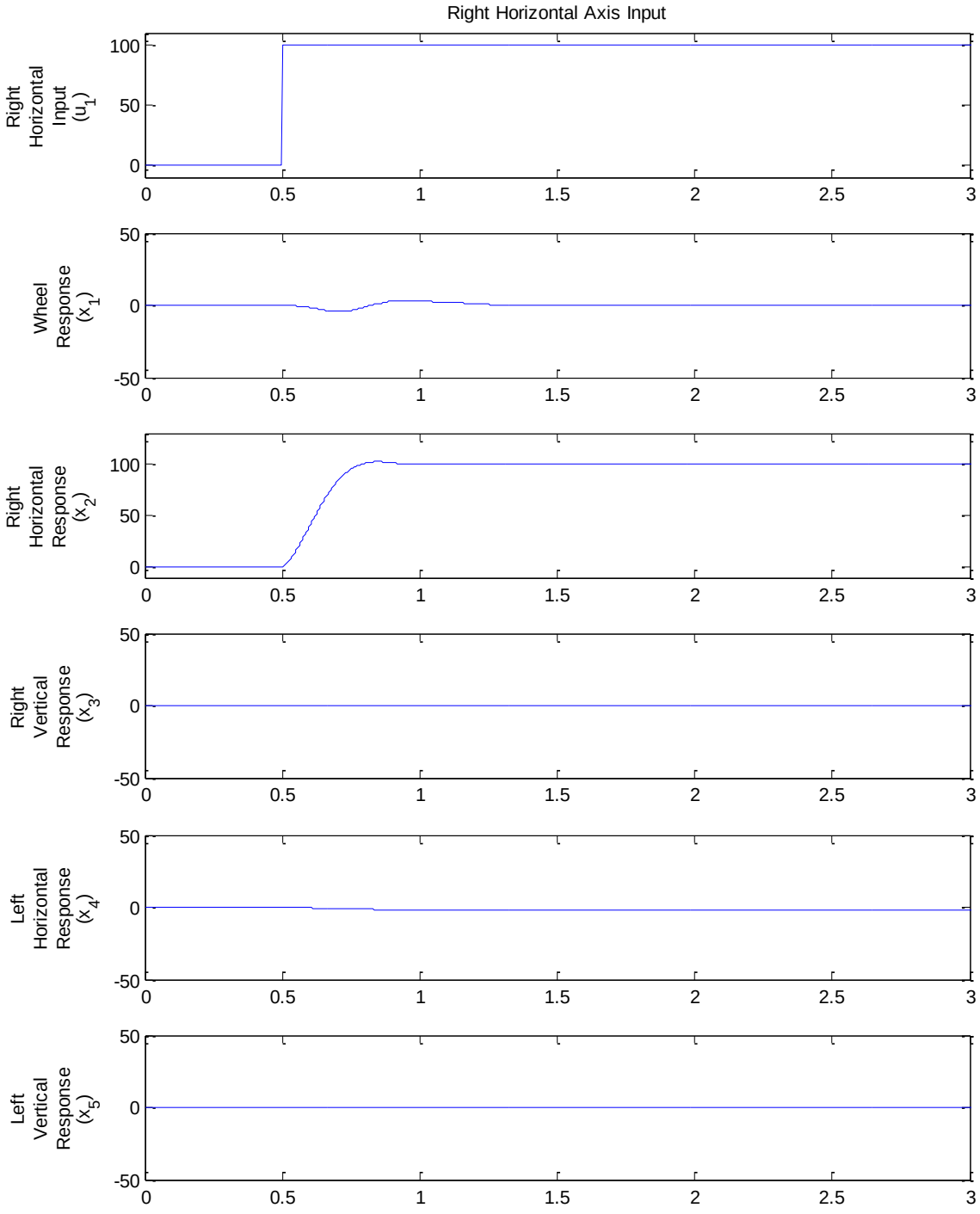

Figure 60 Coupling Interaction caused by Right Horizontal Input

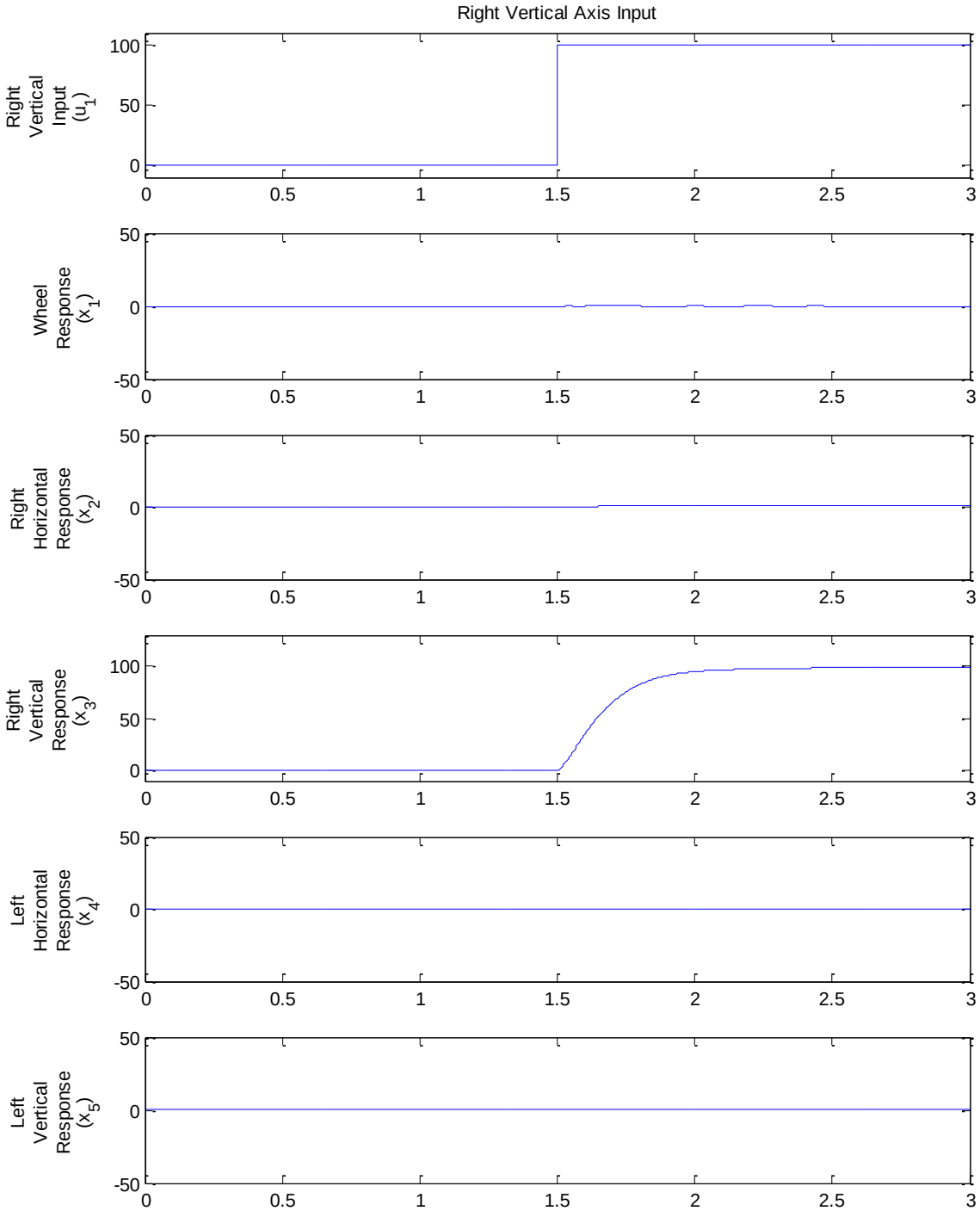

Figure 61 Coupling Interaction caused by Right Vertical Input

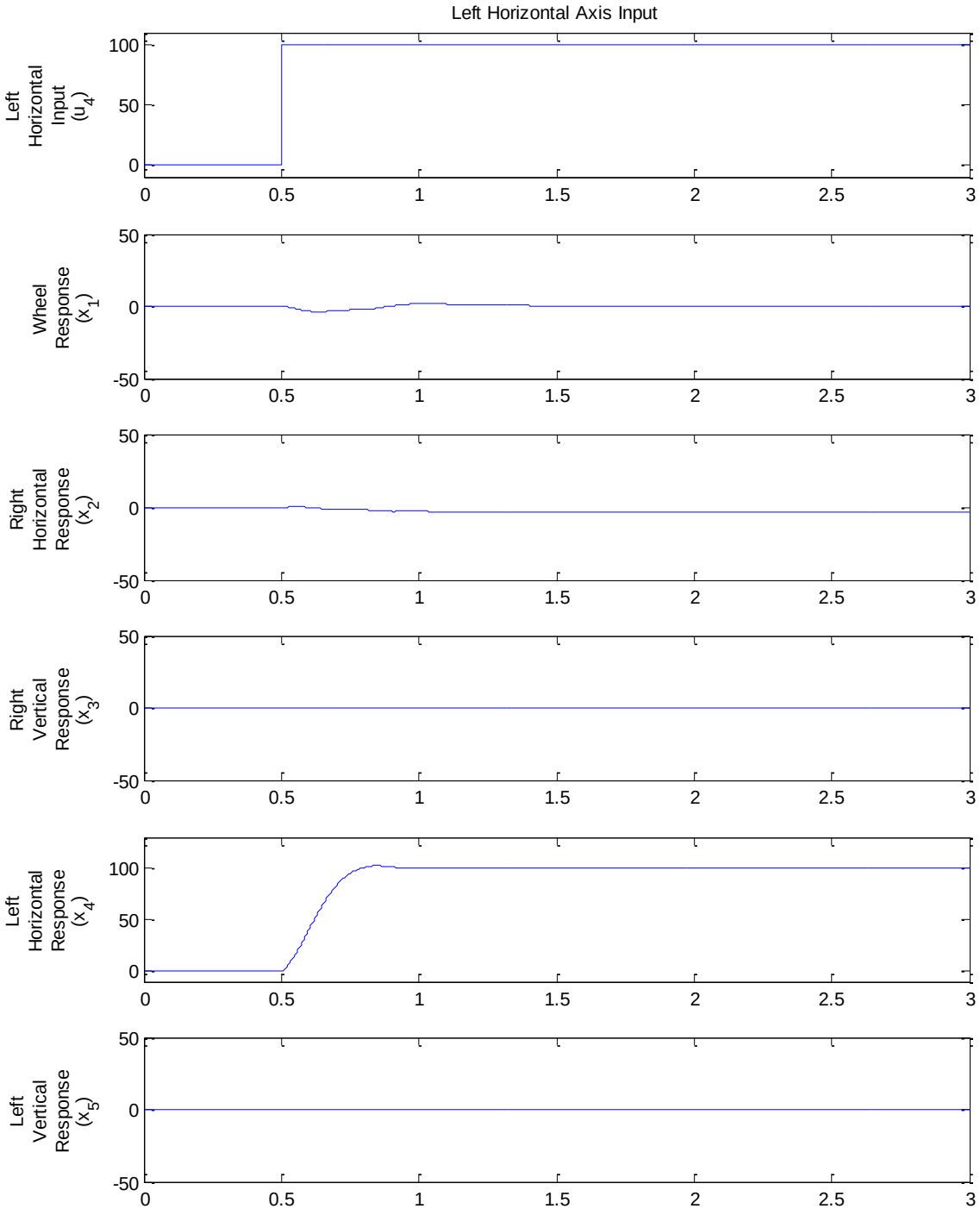

Figure 62 Coupling Interaction caused by Left Horizontal Input

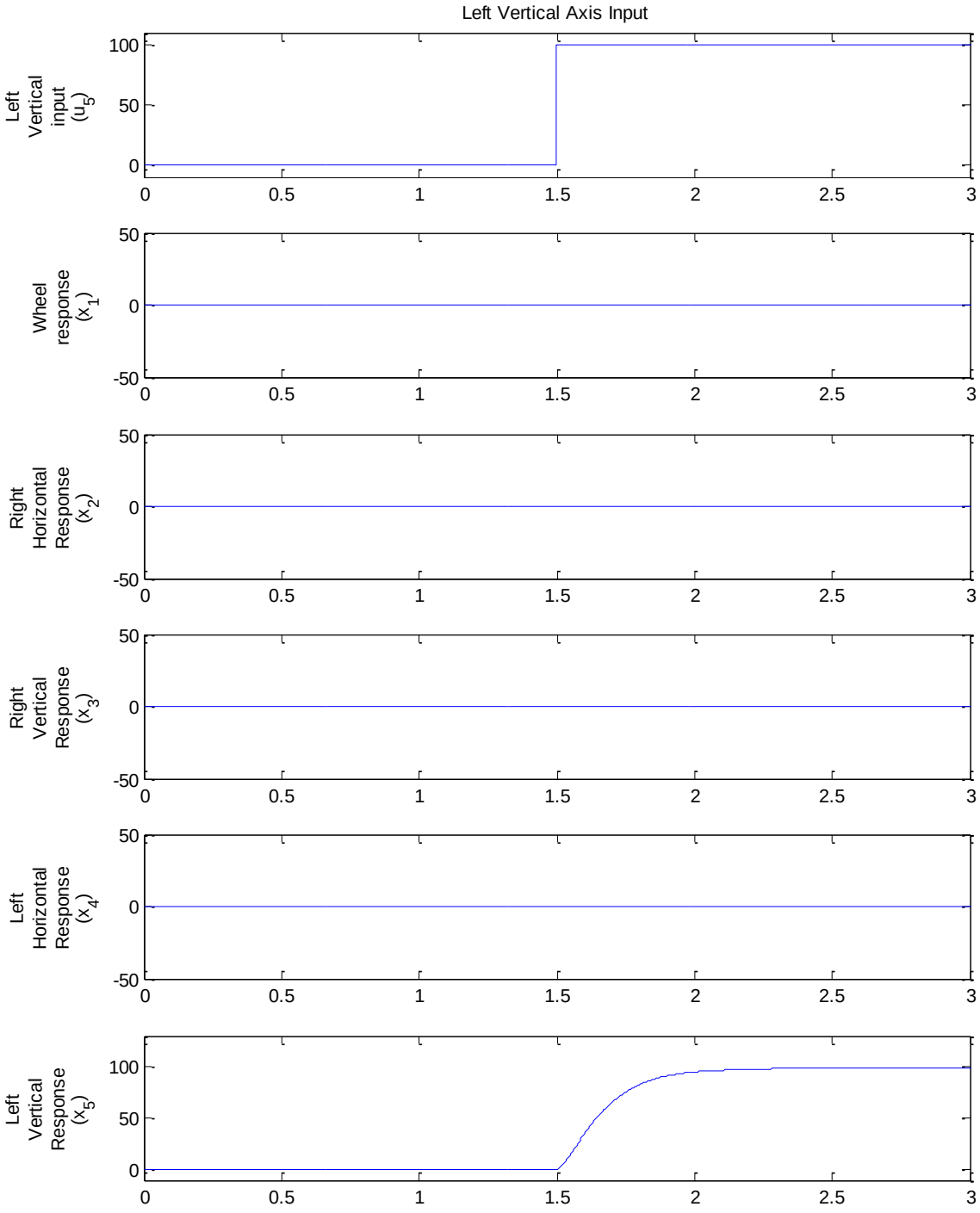

Figure 63 Coupling Interaction caused by Left Vertical Input

Table 7 Coupling Effects

	u_1	u_2	u_3	u_4	u_5
x_1		Coupling	No Coupling	Coupling	No Coupling
x_2	Coupling		No Coupling	No Coupling	No Coupling
x_3	No Coupling	No Coupling		No Coupling	No Coupling
x_4	Coupling	No Coupling	No Coupling		No Coupling
x_5	No Coupling	No Coupling	No Coupling	No Coupling	

The vertical channels do not exhibit any cross coupling. Each horizontal axis is affected by the platform, and each horizontal axis impacts the platform, but the horizontal axes do not affect each other.

By recognizing that the horizontal axes can be modeled using the same coefficients, an expanded state space system $\dot{x} = Ax + bu; y = Cx + Du$ can be created where A is *10 x 10*, B is *10 x 5*, C is *5 x 10* and D is *5 x 5*. The resulting plant becomes:

$$G = \begin{bmatrix} G_{11} & G_{12} & 0 & G_{12} & 0 \\ G_{21} & G_{22} & 0 & G_{24} & 0 \\ 0 & 0 & G_{33} & 0 & 0 \\ G_{21} & G_{24} & 0 & G_{22} & 0 \\ 0 & 0 & 0 & 0 & G_{33} \end{bmatrix} \quad (65)$$

$$G_{11} = \frac{91.7s^2 + 760s + 1565}{s^4 + 10.5s^3 + 32.9s^2 + 27.6} \quad (66)$$

$$G_{12} = \frac{-91.7s^2 - 405s}{s^4 + 10.5s^3 + 32.9s^2 + 27.6} \quad (67)$$

$$G_{21} = \frac{-157s^2 - 695s}{s^4 + 10.5s^3 + 32.9s^2 + 27.6} \quad (68)$$

$$G_{22} = \frac{2491s^2 + 14780s + 15560}{s^4 + 10.5s^3 + 32.9s^2 + 27.6} \quad (69)$$

$$G_{24} = \frac{-254s}{s^4 + 10.5s^3 + 32.9s^2 + 27.6} \quad (70)$$

$$G_{33} = \frac{3043}{s^2 + 28.2s} \quad (71)$$

Notice there is now a coupling term, G_{24}, between the two horizontal axes. This can be understood by recognizing the relationship between the horizontal axes and the platform. If the right horizontal axis is moved, the platform will move. If the platform moves, the left horizontal axis moves.

8.2 Decoupled Control

Several methods have been developed to decouple multiple degree of freedom systems. This work will consider three methods in simulation, comparing two of these methods in implementation. A comparison of these methods can be found in [63]. In the block diagram shown in Figure 64, K_d is a diagonal control matrix. Each diagonal element of K_d can contain any desired control scheme. For the TFS, a PD controller with different values of K_p and K_d is appropriate for all five diagonal elements. To decouple the system, it is desirable to find a new control transfer function, K, such that:

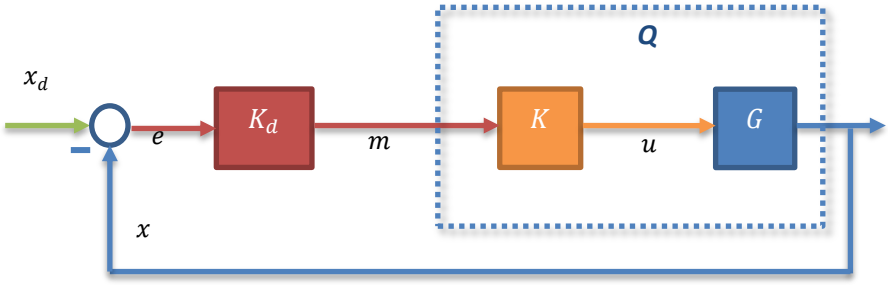

Figure 64 Decoupling Control

$$GK = Q \tag{72}$$

where Q is composed of the desired uncoupled transfer functions. This is referred to as the perceived plant.

$$Q = \begin{bmatrix} Q_{11} & 0 \\ 0 & Q_{22} \end{bmatrix} \tag{73}$$

If the plant can be accurately modeled, and if that model is invertible, the decoupling control can then be solved by

$$K = G^{-1}Q \tag{74}$$

Ideal Decoupling

Ideal decoupling was first postulated by [64]. The designer has the freedom to choose Q according to response characteristics desired. Often, the dynamics of the uncoupled system is used. This allows a seamless transition from independent, uncoupled system actuation to the coupled system actuation.

Applying this method to the TITO system, a controller, K, can be found such that:

$$K = \frac{1}{\det(G)} \begin{bmatrix} Q_{11}G_{22} & -Q_{11}G_{12} \\ -Q_{22}G_{21} & Q_{22}G_{11} \end{bmatrix} \quad (75)$$

where

$$Q_{11} = \frac{\frac{C_p}{m_t}}{s^2 + \frac{b_p}{m_t}s} \quad (76)$$

$$Q_{22} = \frac{\frac{C_a}{m_a}}{s^2 + \frac{b_a}{m_a}s} \quad (77)$$

Notice the mass of the first system is the total mass, $m_t = m_p + m_a$.

The perceived plant Q was chosen to match the uncoupled system, namely the diagonal elements of G. This allows tuning to be done on the individual, uncoupled channels and implemented on the total system. While demonstrated with a two-by-two matrix for simplicity, the technique has been generalized for any *n*-by-*n* system, where *n* is the number of input-output channels. [65]

There are several disadvantages to the ideal decoupling method. The first comes in the implementation of the control. The elements of the decoupling transfer function can be polynomials of a high order. For instance, consider the decoupling control of the 2-by2 system described above.

$$G = \begin{bmatrix} \frac{91.7\,s + 273}{s^3 + 4.5\,s^2 + 3.93\,s} & -\frac{18.4\,s}{s^3 + 4.5\,s^2 + 3.93\,s} \\ -\frac{91.7\,s}{s^3 + 4.5\,s^2 + 3.93\,s} & \frac{291\,s + 359}{s^3 + 4.5\,s^2 + 3.93\,s} \end{bmatrix} \quad (78)$$

$$Q = \begin{bmatrix} \frac{273}{s^2 + 2.98\,s} & 0 \\ 0 & \frac{85.94}{s^2 + 1.24\,s} \end{bmatrix} \quad (79)$$

$$K = \begin{bmatrix} \frac{s^4 + 5.7\,s^3 + 9.5\,s^2 + 4.85\,s}{s^4 + 5.7\,s^3 + 9.5\,s^2 + 4.85\,s} & \frac{0.3\,s^4 + 1.4\,s^3 + 1.2\,s^2}{s^4 + 5.7\,s^3 + 9.5\,s^2 + 4.85\,s} \\ \frac{0.2\,s^4 + 0.9\,s^3 + 0.8\,s^2}{s^4 + 7.5\,s^3 + 17.3\,s^2 + 11.7\,s} & \frac{s^4 + 7.5\,s^3 + 17.3\,s^2 + 11.7\,s}{s^4 + 7.5\,s^3 + 17.3\,s^2 + 11.7\,s} \end{bmatrix} \quad (80)$$

This type of control is typically executed by using partial fraction decomposition to break the terms into first order polynomials and summing the results. Each of these terms is called a Lead-Lag element [59].

Care must be taken to ensure that the transfer function Q stays diagonal even when the control to the plant, G, is saturated. The transfer function Q^* in Figure 65 is not identically equal to Q in Figure 64. The addition of an imposed input saturation in Figure 67 ensures that Q^* is nearly diagonal.

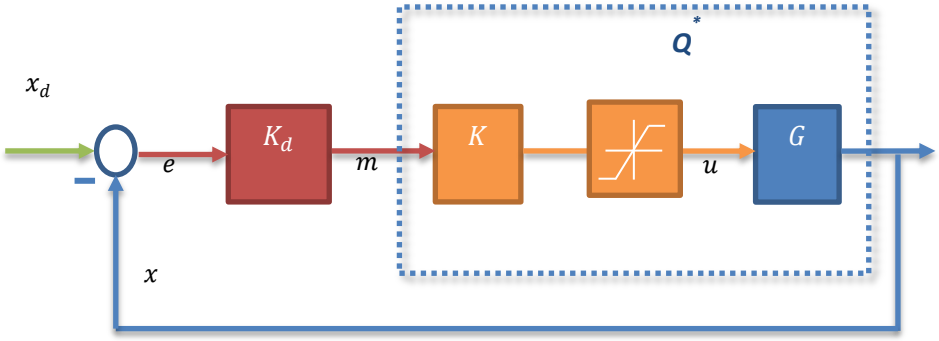

Figure 65 Decoupling Control with Saturation

Simplified Decoupling

[66] first proposed the notion of simplified decoupling. The concept of this technique is to create a decoupling scheme that is easier to implement. Again from Figure 64, the transfer function Q is desired to be diagonal. The decoupling transfer function K contains unity elements along the diagonal. Each of the off-diagonal elements are defined as

$$K_{ij} = -\frac{G_{ij}}{G_{ii}} \tag{81}$$

Figure 66 shows an expanded view of simplified decoupling for a *3 x 3* system. Following the work of [67], a *2 x 2* example is continued below to illustrate the concept.

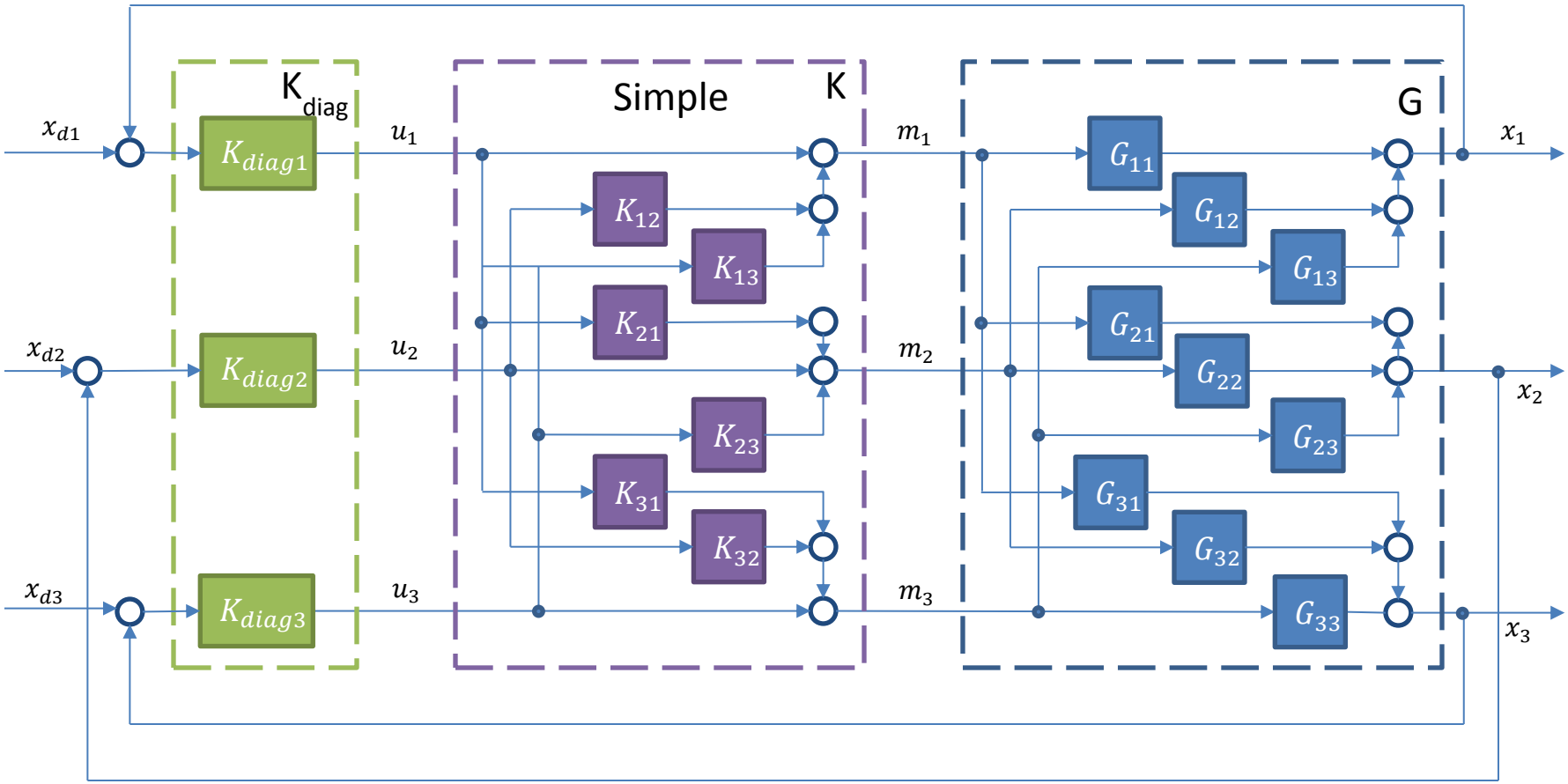

Figure 66 Simple Decoupling Expanded

$$K_{21} = -\frac{G_{21}}{G_{22}} = \frac{91.7\,s^4 + 413\,s^3 + 360\,s^2}{291\,s^4 + 1670\,s^3 + 2760\,s^2 + 1410\,s} \approx \frac{0.315}{s + 1.24} \quad \textbf{(82)}$$

The simplification of K_{21} can be seen by using Partial Fraction Decomposition, and setting all elements equal to zero that have a numerator smaller than 10^{-4}. The perceived plant now becomes

$$Q = \begin{bmatrix} \frac{G_{11}G_{22} - G_{12}G_{21}}{G_{22}} & 0 \\ 0 & \frac{G_{11}G_{22} - G_{12}G_{21}}{G_{11}} \end{bmatrix} \quad \textbf{(83)}$$

$$Q_{22} = \frac{272\,s^8 + 4.9e^3\,s^7 + 3.3e^4s^6 + 1.6e^5s^5 + 4.2e^5s^4 + 6.9e^5s^2 + 3.8e^5s^1 + 9e^4}{s^{10} + 21s^9 + 2e^2s^8 + 1e^3s^7 + 3e^2s^6 + 7e^3s^5 + 1e^4s^4 + 9e^2s^3 + 4e^3s^2 + 1e^3} \quad \textbf{(84)}$$

The disadvantage to the simple decoupling method is that the perceived plant can be very different from the original uncoupled plant. [68] This is especially important when the system has the capability to operate with only some of the elements active. For instance, if the wheels to the platform are locked and the power to the wheels is disabled, the axes are naturally uncoupled. It might be necessary, therefore, to use one controller, K_d, for the uncoupled scenario, and a different controller for the coupled scenario. It is likely that the two scenarios cannot be tuned to behave in an identical manner.

In addition to the ease of implementation, the simple decoupler has an advantage of being able to adjust for saturation. Figure 67 demonstrates that the input m to the decoupling controller K can become saturated, and the perceived plant, Q^*, will remain decoupled.

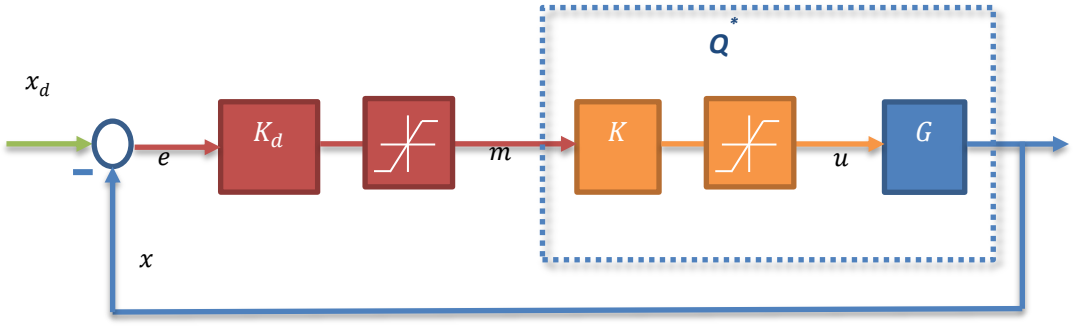

Figure 67 Decoupling Control with Input Saturation

INVERTED DECOUPLING

Inverted decoupling is a specialized form of ideal decoupling. [69] It was touted as combining the design flexibility of the ideal method, while retaining the implementation ease of the simple method. Its use in industry has been rather limited, because the feed forward elements can introduce instability to the system. [70] It should be noted that all decoupling methods are heavily dependent on accurate modeling of the plant, and, in that sense, the decoupling control effort is always a form of feed forward.

Until recently, [68], ideal decoupling was only performed on 2x2 systems. It was demonstrated as having the same elements of the simple control, but the summing and takeoff elements of the control occur in a different order. [68] generalized this concept for an *n by n* transfer function. Figure 68 shows the scheme in matrix form. The result of this work is summarized for completeness.

$$K = K_d\left(I - K_{off}K_d\right)^{-1} \quad \textbf{(85)}$$

Inverting K and (72) yields

$$K^{-1} = K_d^{-1} - K_{off} = Q^{-1}G \quad \textbf{(86)}$$

The components of K are defined such that K_d is a diagonal matrix and K_{off} has zero elements on the diagonal and non-zero elements elsewhere. The inverted decoupling scheme is expanded for a *3 x 3* system in Figure 69.

The decoupling matrix is realizable if each element is proper. For all physical systems, the original plant, G, is proper, therefore, there is always an input-output channel combination that allows the decoupling matrix to be proper. Without the loss of generality, it is always possible to reassign the

input-output channels such that the diagonal elements of G represent the desired uncoupled control channels. [67]

The inverted coupling can use the same decoupling elements defined for the simple case, but the resulting perceived plant will behave like the uncoupled plant, thus allowing the same controller K_d for the uncoupled and coupled scenario. The inverted coupling also allows the effects of saturation to be accounted for, so the system remains decoupled even when the input is saturated. [71, 72]

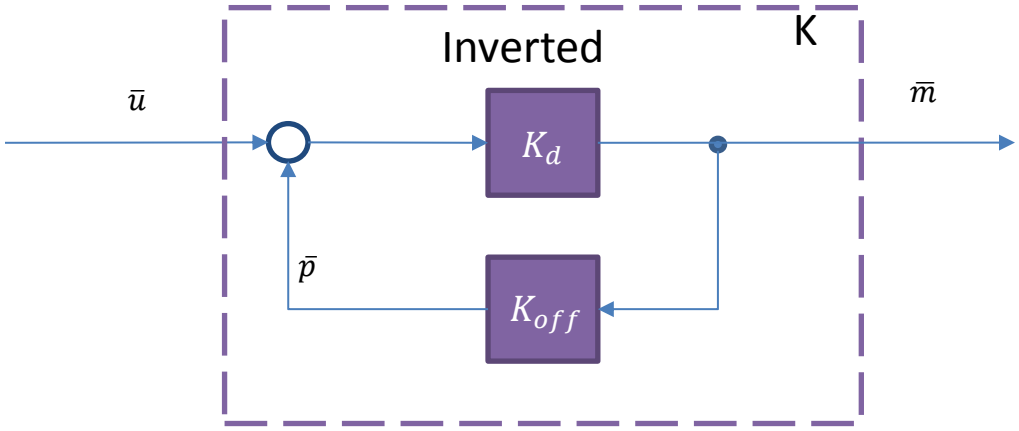

Figure 68 Inverted Decoupling in Matrix Form

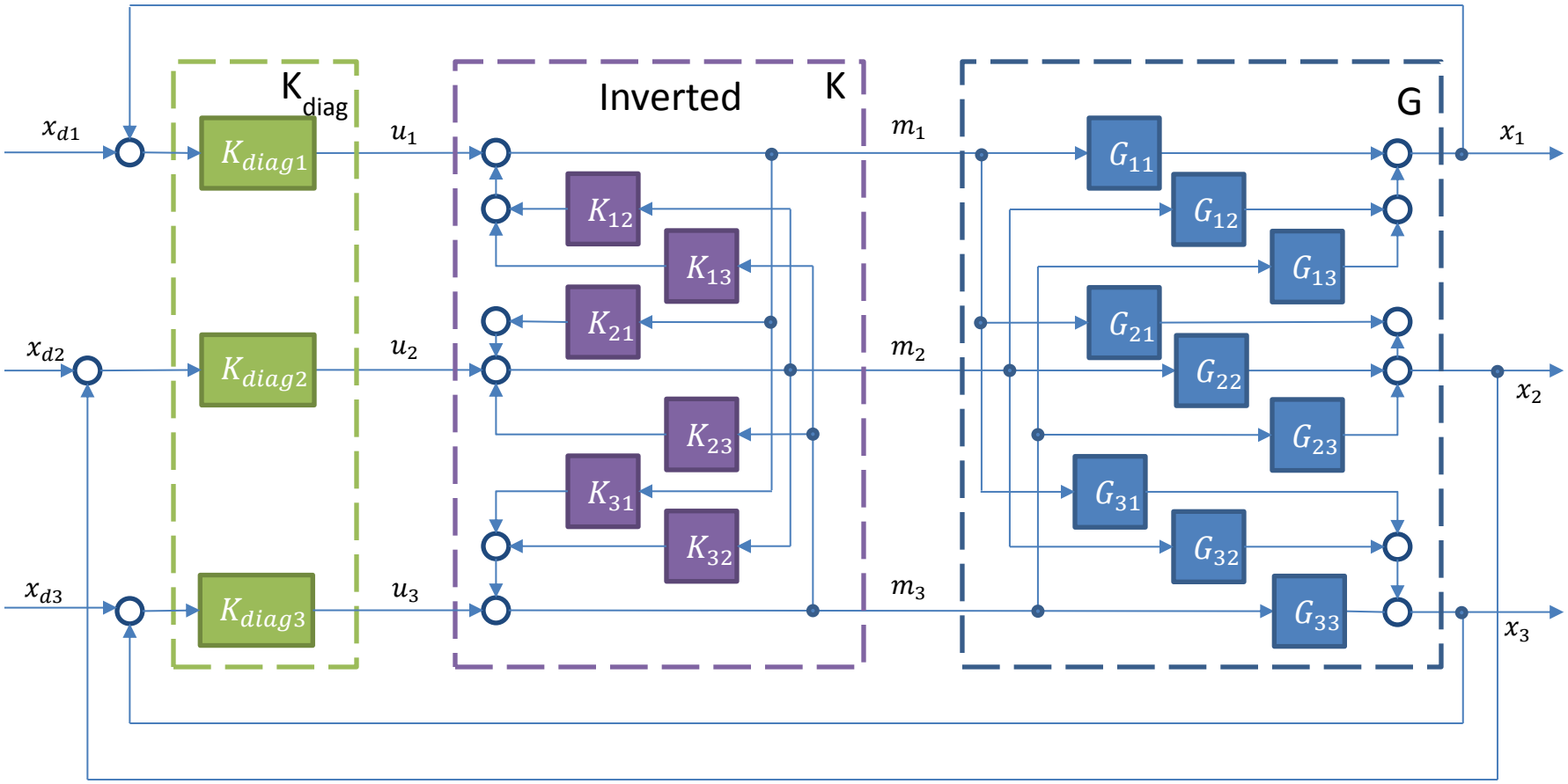

Figure 69 Inverted Coupling Expanded

COUPLING SCHEMES COMPARED

The plant transfer function in (97) was placed in Simulink. The controllers (19) and (27) from Chapter 6 and Chapter 7 were implemented for the platform and the left horizontal axis. Saturation was included in the control effort. Applying a step input first to the axis and then to the platform clearly shows the coupling effect. Figure 70 compares the coupled system with Ideal, Simplified and Inverted decoupling strategies. All three strategies are successful at fully decoupling the system. Although the resulting perceived plant has higher order terms for simplified and inverted coupling, the response is very similar between the three methods. The response for the Simplified Coupling method is slightly slower, but the extra expense of the ideal decoupling implementation is not worth the increase in response time.

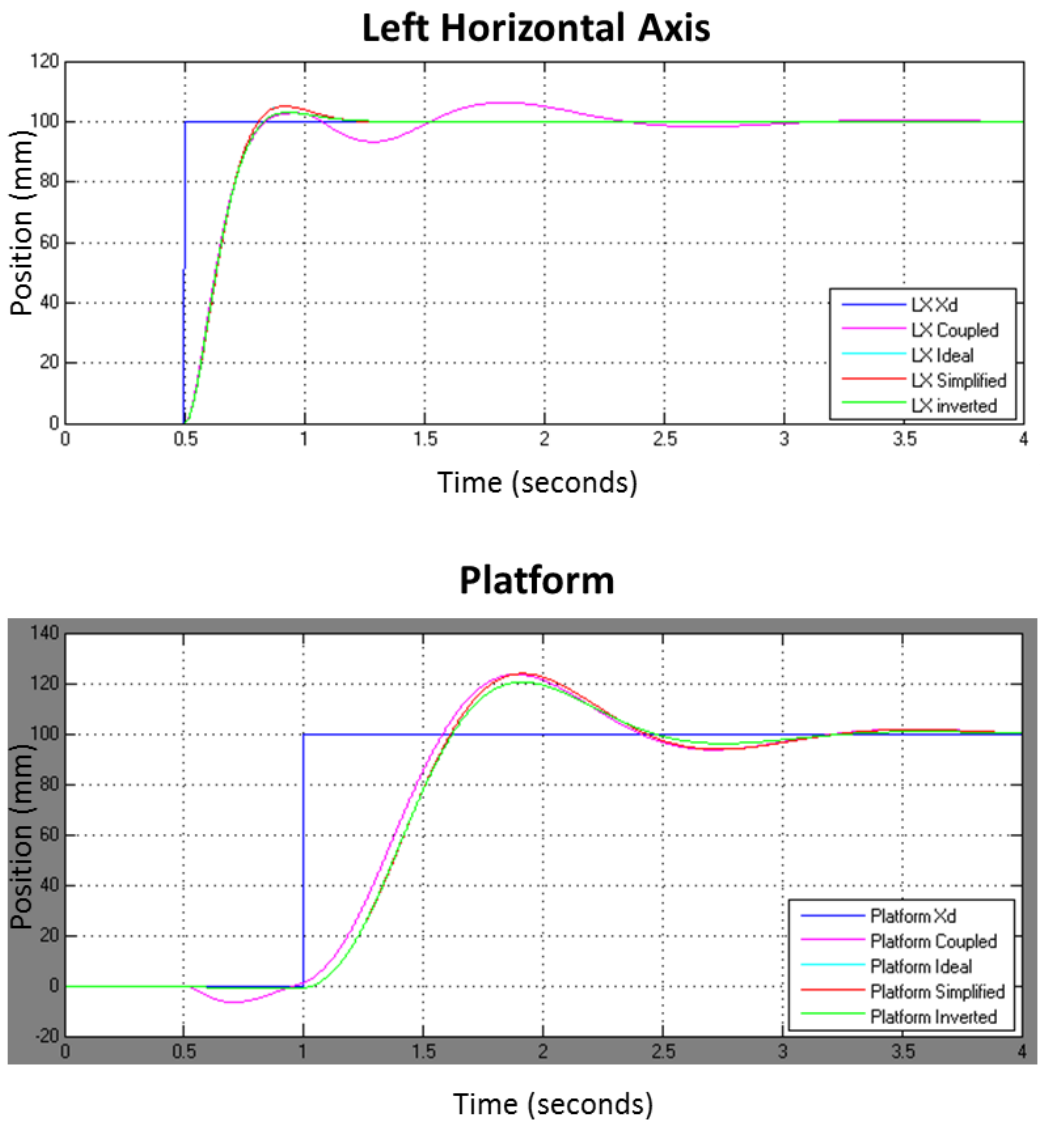

Figure 70 Decoupling Techniques Compared for TITO System

8.3 Total System Inputs

For translational tracking procedures, only three human inputs are needed to drive the system. The platform should follow the human subject, both the horizontal axes should follow the horizontal motion of the joint, and both the vertical axes should follow the vertical motion of the joint. Because of x-ray safety constraints, it is also necessary to guarantee that the x-ray emitter and collector stay aligned for all motion. To date, this was achieved by adding a P-controller to drive a slave axis to the master axis, as shown as the green block in Figure 71. The cost of the new

P-controller is an additional tuning parameter and an additional control loop. It is suggested that both horizontal axes can be driven to the same location without a master-slave configuration by recognizing the physical significance of the camera image. Consider a camera mounted to the right axes with a joint located in the camera view. It is desired to drive the axes to a location that has the joint in the center of the image. The control error for the right horizontal axis is the distance of the joint from the center of the camera image, and can be expressed as

$$e_2 = x_{joint/x_2} \quad (87)$$

From Figure 3 and Figure 20 this distance can also be expressed from the ground frame as

$$e_2 = x_{joint/g} - x_{p/g} - x_{a/p} = x_{joint/g} - x_1 - x_2 \quad (88)$$

It is desired to drive the left horizontal axis to the same location, namely $x_{joint/g}$.

$$e_4 = x_{joint/g} - x_1 - x_4 \quad (89)$$

Substituting (106) and (107) into (108)

$$e_4 = \left(x_{joint/g} - x_1 - x_2\right) + x_2 - x_4 = e_2 + x_2 - x_4 \quad (90)$$

This method uses the camera image and the two encoder locations of the horizontal platforms to create the control error. Both axes with converge at the same location, but the axes-alignment effort is controlled in the same loop with the same control gains as the joint-following effort. Figure 72 shows this independent axis control scheme. The vertical axes can be treated in the same manner.

If the axes were identical, the response of the two axes would be the same as the response of one axis that is twice as heavy. From Chapters 6 and 7, it was found that the axes are close enough to each other to be modeled as identical. With the additional control effort described by Figure 72, it is now possible to treat the axes as one horizontal axis and one vertical axis. To demonstrate this, a step input of 100 mm was injected to the system as a joint displacement seen by a virtual camera on the right axis. Figure 73 shows the response of the two axes. The axes were never more than 3 mm apart for the entire step, demonstrating that the axes stay aligned and that the axes can be modeled as a single unit. This is true for all activities in the linear direction. As long as the mass of the manipulators move together, the resultant forces are the same as one large manipulator. This allows the results of the TITO scheme for inverted and simplified coupling to be utilized in decoupling the system. This assumption is no longer valid if the platform undergoes rotational motion.

A step input was applied to the axes of 100mm, followed by a step input of 100 mm applied to the platform. In Figure 74, the actual results were compared with predicted results from the model of the coupled system in Simulink.

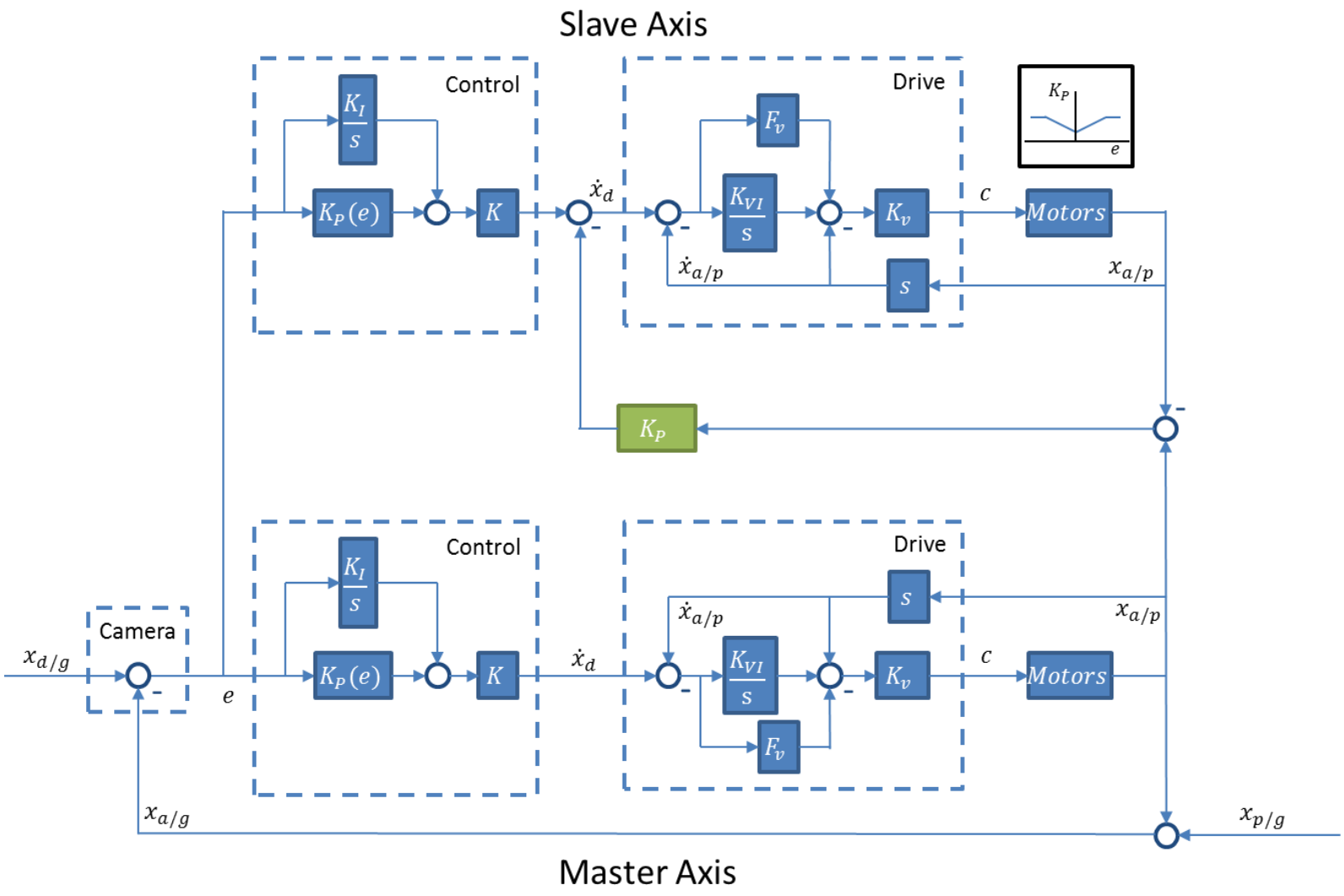

Figure 71 Master-Slave Control Scheme

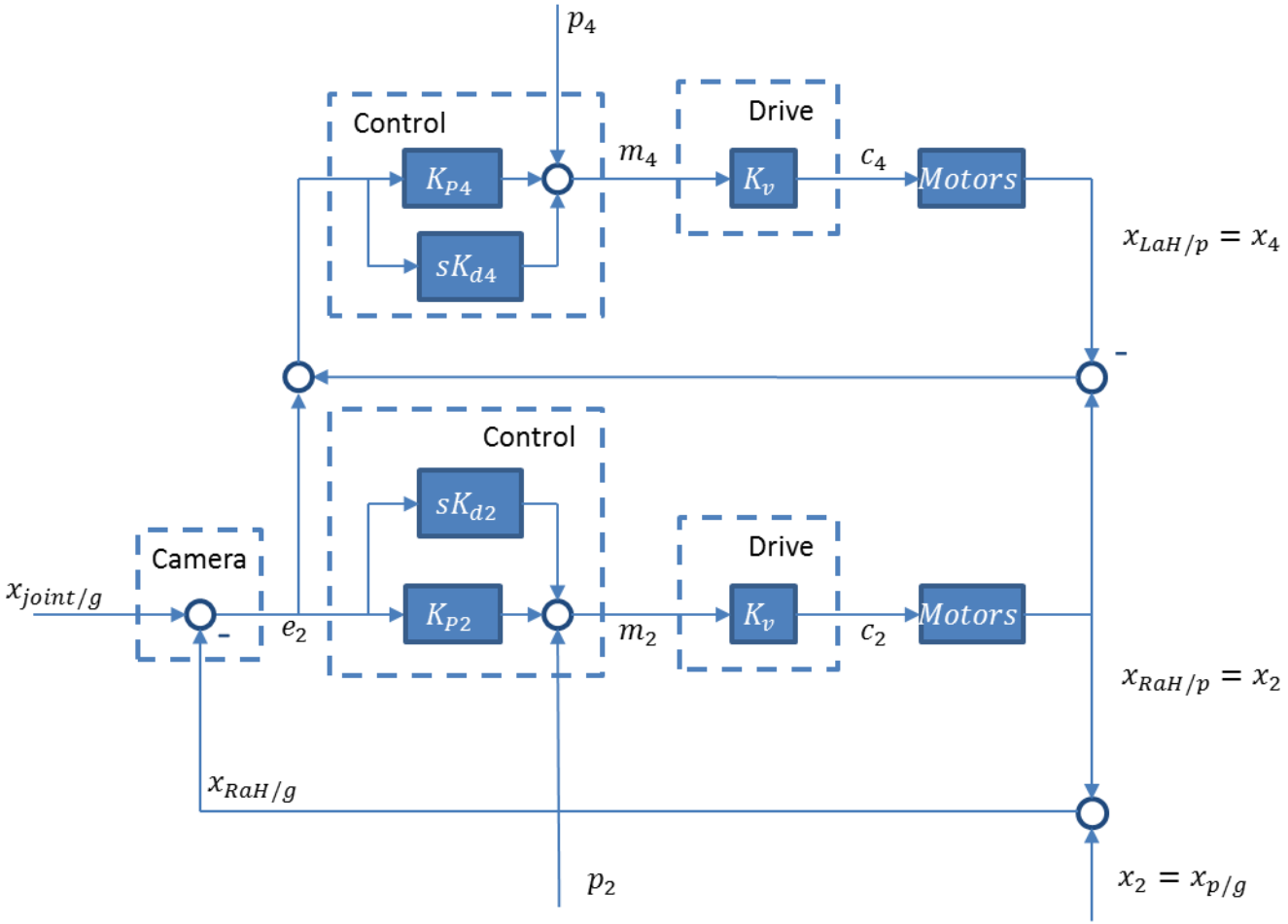

Figure 72 Sensor-Driven Independent Control Scheme

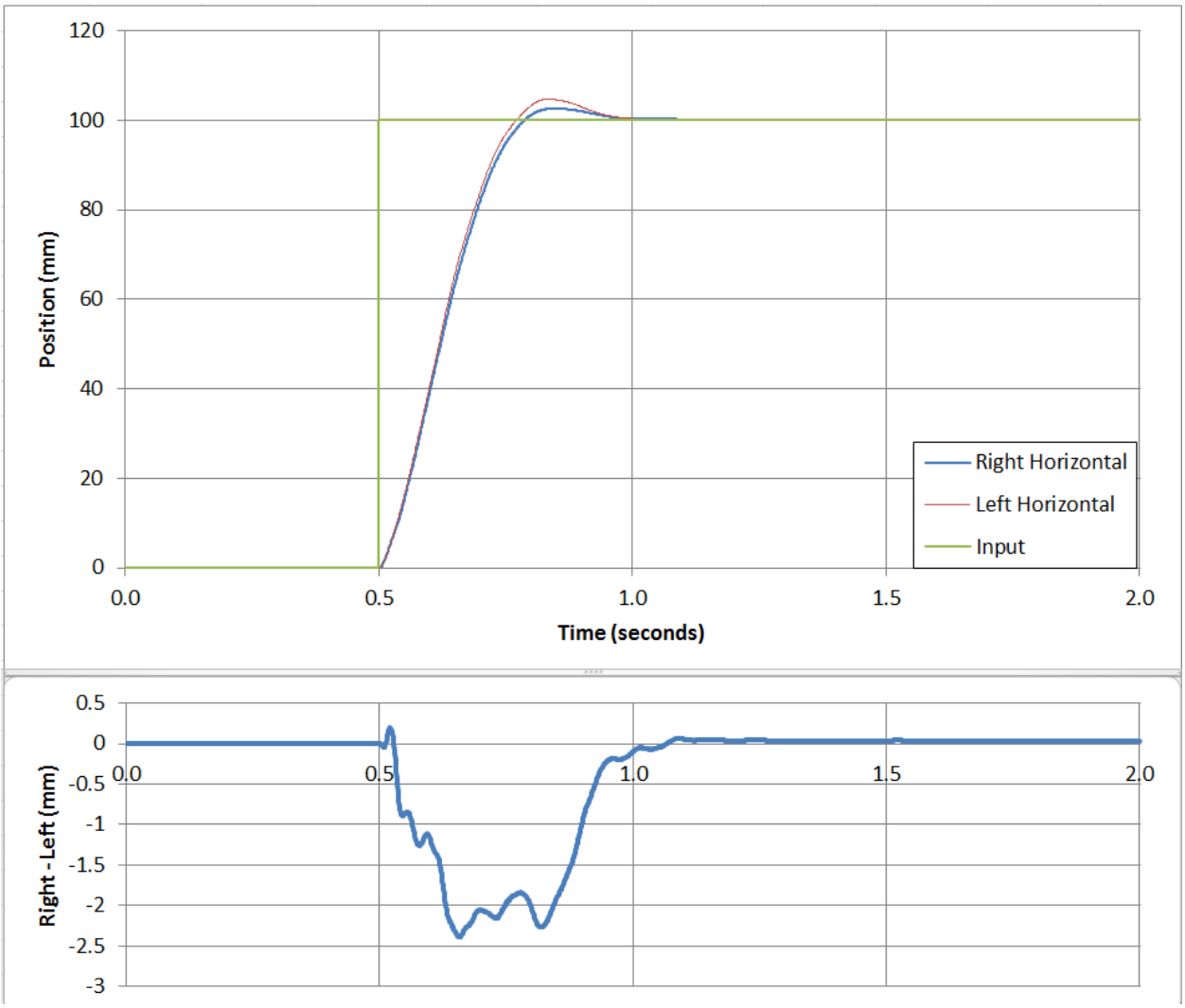

Figure 73 Response of Horizontal Axes to Virtual Step Input

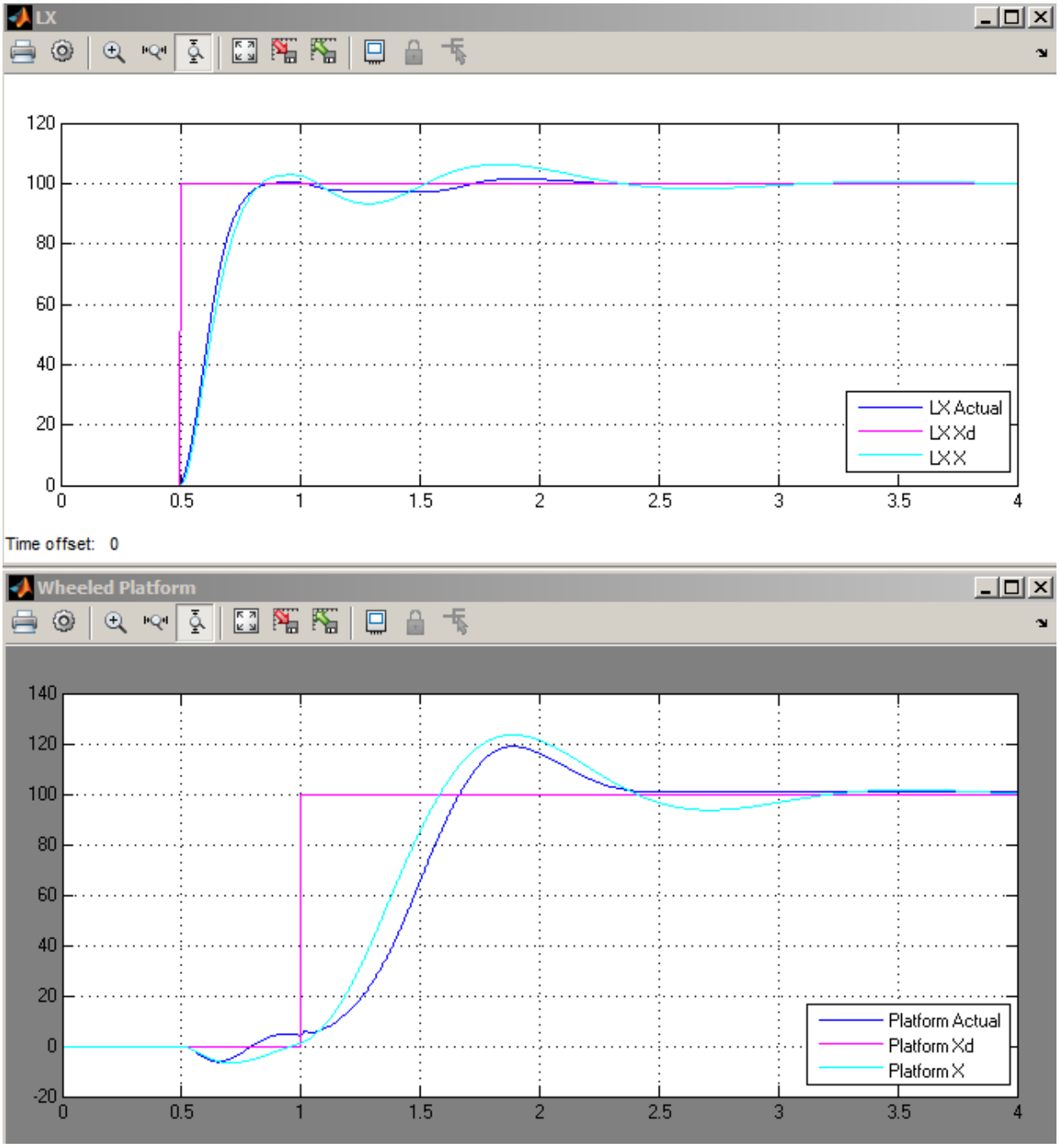

Figure 74 Model vs Actual Coupled Results of Step Inputs

8.4 Discussion Regarding Simulation Results

The desired input into the TFS is not a step input, rather it is driven from the human activity being recorded. The walking data collected from the 66-inch person were used to simulate a camera and laser input into the system. The diagonal controller components for each of the five channels were determined by tuning the uncoupled system step response. First, only one horizontal axis was allowed to move. This was to compare the TITO decoupling. The results are shown in Figure 75 and Figure 76.

The horizontal axes show a slight advantage to using either of decoupling methods. The decoupling methods did not reduced the maximum error, as all three methods had an error of about 20mm at 2.3 seconds. For most portions of the activity, the inverted control performed best, while the natural, coupled system performed worse. The inverted method decreased the average error by 1.7 mm over the course of the activity. While the improved performance is sustained throughout the activity, it is minimal. This means that the coupling effect of the physical TFS components is not a major contribution of joint tracking error for the input conditions considered

The current fluoroscope device will continue to have the TP and the full joint of interest in the field of view as long as the tracking error is below 40 mm. Past control configurations yielded a tracking errors of about 100 mm. [52] This means that even without the decoupling methods, the TFS should be able to track a normal walk nearly five times more accurately using PD controllers. Figure 76 shows that the maximum control effort exerted by the horizontal axis was less than three volts, which is less than thirty percent of the capabilities of the full system. As discussed in Chapter 6, increasing the proportional gain would reduce the rise time of the system, which would yield a faster response. This must be balanced by increasing the derivative gain to ensure that the system response remains stable. In the physical system, the derivative gain cannot be increase because it introduces chatter into the system. A feedback device that measures velocity directly, such as a tachometer, would allow a higher derivative gain, which would allow the system to respond with less tracking error.

The platform response reveals a large advantage to using the decoupling methods. The maximum error was reduced from 179 mm in the coupled response to 93 mm using the simple method and 83 mm using the inverted method. During fluoroscopic procedures, only the joint tracking error affects the quality of the image. This means that the reduction of maximum platform error does not directly provide better knee fluoroscopic data. The reduced platform error does improve the speed at which activities could be done, and the amount of horizontal track needed to achieve the activity. It would also be much more important for A-P hip tracking when the clearance between the subject and the TFS is more restrictive. Figure 77 shows the location of the axis during the three trials. All trials needed roughly 250 mm of space to follow the knee, but the decoupling methods allowed the joint to stay more centered in the track.

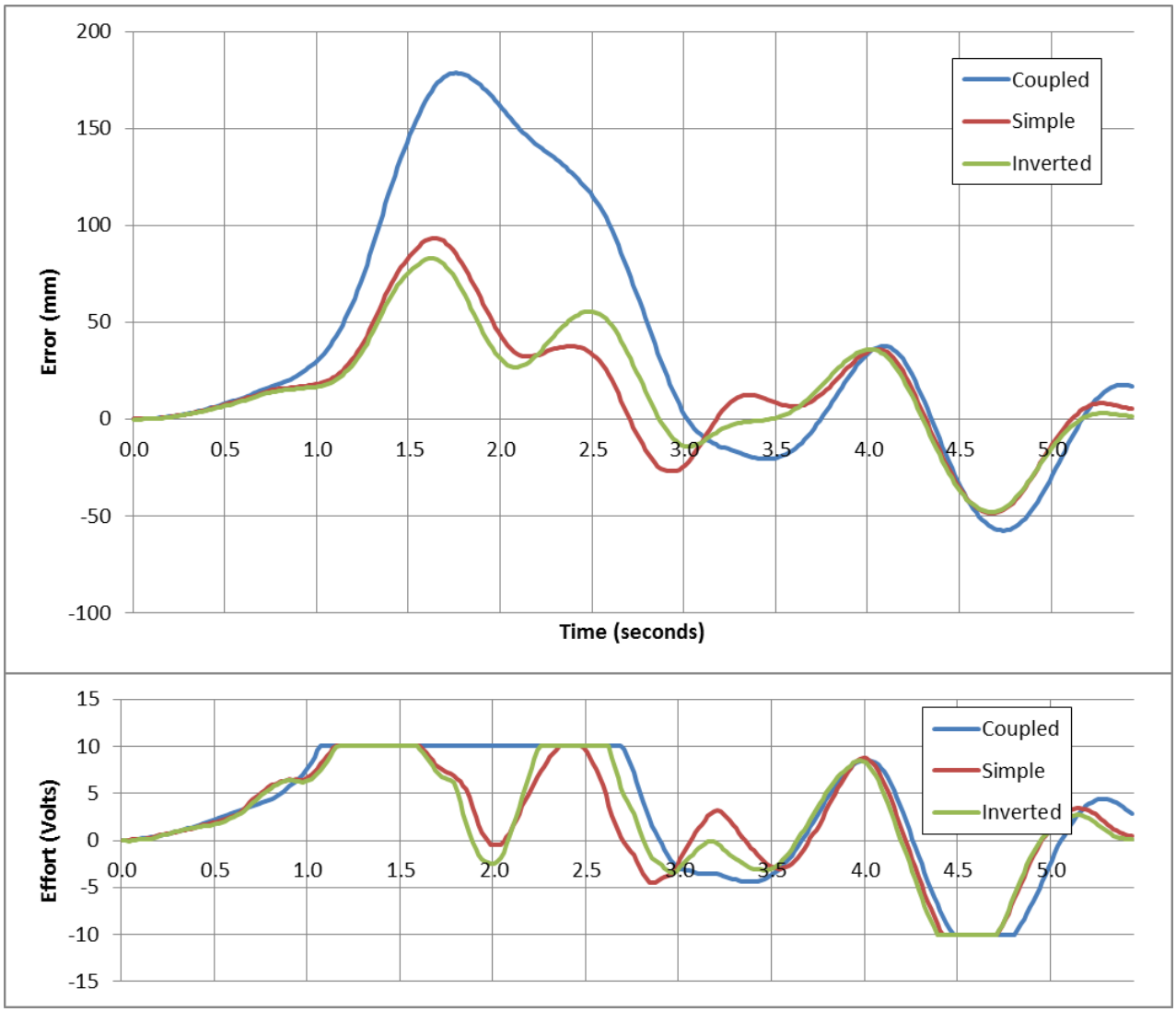

Figure 75 Platform Error and Effort during Walk with TITO Decoupling Methods

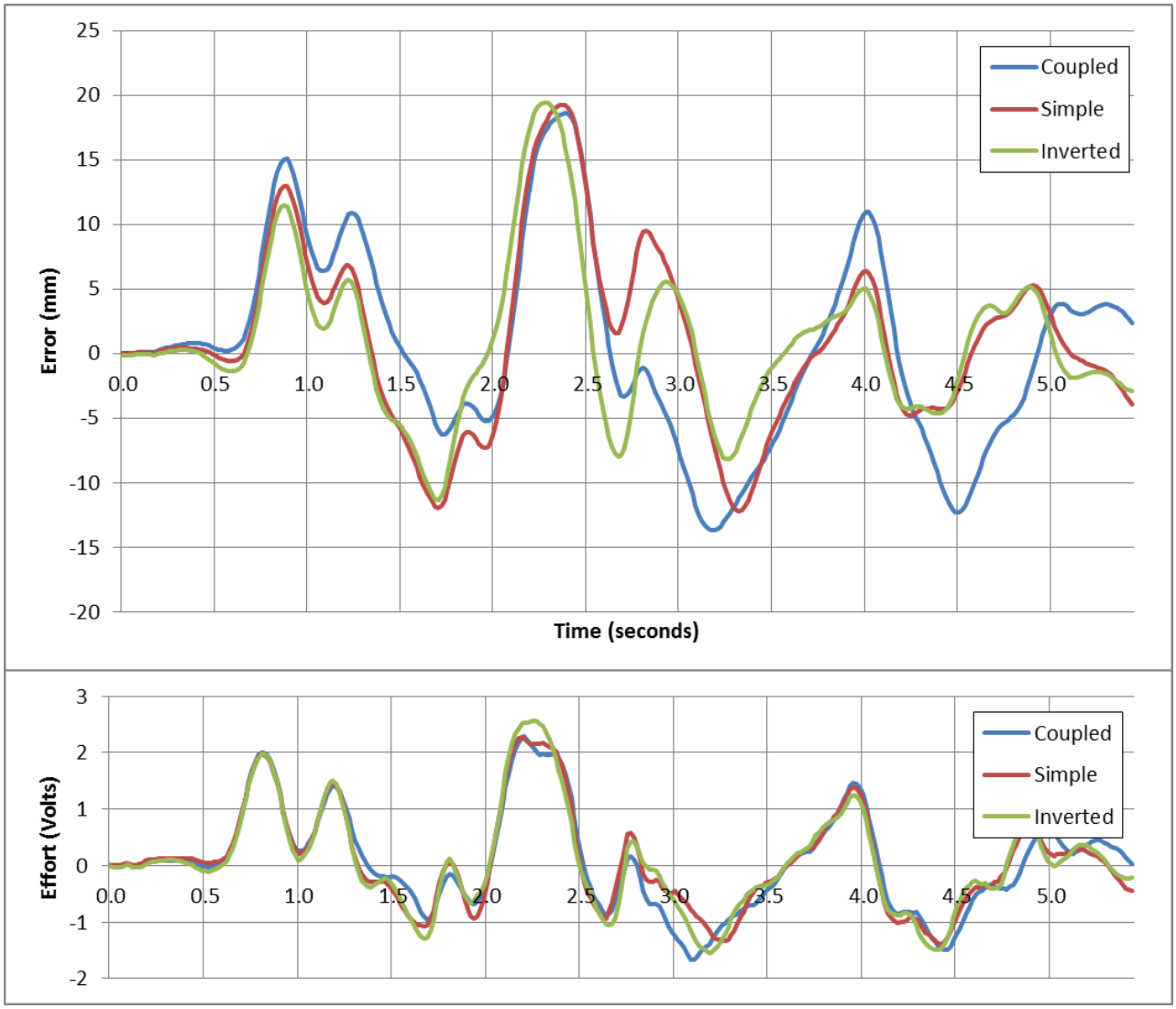

Figure 76 Axis Error and Effort during Walk with TITO Decoupling Methods

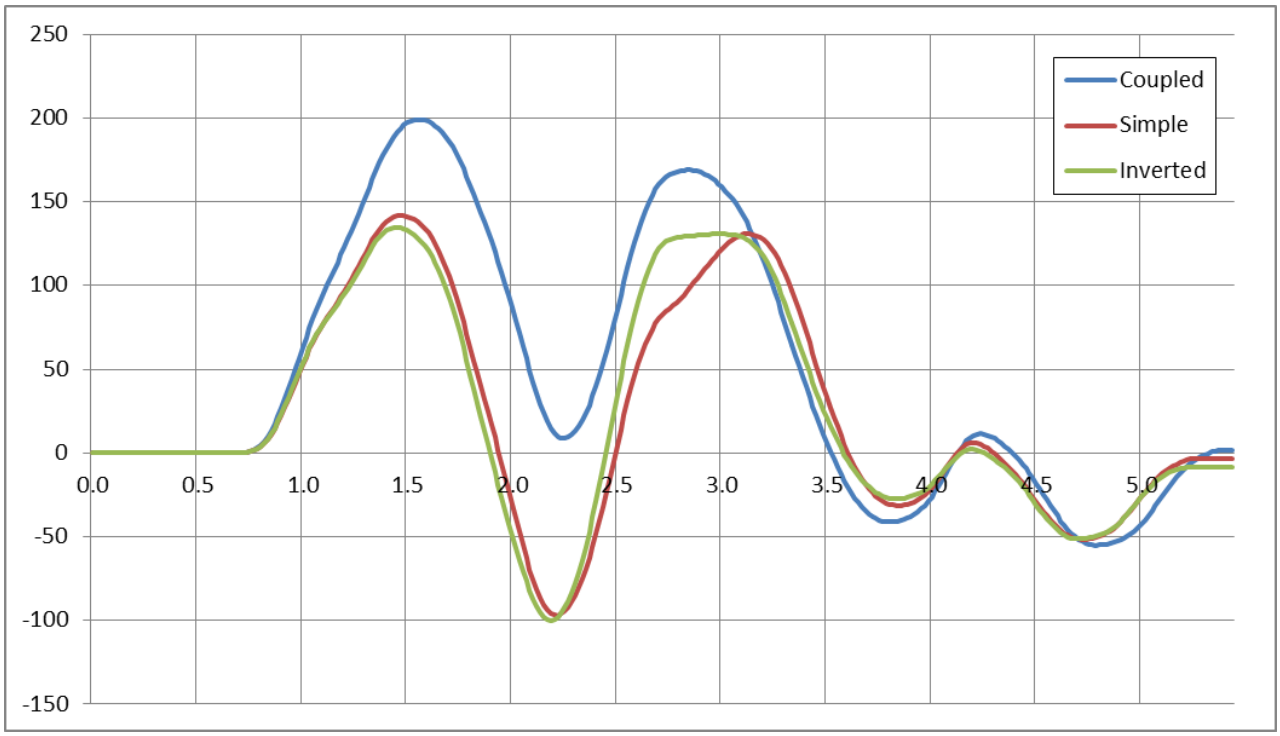

Figure 77 Axis Location During TITO Walk

The walking data were then applied to the full system. Figure 78 shows that the advantage of decoupling does not necessarily scale with weight. The inverted decoupling method reduced the maximum tracking error by 40 mm from the natural, coupled system. Figure 79 and Figure 80 show the results of the decoupling methods in the horizontal axes. The decoupling methods improved the response for most of the activity. The bounded error for the decoupling methods, however was 25 mm, 5 mm worse than the natural, coupled system.

The deviation between the two horizontal axes was less than 2.5 mm. This is tight enough to ensure that all the x-rays emitted by the source are captured by the collector. Figure 81 shows the results.

Figure 82 compares the vertical axes. As in the case of the uncoupled system, the error for a walking activity is small for the vertical axes.

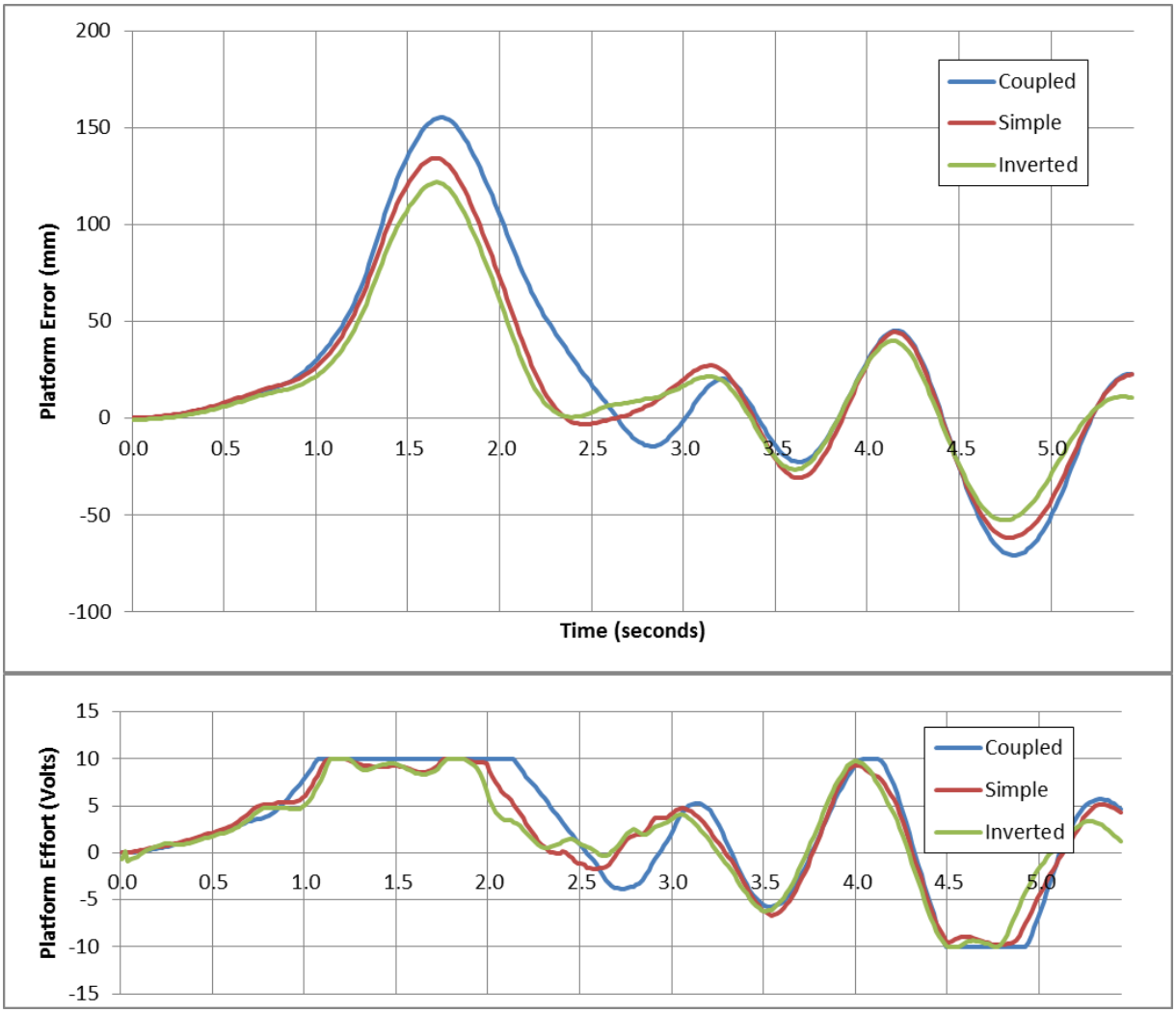

Figure 78 Platform Error and Effort during Walk with MIMO Decoupling Methods

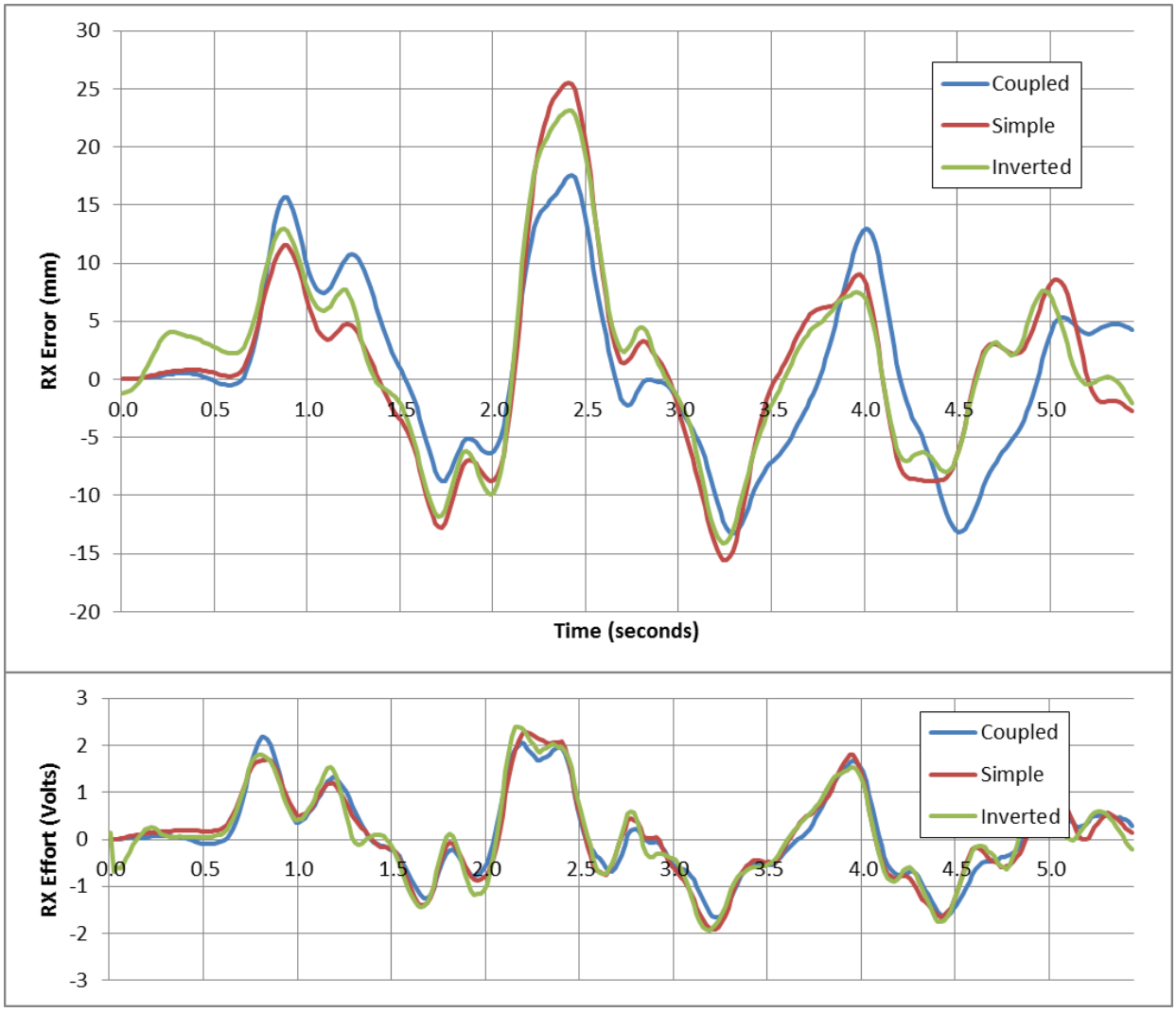

Figure 79 RX Error and Effort during Walk with MIMO Decoupling Methods

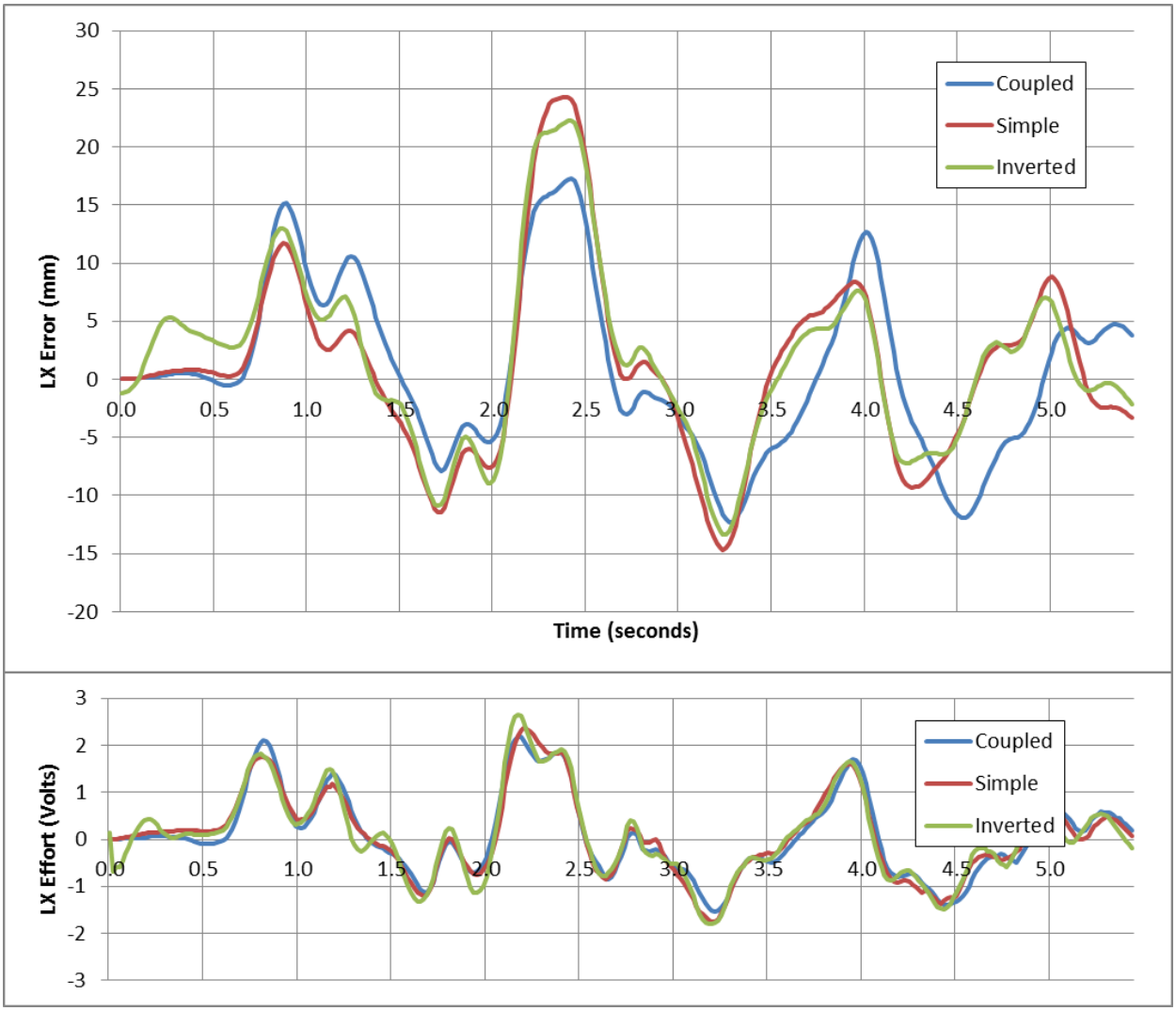

Figure 80 LX Error and Effort during Walk with MIMO Decoupling Methods

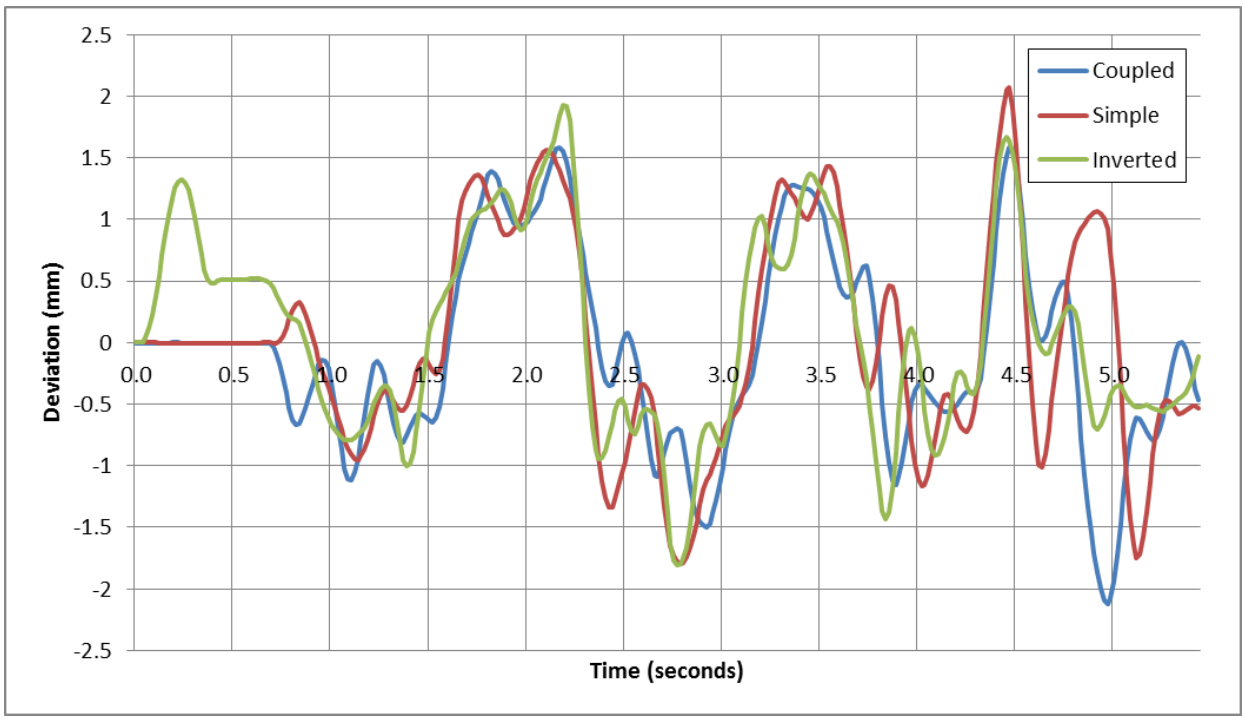

Figure 81 Horizontal Axes Deviations during Walk

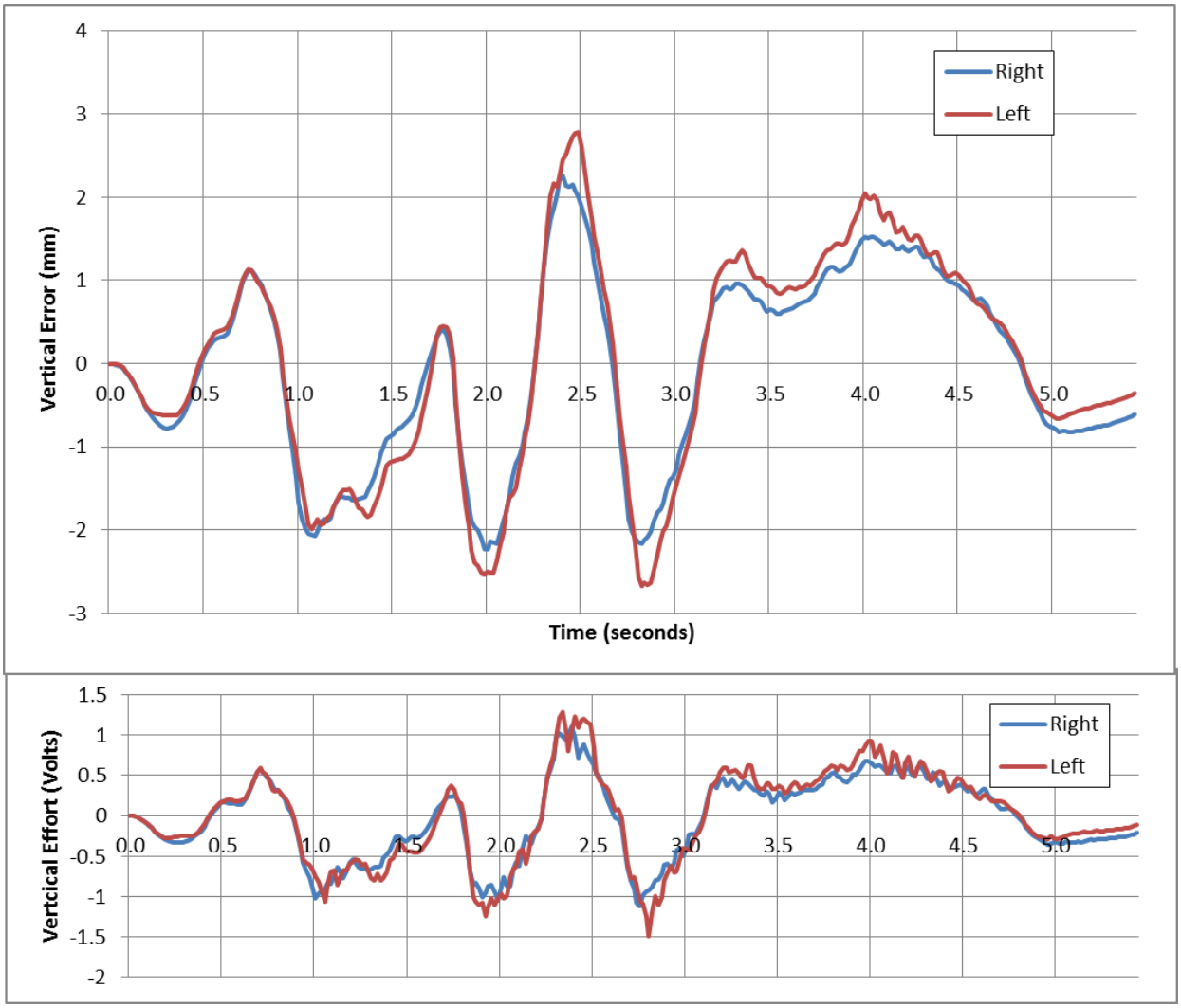

Figure 82 Vertical Axes Error and Effort during Walk

CHAPTER 9. FEASIBILITY OF EXTERNAL SHOULDER MODULE

9.1 SHOULDER MODULE INTRODUCTION

To date, the TFS has only been used in clinical studies for knee implants. It is likely that at least one clinical trial involving the analysis of hips will occur in 2014. While limited ankle analysis is also possible, the concept of the TFS is valid for other musculoskeletal joints of interest.

This system could be expanded to view other joints by creating attachable modules that could be designed for specific joints and tests. This chapter sought to expand the focus of the research by analyzing the steps needed to make a modular pedestal for another joint. The glenohumeral joint (shoulder) was chosen to a great extent because of the three-dimensional complex tracking that would be required. While this is a difficult problem to address, it would be a good first step to understanding the challenges a modular system would present.

9.2 ANATOMY OF THE GLENOHUMERAL JOINT

The glenohumeral joint is one of the most complicated joints in the human body. The joint classified as a ball in socket joint and is formed by the humeral head and the glenoid cavity. It is held together by ligaments that connect to the clavicle and the scapula at the coracoids process and the acromion. It is strengthened by five tendons connecting to many muscles, including the deltoid, bicep, triceps and Teres minor. [73]

The shoulder joint is the most maneuvrable joint in the human body. This is facilitated by a socket that is comprised of cartilage at the bottom and muscles and tendons at the top. The looseness associated with this connection and the interaction with the joint at the clavicle and scapula allow the joint to have a vast range of motion. [73] The size of the humerus head and the attachment of the major tendons allow the shoulder joint to experience tremendous angular accelerations. [74]

9.3 SHOULDER JOINT TRACKING – CHALLENGES AND REFERENCE MOTION

In order to track a shoulder joint while a patient undergoes a natural movement it is essential to begin by understanding the relationship that shoulder motion has with the ground. In addition to the arm being capable of rotating around three orthogonal axes at a point within the joint itself, this coordinate system can make dynamic transformations and rotations relative to the ground due to the motion of other joints within the body. Most natural throwing and swinging motions that the shoulder performs are highly dependent on these base motions, and an attempt to get an accurate fluoroscopic image requires the inclusion of these motions by the patient.

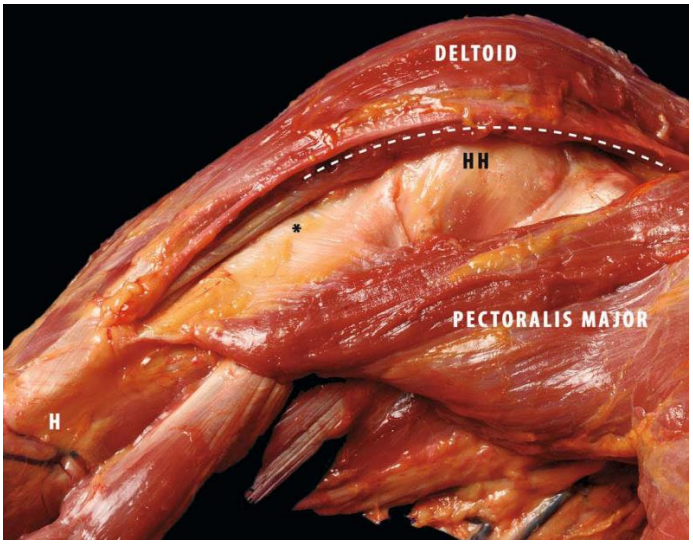

Figure 83 Glenohumeral Joint surrounded by muscles. [75]

This combination of large ranges of motion and high angular accelerations with multiple joint interactions present some of the greatest control problems for a robot to encounter and overcome. An initial consideration revealed that allowing the full motion that the shoulder is capable of is impossible with the techniques and technologies used by the current fluoroscopic research. It was decided that the best approach to solving these issues would be to have the patient perform a standard activity that is known to keep the shoulder motion within the frame that can be analyzed by the current fluoroscopic equipment. Two possible motions were considered: a standard golf swing and a baseball pitch. The choice of these two motions hinged on the availability of current studies and the apparent usefulness of information that new fluoroscopic images would provide to the scientific community.

One of the most strenuous movements that athletes undergo is the baseball pitch. Much data have been analyzed to increase ball speed, decrease shoulder injury and increase the amount of throws that a pitcher is capable of. The most common breakdown of the pitch reduces it to six stages: windup, stride, arm cocking, acceleration, arm deceleration, and follow through. Rephrasing this breakdown by changes in kinematics, the stages are separated by seven positions: rest, maximum knee height, stride foot contact, maximum arm external rotation, release, maximum internal rotation and follow though. [76] Figure 84 demonstrates a typical pitch as seen from six different perspectives.

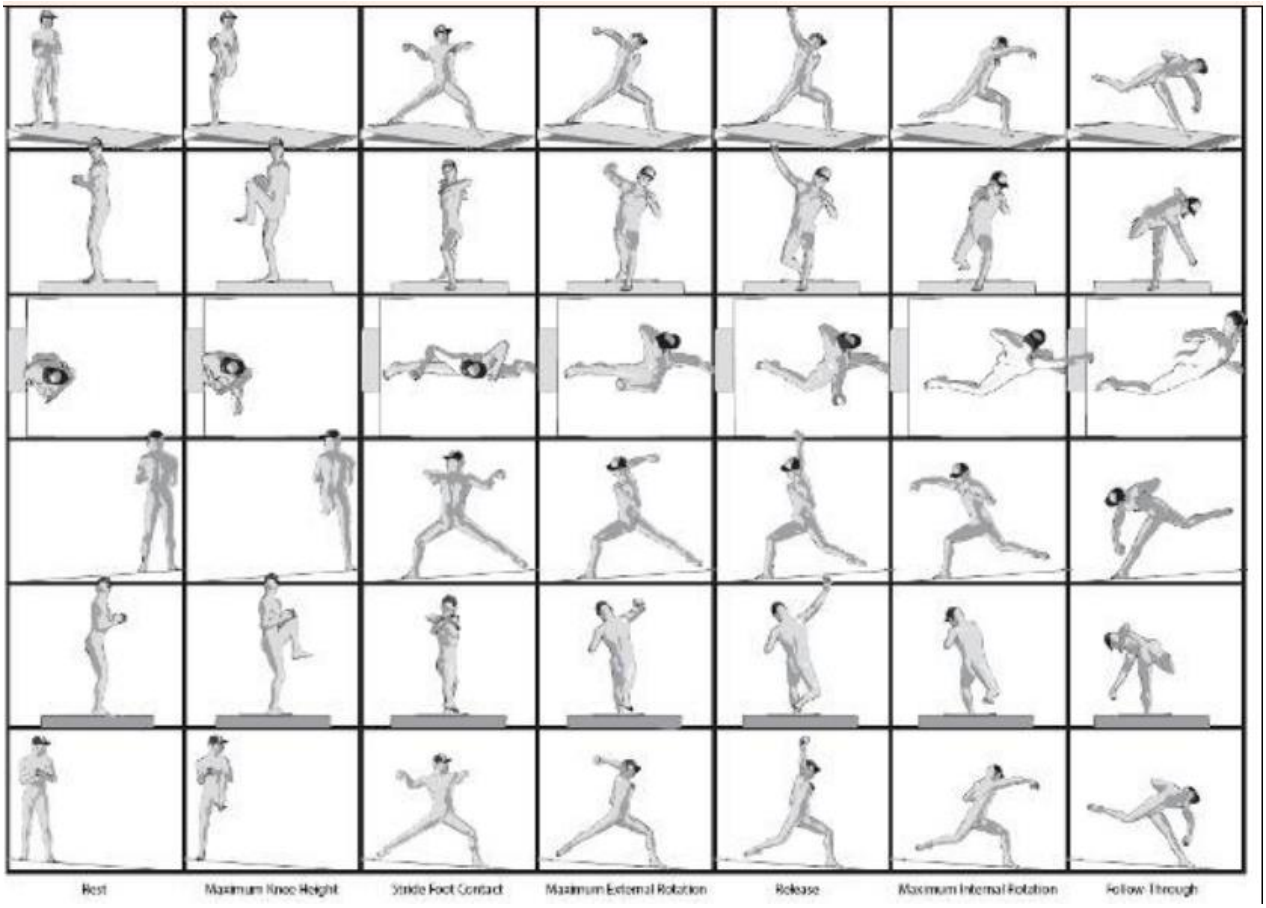

Figure 84 Table of Typical Stages of Pitching [76]

9.4 BASIC KINEMATICS THEORY

Before a solution can be found for simulating the joint tracking algorithm, some basic kinematic theory is needed. The solution uses both forward and inverse kinematics.

FORWARD KINEMATICS

Forward kinematics is a fairly straightforward way of obtaining the location and orientation of the end of a multiple degree of freedom system using joint angles and information about how the joints are linked. The robotics standard in coordinate transformation definitions is the Denavit-Hartenberg, or DH, naming convention.

The DH convention breaks the system into a series of joints that are each composed of four transformations: link length, link twist, link offset and joint angle. These parameters are typically designated by a, alpha, d and theta, respectively. For each of the joints, three of the parameters are constant and one is dynamic.

Figure 85 shows the four parameters between two joints and their corresponding frames of reference. The value this convention provides is that a movement in that joint can be broken down into four independent transformations, one for each parameter.

The first parameter is a rotation around the z_{i-1} axis.

$$H_{\theta_i} = \begin{bmatrix} \cos(\theta_i) & -\sin(\theta_i) & 0 & 0 \\ \sin(\theta_i) & \cos(\theta_i) & 0 & 0 \\ 0 & 0 & 1 & 0 \\ 0 & 0 & 0 & 1 \end{bmatrix}$$

The second parameter is an offset in the z_{i-1} direction.

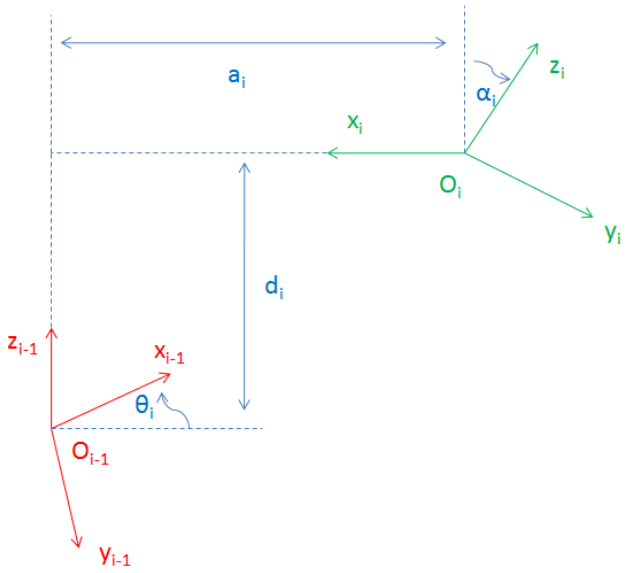

Figure 85 DH Convention [77]

$$H_{d_i} = \begin{matrix} 1 & 0 & 0 & 0 \\ 0 & 1 & 0 & 0 \\ 0 & 0 & 1 & d_i \\ 0 & 0 & 0 & 1 \end{matrix}$$

The third parameter is an offset in the x_i direction.

$$H_{\alpha_i} = \begin{matrix} 1 & 0 & 0 & 0 \\ 0 & \cos(\alpha_i) & -\sin(\alpha_i) & 0 \\ 0 & \sin(\alpha_i) & \cos(\alpha_i) & 0 \\ 0 & 0 & 0 & 1 \end{matrix}$$

The last parameter is a rotation around the x_i axis.

$$H_{a_i} = \begin{matrix} 1 & 0 & 0 & a_i \\ 0 & 1 & 0 & 0 \\ 0 & 0 & 1 & 0 \\ 0 & 0 & 0 & 1 \end{matrix}$$

These can be combined to form the joint transformation, $A_i = H_{\theta_i} H_{d_i} H_{a_i} H_{\alpha_i}$, that is valid for any joint, *i*.

$$A_i = \begin{bmatrix} \cos(\theta_i) & -\sin(\theta_i)\cos(\alpha_i) & \sin(\theta_i)\sin(\alpha_i) & a_i\cos(\theta_i) \\ \sin(\theta_i) & \cos(\theta_i)\cos(\alpha_i) & -\cos(\theta_i)\sin(\alpha_i) & a_i\sin(\theta_i) \\ 0 & \sin(\alpha_i) & \cos(\alpha_i) & d_i \\ 0 & 0 & 0 & 1 \end{bmatrix} \quad (91)$$

Notice that this matrix has only one variable. For prismatic joints, the variable is d_i. For revolute joints, the variable is θ_i.

After a multiple degree of freedom object has been broken down into the DH convention, forward kinematics multiplies all the matrices together to get a final transformation matrix from the origin to the end of the object. Consider a robot that consists of three rotational joints: B, C and D. There exist three matrices (A_B, A_C *and* A_D) that describe each of the three joints. A matrix, T, that describes the transformation from the grounded coordinate frame to the coordinate frame at D could be expressed:

$$T = A_B A_C A_D \quad (92)$$

Furthermore, it can be shown that the matrix T can be written:

$$T = \begin{bmatrix} \begin{bmatrix} Orientation\ of\ D \\ (3x3) \end{bmatrix} & \begin{matrix} x_D \\ y_D \\ z_D \end{matrix} \\ \begin{matrix} 0 & 0 & 0 \end{matrix} & 1 \end{bmatrix} = \begin{bmatrix} \begin{bmatrix} R_D^0 \\ (3x3) \end{bmatrix} & o_D^0 \\ 0 \quad 0 \quad 0 & 1 \end{bmatrix} \quad (93)$$

The location of D with respect to the ground is the point $\left(o_{D_x}^0, o_{D_y}^0, o_{D_z}^0\right)$. It should be noted that there are many ways of expressing R_D^0. Some of the most well known are the ZYZ-Euler representation, the "yaw-pitch-roll" representation and the "axis/angle" representation. Each of these attempt to discretize the rotation, the first two by breaking the rotation down into three separate rotations and the last by recognizing that all rotations can be expressed as a single rotation of magnitude theta around a vector, k.

For a given transformation matrix, T

$$T = \begin{bmatrix} \begin{bmatrix} R \\ (3x3) \end{bmatrix} & 0 \\ 0 \quad 0 \quad 0 & 1 \end{bmatrix} \quad (94)$$

$$\cos\theta = \left(\frac{Trace\ (R) - 1}{2}\right) \quad (95)$$

$$k = \frac{1}{2\sin\theta}\begin{bmatrix} r_{32} - r_{23} \\ r_{13} - r_{31} \\ r_{21} - r_{12} \end{bmatrix} \quad (96)$$

It can be shown that k is a unit vector by recognizing that R is a rotational matrix and solving for the sum of the square of the terms of k.

INVERSE KINEMATICS

While the problem of forward kinematics is straightforward, solving the inverse kinematics is more difficult. One of the reasons for this added complexity is that the majority of all robots use revolute joints, and rotations are highly nonlinear. Also, for a given set of joint angles there exists only one point and orientation in Cartesian space where the end effector can exist. For a given point and orientation in Cartesian space, however, there very often exists more than one set of joint angles that can allow the end effector this orientation. The answer in this case is singular. There are many approaches to solving this problem. [78] reviews the standard procedures of inverse kinematics developed before 1990. [79]lays down basic linear algebra theory used in inverse kinematics. [80]and [81]deal with Jacobian methods for redundant manipulators, with [81] discussing additional constraints, such as obstacle avoidance and trajectory planning methods. [82] discusses the weakness of Moore-Penrose psuedoinverse around kinematic singularities. It includes various other inverse techniques including a damped least-square solution, which provides robustness at the expense of accuracy. For this project, the Moore-Penrose psuedoinverse is used and robustness is providing by SVD methods.

For an end effector to be represented by the base coordinate frame, 0,

$$P^o = T^o_{end}(q)P^{end} \quad (97)$$

From the definition of T^o_{end},

$$p^o = R^o_{end}(q)p^{end} + o^o_{end}(q) \quad (98)$$

If the joints, q, are a function of time,

$$\dot{p}^o = \dot{R}^o_{end}(q)p^{end} + \dot{o}^o_{end}(q) \quad (99)$$

From [77],

$$\frac{d}{d\theta}R = S(k)R \quad (100)$$

where k is the unit vector about which the rotation occurs. The derivative of R with respect to time is:

$$\frac{d}{dt}R = \dot{R} = S\big(\omega(t)\big)R(t) \quad \textbf{(101)}$$

Where $\omega = \theta k$

$$\dot{p}^o = S(\omega^o)R^o_{end}p^{end} + \dot{o}^o_{end} \quad \textbf{(102)}$$

Letting $r = R^o_{end}\ and\ v = \dot{o}^o_{end}$

$$\dot{p}^o = (\omega\ x\ r) + v \quad \textbf{(103)}$$

This leads to the definition of the Jacobian.

Letting

$$z_{i-1} = R^o_{i-1}\begin{bmatrix}0\\0\\1\end{bmatrix} = \begin{bmatrix}H_{i-1_{13}}\\H_{i-1_{23}}\\H_{i-1_{33}}\end{bmatrix} \quad \textbf{(104)}$$

and

$$o_{i-1} = \begin{bmatrix}H_{i-1_{14}}\\H_{i-1_{24}}\\H_{i-1_{34}}\end{bmatrix} \quad \textbf{(105)}$$

$$J = \begin{bmatrix}J_v\\J_\omega\end{bmatrix}\ and\ \zeta = \begin{bmatrix}v^o_{end}\\\omega^o_{end}\end{bmatrix} \quad \textbf{(106)}$$

$$\begin{matrix}v^o_{end} = J_v\dot{q}\\ \omega^o_{end} = J_\omega\dot{q}\end{matrix} \quad \textbf{(107)}$$

For a robot with seven revolute joints expressed in DH parameters,

$$T^o_7 = H^o_1H^1_2H^2_3H^3_4H^4_5H^5_6H^6_7 \quad \textbf{(108)}$$

$$J_{v_i} = z_{i-1}\ x\ (o_7 - o_{i-1}) \quad \textbf{(109)}$$

$$J_{\omega_i} = z_{i-1} \quad \textbf{(110)}$$

$$\zeta = J\dot{q} \quad (111)$$

To find the joint angles, the above equation is solved for the change in joint angles.

$$\dot{q} = J^{-1}(q)\zeta \quad (112)$$

Moving to the discrete domain,

$$\Delta q = J^{-1}(q)\zeta \quad (113)$$

When the Jacobian matrix is nonsingular, there exists only one solution. When the Jacobian is not square, the full inverse does not exist. Since there are only six degrees of freedom in SO(3) and this robot has seven degrees of freedom, J will be six by seven. Recognizing that the multiplication of the Jacobian and its transpose produces a square matrix,

$$I = (JJ^T)(JJ^T)^{-1} = JJ^+ \quad (114)$$

where J^+ is the Moore-Penrose psuedoinverse. The solution to the difference in joint angles becomes

$$\Delta q = J^+\zeta + (I - J^+J)b \quad (115)$$

where b is an arbitrary vector. Since the answer is singular, there are many solutions to the equation above. The right hand part of the equation is from the null space of J. To minimize the amount of motion that is necessary to move the joint from one position to another, b can be set to zero. This will provide a value for $\dot{q}$ that is unique for every initial position of q and final position and orientation.

9.5 IMPLEMENTATION

To consider the possibilities and problems in tracking a shoulder joint, an algorithm is needed that would be capable of recognizing the shoulder joint and reporting its movements to a computer. The current research has focused its attention on pattern recognition from the fluoroscopic image to designate an image center and joint center. The algorithm then computes the difference between these values in pixels, and converts them to units of length and directs the drives to move the source the distance needed to return the joint center to the image center. [51]While the shoulder joint becomes a three dimensional problem, instead of two dimensional, this aspect of the control strategy is presumed to be accomplishable by similar methods. One might measure the intensity of the image contrast, for instance, to determine the depth the joint has from the source. It is also important to note that a joint center is needed, but very likely a point along the humerus would also be needed to determine the rotation of the arm with respect to the trunk. [83], [84], and [85] each have unique ways of visual tracking. With the basic assumption that a desired position and

orientation can be found by analyzing the patient's current position, focus was turned to the possibility of a robot being able to respond to the information provided by the fluoroscope.

There are many types of robots that are commercially available that would provide the basic range of motion to yield information about the feasibility of a shoulder tracking fluoroscope. The robot chosen for this study was the Mitsubishi PA-10, which is a seven degree of freedom redundant robot. This robot was chosen because of its prevalence within the research and medical community, and the availability of a fully adaptable RoboWorks model of the PA-10.

An accurate model of a standard motion as complex as a baseball pitch is a difficult undertaking. The approach to find a solution was to use virtual modeling and graphical representation. Aid was elicited from RoboWorks, created by Chetan Kapoor and licensed, distributed and copyrighted by Newtonium. RoboWorks uses simple transformations, rotations and surfaces to model three dimensional objects. After joints are created, they can be manipulated to model actual human movements. A model was created that contains twenty one active joints from the ankles to the elbow. Figure 86 shows the completed model of a man with all joints set to zero degrees.

Figure 84 was then analyzed and the model was manipulated into the seven positions of a baseball pitch. Figure 87 and Figure 88 show the seven positions.

The joint movements needed to place the model in these positions were recorded and stored in a .dat file that RoboWorks can import as an animation file. While the scope of this project was focused on only one motion, the same process could be used for a golf swing, or any other motion.

An X-Ray source and Intensifier were modeled on either side of the shoulder with a bracket connecting them. The location and orientation of the point that the robot needs to attach to the bracket is found by doing a forward kinematics transformation of the man starting at the left ankle joint and moving to the bracket, as shown in Figure 89 and Figure 90.

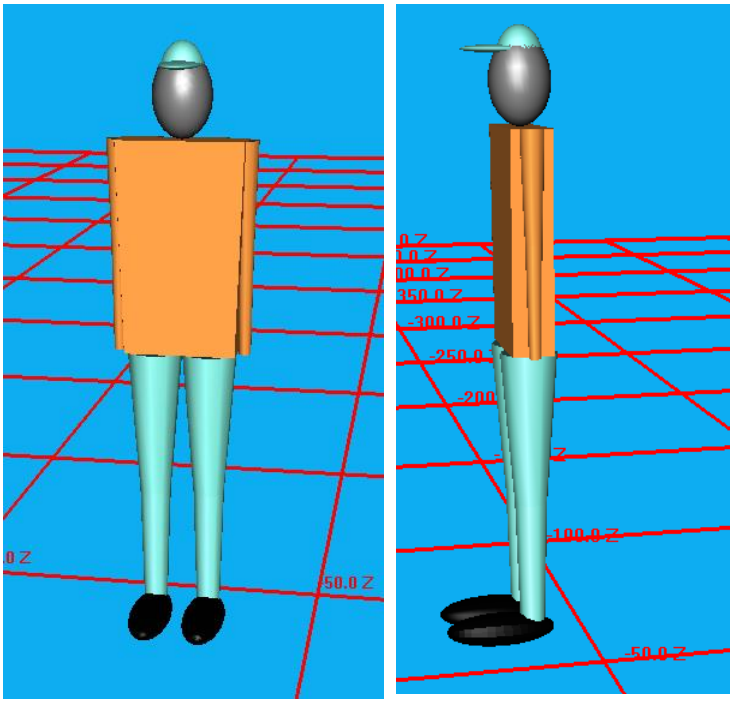

Figure 86 RoboWorks Model, Front and Side

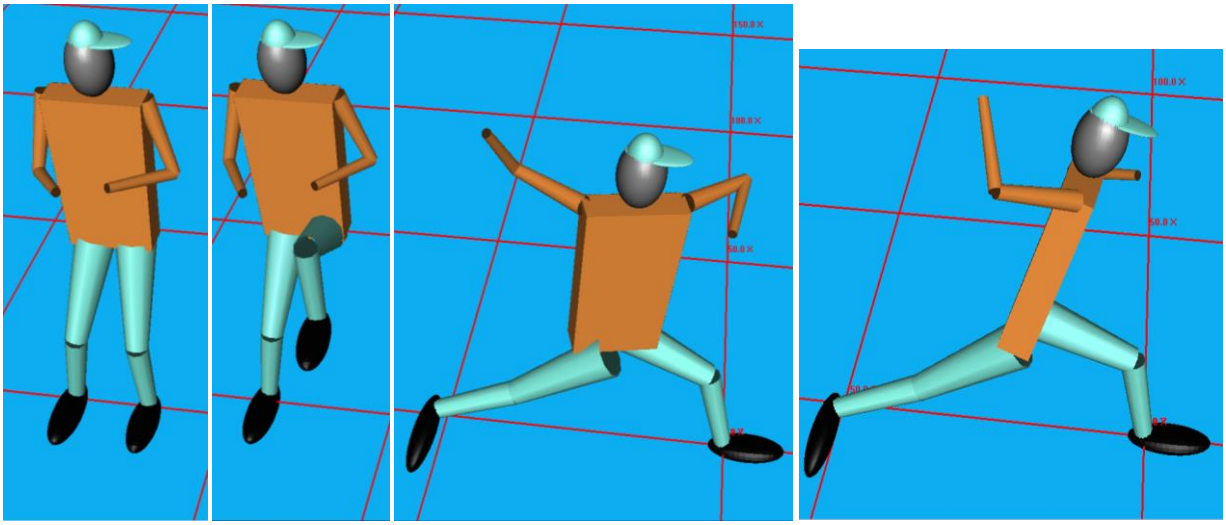

Figure 87 Rest, Maximum Knee Height, Stride Foot Contact and Maximum Arm External Rotation.

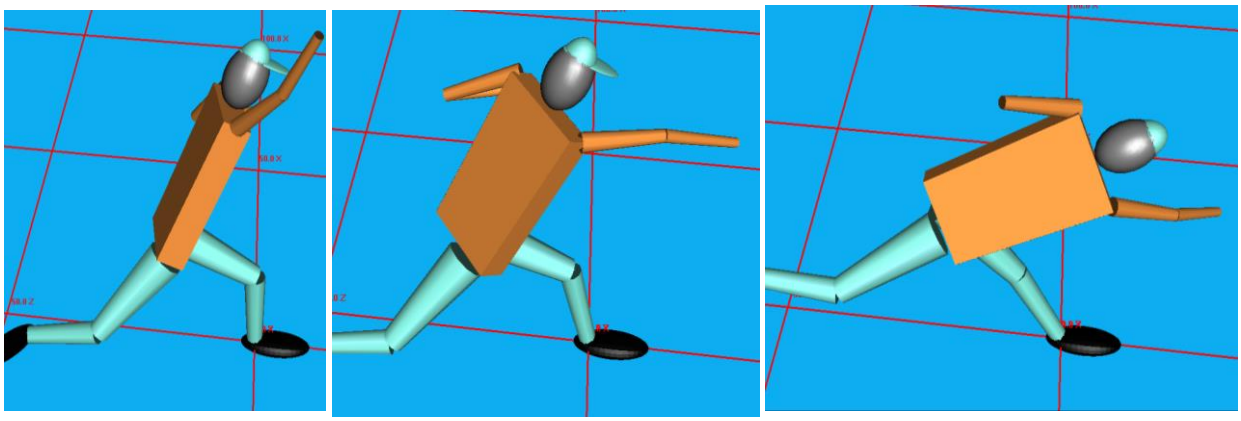

Figure 88 Release, Maximum Internal Rotation and Follow Through.

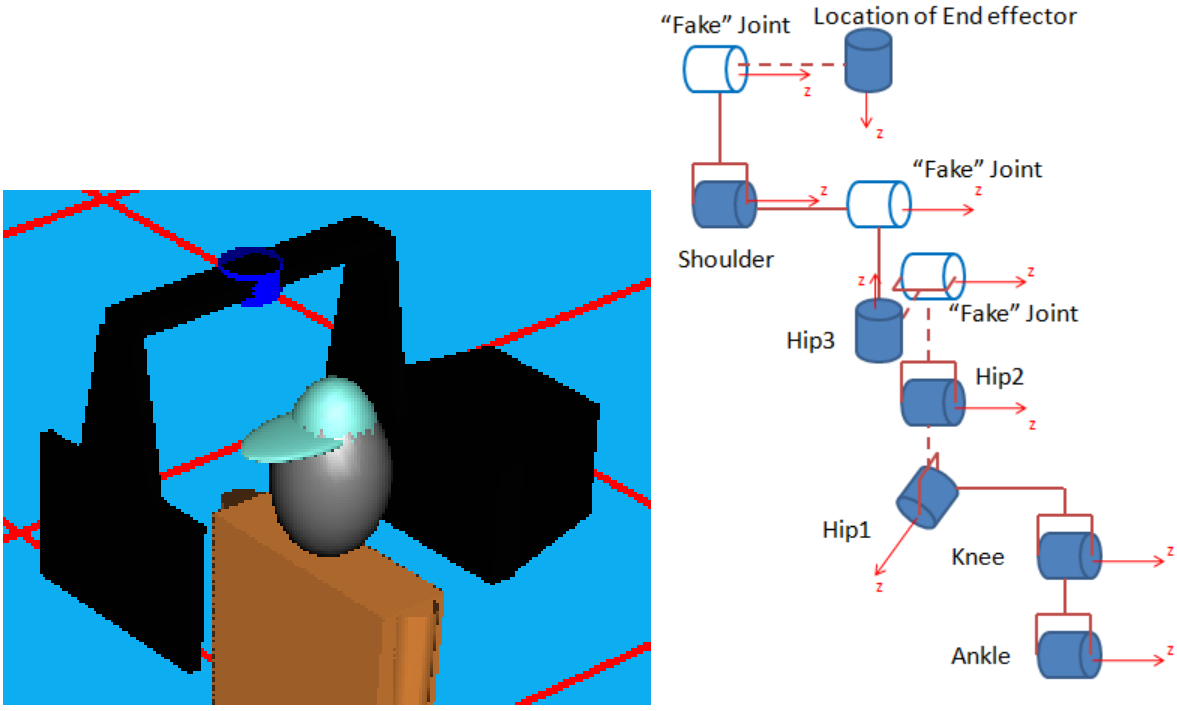

Figure 89 Construction of Sequential Joints of the Modeled Man from the Base Frame to the Desired End Effector

This forward transformation uses ten revolute joints. The values for *theta*, *d*, *a* and *alpha* are from the RoboWorks model of a man. The format of the variable theta corresponds to the control name for the joint within RoboWorks.

Table 8 Values for Man DH Parameters

theta	d	a	alpha
LAnkle	0	16	0
Lknee	-3.5	18.7	-90
HipZ	0	0	90
HipX	0	0	0
90	0	0	90
HipY	26.7	0	-90
-90	-8	0	0
RShoX	0	15.5	0
90	0	0	-90

Three of the transformations are fixed for any movement the man has. These are used to keep all transformations in DH format. The final location of the end effector is $T_{man}(q_{man})$, where q_{man} is six by one and

$$T_{man} = A_{LAnkle}A_{LKnee}A_{HipZ}A_{HipX}A_{\theta=90}A_{HipY}A_{\theta=-90}A_{RShoX}A_{\theta=90}$$

The Mitsubishi PA10-7C robot has seven joints. These are configured in such a way as to create three overlapping spherical wrists. Joints 1, 2 and 3 form a spherical wrist, as do joints 3, 4 and 5 and joints 5, 6 and 7. See Figure 90.

The DH parameters for the robot are in Table 9.

Table 9 DH Parameters of PA-10

theta	d	a	alpha
SNS1	0	0	-90
SNS2	0	0	90
SNS3	17.7165	0	-90
SNS4	0	0	90
SNS5	18.8976	0	-90
SNS6	0	0	90
SNS7	2.7559	0	0

The robot is placed in a position that is horizontal to the man.

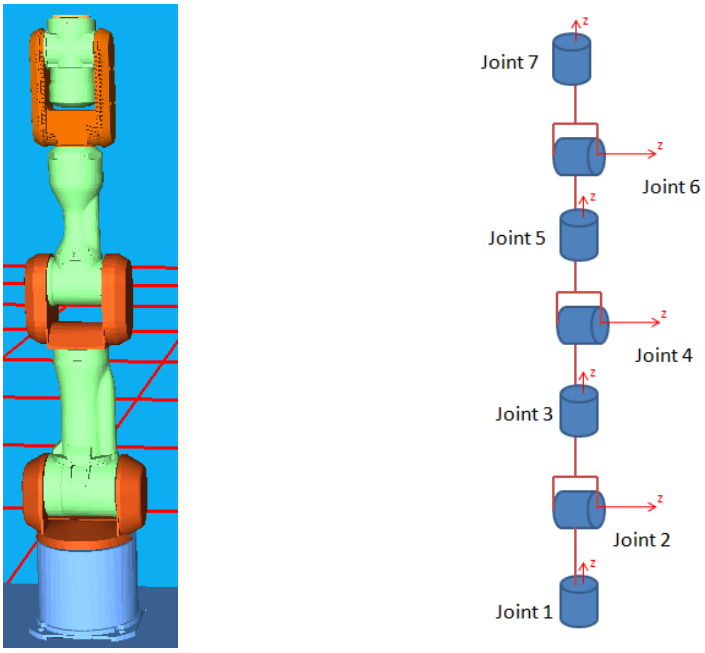

Figure 90 Construction of Sequential Joints of a PA-10 robot

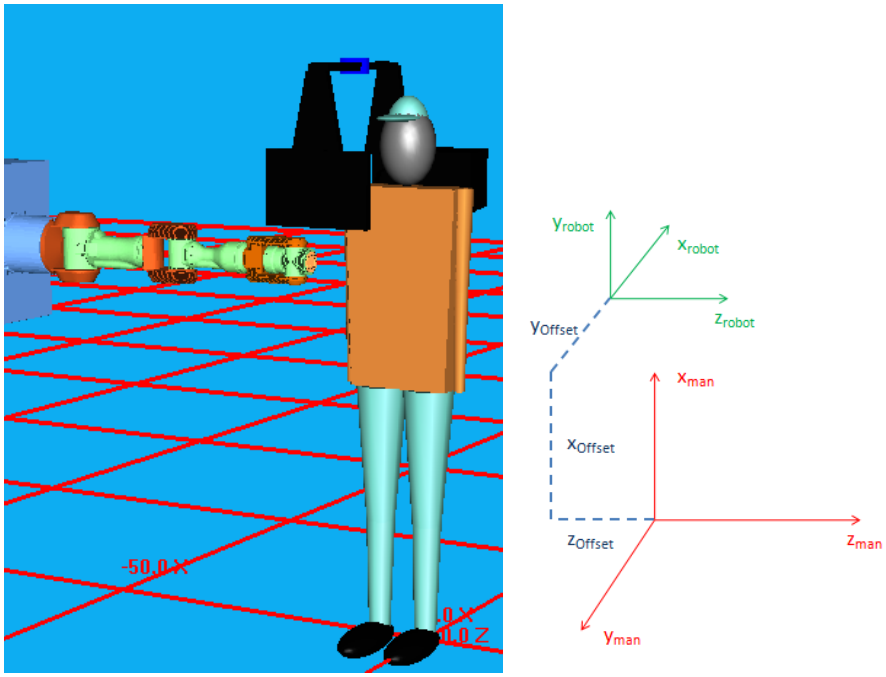

Figure 91 Man and Robot with All Joints Angles Set to Zero

The base coordinate frame, as defined from DH parameters, of the robot is in a different orientation from the base coordinate of the man. To place the robot correctly, a transformation must be done before the forward kinematics of the robot can be achieved. The transformational matrix is:

$$A_{Offset} = \begin{bmatrix} 0 & 1 & 0 & x_{Offset} \\ -1 & 0 & 0 & y_{Offset} \\ 0 & 0 & 1 & z_{Offset} \\ 0 & 0 & 0 & 1 \end{bmatrix}$$

The values in of the offset are derived from Figure 91.

To simulate the man throwing a ball, the change in angle parameters was assumed to be linear. While this is not a valid assumption for an actual baseball pitch, a reasonable trajectory path for the robot to follow can be found.

$$M_{n_i} = M_n + \frac{M_{n+1} - M_n}{step} i \quad \textbf{(116)}$$

In this equation, M_n is the nth position of the pitch, step is the number of steps between positions and $M_{n_i} = M_j$ is the current position of the man. The dimensions of *M* are j x 21, where

$$j = (n - i)step + 1. \quad \textbf{(117)}$$

From the 21 columns of *M*, the joint angles, q_{man} can be drawn.

At any point, *j*, during the pitch, the desired location for the robot can be found by $T_{man}(q_{man_j})$.

The location and orientation of the end effector of the robot is $T_{robot_{i-1}} = A_{Offset}A(q_{robot_{i-1}})$, where q_{robot} is the seven joints of the robot.

$$\zeta = \begin{bmatrix} v_{end}^{o} \\ \omega_{end}^{o} \end{bmatrix}$$

$$v_{i}{}_{end}^{o} = \begin{bmatrix} T_{man_{i_{14}}} - T_{robot_{i-1_{14}}} \\ T_{man_{i_{24}}} - T_{robot_{i-1_{24}}} \\ T_{man_{i_{34}}} - T_{robot_{i-1_{34}}} \end{bmatrix} \quad \textbf{(118)}$$

Letting $T_{man_i} = \begin{bmatrix} R_{man_i} & o_{man_i} \\ 0 & 1 \end{bmatrix}$ and $T_{robot_i} = \begin{bmatrix} R_{robot_i} & o_{robot_i} \\ 0 & 1 \end{bmatrix}$, the angular rotation, ω_{end}^{o} can be found.

$$p^{\,o} = R_{robot_{i-1}} p^{robot_{i-1}} \quad \textbf{(119)}$$

$$R_{robot_{i-1}}{}^{T} p^{\,o} = p^{robot_{i-1}} = p^{current} \quad (120)$$

Similarly,

$$R_{man_i}{}^{T} p^{\,o} = p^{man_{i-1}} = p^{final} \quad (121)$$

Realizing that

$$p^{final} = R_{final}^{current} p^{current} \quad (122)$$

$$R_{man_i}{}^{T} p^{\,o} = R_{i\,final}^{current} R_{robot_{i-1}}{}^{T} p^{\,o} \quad (123)$$

Dividing by $p^{\,o}$ and rearranging,

$$R_{i\,final}^{current} = R_{man_i}{}^{T} R_{robot_{i-1}} \quad (124)$$

This rotational matrix can be expressed in k and θ.

$R_{i\,final}^{current} \rightarrow k_{cf}\ and\ \theta_{cf}$

$$\omega_{i}{}_{end}^{o} = \theta_{i_{cf}} k_{i_{cf}} \quad (125)$$

From Equation 24, the Jacobian maps $\dot{q}$ to ζ. Since the implementation of the Jacobian is discrete, as $\Delta t \rightarrow 0,\ \Delta q \rightarrow \dot{q}$ where $\Delta t = \frac{1}{step}$. The Jacobian is more accurate when used for large values of *step*, which corresponds to small changes in q. Once the total values of $v_{i}{}_{end}^{o}$ and $\omega_{i}{}_{end}^{o}$, it is appropriate to break them into small pieces. If the maximum amount of movement to be allowed is r_{max},

$$dv_{i}{}_{end}^{o} = \frac{v_{i}{}_{end}^{o}}{r_{max}} \quad (126)$$

$$d\omega_{i}{}_{end}^{o} = \frac{\theta_{i_{cf}}}{r_{max}} k_{i_{cf}} \quad (127)$$

$$d\zeta = \begin{bmatrix} dv_{i}{}_{end}^{o} \\ d\omega_{i}{}_{end}^{o} \end{bmatrix} \quad (128)$$

$$F(t) = r * T(t) \quad (129)$$

The final equation becomes

$$q_i = q_{i-1} + \sum_{1}^{\frac{\theta_{i_{cf}}}{r_{max}}} \Delta dq = q_{i-1} + \sum_{1}^{\frac{\theta_{i_{cf}}}{r_{max}}} J^{+}(dq)d\zeta \quad \textbf{(130)}$$

As with any implementation, there is some error inherent in the system. One source of error comes from the rounding of $\frac{\theta_{i_{cf}}}{r_{max}}$ to a whole number in the sum. This error is reduced by ensuring that r_{max} is very small.

Another source of positioning error is introduced on purpose to ensure the stability of J^{+}. If J is m x n where n > m,

$$J = U\Sigma V^{T} \quad \textbf{(131)}$$

$$\Sigma = \begin{matrix} \sigma_1 & 0 & 0 \\ 0 & \ddots & 0 \\ 0 & 0 & \sigma_n \end{matrix} \quad \textbf{(132)}$$

J is rank deficient if $\frac{\sigma_1}{\sigma_n} \to \infty$. This will occur as J approaches kinematic singularity points. This will correspond to large changes in q for very small changes in ζ. To ensure the existence of J^{+}, the last two values of sigma are checked to ensure they are not too close to zero. If $\frac{\sigma_1}{\sigma_6} > 300$

$$J^{+} = V\Sigma^{-1}U^{T} \approx V \begin{bmatrix} 0 & 0 & 0 \\ 0 & \ddots & 0 \\ 0 & 0 & \frac{1}{\sigma_1} \end{bmatrix} U^{T} \quad \textbf{(133)}$$

If $\frac{\sigma_1}{\sigma_5} > 300$ as well,

$$\sigma^{-1}(1) = \sigma^{-1}(2) = 0 \quad \textbf{(134)}$$

This decreases the accuracy of the tracking, but it increases the stability of the system.

9.6 SUMMARY

It was found that the desired end effector position for the entire pitch was often outside the workspace of the PA-10. The algorithm was applied to part of the pitch, shown in Figure 92. The result was very accurate tracking for most of the range. Some of the points, even within the limited throw, were out of range. For these points, the robot gets as close as it can.

It is not possible to track any random motion of a glenohumeral joint with algorithms employed by the current fluoroscope tracking research at the University of Tennessee. A plethora of potential research could further the capabilities and scope of fluoroscopic tracking. Many of these are mentioned below. Also, the range of motion required and the speed of rotation of the glenohumeral joint would exceed the conceivable mechanical limits of robot tracking using a single PA-10 robot module.

It would be feasible, however, to track a planned motion where the subject moves through a predefined type of motion, but where the subject was allowed the freedom to accomplish this movement naturally. An example of pitching a baseball was used, and a control algorithm was developed that accurately tracked the simulated motion of a partial baseball throw.

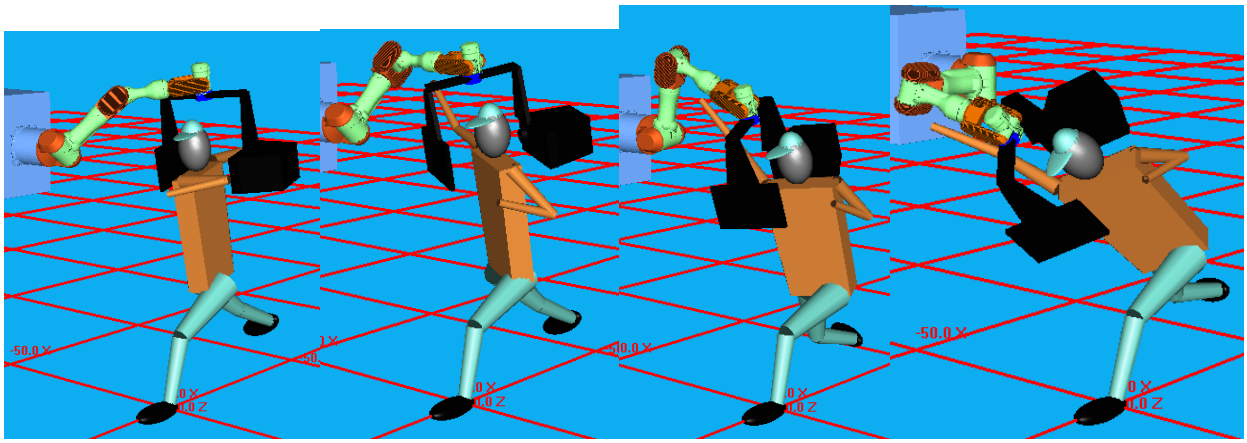

Figure 92 Robot Tracking the Shoulder.

9.7 Implementation of a PA-10 Tracking Module

There are many directions this research could explore. To continue use of the PA-10, it would be necessary to add some degrees of freedom by attaching the PA-10 to one or two prismatic joints. This would provide the necessary workspace of the robot to allow a pitcher to perform a complete throw. The added dimensions could also be used for obstacle avoidance as the pitcher moves. Another vital part of this would be to create a routine that can guarantee the best placement of the robot to achieve the closest tracking possible.

Another robot with greater range of motion could be considered. Similarly, two PA-10s could be utilized on each side of the man. Because of the nature of fluoroscopic technology, two end effector positions and orientations would be required, but the orientations would only need to provide information about the location of the z-axis. In other words, there might be an additional degree of freedom from each robot that could be utilized in obstacle avoidance. [86] discusses a "Coach-Trainee" method that can handle multiple end effectors and the creation of boundary regions near a half-space boundary, which is used to create a transitional function to ensure the continuity of the control strategy.

One of the principle advantages of the PA-10 is the redundancy it provides. For a given motion that a subject is to go through, advanced path planning could be used to ensure that the robot arm does not impede the natural motions of the subject, while allowing accurate tracking. [87]creates randomly placed so-called "embryos" of starting points of the robot, then calculates trajectories and chooses the "best" solution. [88]and [89]use genetic terminology to randomly place "new" positions and to choose the "best fit" solution.

Work could be done on the safety aspect of such a device. All robots whose workspace is potentially overlapping with a human need to have some sort of force control. If a person was to contact the robot, the response should be that the person could easily push the robot away. [90]deals with dynamics in mobile platforms, but the method could easily be converted to revolute robotic arms. In addition, it might be desired to create a zone of proximity sensors that are attached to the robot. A control strategy would then be designed to keep an object from entering a predefined buffer zone.

The PA-10 has been analyzed in numerous studies. [91] considers the inherent friction of each joint and does experiments with velocity control. [92]and [93]consider response techniques when the desired position is outside the workspace of the robot. It would be advantageous to apply the dynamic modeling and control techniques developed in[94] to this problem.

CHAPTER 10. CONTRIBUTIONS

It was proposed that this research would make four fundamental contributions:

- A comprehensive dynamic model and simulation of a multi-dof mobile robotic fluoroscope.
- Exploration of a novel metric for Wheeled Mobile Manipulators with significant cross coupling effects.
- Real-time digital control system design and performance analysis of a multi-dof robotic fluoroscope in both computer simulation and prototype experimentation.
- Exploration of new concepts for future robotic fluoroscope systems.

In addition to these contributions, this work also makes the following contribution:

- A robust simulation test bed capable of recording approximate skeletal data for a broad spectrum of human activities and transforming that data into a suitable form to input into the dynamic model or the physical system.

In the sections that follow, each of these contributions is discussed.

10.1 COMPREHENSIVE DYNAMIC MODEL

A dynamic model was developed for the TFS by analyzing each channel independently as a lumped-mass second order system. It was found that

- The wheels have transient non-linear damping components that can be ignored by analyzing the closed loop position response,
- The linear motors currently employed as horizontal axes on the TFS have non-linear bidirectional damping that cannot be neglected. The correct damping term can be chosen by examining the sign of the control input.
- The horizontal vertical motors were accurately modeled as linear systems after a gravity compensation term was added to the output.

10.2 NOVEL METRIC FOR CROSS COUPLING EFFECTS IN WHEELED MOBILE MANIPULATORS

A full analysis of the dynamics of the TFS revealed that the system only exhibited cross coupling effects between the platform and the horizontal axes. The axes did not affect each other, nor did the vertical axes affect the platform. Since the coupling between the platform and either horizontal axis was caused by the same physical conditions, only one metric could be derived for this system. From the equation of motion (41) and (43), linear state equations (44) and (45) were derived in which the metric of coupling was found to be $\zeta = \frac{m_a}{m_p}$. The cross coupling was demonstrated dynamically in the off diagonal term by a factor of ζ, and statically in the diagonal term of the axes by a factor of $(1 + \zeta)$.

10.3 SIMULATION TEST BED

The skeleton generator of the Microsoft Kinect sensor was found to be useful for extracting joint coordinates from humans performing natural activities. These joint coordinates can be resampled

to match the input sensors of the TFS, transformed to match the coordinate system of the TFS, and the stored for future evaluations. Human activities that can be captured by the Kinect are limited by the constraints of the Kinect skeleton generator. The generator requires that the human must be roughly perpendicular to the system and that most of the body is in the field of view of the sensor. The maximum distance that the Kinect can detect a human is about one meter, and the minimum distance needed is about 0.2m. This gives the Kinect a working distance of about 0.8 meters. All human activities must be constrained within this distance.

10.4 Real-Time Digital Control System Design

A new supervisory control architecture was designed and implemented to decrease communication delays and obtain direct access to the low-level servo control loops. This change included:

- FPGA hardware implementation,
- Control loop modification from velocity control to torque control,
- Prioritized control execution, and
- Soft position limits for horizontal axis motion.

The control system also was designed to account for the coupling effect of the physical components of the TFS.

10.5 Performance Analysis of the Current System

The capabilities of the current system were analyzed.

- The primary cause of subject tracking error is the lack of power of the MIWD units to push the platform, which is much more massive than originally envisioned. While adding additional MIWDs would help reduce tracking error, it should not be expected to achieve the acceleration of a human starting from rest. Tight tracking control is not needed to analyze a specific joint of interest, so this is not a major constraint.
- Coupling can be a major contributor to subject tracking error. Providing a simple or inverted decoupling scheme will significantly reduce the tracking error, allowing the axes to remain centered about their origin.
- No coupling affect was found in the vertical axes. For walking activities, the axes recorded less than 3 mm of tracking error and exerted less than 15 percent of the available control effort. The maximum tracking error for the vertical axes was less than 10 mm and occurred during a step up activity. The axes never exerted more than 40 percent of the available control effort. The redesigned control scheme reduced the tracking error by 100 percent.
- Current configurations on the TFS make stair climbing difficult to track. This work reveals that the problem is not related to the power of the vertical drives. Such activities are difficult to track because of occlusions due to opposing leg coincidence, and dropped frames.
- The horizontal axes tracking error was reduced by 100 percent by redesigning the control loop. A PD controller was found that keeps the tracking error to within 20 mm.

- Additional improvements to the horizontal axes are likely. Maximum control effort exerted during the trials was only thirty percent of the maximum allowable effort. To increase the control effort, it would be necessary to employ a feedback sensor that measures velocity directly.
- Synchronization of the vertical and horizontal axes do not necessitate a master-slave control configuration. By recognizing the coordinate system of the fluoroscope image, it is possible to drive both coordinated axes independently to the same location relative to the platform. Deviations between the left and right sides drives were kept within 3 mm, which is acceptable synchronization.

10.6 Future Research

The tracking fluoroscope concept is a novel data collection method with many applications. A major contribution of this work is to gain insight into the types of future research that could be accomplished using this method.

Several major subcomponents of the TFS are being replaced by updated equipment. The original horizontal linear drives are being replaced by toothed belt drives. This will increase the maximum speed of the horizontal axis. The vertical axes are being replaced by a ball screw assembly, instead of an Acme thread. This will reduce the frictional losses during high-velocity tracking maneuvers. Two additional MIWD units are being incorporated increase the maximum acceleration of the unit. The x-ray generator is being replaced by a lighter, more compact model. The image collector is being replaced by a solid state flat panel. The flat panel has a reduced footprint, lighter weight, higher resolution and increased field of view.

As these new systems are integrated and come online, expected performance benchmarks can be set by using the modeling techniques established in this work. This will provide insight into the full capabilities and limitations of the reconfigured system.

One of the chief difficulties with using x-ray images to perform video servoing is the obstructions caused by other body parts occluding the joint of interest during the human gait. Additional sensors, such as RGB-D and Time-of-Flight cameras could be used to supplement the video image. Better image processing algorithms would make the pattern recognition portion of the image processing more robust and easier to set up. The data collected by the Kinect could aid in the creation of a dynamic human model. This could be combined with particle filtering techniques or Kalman filtering to further add to the robustness of the system.

The new drives are stronger, but they also are heavier, while the overall weight of the TFS is expected to remain the same. The increased weight ratio of the wings to the platform is expected to increase the coupling of the new system. With the decoupling techniques developed in this work, the new drives could be tuned to new levels of control. The tuned system would perform the current activities with superior accuracy, and data collection could be extended to include new activities.

Control should be extended to curvilinear motion. The Kinect data recorded in this work will serve as a base to test and refine the control of the system before the control is actually implemented. The Labview platform offers extensive simulation capabilities, allowing the controllers to be designed using simulation, then seamlessly implemented on the system.

Modules, such as the 7 dof PA-10, could be designed to add to the collection capabilities of the TFS. These modules could be capable of capturing activities that require higher speeds and greater flexibility than a mobile platform with linear actuators can achieve.

List of References

[1] RIA, "2011 is Record-Breaking Year for North American Robotics Industry," 2012, pp. http://www.robotics.org/content-detail.cfm/Industrial-Robotics-News/2011-is-Record-Breaking-Year-for-North-American-Robotics-Industry/content_id/3240

[2] R. D. Komistek, "Method and Apparatus for Imaging Tracking," 2006, pp.

[3] S. Zingde, F. Leszko, J. K. Mueller, M. Mahfouz, D. Dennis and R. Komistek. (2012, September 1, 2012). In Vivo Determination of the Cam-Post Engagement in Fixed and Mobile Bearing Tka. *Journal of Bone & Joint Surgery, British Volume.* [Online]. 94-B (*SUPP XL*), 225. Available: http://www.bjjprocs.boneandjoint.org.uk/content/94-B/SUPP_XL/225.abstract

[4] D. K. Ramsey and P. F. Wretenberg. (1999, 11//). Biomechanics of the knee: methodological considerations in the in vivo kinematic analysis of the tibiofemoral and patellofemoral joint. *Clinical Biomechanics.* [Online]. 14 (*9*), 595-611. Available: http://www.sciencedirect.com/science/article/pii/S0268003399000157

[5] C. Reinschmidt, A. J. van den Bogert, B. M. Nigg, A. Lundberg and N. Murphy. (1997, 7//). Effect of skin movement on the analysis of skeletal knee joint motion during running. *Journal of Biomechanics.* [Online]. 30 (*7*), 729-732. Available: http://www.sciencedirect.com/science/article/pii/S0021929097000018

[6] R. D. Komistek, J. A. Murphy and T. L. O'Dell. Clinical and Kinematic Outcomes of A Rotating Platform Posterior Stabilized Total Knee System. *The Journal of Arthroplasty.* [Online]. (*0*), Available: http://www.sciencedirect.com/science/article/pii/S0883540312005803

[7] E. Atalar, D. L. Kraitchman, B. Carkhuff, J. Lesho, O. Ocali, M. Solaiyappan, M. A. Guttman and H. K. Charles. (1998, Catheter - tracking FOV MR fluoroscopy. *Magnetic resonance in medicine.* [Online]. 40 (*6*), 865-872. Available:

[8] A. K. Jain, T. Mustafa, Y. Zhou, C. Burdette, G. S. Chirikjian and G. Fichtinger. (2005, FTRAC—A robust fluoroscope tracking fiducial. *Medical physics.* [Online]. 32 3185. Available:

[9] E. E. Tuna, T. J. Franke, O. Bebek, A. Shiose, K. Fukamachi and M. C. Cavusoglu. (2011, Heart Motion Prediction Based on Adaptive Estimation Algorithms for Robotic-Assisted Beating Heart Surgery. [Online]. Available:

[10] W. R. Hamel, "A Tracking Robot Conecpt for Human Musculoskeletal Diagnosis," 2005, pp.

[11] R. D. Komistek, W. R. Hamel and D. A. Dennis, "Method and apparatus for imaging tracking," Google Patents, 2005, pp.

[12] G. R. Preliasco, "Motion control for a tracking fluoroscope system," Master of Science Thesis, Mechanical, Aerospace, and Biomedical Engineering Department, University of Tennessee, Knoxville, TN, 2005.

[13] R. B. Cunningham, "Mechanical Design and Integration of a Tracking Fluoroscope System," Master of Science Thesis, Mechanical, Aerospace, and Biomedical Department, University of Tennessee, Knoxville, TN, 2005.

[14] A. Nycz and W. H. Hamel. (2009, October). Active Tracking Control between a Bio-robot and a Human Subject. *IEEE/RSJ International Conference on Intelligent Robots and Systems.* [Online]. 2569-2574. Available:

[15] W. R. Hamel, R. D. Komistek, D. Dennis and A. Nycz. (2011, November 1, 2011). A886. A NEW METHOD FOR OBTAINING IN VIVO FLUOROSCOPIC ARTHOPLASTY EVAULATIONS WITH NORMAL PATIENT MOVEMENT. *Journal of Bone & Joint Surgery, British Volume.* [Online]. 93-B (*SUPP IV*), 457. Available: http://www.bjjprocs.boneandjoint.org.uk/content/93-B/SUPP_IV/457.1.abstract

[16] W. Hamel, R. Komistek and D. Dennis. (2012, September 1, 2012). Results From a New Method for Obtaining in Vivo Fluoroscopic Arthoplasty Evaulations With Normal Patient Movement. *Journal of Bone & Joint Surgery, British Volume.* [Online]. 94-B (*SUPP XL*), 63. Available: http://www.bjjprocs.boneandjoint.org.uk/content/94-B/SUPP_XL/63.abstract

[17] J. C. Alexander and J. H. Maddocks. (1989, October). On the Kinematics of Wheeled Mobile Robots. *The International Journal of Robotics Research.* [Online]. 8 (*5*), 15-27. Available:

[18] G. Campion, G. Bastin and B. D. Andrea-Novel. (1996, February). Structural properties and classification of kinematic and dynamic models of wheeled mobile robots. *IEEE TRANSACTIONS ON ROBOTICS AND AUTOMATION.* [Online]. 12 (*1*), 47-62. Available:

[19] J. Borenstein. (1995, February). CONTROL AND KINEMATIC DESIGN OF MULTI-DEGREE-OF-FREEDOM MOBILE ROBOTS WITH COMPLIANT LINKAGE. *IEEE TRANSACTIONS ON ROBOTICS AND AUTOMATION.* [Online]. 11 (*1*), 21-35. Available:

[20] M. Galicki. (2005, Control-based solution to inverse kinematics for mobile manipulators using penalty functions. *JOURNAL OF INTELLIGENT & ROBOTIC SYSTEMS.* [Online]. 42 (*3*), 213-238. Available:

[21] M. Haddad, S. Hanchi and H. Lehtihet. (2009, Point-to-point trajectory planning of wheeled mobile manipulators with stability constraint. Extension of the random-profile approach. *European Journal of Mechanics-A/Solids.* [Online]. 28 (*3*), 477-493. Available:

[22] Q. Huang, S. Sugano and K. Tanie. "Motion planning for a mobile manipulator considering stability and task constraints," in Robotics and Automation, 1998. Proceedings. 1998 IEEE International Conference on, Year, pp. 2192-2198.

[23] Q. Huang, K. Tanie and S. Sugano. (2000, Coordinated motion planning for a mobile manipulator considering stability and manipulation. *The International Journal of Robotics Research.* [Online]. 19 (*8*), 732-742. Available:

[24] J. Kim, W. K. Chung, Y. Youm and B. H. Lee. "Real-time ZMP compensation method using motion for mobile manipulators," in Robotics and Automation, 2002. Proceedings. ICRA'02. IEEE International Conference on, Year, pp. 1967-1972.

[25] M. Korayem, V. Azimirad, A. Nikoobin and Z. Boroujeni. (2010, Maximum load-carrying capacity of autonomous mobile manipulator in an environment with obstacle considering tip over stability. *The International Journal of Advanced Manufacturing Technology.* [Online]. 46 (*5*), 811-829. Available:

[26] M. Vukobratović and B. Borovac. (2004, Zero-moment point—thirty five years of its life. *International Journal of Humanoid Robotics.* [Online]. 1 (*01*), 157-173. Available:

[27] X. Yun and N. Sarkar. (1998, August). Unified Formulation of Robotic Systems with Holonomic and Nonholonomic Constraints. *IEEE TRANSACTIONS ON ROBOTICS AND AUTOMATION.* [Online]. 14 (*4*), 640-650. Available:

[28] J. H. Chung and D. H. Hong. (1999, September). Comparative study of tracking control for a mobile manipulator: Nonholonomic and dynamic cases. *KSME INTERNATIONAL JOURNAL.* [Online]. 13 (*9*), 585-595. Available:

[29] B. Bayle, J. Y. Fourquet and M. Renaud. (2003, July-August). Manipulability of wheeled mobile manipulators: Application to motion generation. *INTERNATIONAL JOURNAL OF ROBOTICS RESEARCH.* [Online]. 22 (*7-8*), 565-581. Available:

[30] Y. Yamamoto and X. Yun. (1994, June). Coordinating Locomotion and Manipulation of a Mobile Manipulator. *IEEE TRANSACTIONS ON AUTOMATIC CONTROL.* [Online]. 39 (*6*), 1326-1332. Available:

[31] X. Dong, D. Zhao, Y. Jianqiang and T. Xiangmin. (2009, June). Trajectory Tracking Control of Omnidirectional Wheeled Mobile Manipulators: Robust Neural Network-Based Sliding Mode Approach. *IEEE TRANSACTIONS ON SYSTEMS, MAN, AND CYBERNETICS—PART B: CYBERNETICS.* [Online]. 39 (*3*), 788-799. Available:

[32] K. WATANABE, K. SATO, K. IZUMI and Y. KUNITAKE. (2000, January). Analysis and Control for an Omnidirectional Mobile Manipulator. *Journal of Intelligent and Robotic Systems.* [Online]. 27 (*1-2*), 3-20. Available:

[33] M. Fruchard, P. Morin and C. Samson. (2006, August). A framework for the control of nonholonomic mobile manipulators. *INTERNATIONAL JOURNAL OF ROBOTICS RESEARCH.* [Online]. 25 (*8*), 745-780. Available:

[34] J. D. Tan, XiN and Y. C. Wang. (2003, May). Integrated task planning and control for mobile manipulators. *INTERNATIONAL JOURNAL OF ROBOTICS RESEARCH.* [Online]. 22 (*5*), 337-354. Available:

[35] S. Hutchinson, G. D. Hager and P. I. Corke. (1996, October). A Tutorial on Visual Servo Control. *IEEE Transaction on Robotics and Automation.* [Online]. 12 (*5*), 651-670. Available:

[36] C. C. de Wit, P. Tsiotras, E. Velenis, M. Basset and G. Gissinger. (2002, March). Dynamic Friction Models for Road/Tire Longitudinal Interaction. *VEHICLE SYSTEM DYNAMICS.* [Online]. 39 (*3*), 189-226. Available:

[37] M. Seelinger, J.-D. Yoder, E. T. Baumgartner and S. B. Skaar. (2002, December). High-Precision Visual Control of Mobile Manipulators. [Online]. 18 (*6*), 957-965. Available:

[38] C.-C. Wang and C.-T. Shen. (2008, June). Implementation of Wireless Image Tracking for Wheeled Mobile Robots. *3rd International Conference on Innovative Computing Information and Control.* [Online]. 163. Available:

[39] J. Wang and Y. Li. (2009, February). Dynamic Modeling of a Mobile Humanoid Robot. *IEEE International Conference on Robotics and Biomimetics.* [Online]. 639-644. Available:

[40] M. Draelos, N. Deshpande and E. Grant. "The Kinect up close: Adaptations for short-range imaging," in Multisensor Fusion and Integration for Intelligent Systems (MFI), 2012 IEEE Conference on, Year, pp. 251-256.

[41] R. A. El-laithy, H. Jidong and M. Yeh. "Study on the use of Microsoft Kinect for robotics applications," in Position Location and Navigation Symposium (PLANS), 2012 IEEE/ION, Year, pp. 1280-1288.

[42] J. Fabian, T. Young, J. C. P. Jones and G. M. Clayton. (2012, Integrating the Microsoft Kinect With Simulink: Real-Time Object Tracking Example. *Mechatronics, IEEE/ASME Transactions on.* [Online]. PP (*99*), 1-9. Available:

[43] E. Machida, C. Meifen, T. Murao and H. Hashimoto. "Human motion tracking of mobile robot with Kinect 3D sensor," in SICE Annual Conference (SICE), 2012 Proceedings of, Year, pp. 2207-2211.

[44] C. V. Angelino, V. R. Baraniello and L. Cicala. "UAV position and attitude estimation using IMU, GNSS and camera," in Information Fusion (FUSION), 2012 15th International Conference on, Year, pp. 735-742.

[45] H. Joong-hee, J. H. Kwon, L. Impyeong and C. Kyoungah. "Position and Attitude Determination for UAV-Based GPS, IMU and AT without GCPs," in Multi-Platform/Multi-Sensor Remote Sensing and Mapping (M2RSM), 2011 International Workshop on, Year, pp. 1-5.

[46] L. Sahawneh and M. A. Jarrah. "Development and calibration of low cost MEMS IMU for UAV applications," in Mechatronics and Its Applications, 2008. ISMA 2008. 5th International Symposium on, Year, pp. 1-9.

[47] K. Saktaweekulkit and T. Maneewarn. "Motion classification using IMU for human-robot interaction," in Control Automation and Systems (ICCAS), 2010 International Conference on, Year, pp. 2295-2299.

[48] L. Taehee, S. Joongyou and D. Cho. "Position estimation for mobile robot using in-plane 3-axis IMU and active beacon," in Industrial Electronics, 2009. ISIE 2009. IEEE International Symposium on, Year, pp. 1956-1961.

[49] O. Wongwirat and C. Chaiyarat. "A position tracking experiment of mobile robot with Inertial Measurement Unit (IMU)," in Control Automation and Systems (ICCAS), 2010 International Conference on, Year, pp. 304-308.

[50] A. Nycz and W. R. Hamel. (2009, The development of the tracking fluoroscope system. *Methods and Models in Automation and Robotics.* [Online]. 14 (*1*), 168-173. Available:
[51] A. Nycz, M. A. Young and W. R. Hamel, "A Bio-Robotics Approach to Real–time Skeletal Joint Fluoroscopy during Natural Movements," 2011, pp.
[52] A. Nycz. (2012, Vision-Based Robot Control in the Context of Human-Machine Interactions. [Online]. Available:
[53] Evan-Amos, "The Microsoft Kinect peripheral for the Xbox 360," 2011, pp.
[54] Mircosoft, "Kinect for Windows Sensor Components and Specifications," 2014, pp. http://msdn.microsoft.com/en-us/library/jj131033.aspx
[55] U. o. Leeds, "Kinesthesia Toolkit fo Microsoft Kinect - University of Leeds," National Instruments, 2014, pp. http://sine.ni.com/nips/cds/view/p/lang/en/nid/210938
[56] "Anthropometric Reference Data for Children and Adults: United States, 2007-2010," Centers for Disease Control and Prevention, 2012, pp.
[57] M. U. Rubbers, "Properties and Characteristics of Urethane," MiSUMi, USA, pp. http://us.misumi-ec.com/maker/misumi/mech/product/ur/detail/detail.html
[58] R. Rajagopalan. (1997, A Generic Kinematic Formulation for Wheeled Mobile Robots. *JOURNAL OF ROBOTIC SYSTEMS.* [Online]. 14 (*2*), 77-91. Available:
[59] O. Katsuhiko, *Modern Control Engineering.* 3. Upper Saddle River, New Jersey: Prentice Hall, 1997, pp.
[60] "Platinum Direct Drive Linear Motor Catelog," Danaher Motion, 2004, pp.
[61] C. Makkar, W. Dixon, W. Sawyer and G. Hu. "A new continuously differentiable friction model for control systems design," in Advanced Intelligent Mechatronics. Proceedings, 2005 IEEE/ASME International Conference on, Year, pp. 600-605.
[62] H. A. Rothbart, "Power Screws: Forces," in *Mechanical Design Handbook*, ed. USA: McGraw-Hill, 1996, ch. 20.2, sec. pp. 20.22-20.24.
[63] E. Gagnon, A. Pomerleau and A. Desbiens. (1998, Simplified, ideal or inverted decoupling? *ISA transactions.* [Online]. 37 (*4*), 265-276. Available:
[64] W. L. Luyben. (1970, Distillation decoupling. *AIChE Journal.* [Online]. 16 (*2*), 198-203. Available:
[65] J. Garrido, F. Vázquez and F. Morilla. (2012, Centralized multivariable control by simplified decoupling. *Journal of Process Control.* [Online]. 22 (*6*), 1044-1062. Available:
[66] P. S. Buckley, "Chemical Engineering Seminar," Ohio University, 1967, pp.
[67] H. L. Wade. (1997, Inverted decoupling: a neglected technique. *ISA transactions.* [Online]. 36 (*1*), 3-10. Available:
[68] J. Garrido, F. Vázquez and F. Morilla. (2011, An extended approach of inverted decoupling. *Journal of Process Control.* [Online]. 21 (*1*), 55-68. Available:
[69] F. G. Shinskey. (1967, Process-control systems; application, design, adjustment. [Online]. Available:
[70] Y. Arkun, B. Manousiouthakis and A. Palazoglu. (1984, Robustness analysis of process control systems. A case study of decoupling control in distillation. *Industrial & Engineering Chemistry Process Design and Development.* [Online]. 23 (*1*), 93-101. Available:
[71] J. G. Balchen and B. Sandrib. "Input saturation in nonlinear multivariable processes resolved by nonlinear decoupling," in Control Applications, 1994., Proceedings of the Third IEEE Conference on, Year, pp. 39-44.
[72] K. Walgama and J. Sternby. "Conditioning technique for multiinput-multioutput processes with input saturation," in Control Theory and Applications, IEE Proceedings D, Year, pp. 231-242.
[73] H. Gray, *Anatomy of the human body.* Lea & Febiger, 1918, pp.

[74] A. M. Pappas, R. M. Zawacki and T. J. Sullivan. (1985, Biomechanics of baseball pitching A preliminary report. *The American journal of sports medicine.* [Online]. 13 (*4*), 216-222. Available:
[75] G. Di Giacomo, N. Pouliart, A. Costantini and A. De Vita, *Atlas of functional shoulder anatomy.* Springer, 2008, pp.
[76] R. Whiteley. (2007, Baseball Throwing Mechanics as they relate to Pathology and Performance - A Review. [Online]. Available:
[77] M. W. Spong, S. Hutchinson and M. Vidyasagar, *Robot modeling and control.* John Wiley & Sons New York, 2006, pp.
[78] I.-M. Chen, G. Yang and I.-G. Kang. (1999, Numerical inverse kinematics for modular reconfigurable robots. *JOURNAL OF ROBOTIC SYSTEMS.* [Online]. 16 (*4*), 213-225. Available:
[79] L. Sciavicco and B. Siciliano. (1988, A solution algorithm to the inverse kinematic problem for redundant manipulators. *Robotics and Automation, IEEE Journal of.* [Online]. 4 (*4*), 403-410. Available:
[80] B. Siciliano. (1990, Kinematic control of redundant robot manipulators: A tutorial. *Journal of Intelligent and Robotic Systems.* [Online]. 3 (*3*), 201-212. Available:
[81] H. Seraji, M. K. Long and T. S. Lee. (1993, Motion control of 7-DOF arms: the configuration control approach. *Robotics and Automation, IEEE Transactions on.* [Online]. 9 (*2*), 125-139. Available:
[82] S. Chiaverini. (1997, Singularity-robust task-priority redundancy resolution for real-time kinematic control of robot manipulators. *Robotics and Automation, IEEE Transactions on.* [Online]. 13 (*3*), 398-410. Available:
[83] Y. Huang and T. S. Huang. "Model-based human body tracking," in Pattern Recognition, 2002. Proceedings. 16th International Conference on, Year, pp. 552-555.
[84] J. M. Rehg and T. Kanade, "Visual tracking of high dof articulated structures: an application to human hand tracking," in *Computer Vision—ECCV'94*, ed. Springer, 1994, ch. sec. pp. 35-46.
[85] C. Sminchisescu and B. Triggs. "Kinematic jump processes for monocular 3D human tracking," in Computer Vision and Pattern Recognition, 2003. Proceedings. 2003 IEEE Computer Society Conference on, Year, pp. I-69-I-76 vol. 61.
[86] R. Boulic and D. Thalmann. "Combined direct and inverse kinematic control for articulated figure motion editing," in Computer graphics forum, Year, pp. 189-202.
[87] J. M. Ahuactzin and K. K. Gupta. (1999, The kinematic roadmap: A motion planning based global approach for inverse kinematics of redundant robots. *Robotics and Automation, IEEE Transactions on.* [Online]. 15 (*4*), 653-669. Available:
[88] A. C. Nearchou. (1998, Solving the inverse kinematics problem of redundant robots operating in complex environments via a modified genetic algorithm. *Mechanism and machine theory.* [Online]. 33 (*3*), 273-292. Available:
[89] D. Berenson, S. S. Srinivasa, D. Ferguson, A. Collet and J. J. Kuffner. "Manipulation planning with workspace goal regions," in Robotics and Automation, 2009. ICRA'09. IEEE International Conference on, Year, pp. 618-624.
[90] R. Fierro and F. L. Lewis. "Control of a nonholonomic mobile robot: backstepping kinematics into dynamics," in Decision and Control, 1995., Proceedings of the 34th IEEE Conference on, Year, pp. 3805-3810.
[91] C. W. Kennedy and J. P. Desai. (2005, Modeling and control of the Mitsubishi PA-10 robot arm harmonic drive system. *Mechatronics, IEEE/ASME Transactions on.* [Online]. 10 (*3*), 263-274. Available:

[92] R. S. Jamisola Jr, A. A. Maciejewski and R. G. Roberts. "Failure-tolerant path planning for the PA-10 robot operating amongst obstacles," in Robotics and Automation, 2004. Proceedings. ICRA'04. 2004 IEEE International Conference on, Year, pp. 4995-5000.

[93] R. Jamisola. (2010, Optimization of failure-tolerant workspaces for redundant manipulators. *Philippine Science Letters. v3 i1.* [Online]. 66-75. Available:

[94] R. Jamisola, M. Ang Jr, T. M. Lim, O. Khatib and S. Y. Lim. "Dynamics identification and control of an industrial robot," in The Ninth Intl. Conf. On Advanced Robotics, Year, pp. 323-328.

APPENDICES

APPENDIX A – LABVIEW CODE FOR WINDOWS

APPENDIX A.1 – KINECT CAPTURE CODE

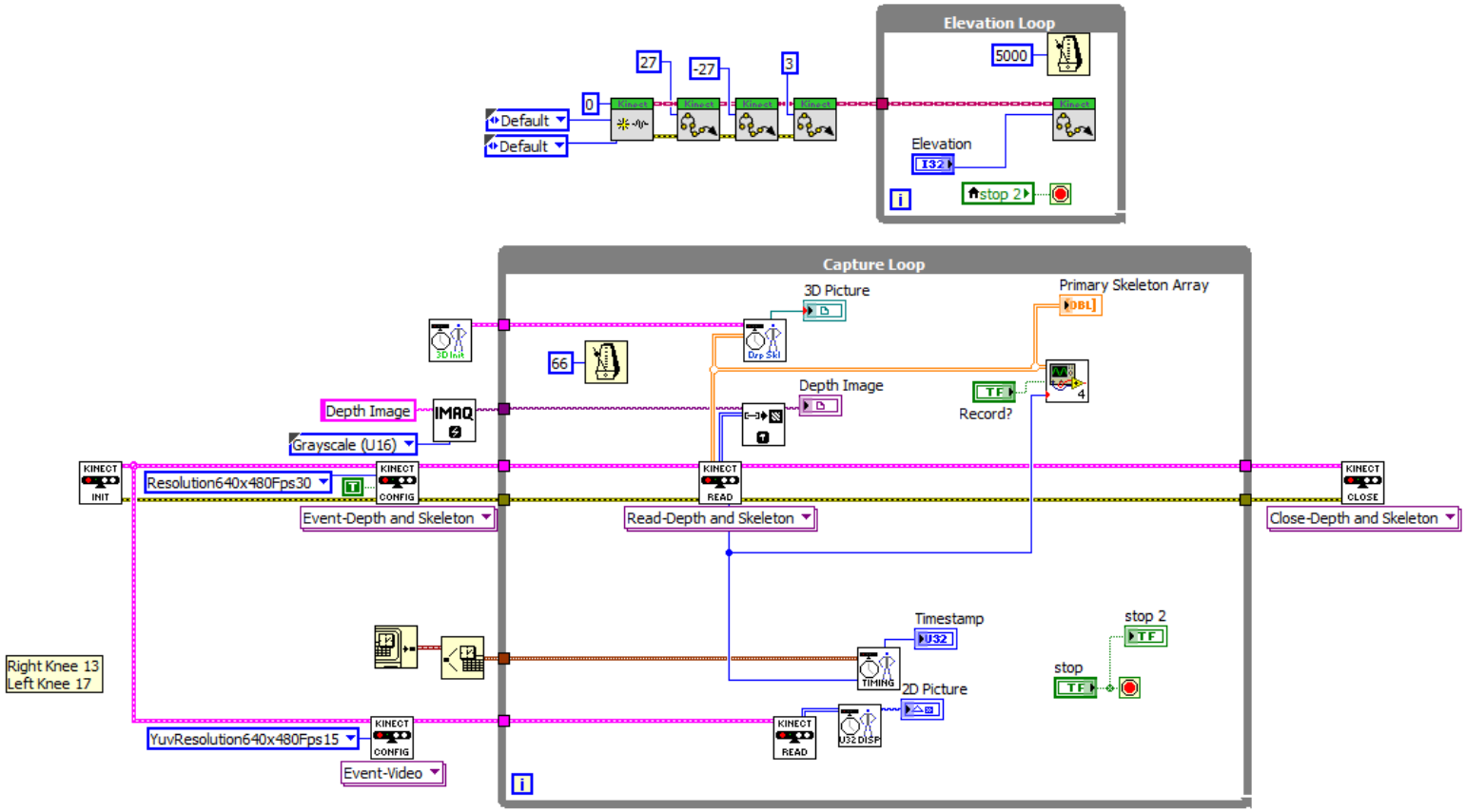

APPENDIX A.2 – KINECT DATA DISPLAY FRONT PANEL

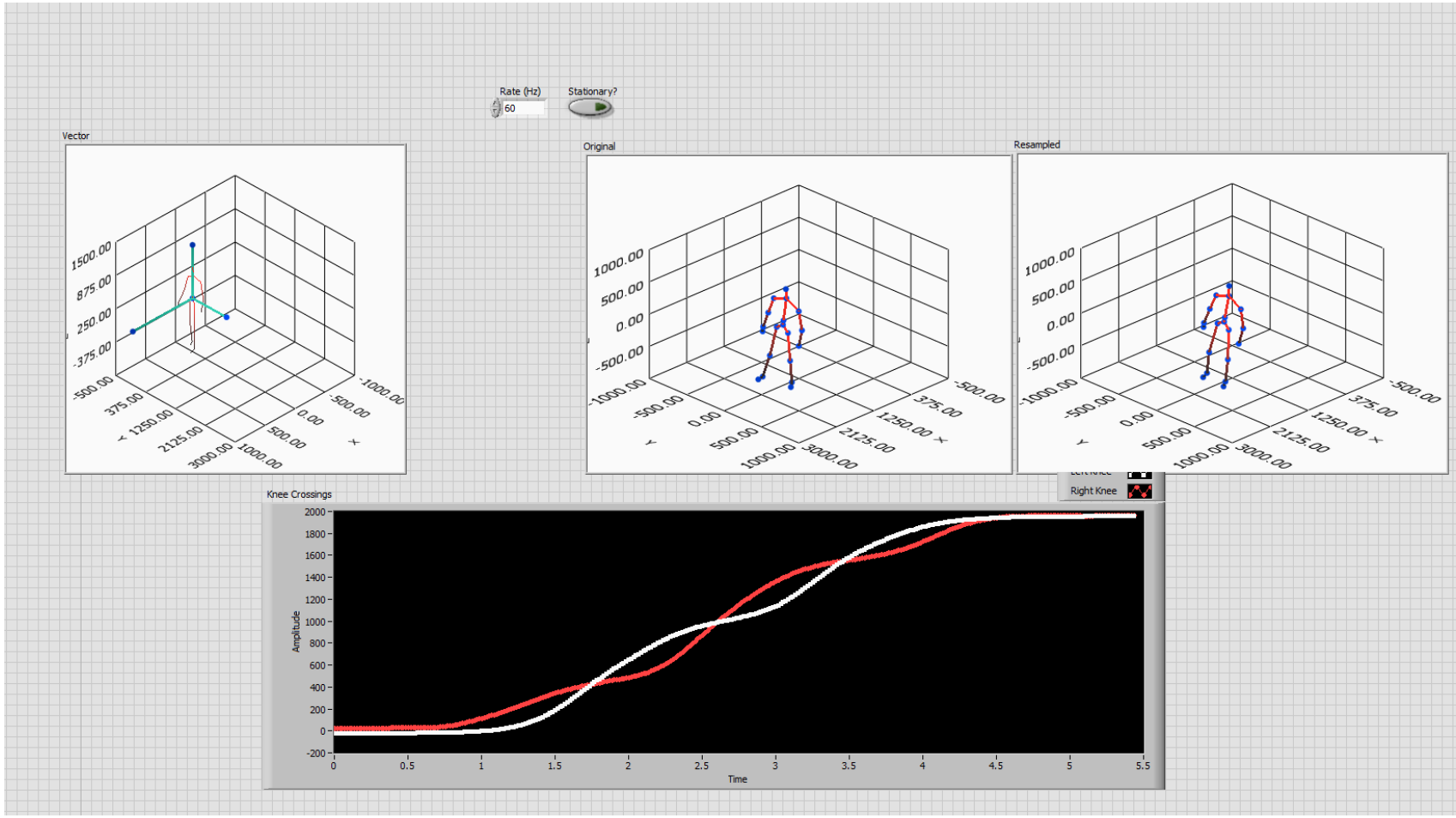

APPENDIX A.3 – KINECT DATA DISPLAY BLOCK DIAGRAM

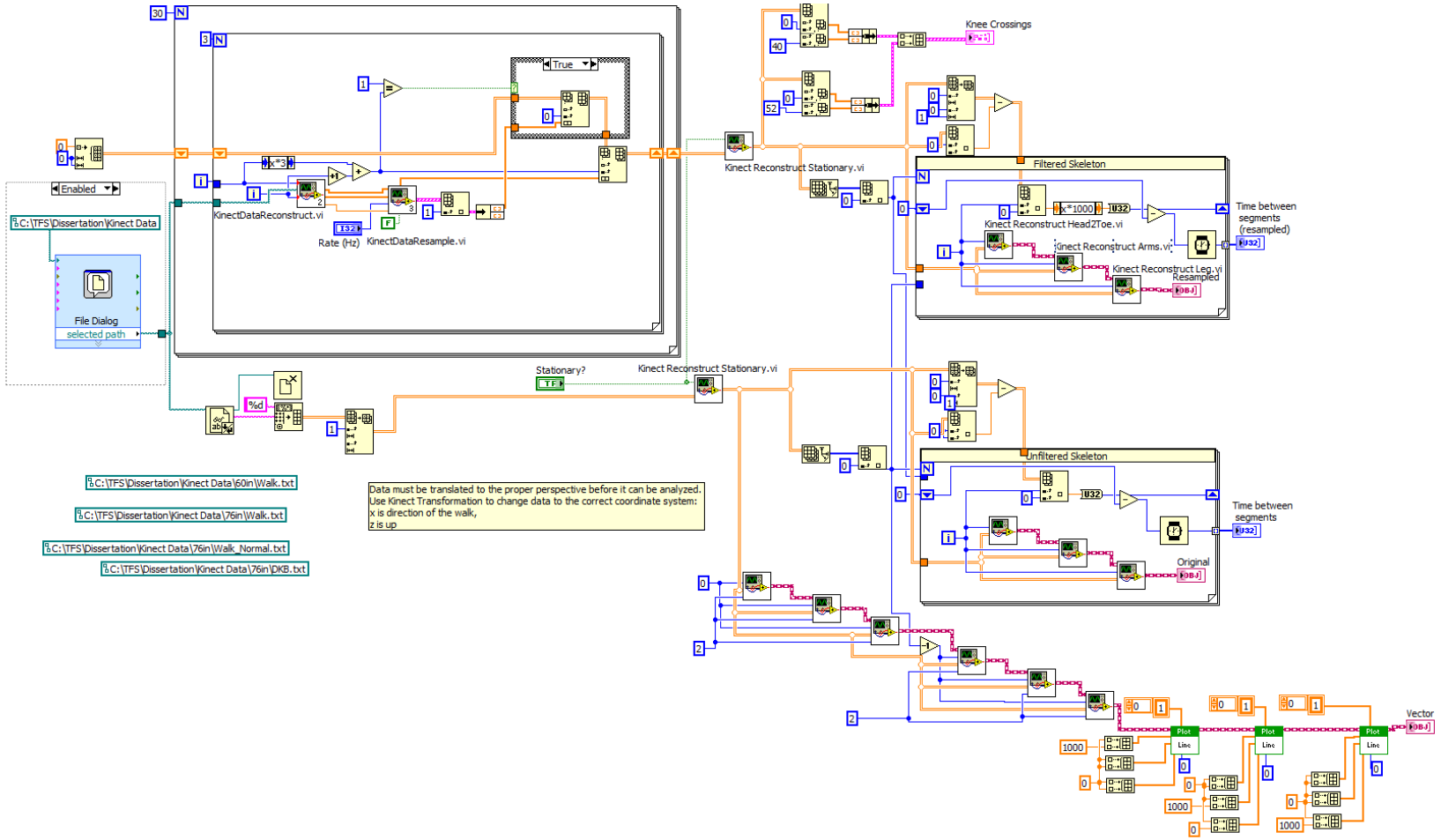

APPENDIX A.4 – KINECT DATA RECONSTRUCT

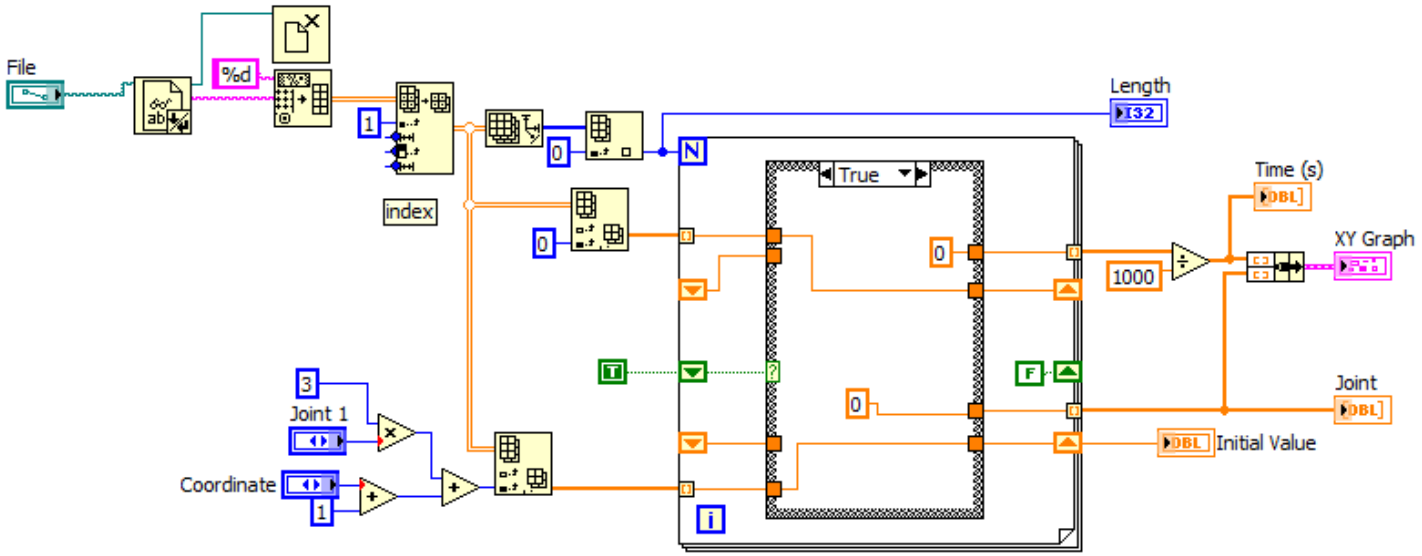

APPENDIX A.5 – KINECT DATA RESAMPLE

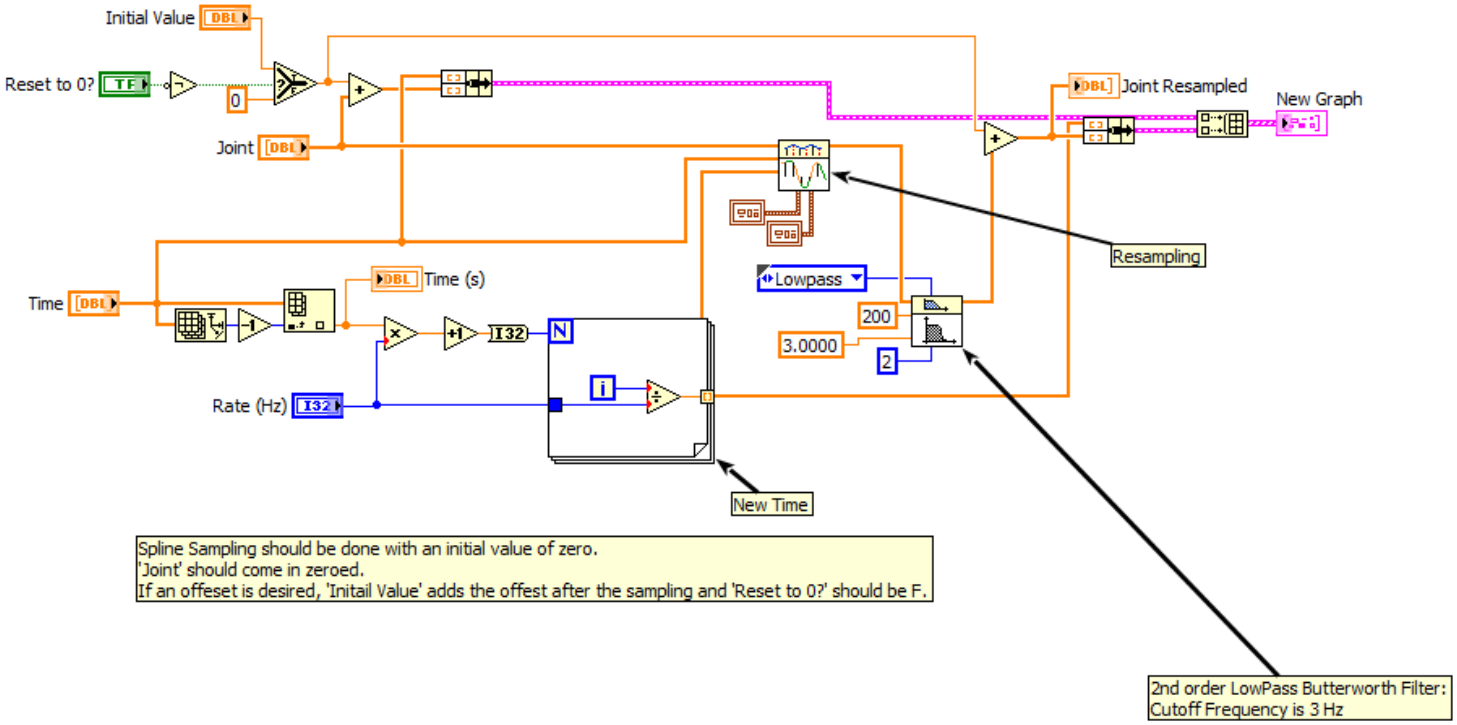

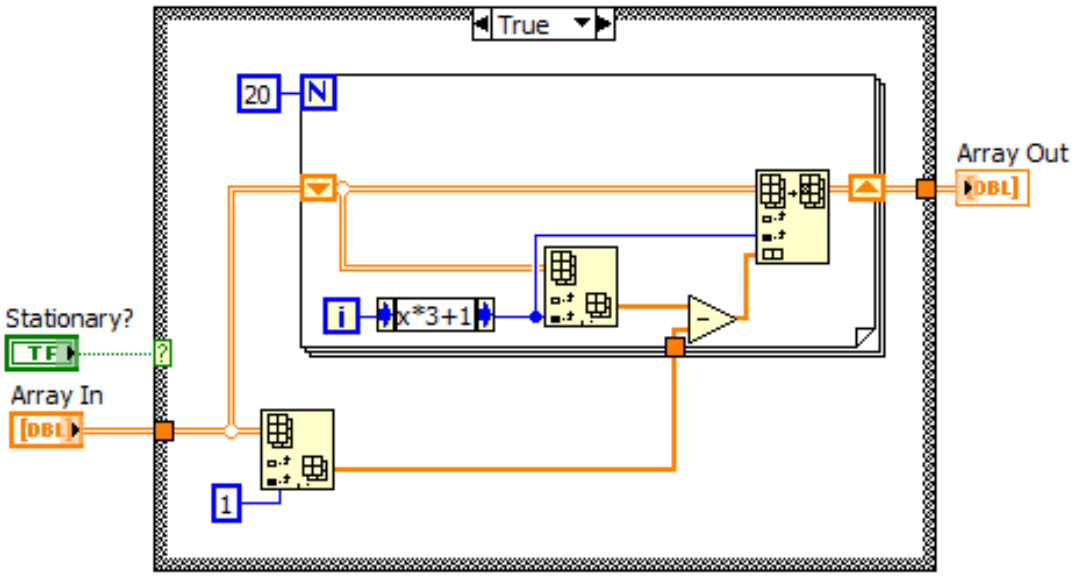
True
20
N
Array Out
DBL
Stationary?
TF
?
Array In
DBL
i
x*3+1
1

APPENDIX A.7 – KINECT 3D PERSON HEAD TO TOE

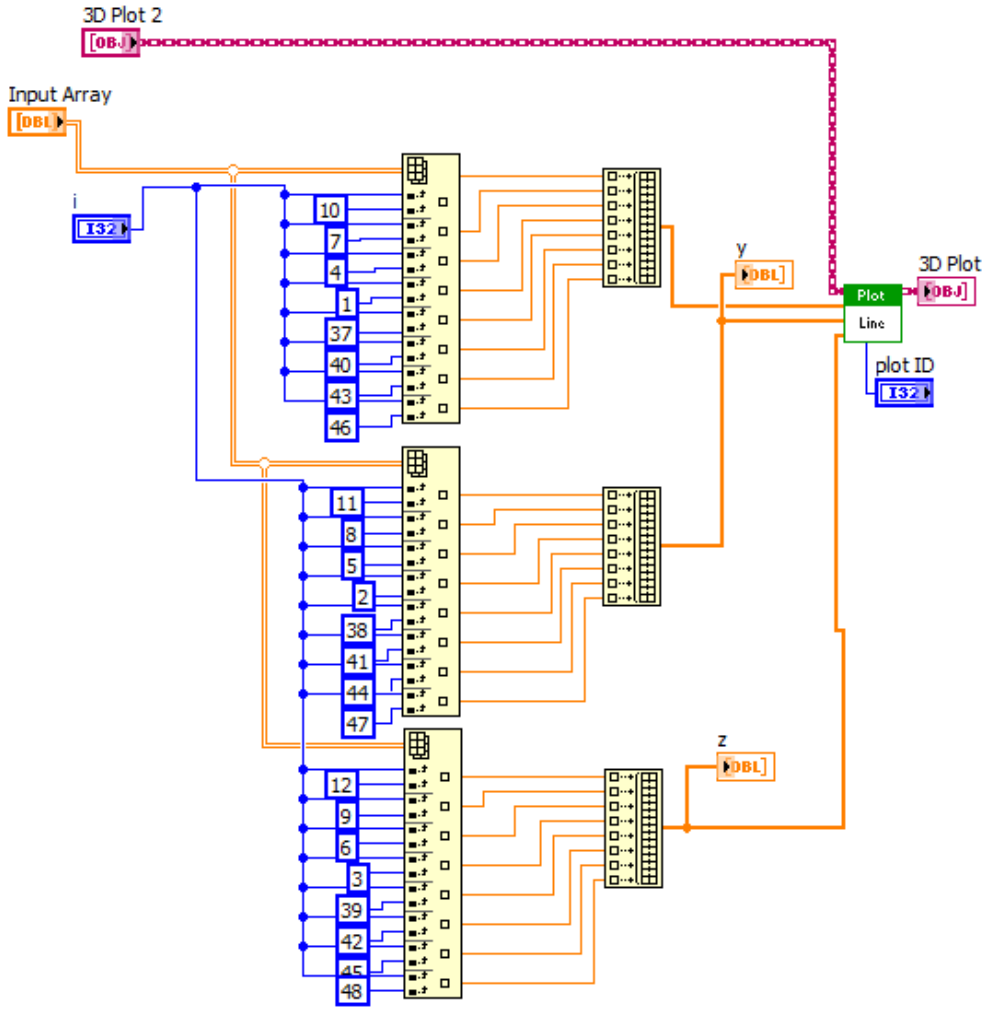

APPENDIX A.8 – KINECT 3D PERSON ARMS

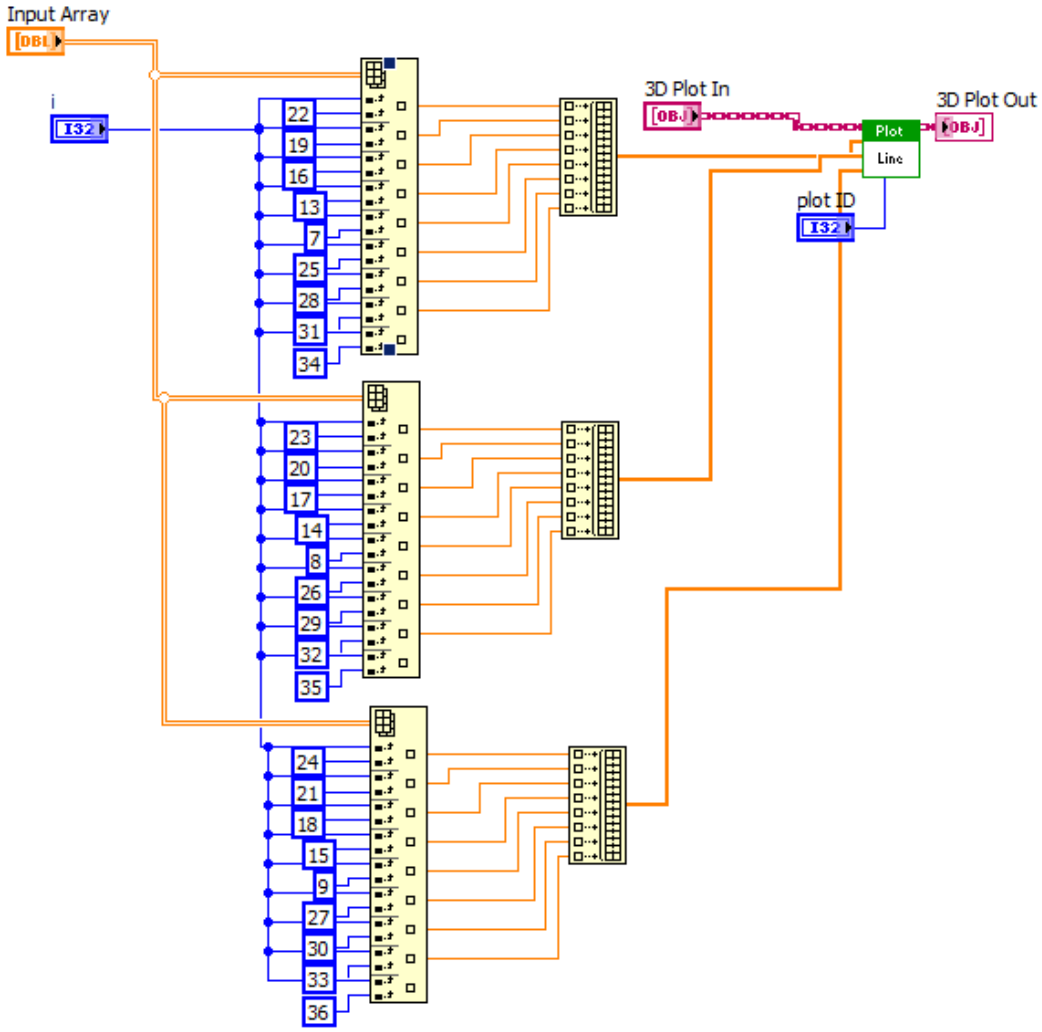

APPENDIX A.9 – KINECT 3D PERSON LEG

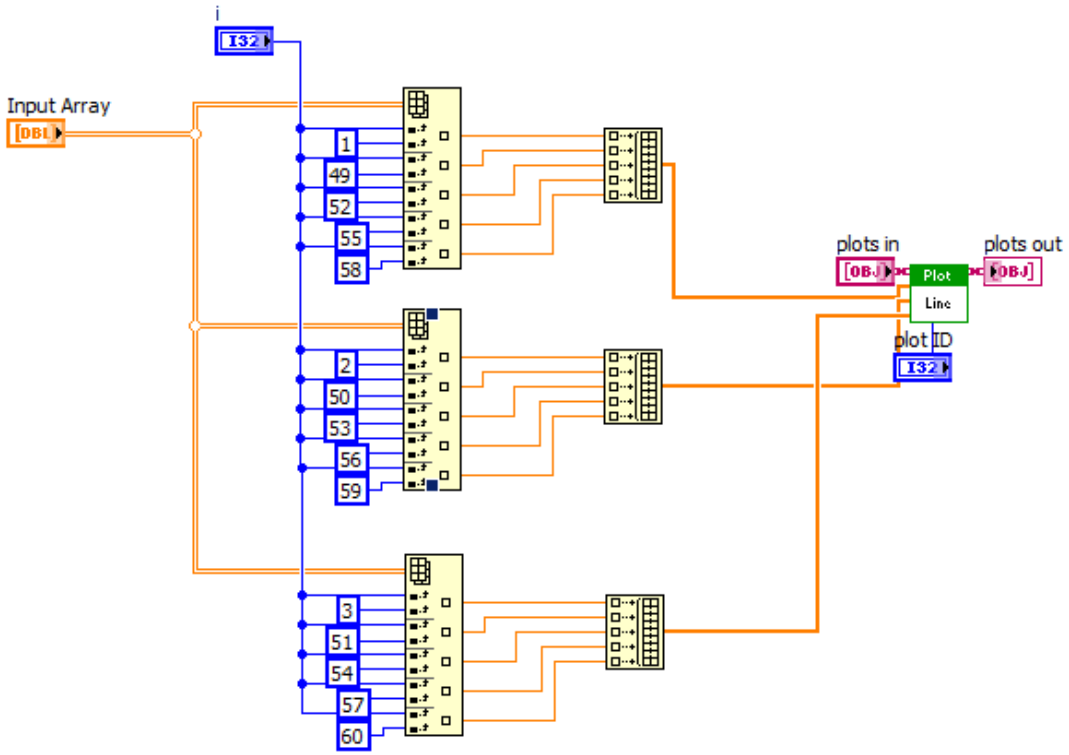

APPENDIX A.10 – KINECT TRANSFORMATION

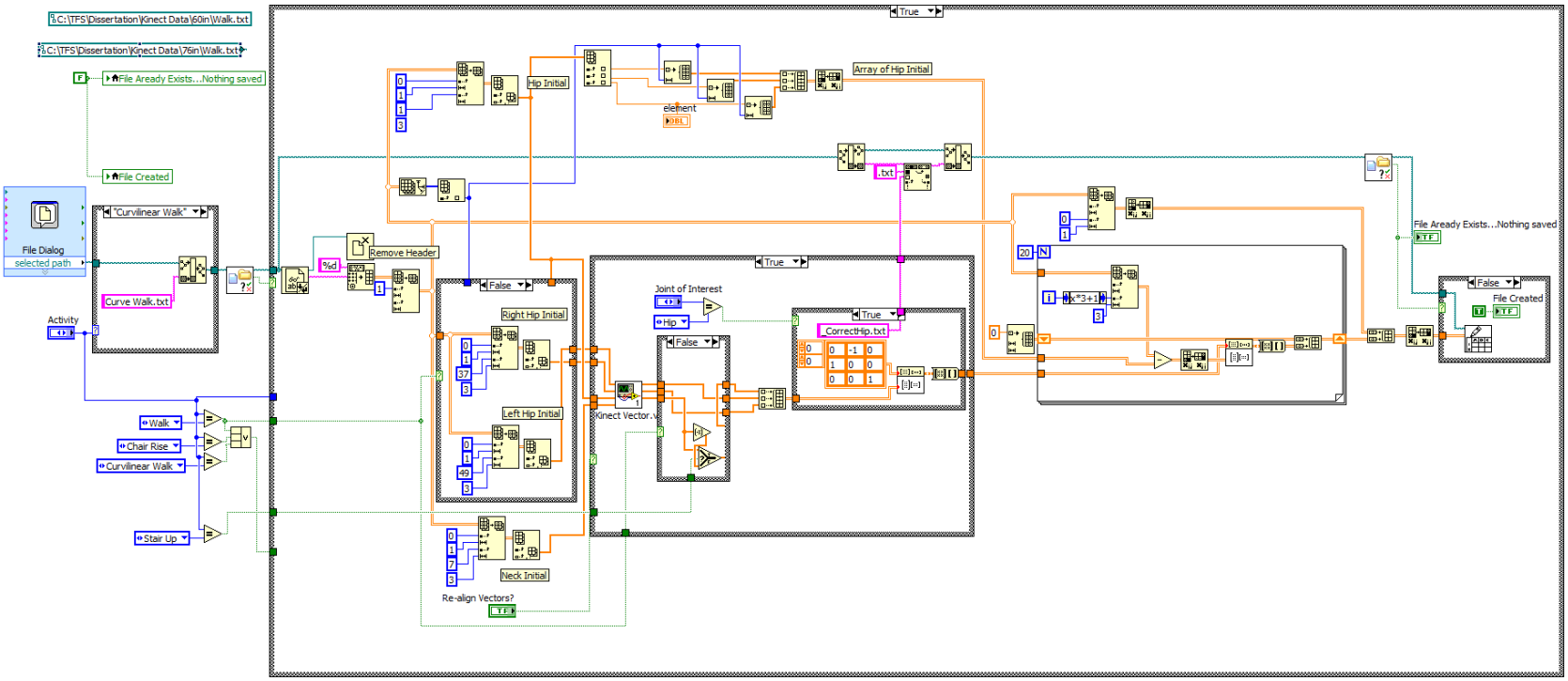

APPENDIX A.11 – KINECT TRANSFORMATION VECTORS

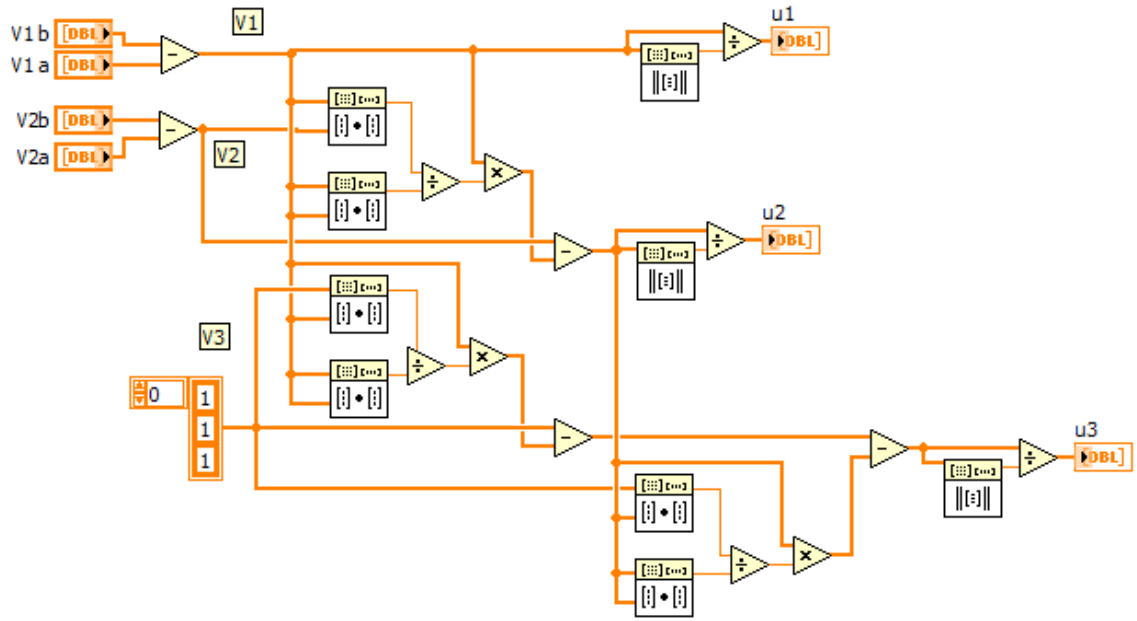

APPENDIX A.12 – KINECT DATA

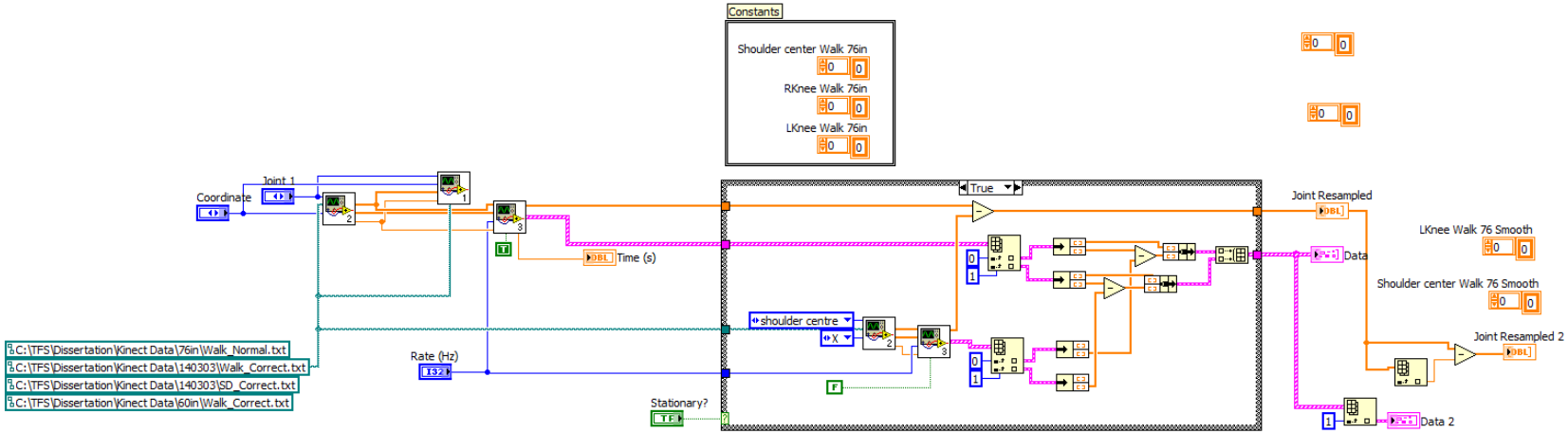

APPENDIX A.13 – X-AXES SIMULATIONS

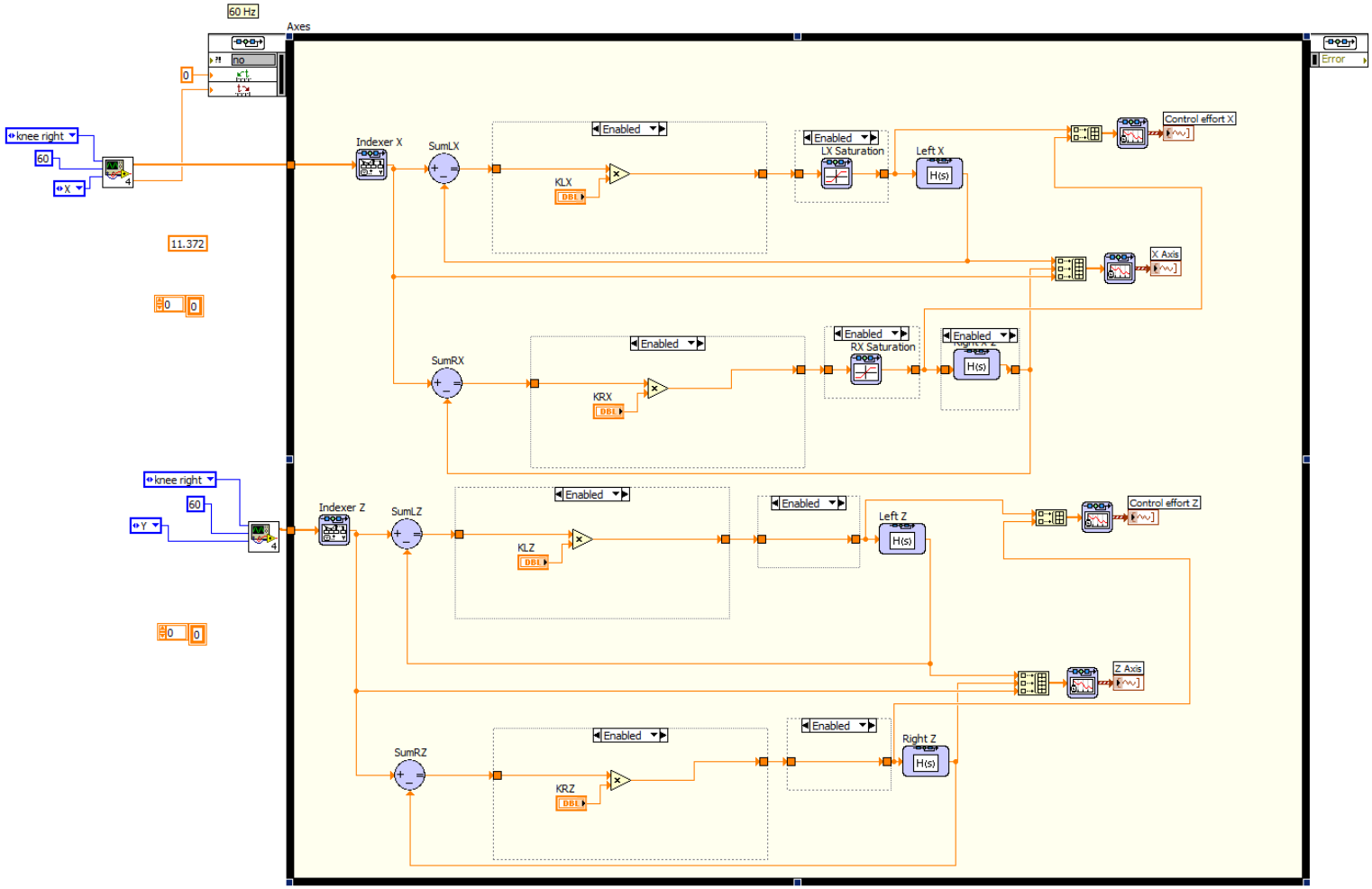

APPENDIX B – LABVIEW CODE FOR REAL TIME OPERATING SYSTEM

APPENDIX B.1 – REMOTE CONTROL FRONT PANEL

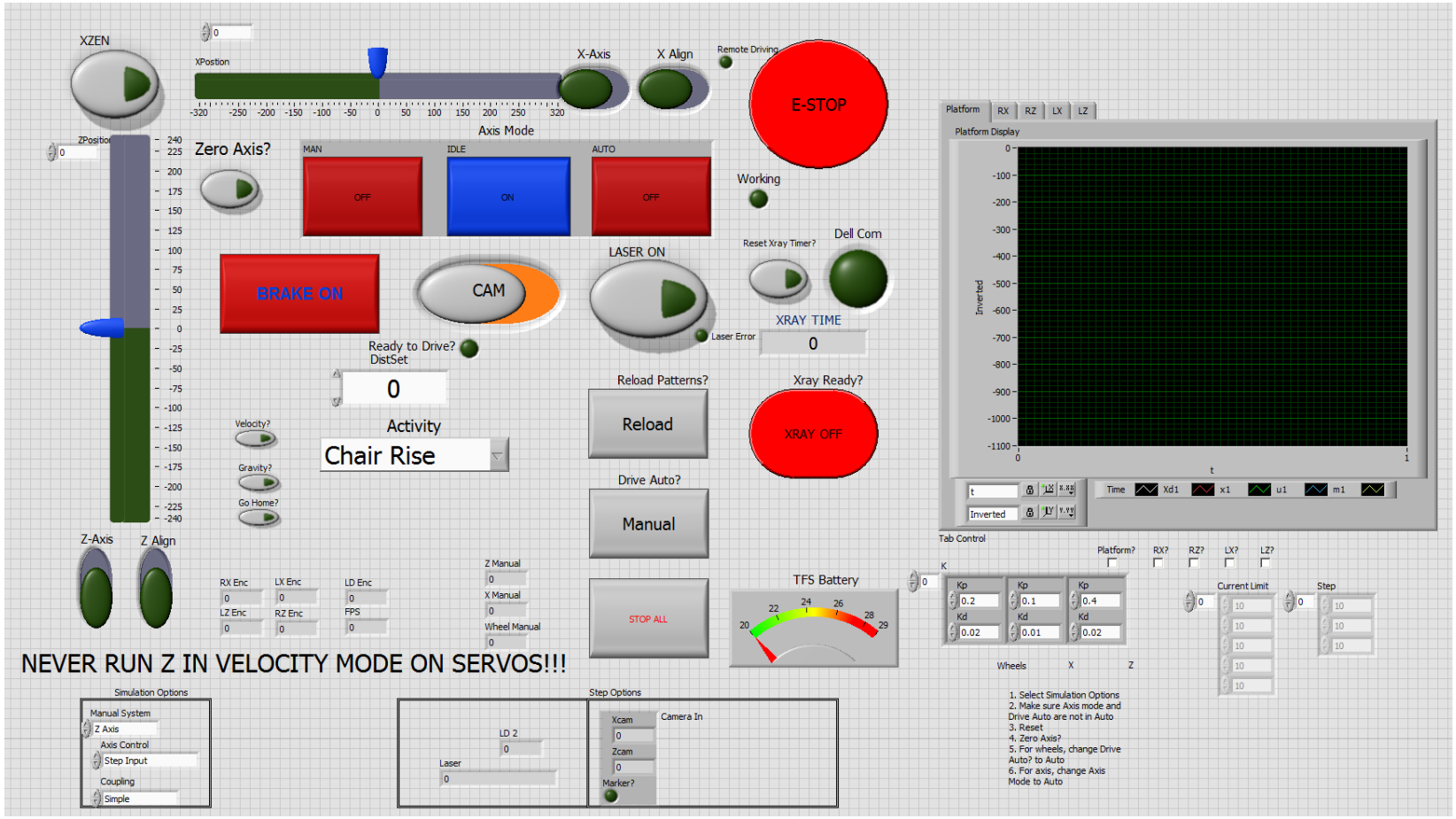

APPENDIX B.2 – REMOTE CONTROL BLOCK DIAGRAM FPGA LOOP

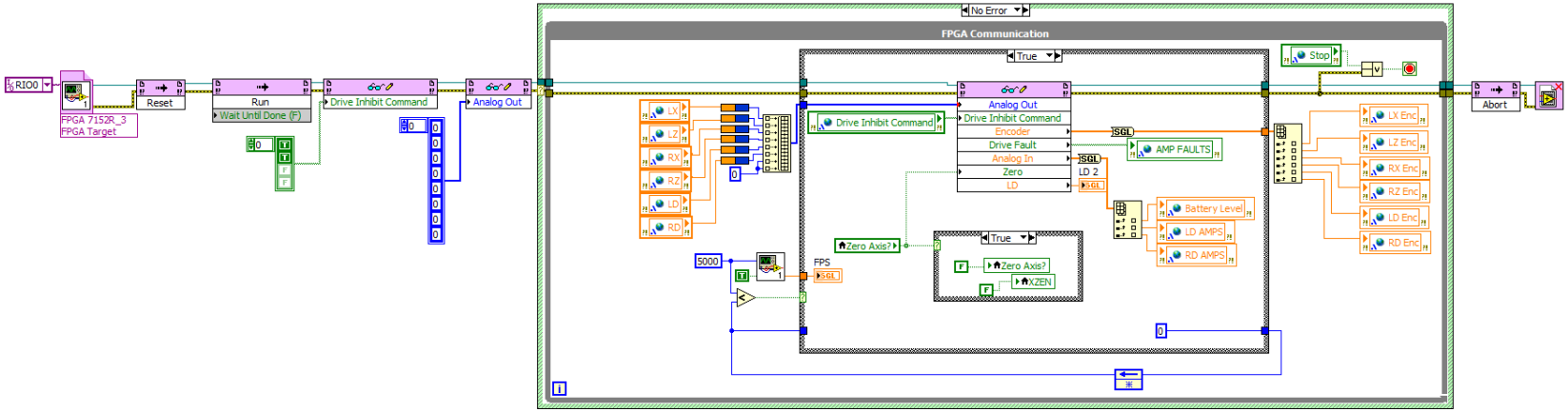

APPENDIX B.3 – REMOTE CONTROL BLOCK DIAGRAM DISPLAY LOOP

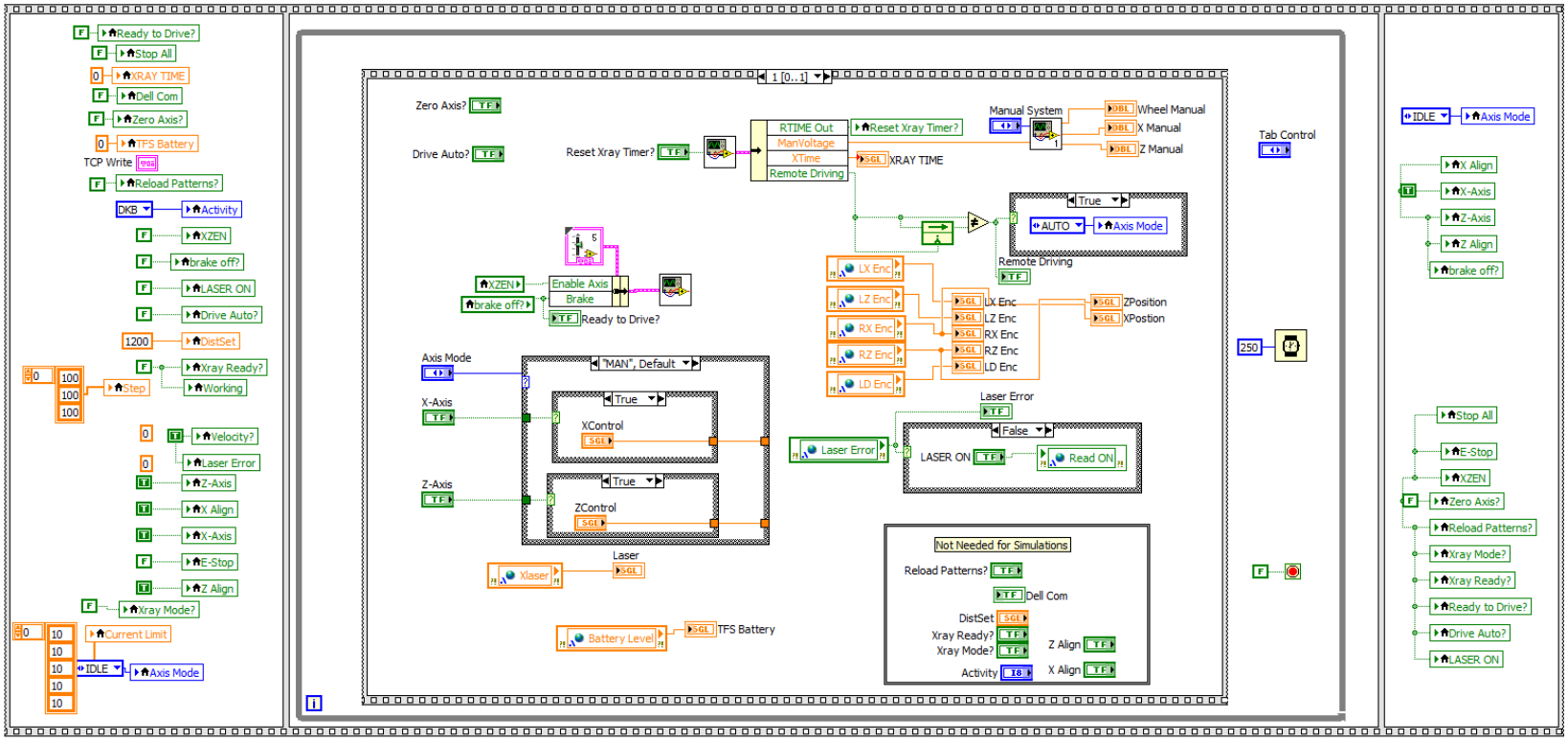

APPENDIX B.4 – REMOTE CONTROL TCP COMMUNICATION LOOP

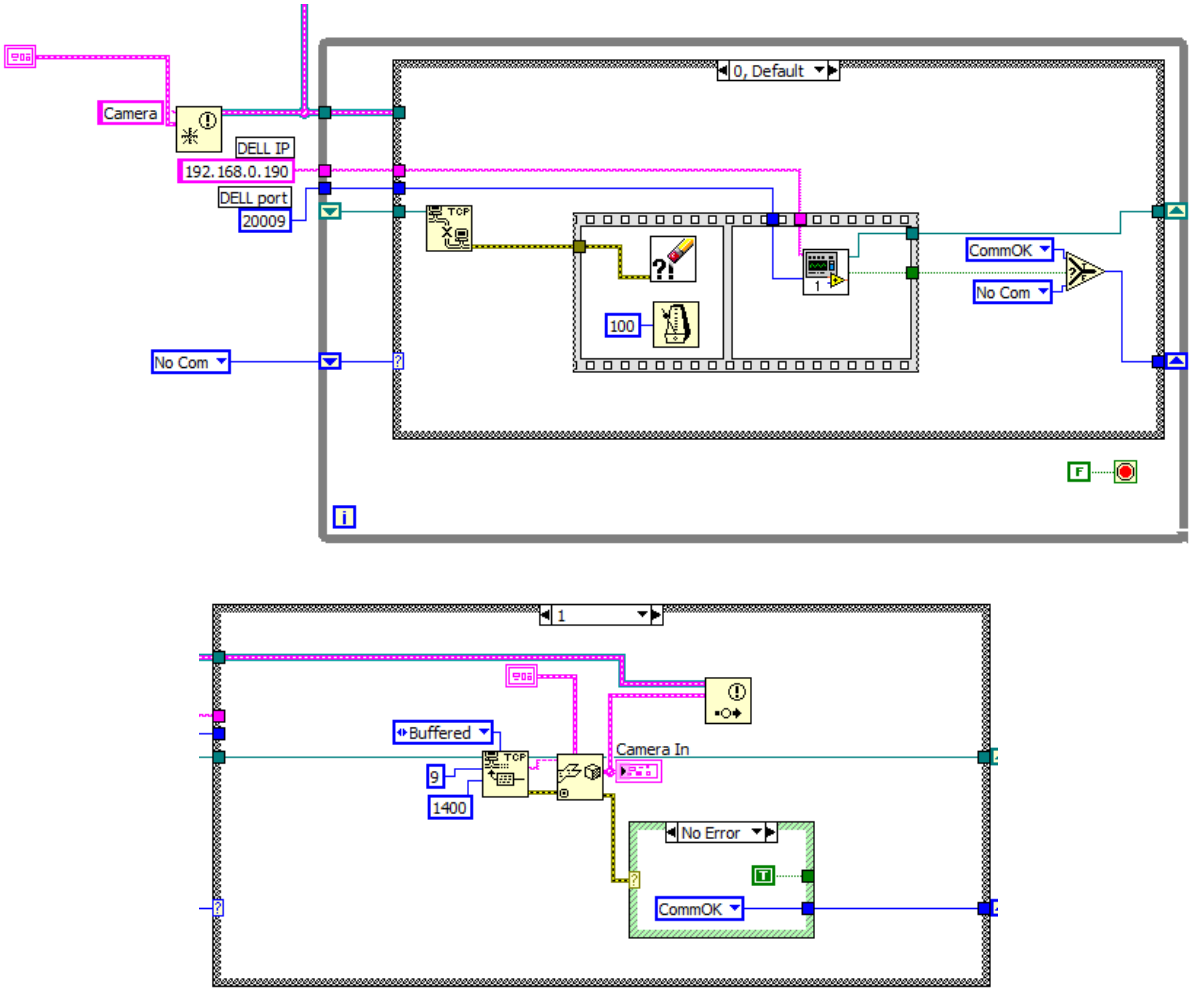

APPENDIX B.5 – REMOTE CONTROL IDLE MODE CONTROL LOOP

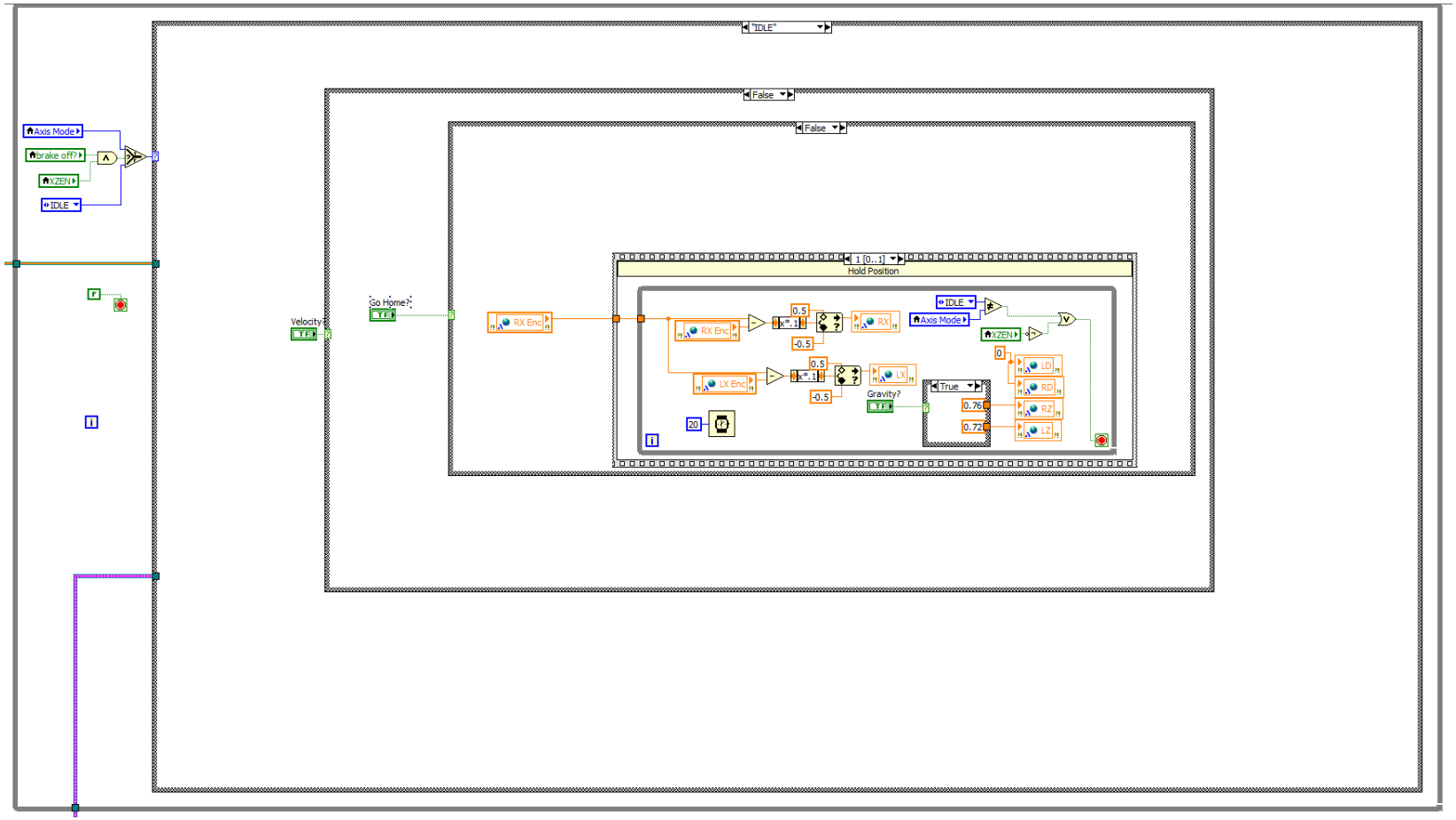

APPENDIX B.6 – REMOTE CONTROL MANUAL MODE CONTROL LOOP

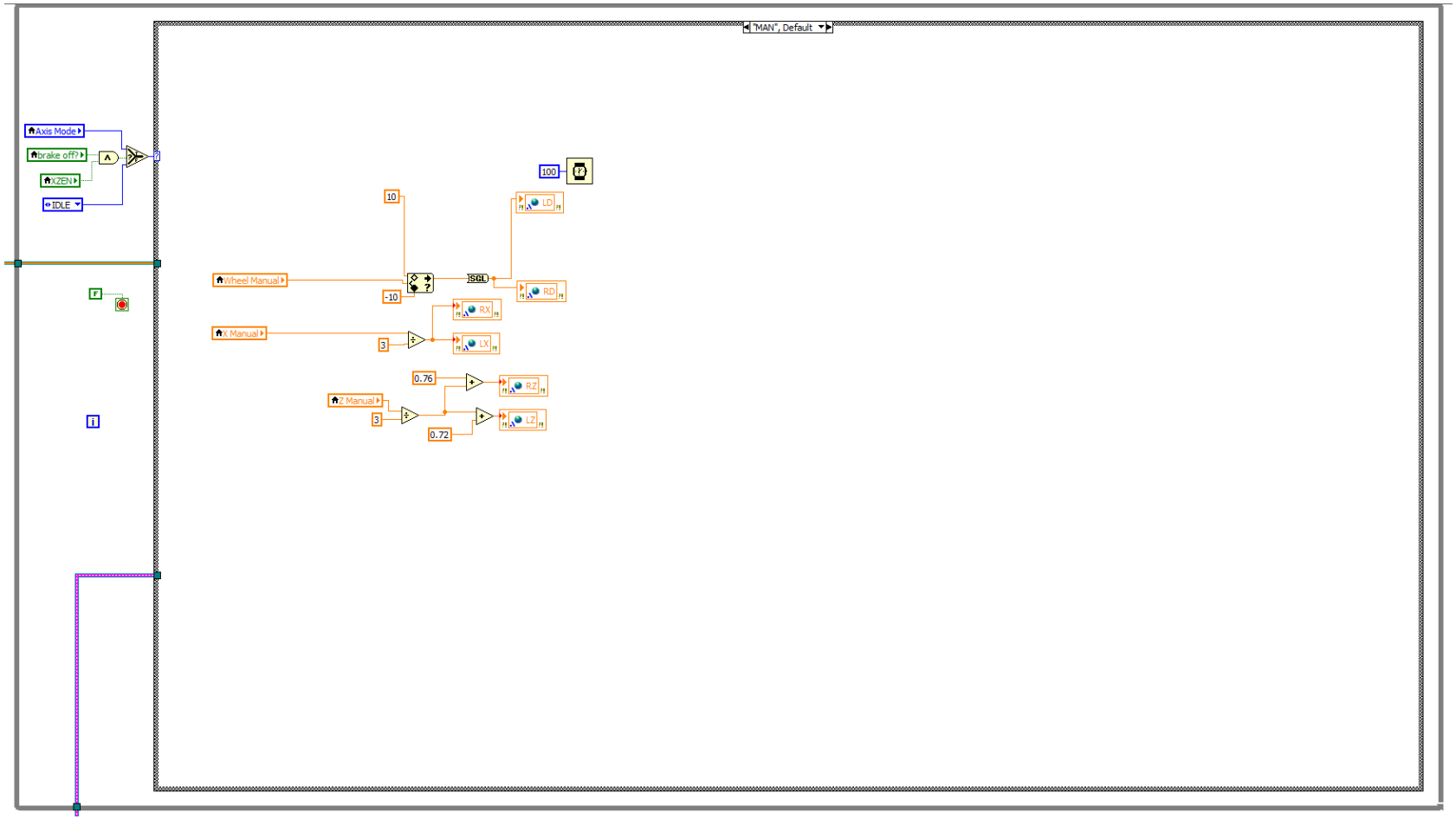

APPENDIX B.7 REMOTE CONTROL AUTO MODE CONTROL LOOP STEP INPUT

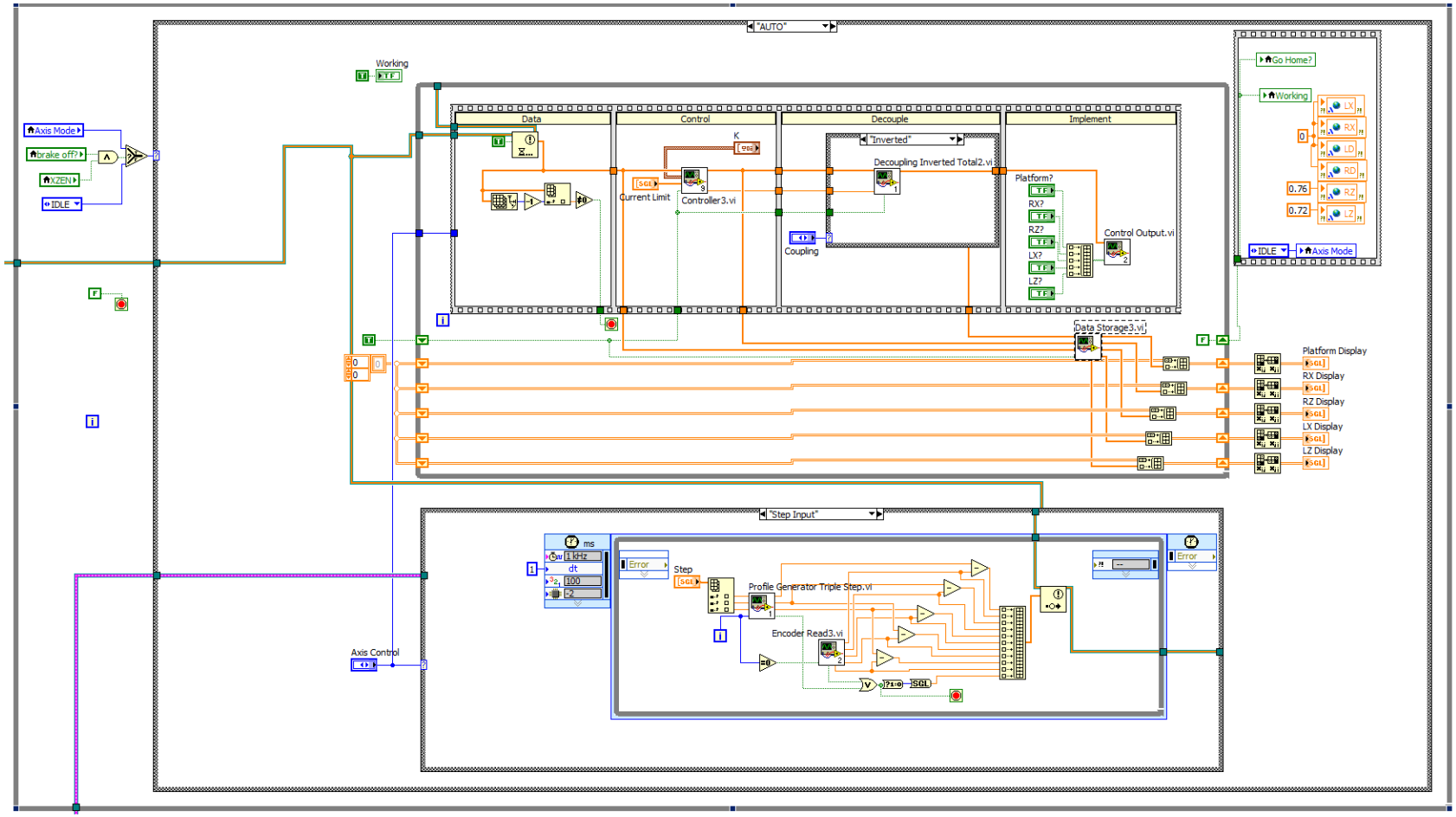

APPENDIX B.8 REMOTE CONTROL AUTO MODE CONTROL LOOP SIMULATION INPUT

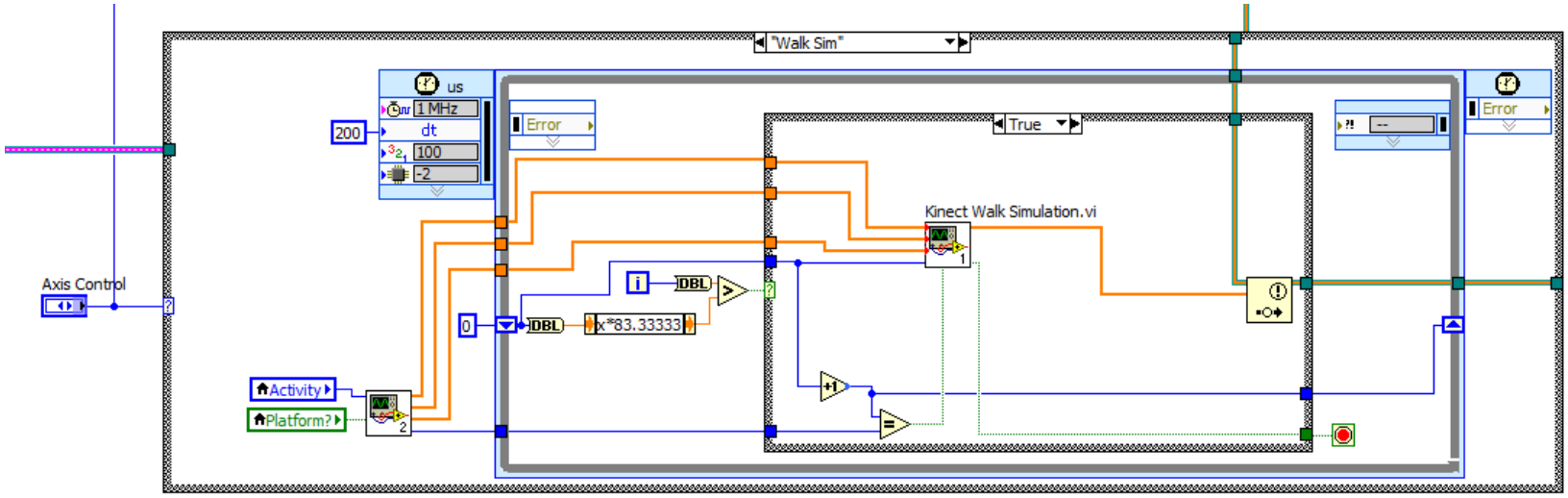

APPENDIX B.8 REMOTE CONTROL AUTO MODE CONTROL LOOP CAMERA INPUT

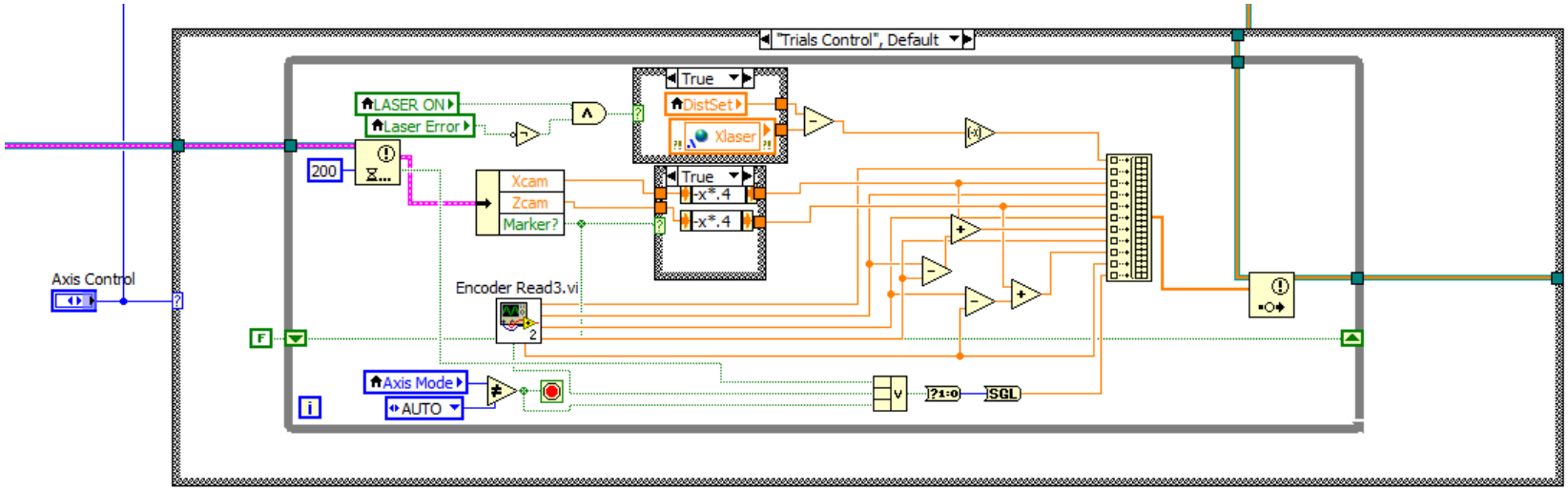

APPENDIX B.9 – PLC WATCHDOG

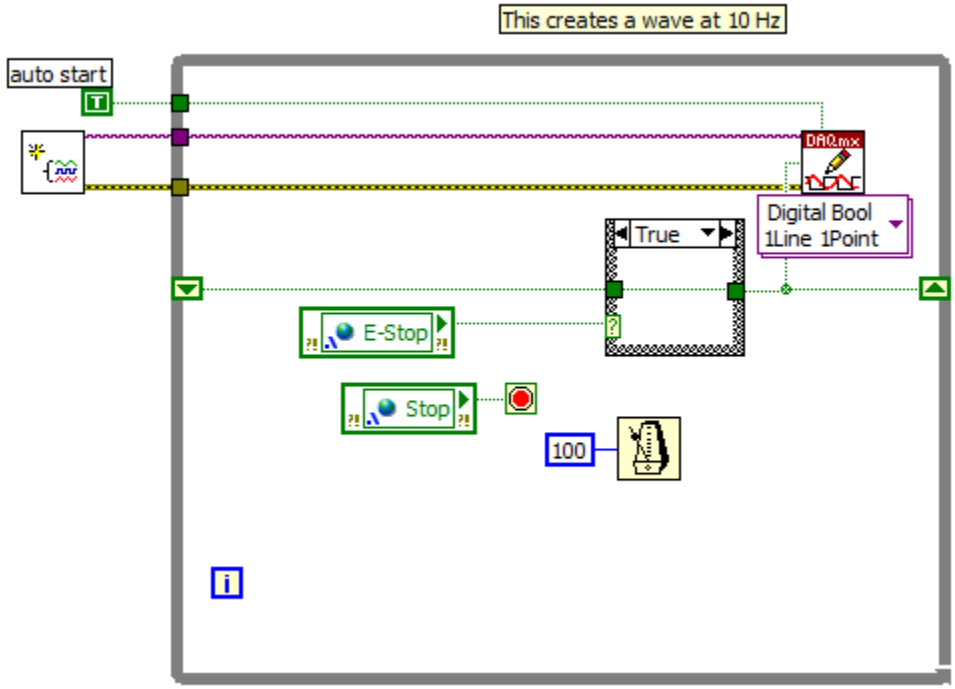

APPENDIX B.10 – LASER PROCESSING IDLE

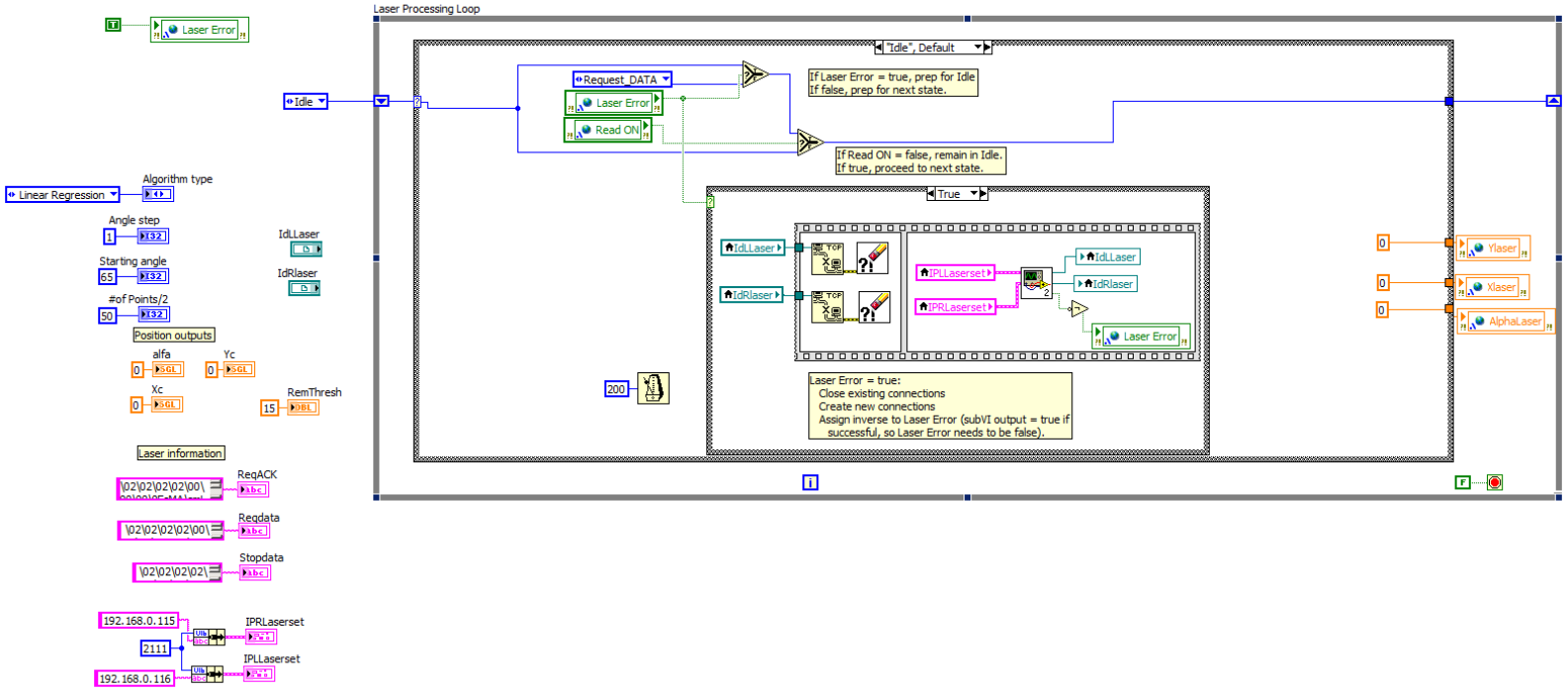

APPENDIX B.11 – LASER PROCESSING REQUEST DATA

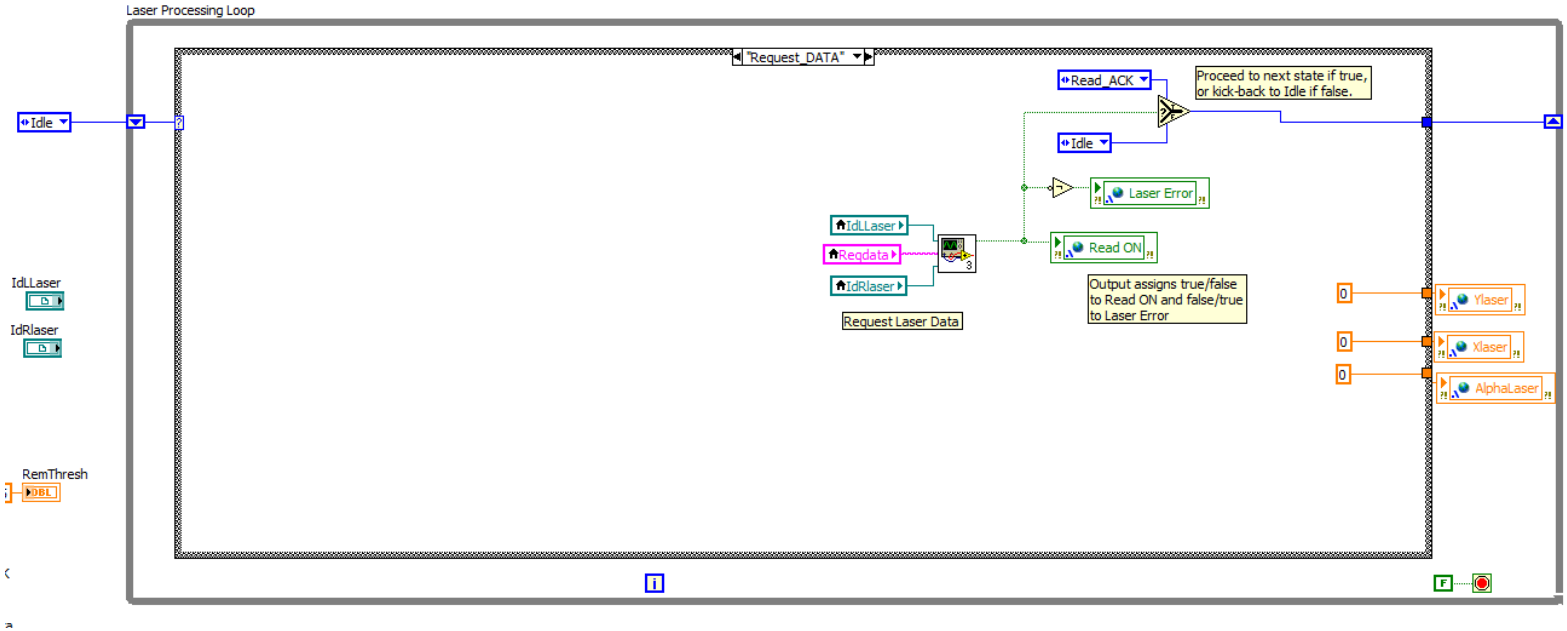

APPENDIX B.12 – LASER PROCESSING ACQUISITION REPLY

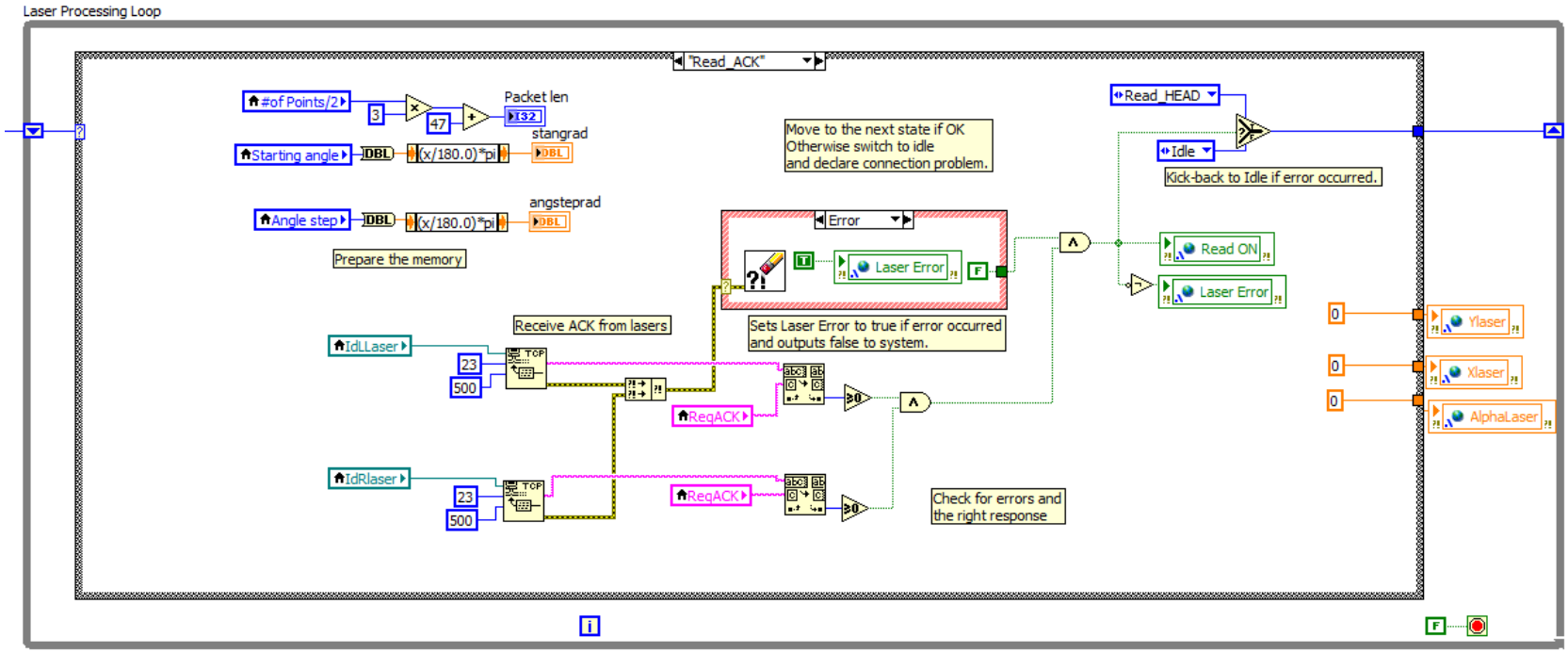

APPENDIX B.13 – LASER PROCESSING READ HEADER

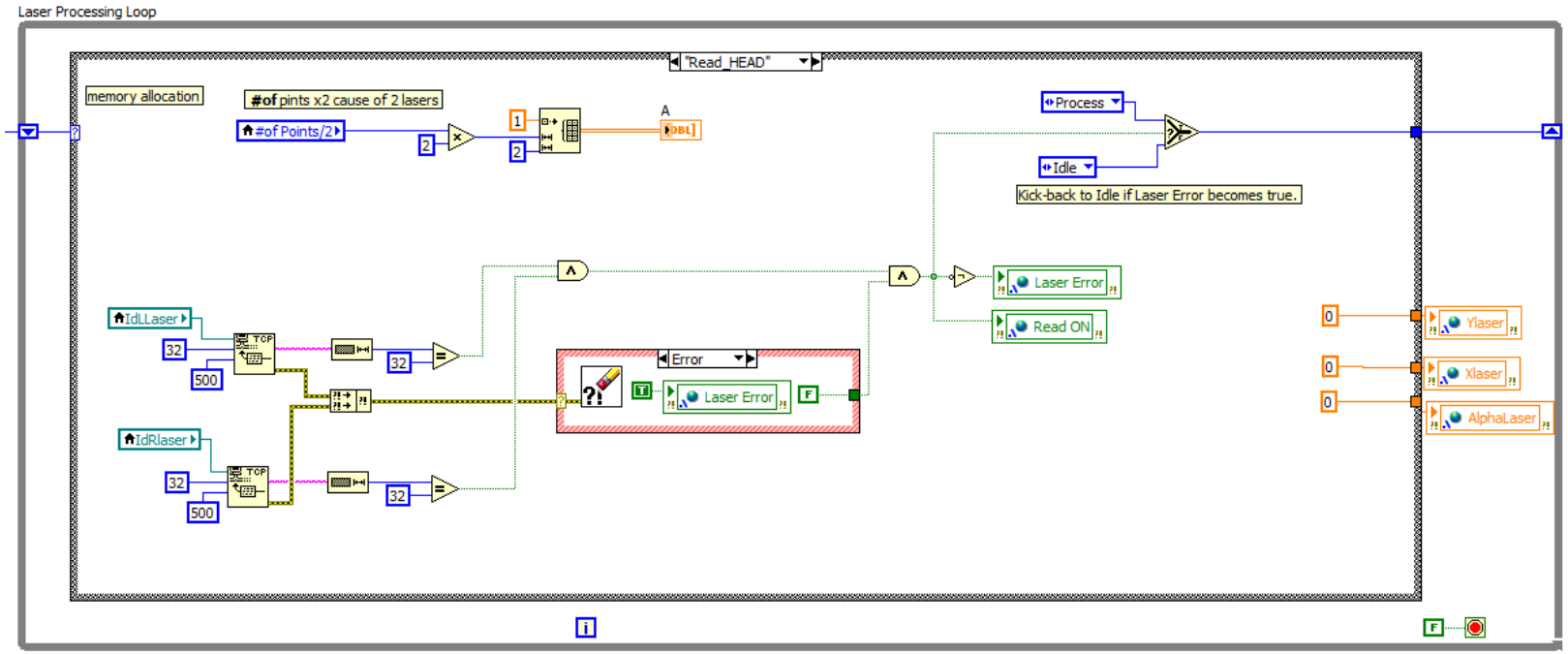

APPENDIX B.14 – LASER PROCESSING PROCESS DATA

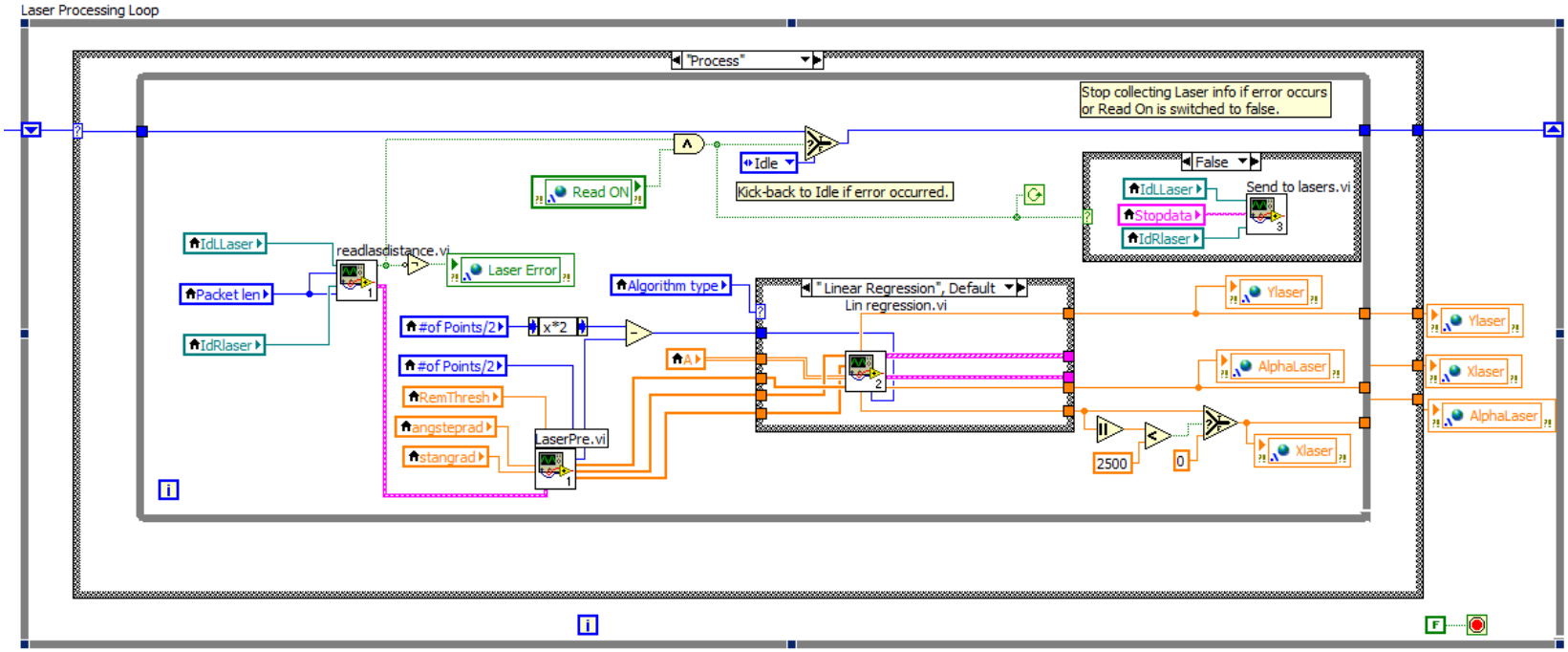

APPENDIX B.15 – CONNECT LASERS

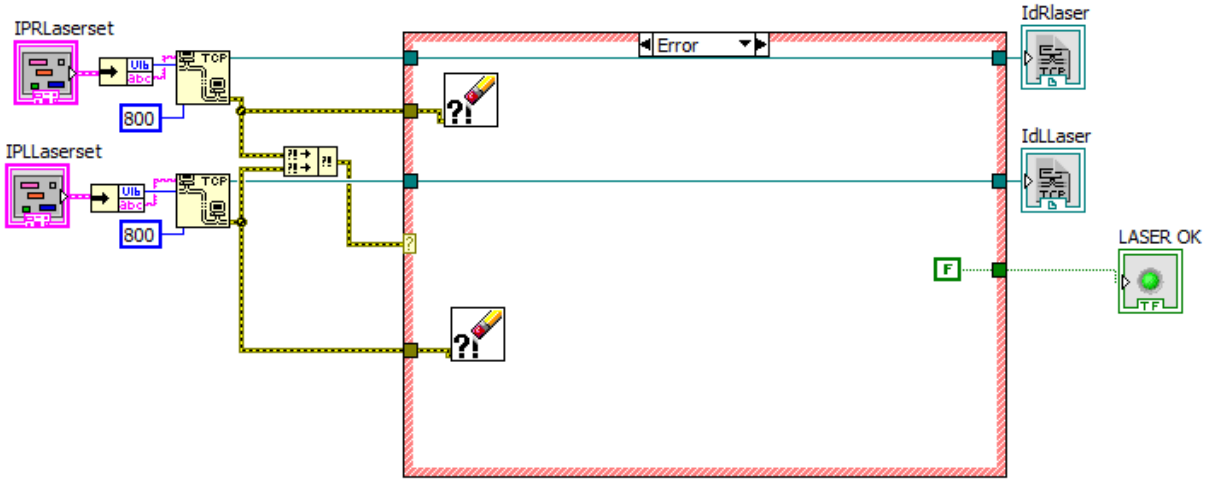

APPENDIX B.16 – SEND TO LASERS

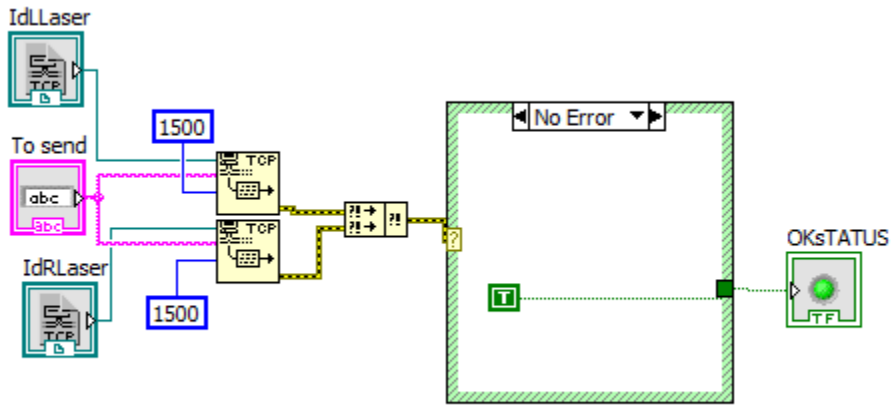

APPENDIX B.17 – READ LASER DISTANCE

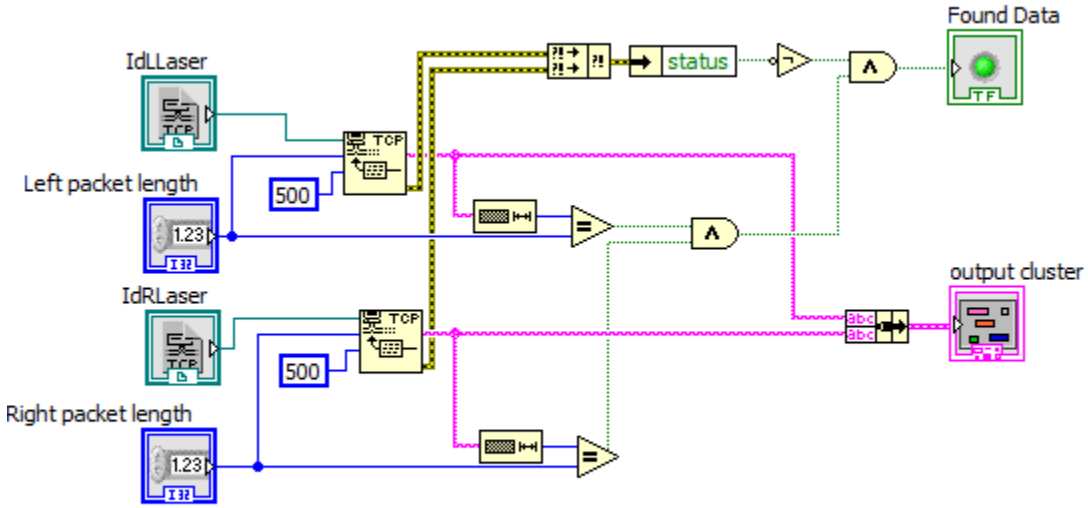

APPENDIX B.18 – PREPROCESS LASER DATA

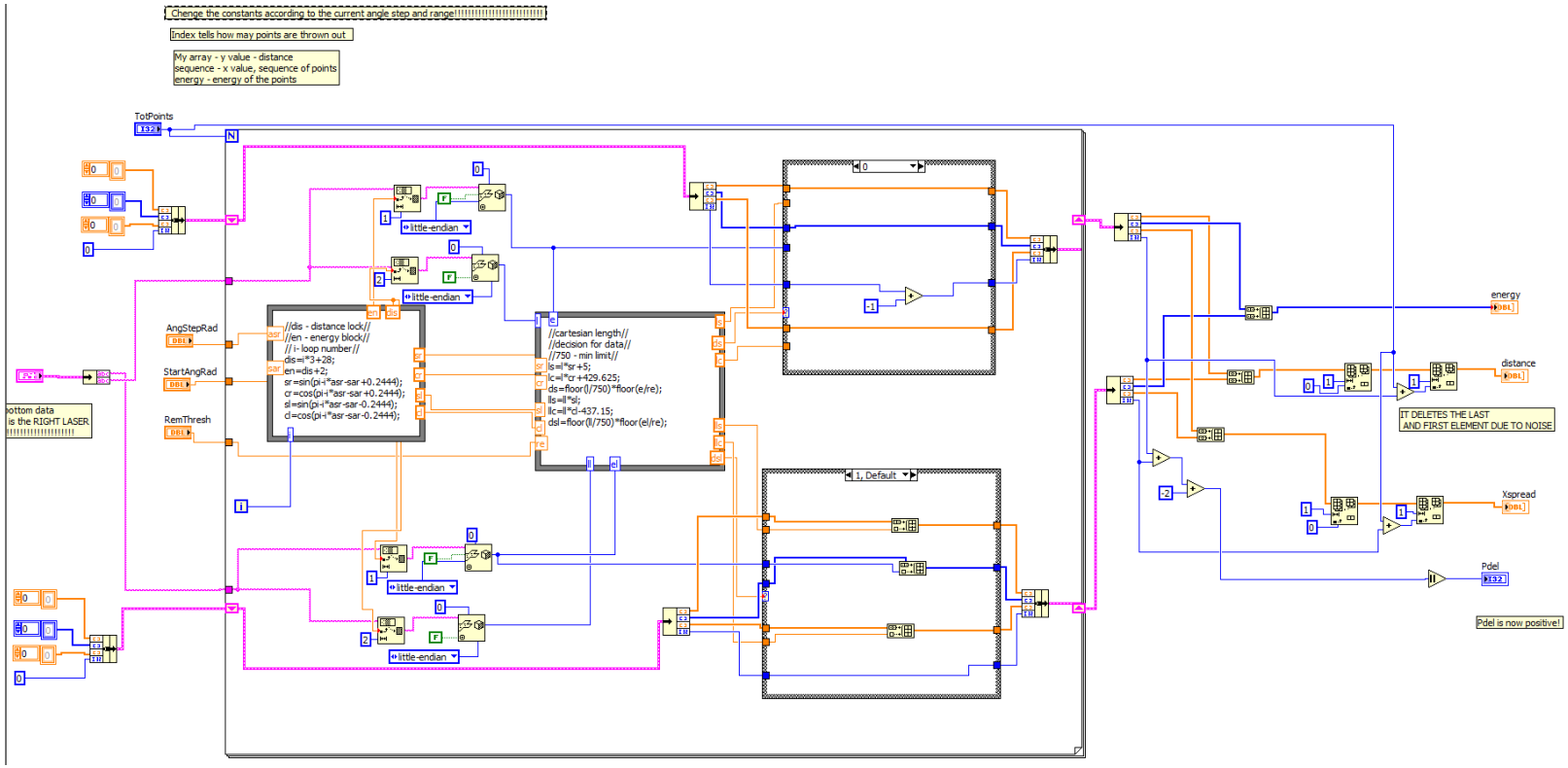

APPENDIX B.19 –LASER POINTS LINEAR REGRESSION

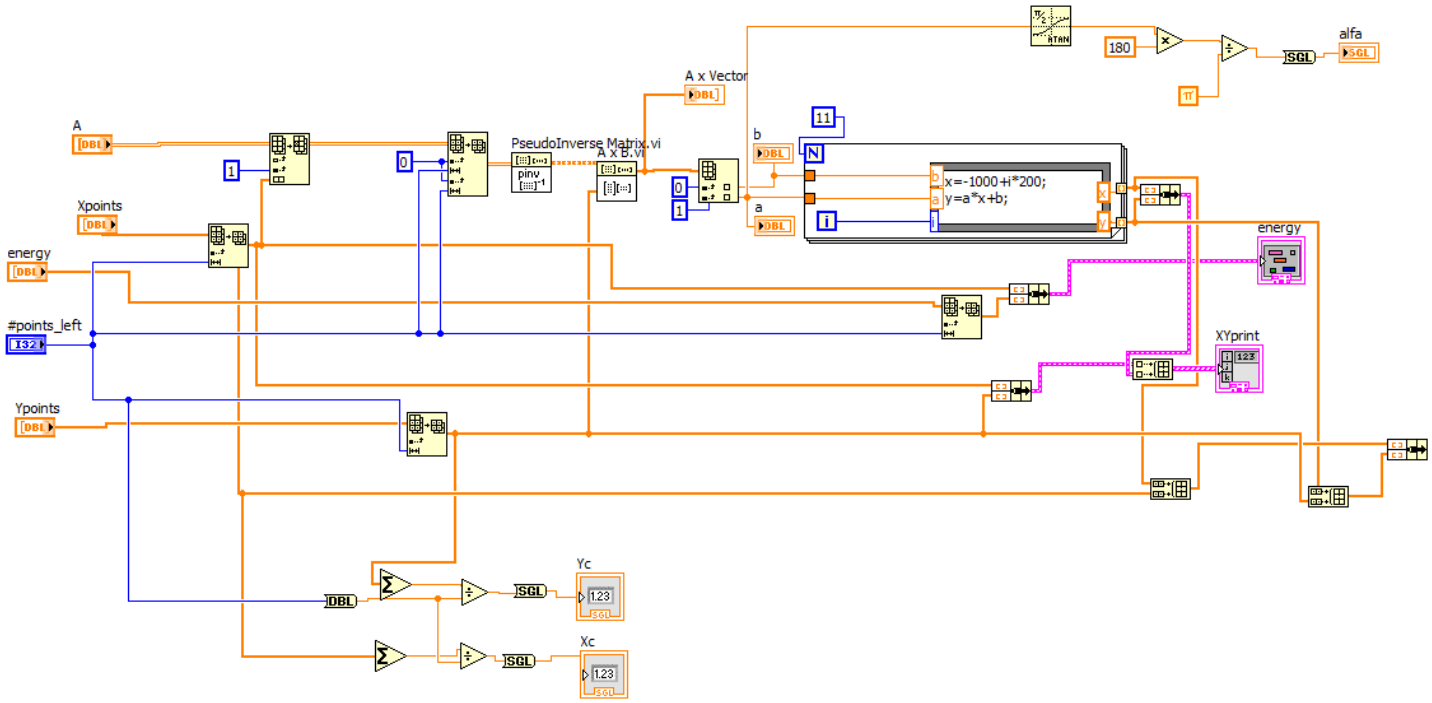

APPENDIX B.20 – READ PCI DAQ CARD

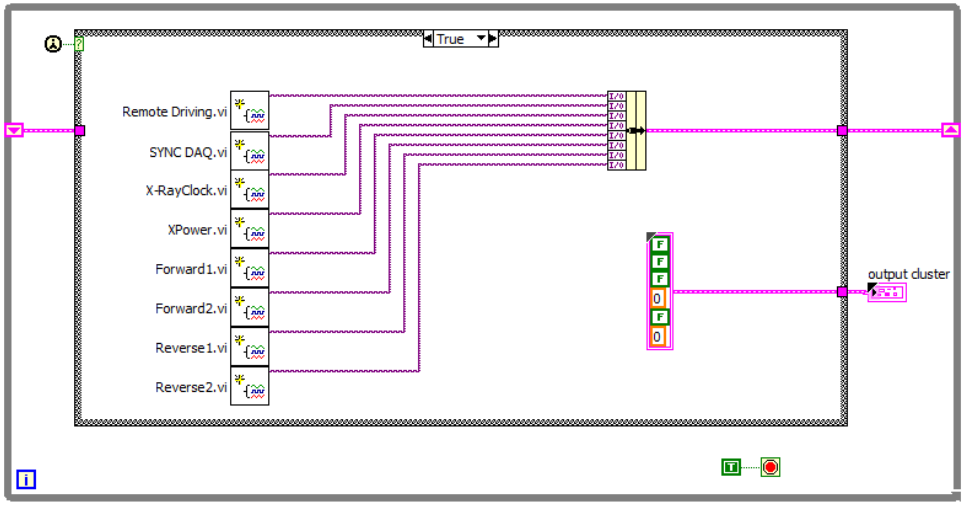

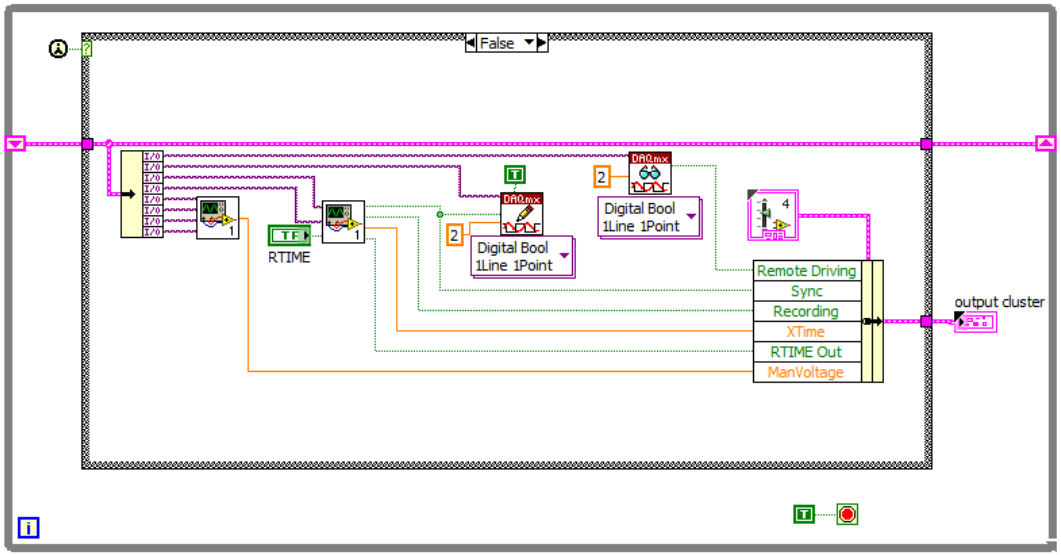

APPENDIX B.21 – WRITE PCI DAQ CARD

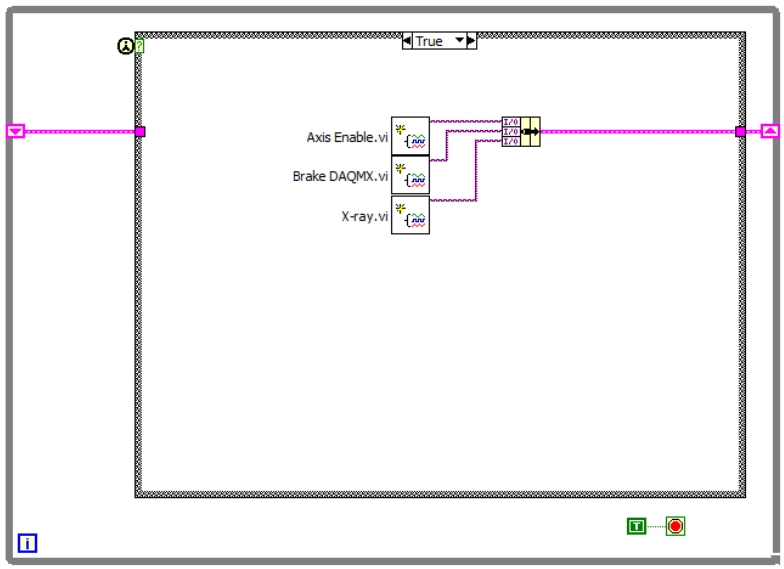

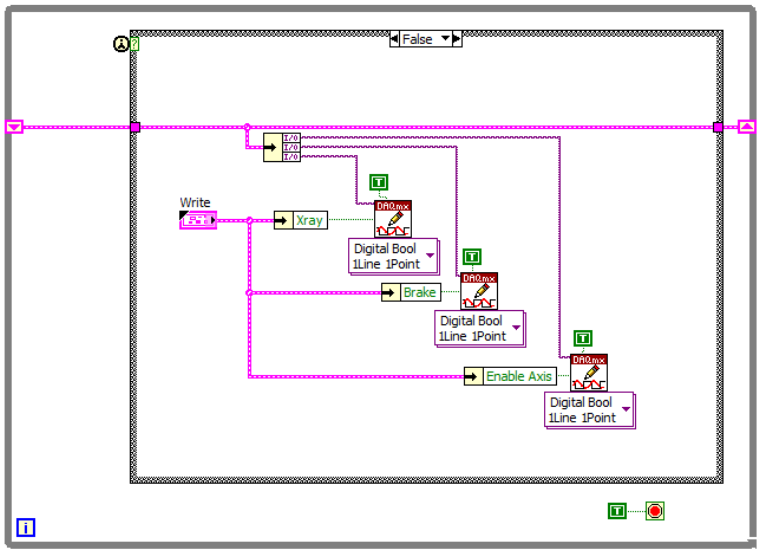

APPENDIX B.22 – CONTROLLER

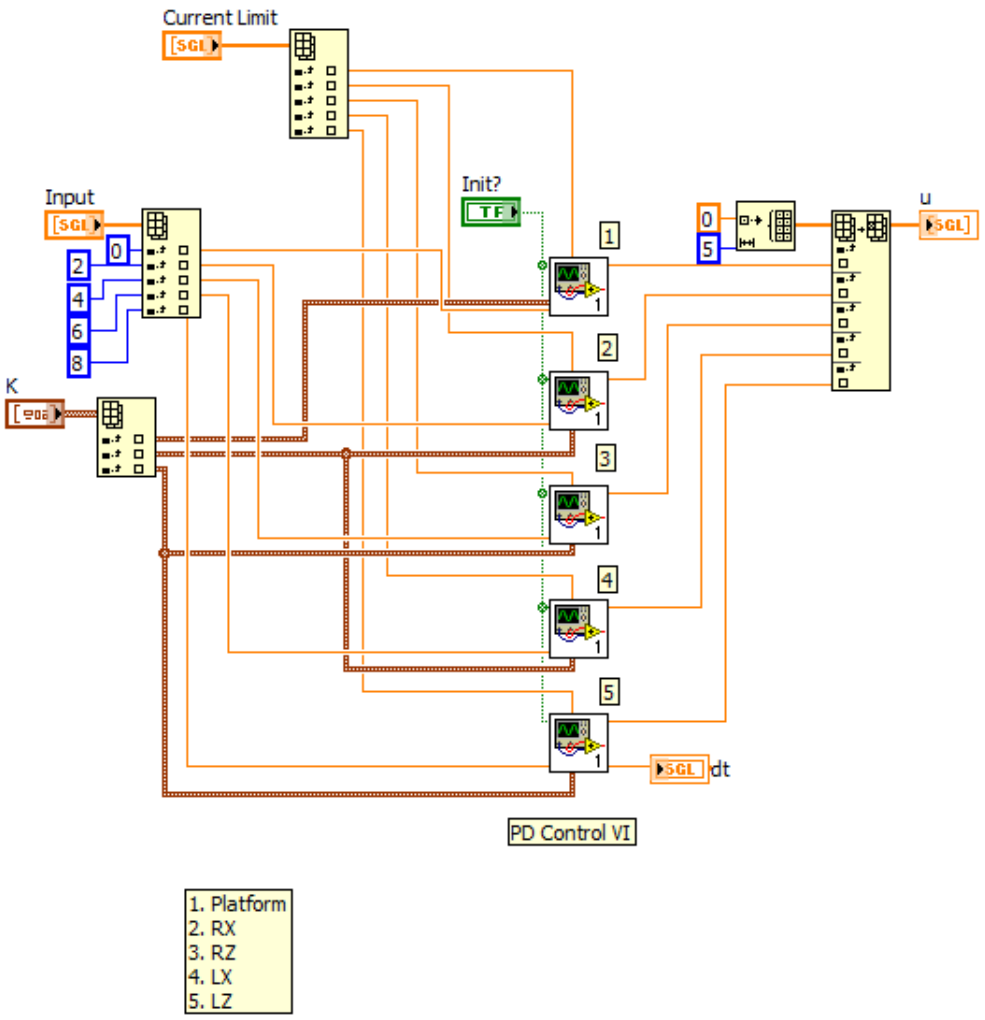

APPENDIX B.23 – PD CONTROL

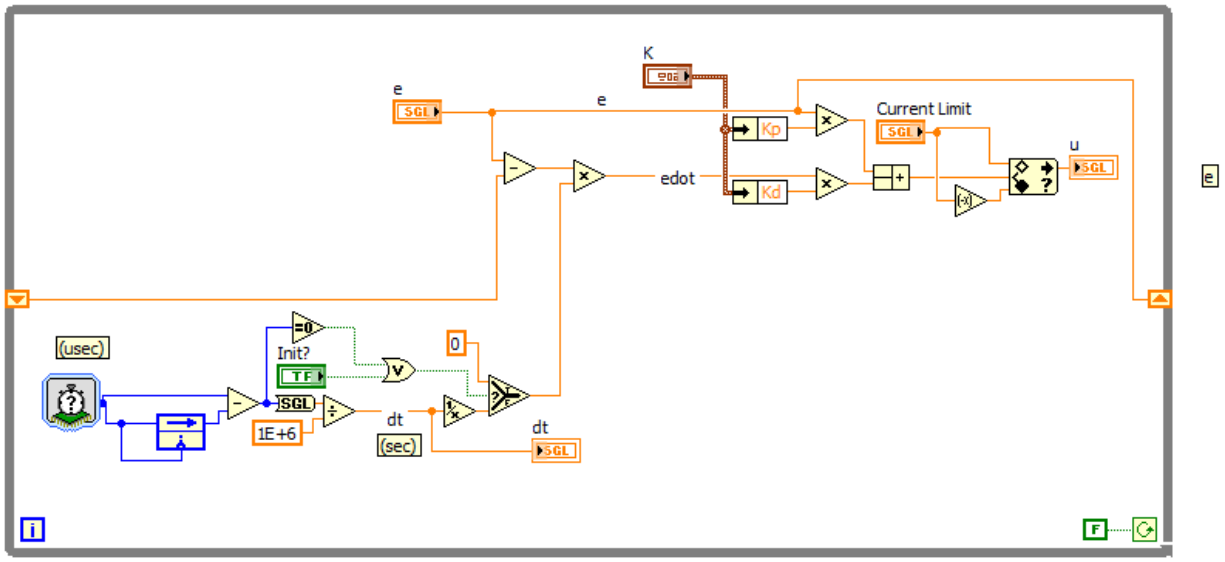

APPENDIX B.24 – INVERTED DECOUPLING

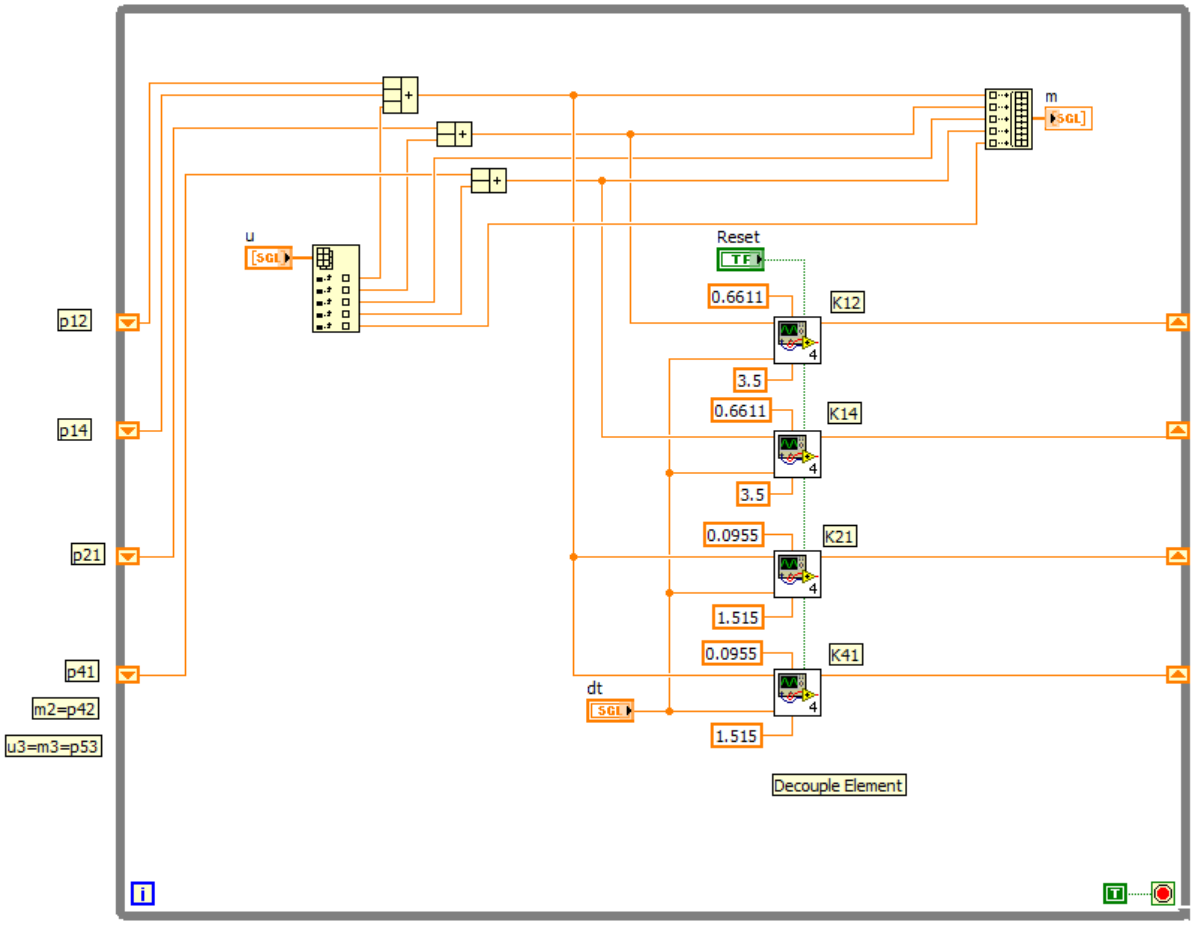

APPENDIX B.25 – SIMPLE DECOUPLING

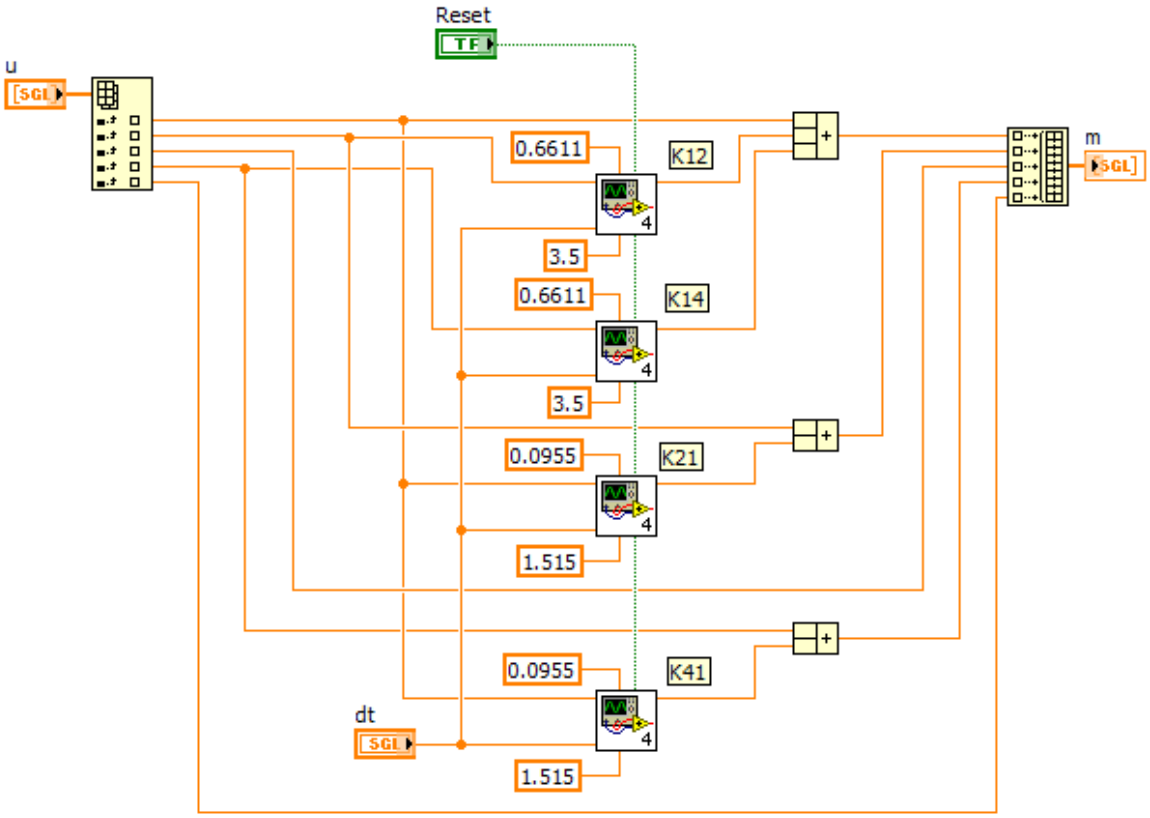

APPENDIX B.26 – DECOUPLING ELEMENT

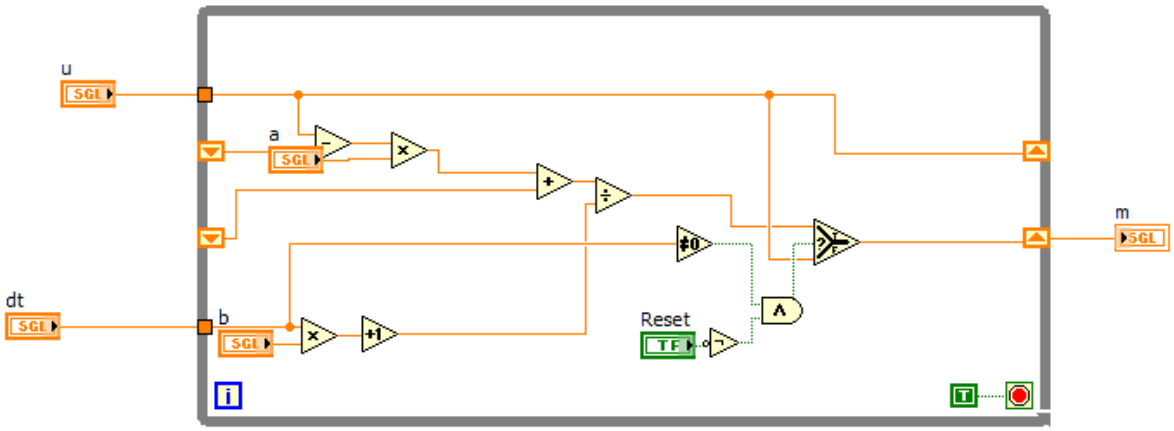

APPENDIX B.27 – CONTROL OUTPUT

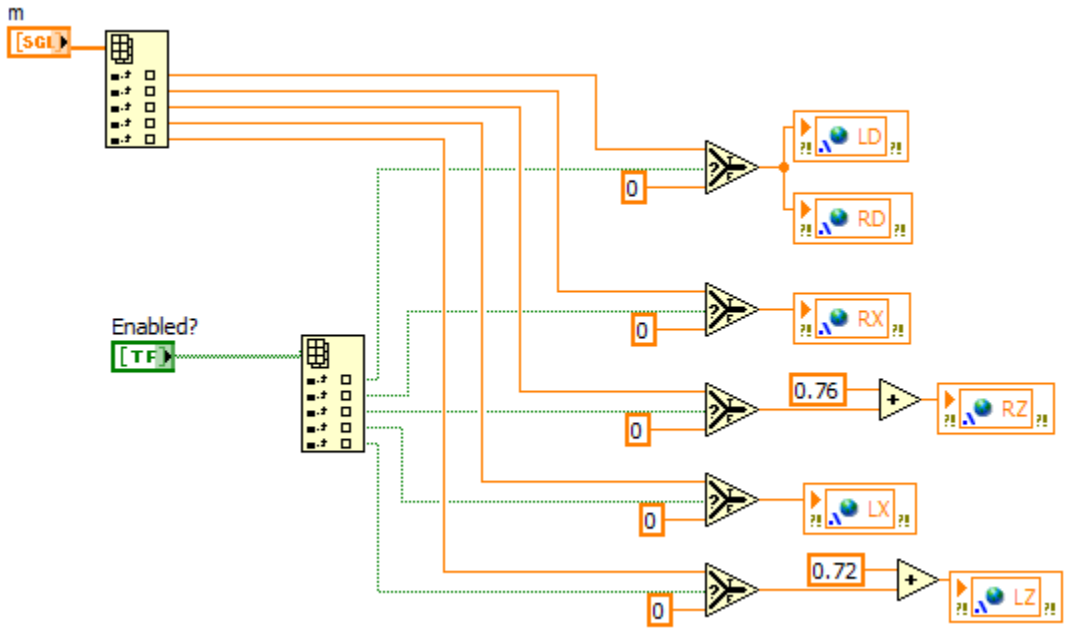

APPENDIX B.28 – STEP PROFILE GENERATOR

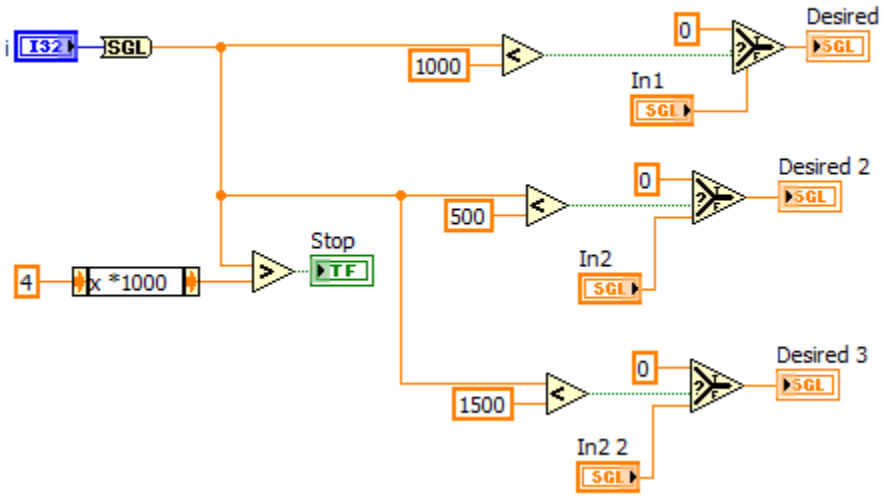

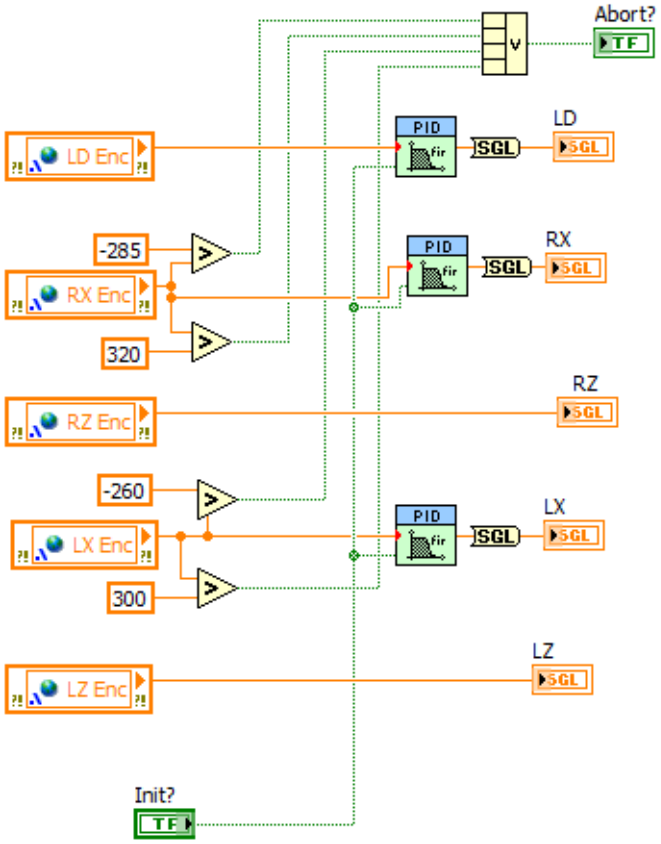

Safety feature aborts simulation if outside the encoder limits.

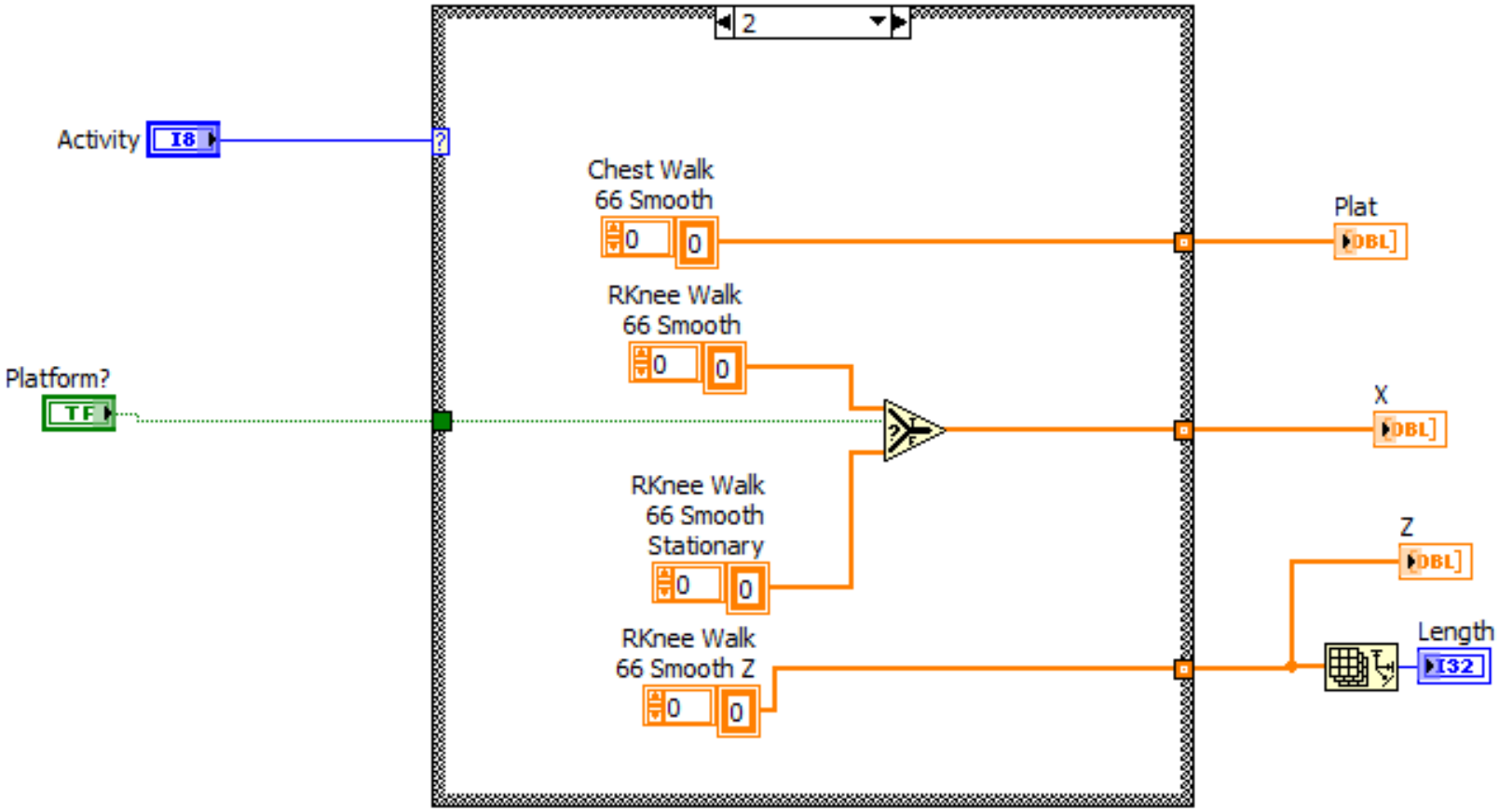
2
Activity
I8
Platform?
TF
Chest Walk
66 Smooth
RKnee Walk
66 Smooth
RKnee Walk
66 Smooth
Stationary
RKnee Walk
66 Smooth Z
Plat
DBL
X
DBL
Z
DBL
Length
I32

APPENDIX B.31 – KINECT SENSOR SIMULATION

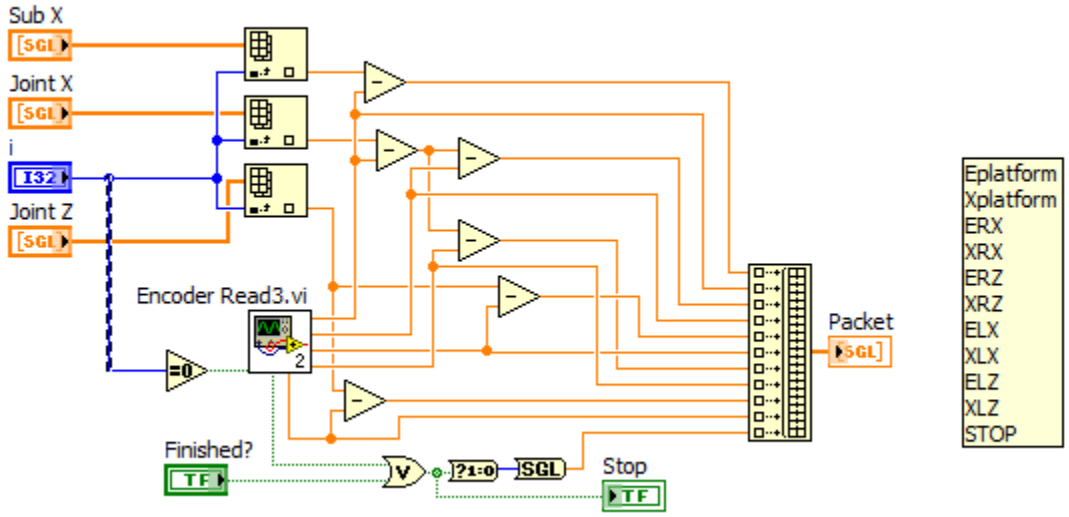

APPENDIX B.32 – VISION PROCESSING

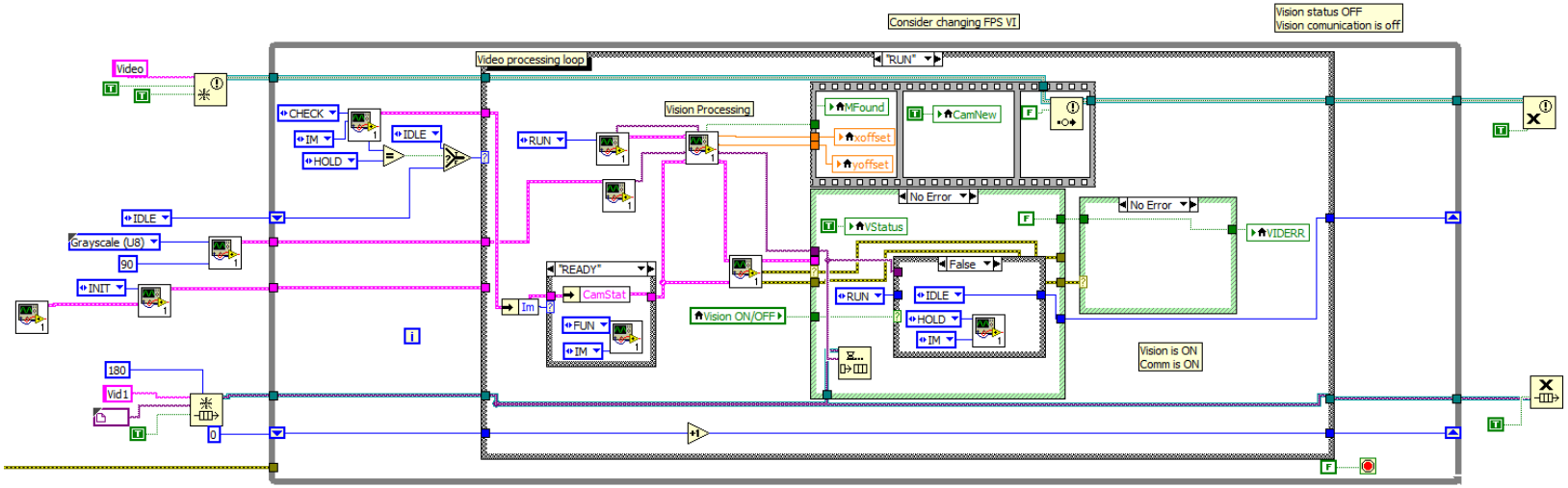

APPENDIX C – MATLAB CODE

```
1   % This file models the Platform (uncoupled)
2
3   % WheelODE is a linear ODE file for OL step inputs.
4   % WheelNL is a ODE file for CL P Controller (with saturation).
5   %   K and m are preset in the file.
6
7   % OLStep1.txt contains open loop input output for different steps
8   % CLPStep1.txt contains CL P Control input-output for 200mm step
9   % CLPDStep1.txt contains CL PD Control input-Output for K and Kd
10  %   combinations.
11  % Walk 76 Med.txt contains Input-Output for tuned PD controller.
12
13  m = 792; %kg
14  % b's and C's are estimated.  In keeping with the notation of the writing,
15  % b = b_p/m_t and C = c_p/m_t.
16  %           C
17  %      -------------
18  %       (s^2) + bs
19
20  % See idnlgreydemo2.m for more information about non-linear estimation.
21
22  %% Import OL Step Data
23
24  OLStep = 'C:\TFS\Dissertation\Modeling\00 Wheels\OLStep1.txt';
25
26  temp = importdata(OLStep);
27  tOL = temp.data(:,1);
28  uOL1 = temp.data(:,3); %4 Volt Step Up Down
29  xOL1 = temp.data(:,8); %4 Volt Step Up Down
30  Ts = 0.001;
31  OL1 = iddata(xOL1,uOL1,Ts);
32  set(OL1, 'OutputName', 'Wheel Position');
33  set(OL1, 'OutputUnit', 'mm');
34  set(OL1, 'Tstart', 0, 'TimeUnit', 's');
35  set(OL1, 'InputName','Amp Input');
36  set(OL1,'InputUnit','Volt');
37  % May be several of these
38
39  %% Create Model for OL
40  ODE        = 'WheelODE';          % File describing the model structure.
```

```
Order       = [1 1 2];              % Model orders [ny nu nx].
Parameters    = {1495;45617};   % Initial parameters.
InitialStates = [0; 0];             % Initial initial states.
ts          = 0;                  % Time-continuous system.
OL = idnlgrey(ODE, Order, Parameters, InitialStates, ts, ...
              'Name', 'OL Wheels');

setinit(OL, 'Minimum', {0 0});   % Initial conditions are zero
setpar(OL, 'Name', {'b'  ...
                    'C'});
setpar(OL, 'Minimum', num2cell(eps(0)*ones(2,1)));   % All parameters > 0!
OL1m = pem(OL1, OL, 'Display', 'Full');
Par = getpar(OL1m);
b_OL1 = Par{1}/m;
C_OL1 = Par{2}/m;

%% Import CL Step Data
CLStep = 'C:\TFS\Dissertation\Modeling\00 Wheels\CLPStep1.txt';

temp = importdata(CLStep);
tCL = temp.data(:,1);
uCL1 = temp.data(:,3);  % Step Input of 200 mm
xCL1 = temp.data(:,8); % K = 1
Ts = 0.001;
CL1 = iddata(xCL1,uCL1,Ts);
set(CL1, 'OutputName', 'Wheel Position');
set(CL1, 'OutputUnit', 'mm');
set(CL1, 'Tstart', 0, 'TimeUnit', 's');
set(CL1, 'InputName','Desired Position');
set(CL1,'InputUnit','mm');
% May be several of these

%% Create Model for CL
ODE         = 'WheelNL';          % File describing the model structure.
Order       = [1 1 2];              % Model orders [ny nu nx].
Parameters    = {978;68069};   % Initial parameters.
InitialStates = [0; 0];             % Initial initial states.
ts          = 0;                  % Time-continuous system.
CL = idnlgrey(ODE, Order, Parameters, InitialStates, ts, ...
              'Name', 'CL Wheels');

setinit(CL, 'Minimum', {0 0});   % Initial conditions are zero
```

```
setpar(CL, 'Name', {'b'  ...
                    'C'});
setpar(CL, 'Minimum', num2cell(eps(0)*ones(2,1)));   % All parameters > 0!
CL1m = pem(CL1, CL, 'Display', 'Full');
Par = getpar(CL1m);
b_CL1 = Par{1}/m;
C_CL1 = Par{2}/m;

%% Import CL PD Step Data
CLPDStep = 'C:\TFS\Dissertation\Modeling\00 Wheels\CLPDStep1.txt';

temp = importdata(CLPDStep);
tCLPD = temp.data(:,1);
uCLPD1 = temp.data(:,3);  % Step Input of 200 mm
xCLPD1 = temp.data(:,22); % K = 0.2, Kd = 0.02
Ts = 0.001;
CLPD1 = iddata(xCLPD1,uCLPD1,Ts);
set(CLPD1, 'OutputName', 'Wheel Position');
set(CLPD1, 'OutputUnit', 'mm');
set(CLPD1, 'Tstart', 0, 'TimeUnit', 's');
set(CLPD1, 'InputName','Desired Position');
set(CLPD1,'InputUnit','mm');
% May be several of these
%% Import Simulations
Sim = 'C:\TFS\Dissertation\Modeling\00 Wheels\Walk 76 Med.txt';

temp = importdata(Sim);
tSim1 = temp.data(:,1);
uSim1 = temp.data(:,3);  %
xSim1 = temp.data(:,4); % K = 0.2 and Kd = 0.02
Tsim = 0.0002;
Sim1 = iddata(xSim1,uSim1,Tsim);
set(Sim1, 'OutputName', 'Wheel Position');
set(Sim1, 'OutputUnit', 'mm');
set(Sim1, 'Tstart', 0, 'TimeUnit', 's');
set(Sim1, 'InputName','Desired Position');
set(Sim1,'InputUnit','mm');
% May be several of these
%% Testing Models

% Simulations using OL
yOL1 = sim(OL1m,OL1); %OL model with OL data
```

```
125
126  % Simulations using CL
127  yCL1 = sim(CL1m,CL1); %CL model with CL data
128
129  %% OL Plots
130  figure (1);
131  subplot(3,1,1)
132  plot(tOL,uOL1,'k')
133  title('Platform OL Step Input')
134  ylabel('Input (V)')
135  set(gca,'xgrid','on')
136  ylim([-4.5 4.5]);
137  xlim([0 12])
138
139  subplot(3,1,2)
140  plot(tOL,xOL1,'b',tOL,yOL1.y,'r')
141  legend('Actual','OL Model')
142  ylabel('Position (mm)')
143  xlabel('Time (seconds)')
144  set(gca,'xgrid','on')
145  xlim([0 12])
146
147  subplot(3,1,3)
148  eOL1 = yOL1.y-xOL1;
149  plot(tOL,eOL1,'m')
150  ylabel('Position (mm)');
151  legend('OL Model error');
152  xlim([0 12])
153
154  %% CL Plots
155  figure (2);
156  subplot(2,1,1)
157  plot(tCL,uCL1,'k',tCL,xCL1,'b',tCL,yCL1.y,'r')
158  title('Platform CL Step Input')
159  ylabel('Position (mm)')
160  set(gca,'xgrid','on')
161  xlabel('Time (seconds)')
162  set(gca,'xgrid','on')
163  legend('Desired','Actual','CL Model')
164  xlim([0 21])
165
166  subplot(2,1,2)
```

```
167  eCL1 = yCL1.y-xCL1;
168  plot(tCL,eCL1,'m')
169  ylabel('Position (mm)');
170  legend('CL Model error');
171  xlim([0 21])
```

APPENDIX C.2 – MOBILE PLATFORM LINEAR DIFFERENTIAL EQUATION

```
1   function [dx, y] = WheelODE(t, x, u, b, C, varargin)
2   %Non-linear Platform approximation:
3   % The equation of motion is:
4   % d^2x/dx^2 = 1/m (-b*dx/dt + C*u)
5
6   m = 792; %kg
7
8   % Output Equation
9   y = x(1);
10
11   %State equations
12   dx = [x(2);            ... % x(2) = velocity
13      1/m*(-b*x(2) + C*u) ... % EOM for OL control
14      ];
```

APPENDIX C.3 – MOBILE PLATFORM NONLINEAR DIFFERENTIAL EQUATION

```
function [dx, y] = WheelNL(t, x, xd, b, C, varargin)
%Non-linear X - Axis approximation:
% The equation of motion is:
% d^2x/dx^2 = 1/m (-b*dx/dt + C*u )


m = 792; %kg
k = 1;
u = k*(xd - x(1));
 % Saturation of input
 if u > 10
    u = 10;
 elseif u < -10
    u = -10;
 end
 % Output Equation
 y = x(1);

 %State equations
 dx = [x(2);          ... % x(2) = velocity
    1/m*(-b*x(2) + C*u) ... % EOM for CL P control
    ];
```

APPENDIX C.4 HORIZONTAL AXIS NON-LINEAR MODELING

```
% This file creates a nonlinear greybox estimate of a step input.
folder = 'C:\TFS\Dissertation\Modeling\00 LX Axis\';
m = 20 + 27; %kg
% The equation of motion is:
% d^2x/dx^2 = 1/m (-ba*dx/dt + C*u - bd*sign(u)*dx/dt)
% ba is the average of 2 damping parameters.
% bd is half of the difference between the 2 damping parameters.
% m is considered known.

% See idnlgreydemo2.m for more information about non-linear estimation.

%% Import Step Data
filename = 'LXOLStep1.txt';
ODE = strcat(folder,filename);
temp = importdata(ODE);
tOL = temp.data(:,1);
uOL1 = temp.data(:,3);
xOL1 = temp.data(:,4);
uOL2 = temp.data(:,5);
xOL2 = temp.data(:,6);
Ts = 0.001;
OL1 = iddata(xOL1,uOL1,Ts);
set(OL1, 'OutputName', 'LX Position');
set(OL1, 'OutputUnit', 'mm');
set(OL1, 'Tstart', 0, 'TimeUnit', 's');
OL2 = iddata(xOL2,uOL2,Ts);
set(OL2, 'OutputName', 'LX Position');
set(OL2, 'OutputUnit', 'mm');
set(OL2, 'Tstart', 0, 'TimeUnit', 's');

%% Create OL Model
opt = greyestOptions('InitialState','zero','DisturbanceModel','none',...
   'Focus','simulation','Display','on');
ODE     = 'LXOL';        % File describing the model structure.
Order       = [1 1 2];           % Model orders [ny nu nx].
Parameters   = {140;90000};  % Initial parameters.
InitialStates = [0; 0];          % Initial initial states.
ts          = 0;                 % Time-continuous system.
OL = idnlgrey(ODE, Order, Parameters, InitialStates, ts, ...
             'Name', 'OL LX Axis');

```

```
setinit(OL, 'Minimum', {0 0});   % Initial conditions are zero
setpar(OL, 'Name', {'b'  ...
                    'C'});
setpar(OL, 'Minimum', num2cell(eps(0)*ones(2,1)));   % All parameters > 0!
OL1m = pem(OL1, OL, 'Display', 'Full');
Par = getpar(OL1m);
b_OL1 = Par{1}/m;
C_OL1 = Par{2}/m;
%% Create OL bidirectional b Model
opt = greyestOptions('InitialState','zero','DisturbanceModel','none',...
   'Focus','simulation','Display','on');
ODE     = 'LXOL2b';         % File describing the model structure.
Order       = [1 1 2];              % Model orders [ny nu nx].
Parameters    = {156;120;90000};   % Initial parameters.
InitialStates = [0; 0];             % Initial initial states.
ts          = 0;                  % Time-continuous system.
OL2b = idnlgrey(ODE, Order, Parameters, InitialStates, ts, ...
              'Name', 'Left Axis Open Loop Bidirectional b');

setinit(OL2b, 'Minimum', {0 0});   % Initial conditions are zero
setpar(OL2b, 'Name', {'b1'  ...
                    'b2'  ...
                    'C'});
setpar(OL2b, 'Minimum', num2cell(eps(0)*ones(3,1)));   % All parameters > 0!
OL2b = pem(OL1, OL2b, 'Display', 'Full');

%% Create Advanced friction model
ODE = 'LXOLaf';
Order = [1 1 2];

Parameters    = {[115; 3300; 21300; ...
                23000; 69; 44;28; 81000]};  % Initial parameters.

InitialStates = [];                 % Initial initial states.
ts          = 0;                  % Time-continuous system.
OLaf = idnlgrey(ODE, Order, Parameters, InitialStates, ts,    ...
              'Name', 'Left Axis Open Loop Advanced Friction', ...
              'InputName', 'Voltage', 'InputUnit', 'Volts',     ...
              'OutputName', 'LX Position', 'OutputUnit', 'mm', ...
              'TimeUnit', 's');
setpar(OLaf, 'Minimum', {zeros(7, 1)});   % All parameters must be >= 0.
OLaf = pem(OL1, OLaf, 'Display', 'Full');
```

```
84
85  %% Testing Models
86  %Open Loop Simple
87  yOL1 = sim(OL1m,OL1);
88  yOL2 = sim(OL1m,OL2);
89  %Open Loop bidirectional
90  yOL2b1 = sim(OL2b,OL1);
91  yOL2b2 = sim(OL2b,OL2);
92  %Open Loop Advanced
93  yOLaf1 = sim(OLaf,OL1);
94  yOLaf2 = sim(OLaf,OL2);
95
96  %% Plotting Results
97  figure (1);
98  subplot(3,2,1)
99  plot(tOL,uOL1,'k')
100  xlim([0,5]);
101  title('LX Step Input')
102  ylabel('Input (Volts)')
103  set(gca,'xgrid','on')
104  ylim([-2 2])
105
106  subplot(3,2,3)
107  plot(tOL,xOL1,'k',tOL,yOL1.y,'m',tOL,yOL2b1.y,'r',tOL,yOLaf1.y,'b')
108  legend('Actual','Simple','Bidirectional','Advanced')
109  ylabel('Position (mm)')
110  xlabel('Time (seconds)')
111  xlim([0,5]);
112  set(gca,'xgrid','on')
113
114  subplot(3,2,5)
115  e1 = yOL1.y-xOL1;
116  e2 = yOL2b1.y-xOL1;
117  e3 = yOLaf1.y-xOL1;
118  plot(tOL,e1,'m',tOL,e2,'r',tOL,e3,'b')
119  legend('Simple','Bidirectional','Advanced')
120  ylabel('Error (mm)')
121  xlim([0,5]);
122  set(gca,'xgrid','on')
123  ylim([-100 150])
124
125  subplot(3,2,2)
```

```
plot(tOL,uOL2,'k')
xlim([0,5]);
title('LX Step Input')
ylabel('Input (Volts)')
set(gca,'xgrid','on')
ylim([-2 2])

subplot(3,2,4)
plot(tOL,xOL2,'k',tOL,yOL2.y,'m',tOL,yOL2b2.y,'r',tOL,yOLaf2.y,'b');
legend('Actual','Simple','Bidirectional','Advanced')
ylabel('Position (mm)')
xlabel('Time (seconds)')
xlim([0,5]);
set(gca,'xgrid','on')

subplot(3,2,6)
e1 = yOL2.y-xOL2;
e2 = yOL2b2.y-xOL2;
e3 = yOLaf2.y-xOL2;
plot(tOL,e1,'m',tOL,e2,'r',tOL,e3,'b')
legend('Simple','Bidirectional','Advanced')
ylabel('Error (mm)')
xlim([0,5]);
set(gca,'xgrid','on')
ylim([-100 150])
```

APPENDIX C.5 HORIZONTAL AXIS NONLINEAR DIFFERENTIAL EQUATION FOR CONSTANT B

```
1   function [dx, y] = LXOL(t, x, u, b, C, varargin)
2   %Non-linear Left X Axis approximation:
3   % The equation of motion is:
4   % d^2x/dx^2 = 1/m (-b*dx/dt + C*u)
5
6   mLX = 20;
7   mLZ = 27;
8
9   m = mLX + mLZ; %Kg
10
11   % Output Equation
12   y = x(1);
13
14   %State equations
15   dx = [x(2);           ... % x(2) = velocity
16      1/m*(-b*x(2) + C*u) ... % EOM for OL control
17      ];
```

APPENDIX C.6 HORIZONTAL AXIS NONLINEAR DIFFERENTIAL EQUATION FOR BIDIRECTIONAL B

```
1   function [dx, y] = LXOL2b(t, x, u, b1, b2, C, varargin)
2   %Non-linear X - Axis approximation:
3   % The equation of motion is:
4   % d^2x/dx^2 = 1/m (-ba*dx/dt + C*u - bd*sign(u)*dx/dt)
5   % ba is the average of 2 damping parameters.
6   m = 20 + 27; % kg
7   ba = (b1 + b2)/2;
8   bd = (b2 - b1)/2;
9
10   % Output equation.
11   y = x(1);                              % Position
12
13   % State equations.
14   dx = [x(2);           ... % x(2) = velocity.
15         1/m*(-ba*x(2) - bd*x(2)*sign(u) + C*u)   ... % Non-linear model.
16        ];
```

APPENDIX C.7 HORIZONTAL AXIS NONLINEAR DIFFERENTIAL EQUATION FOR ADVANCED B

```
function [dx, y] = LXOLaf(t, x, u, g, varargin)
%FRICTION_M  Nonlinear friction model with Stribeck, Coulomb and viscous
%   dissipation effects.

%   See http://www.mathworks.com/products/demos/shipping/ident/idnlgreydemo5.html
m = 20 + 27; %kg

% Friction Force equation.
f =  g(1)*(tanh(g(2)*x(2))-tanh(g(3)*x(2))) ...% Stribeck effect.
    + g(4)*tanh(g(5)*x(2))                ... % Coulomb effect.
    + g(6)*x(2) + g(7)*x(2)*sign(u);          % Viscous dissipation term.

% State Equations
dx = [x(2);...
    1/m*(g(8)*u - f)...
    ];

% Output
y = x(1);
```

APPENDIX C.8 VERTICAL AXIS MODEL

```
% This file creates a nonlinear greybox estimate of a step input.
folder = 'C:\TFS\Dissertation\Modeling\00 LZ Axis\';
m = 27; %kg

% The equation of motion is:
% d^2x/dx^2 = 1/m (-ba*dx/dt + C*u - bd*sign(u)*dx/dt)
% ba is the average of 2 damping parameters.
% bd is half of the difference between the 2 damping parameters.
% m is considered known.

 % See idnlgreydemo2.m for more information about non-linear estimation.

 %% Import Step Data
 filename = 'LZOLStep1.xlsx';
 ODE = strcat(folder,filename);
 temp = importdata(ODE);
 tOL = temp.data(1:5008,1);
 uOL1 = temp.data(1:5008,3);
 xOL1 = temp.data(1:5008,5);
 uOL2 = temp.data(1:5008,7);
 xOL2 = temp.data(1:5008,9);
 Ts = 0.001;
 OL1 = iddata(xOL1,uOL1,Ts);
 set(OL1, 'OutputName', 'LZ Position');
 set(OL1, 'OutputUnit', 'mm');
 set(OL1, 'Tstart', 0, 'TimeUnit', 's');
 OL2 = iddata(xOL2,uOL2,Ts);
 set(OL2, 'OutputName', 'LZ Position');
 set(OL2, 'OutputUnit', 'mm');
 set(OL2, 'Tstart', 0, 'TimeUnit', 's');

 %% Create OL Model
 opt = greyestOptions('InitialState','zero','DisturbanceModel','none',...
    'Focus','simulation','Display','on');
 ODE     = 'LZOL';        % File describing the model structure.
 Order       = [1 1 2];           % Model orders [ny nu nx].
 Parameters   = {760;82148};   % Initial parameters.
 InitialStates = [0; 0];           % Initial initial states.
 ts         = 0;                % Time-continuous system.
 OL = idnlgrey(ODE, Order, Parameters, InitialStates, ts, ...
```

```
41              'Name', 'OL LZ Axis');
42
43  setinit(OL, 'Minimum', {0 0});   % Initial conditions are zero
44  setpar(OL, 'Name', {'b'  ...
45                  'C'});
46  setpar(OL, 'Minimum', num2cell(eps(0)*ones(2,1)));   % All parameters > 0!
47  OL1m = pem(OL1, OL, 'Display', 'Full');
48  Par = getpar(OL1m);
49  b_OL1 = Par{1}/m;
50  C_OL1 = Par{2}/m;
51
52  %% Testing Models
53  yOL1 = sim(OL1m,OL1);
54  yOL2 = sim(OL1m,OL2);
55
56  %% Plotting Results
57  figure (1);
58  subplot(3,2,1)
59  plot(tOL,uOL1,'k')
60  xlim([0,5]);
61  title('LZ Step Input')
62  ylabel('Input (Volts)')
63  set(gca,'xgrid','on')
64  ylim([-2 2])
65
66  subplot(3,2,3)
67  plot(tOL,xOL1,'k',tOL,yOL1.y,'m')
68  legend('Actual','Model')
69  ylabel('Position (mm)')
70  xlabel('Time (seconds)')
71  xlim([0,5]);
72  set(gca,'xgrid','on')
73
74  subplot(3,2,5)
75  e1 = yOL1.y-xOL1;
76
77  plot(tOL,e1,'m')
78  legend('Simple')
79  ylabel('Error (mm)')
80  xlim([0,5]);
81  set(gca,'xgrid','on')
82  ylim([-10 10])
```

```
83
84   subplot(3,2,2)
85   plot(tOL,uOL2,'k')
86   xlim([0,5]);
87   title('LZ Step Input')
88   ylabel('Input (Volts)')
89   set(gca,'xgrid','on')
90   ylim([-2 2])
91
92   subplot(3,2,4)
93   plot(tOL,xOL2,'k',tOL,yOL2.y,'m')
94   legend('Actual','Model')
95   ylabel('Position (mm)')
96   xlabel('Time (seconds)')
97   xlim([0,5]);
98   set(gca,'xgrid','on')
99
100  subplot(3,2,6)
101  e1 = yOL2.y-xOL2;
102
103  plot(tOL,e1,'m')
104  ylabel('Error (mm)')
105  xlim([0,5]);
106  set(gca,'xgrid','on')
107  ylim([-10 10])
```

APPENDIX C.9 VERTICAL AXIS NONLINEAR DIFFERENTIAL EQUATION

```
1   function [dx, y] = LZOL(t, x, u, b, C, varargin)
2   %Non-linear Left X Axis approximation:
3   % The equation of motion is:
4   % d^2x/dx^2 = 1/m (-b*dx/dt + C*u)
5
6   mLZ = 27;
7
8   m = mLZ; %Kg
9
10   % Output Equation
11   y = x(1);
12
13   %State equations
14   dx = [x(2);           ... % x(2) = velocity
15      1/m*(-b*x(2) + C*u) ... % EOM for OL control
16      ];
```

APPENDIX D - SIMULINK MODELS

APPENDIX D.1 PLATFORM AND AXIS COUPLED

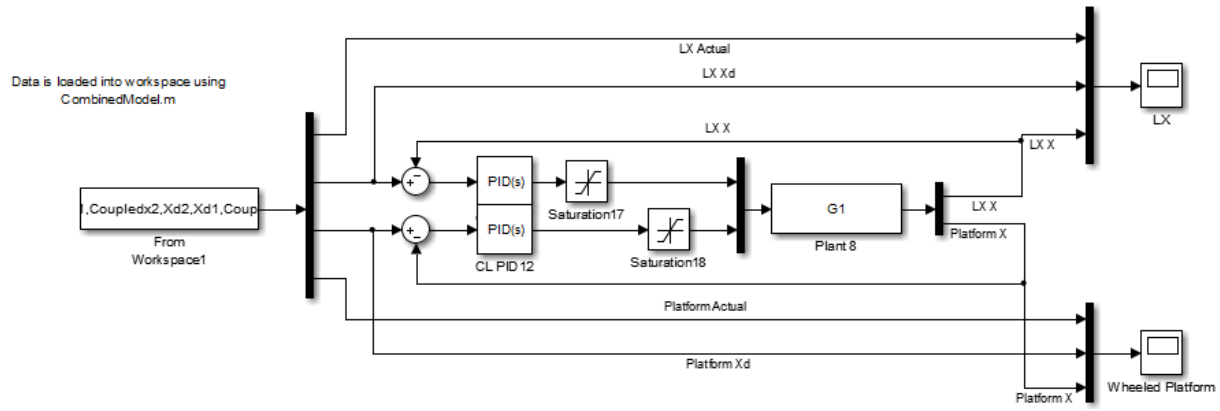

APPENDIX D.2 COUPLED COMPARISONS

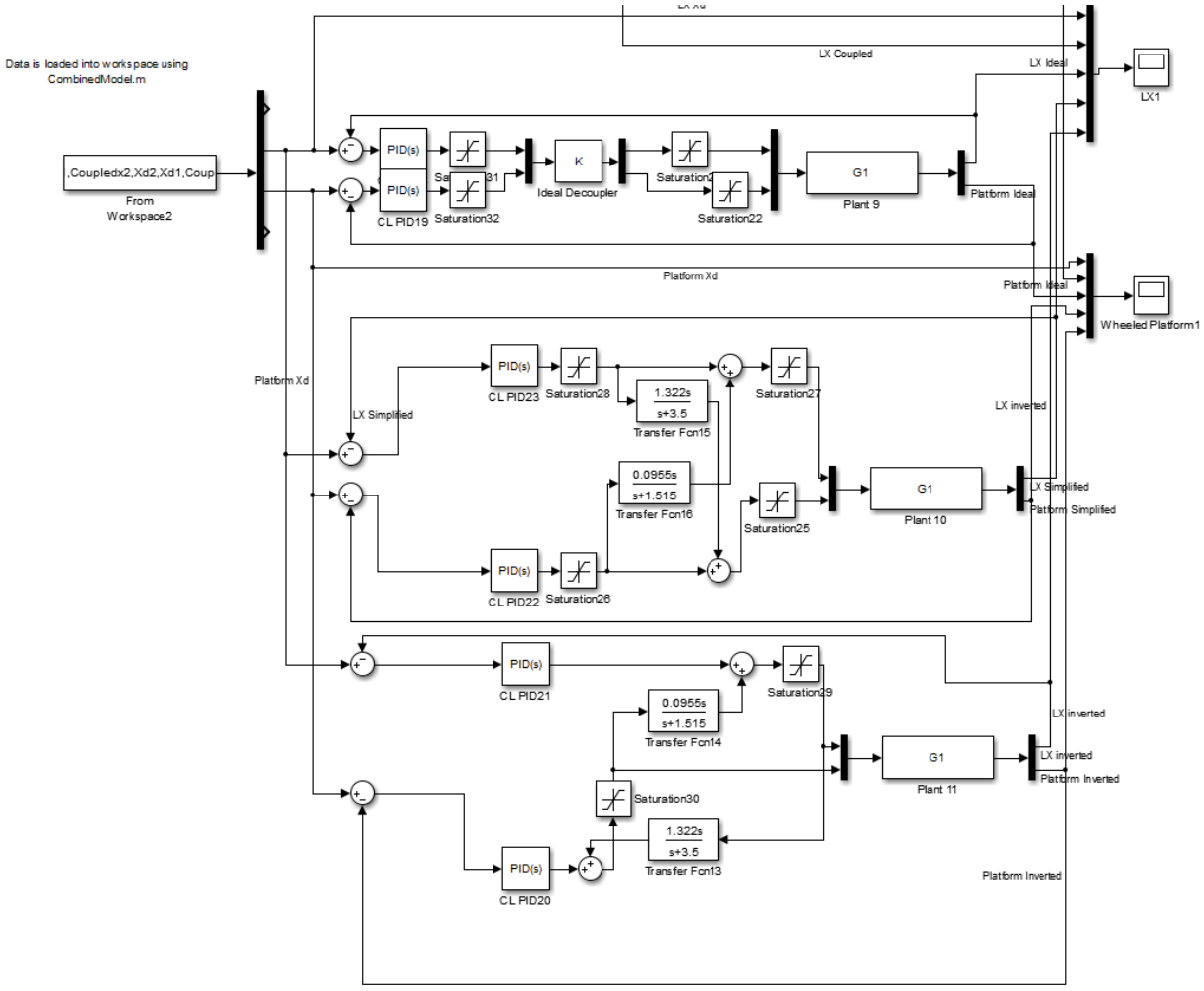

APPENDIX E. INTERNAL REVIEW BOARD

APPENDIX E.1 FORM A

Certification for Exemption from IRB Review for Research Involving Human Subjects

---

A. PRINCIPAL INVESTIGATOR(s) and/or CO-PI(s):
Matthew A. Young

William R. Hamel

B. DEPARTMENT:
Mechanical, Aerospace and Biomedical Engineering

C. COMPLETE MAILING ADDRESS AND PHONE NUMBER OF PI(s) and CO-PI(s):
Matthew A. Young

3204 Lagrange Dr.

Maryville, TN 37804

(865) 309 4702

Dr. William R. Hamel

403 Dougherty Engineering Building

1512 Middle Drive

Knoxville, TN 37996

(865) 974 6588

D. TITLE OF PROJECT:
Modeling, Analysis, and Control of a Mobile Robot for In Vivo Fluoroscopy of Human Joints during Natural Movements

E. EXTERNAL FUNDING AGENCY AND ID NUMBER:
N/A

F. GRANT SUBMISSION DEADLINE:
N/A

G. STARTING DATE :
Upon IRB approval

H. ESTIMATED COMPLETION DATE :
August, 2013

I. RESEARCH PROJECT

1. Objective(s) of Project:
The purpose of this research is to evaluate the control schemes used to control a mobile robot. Human subjects will be recorded doing six activities using a Microsoft Kinect 3D video camera. This camera saves a collection of 20 data locations in 3D space at a frame rate of about 30 frames per second. These data points will be used to drive a virtual robot using various control schemes.

2. Subjects:
No more than fifteen subjects will be selected from the general population using the following criteria:

- Subjects must be between the ages of 18-85 years old and not pregnant. **Minors are excluded from this study as their inclusion would not add information to the study.**
- Subjects must be between 140 cm. and 193 cm. tall.
- Subjects must be able to walk without aid.
- Subjects must be able to fully squat without pain or assistance.
  The exclusionary criteria above are made to ensure that the subjects can perform the activities required by the study with minimal risk.
- Subjects will be chosen independent of gender.

Data is desired for a broad range of human subjects, so individuals with heights near the 95th percentile of adult males, 5th percentile of adult females and cumulative average, as described by the Center for Disease Control, will be preferred**. Recruitment for the study will be strictly by word of mouth.** The data collection will last around thirty minutes. No children or pregnant women will be used in this study.

3. Methods or Procedures:
After an individual has been selected for participation, the researcher will collect data using the following procedure.

A. The researcher will describe the research to the subject. A short video (around thirty seconds) of the robot will be shown to introduce the subject to the research.
B. The six activities will be described and demonstrated for the subject:
    a. Chair rise – The subject will begin by sitting in a chair with her/his knees bent and feet on the floor. The knee in question will start in view of the TFS scope while the opposite leg is position such that it will not obscure the view of the knee in question.
    b. Deep Knee Bend – The subject will begin standing at rest, with the foot from the side in question slightly ahead of the opposite foot. The subject will then slowly squat down until comfortable maximum flexion is achieved.
    c. Normal Gait - The subject will begin standing at rest with her/his feet together. The subject will take a lead step with her/his knee in question and proceed to walk at a comfortable pace for approximately 10 paces, or until instructed to stop.
    d. Stair Ascend – The subject will begin standing at rest with his/her feet together in front of a small set of portable stairs. The subject will then begin to ascend the stair case beginning with her/his lead foot, making sure that with each step, the foot is landing one step above the other.

e. Stair Descend – The subject will begin at the top of the stairs. The subject will begin standing at rest with her/his feet together. The subject will then begin to descend the stair case beginning with her/his lead foot, making sure that with each step, the foot is landing one step below the other.
f. Curvilinear walking – The subject will begin standing at rest with her/his feet together. When instructed, the subject will follow a marked path for about 10 paces, or until instructed to stop.

C. The subject will be encouraged to ask any questions and to practice all the activities. The subject will be asked to sign an informed consent form. The informed consent forms will be stored in a folder in a locked room. Only the principal investigator will have access to this folder. The data collected will be completely anonymous and stored by height of the subject on a laptop or personal computer. The researcher will inform all subjects that they do not have to participate and are free to leave if they wish. Participation is entirely voluntary. Subjects must be willing to sign the **Informed Consent form** in order to participate in the study.
D. The Kinect camera will be turned on and calibrated.
E. The researcher will begin recording with the camera and ask the subject to perform the activities.
   a. The researcher might record all activities as one video, or each activity separately.
   b. **During the recording, only the 3D location of each data point is stored. The subject cannot be identified from these data points.**
F. The subject will be asked to perform each activity at least twice: one time leading with the right foot and one time leading with the left foot.
G. The data will be reviewed, and additional trials will be taken if necessary. **There is no more than minimal risk for performing the activities in this study.**

4. CATEGORY(s) FOR EXEMPT RESEARCH PER 45 CFR 46:

This research is exempt per paragraph (2). Research involving the use of educational tests (cognitive, diagnostic, aptitude, achievement), survey procedures, interview procedures or observation of public behavior, **unless**: (i) information obtained is recorded in such a manner that human subjects can be identified, directly or through identifiers linked to the subjects; **and** (ii) any disclosure of the human subjects' responses outside the research could reasonably place the subjects at risk of criminal or civil liability or be damaging to the subjects' financial standing, employability, or reputation.

J. **CERTIFICATION:** The research described herein is in compliance with 45 CFR 46.101(b) and presents subjects with no more than minimal risk as defined by applicable regulations.

Principal Investigator:

_____ _____ _____

e Signature Date Nam

Student Advisor:

_____ _____ _____

e Signature Date Nam

Department Review Committee Chair:

_____ _____ _____

Signature Date Name

APPROVED:

Department Head:

_____ _____ _____

Signature Date Name

COPY OF THIS COMPLETED FORM MUST BE SENT TO COMPLIANCE OFFICE IMMEDIATELY UPON COMPLETION.

Rev. 01/2005

APPENDIX E.2 INFORMED CONSENT

"Modeling, Analysis and Control of a Mobile Robot for In Vivo Fluoroscopy of Human Joints during Natural Movements"

Principal Investigator: Matthew A. Young

Co-Principal Investigator: Dr. W. R. Hamel

INTRODUCTION

The purpose of this statement is to tell you about the procedures to be followed, the possible risks and discomforts involved, and possible benefits of participating in this study. Please read this form carefully. When you finish reading this form, a representative with ample experience with this research project will answer any questions or address any concerns you may have about the study. If you decide to take part in the study, please put your initials on each page, and sign the form on the last page. If you decide not to take part in the study, there will be no penalty or loss of benefits to you. Participation is entirely voluntary.

You are being asked to take part in a research study because you volunteered to participate.

PURPOSE

The researchers in this study believe that artificial joints can be improved by making them more like normal joints. To further explore this potential, a new device has been designed and created to take accurate fluoroscopic images during routine activities. In this study, the researchers will compare the images gathered from this device from images from past studies to determine the diagnostic merits of the new device.

PROCEDURES

You will be one of up to 15 participants asked to perform any and/or all of six activities under 3D video surveillance. These activities will be: (1) chair rise, (2) deep knee bend, (3) level walking (gait), (4) stair ascent, (5) stair descent, and (6) curvilinear walking. While performing these activities, be sure to stop the motion at the first sign of pain. As you move, the camera will follow your movements and record 20 point locations of your joints at 30 frames per second.

The entire process may take up to 30 minutes, including answering any questions you might have.

POTENTIAL BENEFITS

Participation in this research study will lead to the following personal benefits:
(1) The opportunity to participate in state-of-the-art biorobotics research.

POTENTIAL RISKS

Participation in this research study will not expose you to more than minimal risk. As with all studies, however, this study may involve risks that are currently unforeseeable.

CONFIDENTIALITY Your 3D video data will be stored in a format to fully conceal your identity. The consent form you sign will be reviewed by the researchers, and may be inspected by the Compliance Section of the Office of Research at the University of Tennessee. The results of this research project may be presented at meetings or in publications. The video data may be used in future studies, but will not be linked to your identity. Your identity will not be disclosed in any presentation or publication.

Your complete Informed Consent form will be stored in room M007 Dougherty Engineering Building at the University of Tennessee at Knoxville. These will be accessible by only

approved personnel. They will be kept indefinitely for the possibility of future use in research or publications.
Personnel who will have access to your information include:

- Dr. William R. Hamel, PI (UT Professor, Mechanical, Aerospace and Biomedical Engineering)
- Matthew A. Young, PI (UT PhD Candidate, Mechanical, Aerospace and Biomedical Engineering)

COMPENSATION IN CASE OF INJURY

The University of Tennessee does not "automatically" reimburse participants for medical claims. If physical injury is suffered in the course of research, please notify the investigator in charge: William R. Hamel, PhD, University of Tennessee at Knoxville, (865) 974-6588.

WITHDRAWAL FROM THE STUDY

You may quit the study any time without penalty. If you choose to be removed from the study after participating, the data collected from you as a participant will be destroyed. A copy of the request will be attached to your consent form and placed in a separate secured file for IRB review. To withdraw from the study you may submit your request in a letter to Dr. Hamel. The letter should go to:

William R. Hamel

1512 Middlebrook Drive

403 Dougherty Engineering Building

Knoxville, TN 37996

CONTACTS

If you have questions at any time about the study or the procedures, (or you experience adverse effects as a result of participating in this study,) you may contact the researcher, William R. Hamel, 403 Dougherty Engineering Building, University of Tennessee, Knoxville, TN 37996. If you have questions about your rights as a participant, contact the Compliance Section of the University of Tennessee's Office of Research at (865) 974-3466.

CONSENT SIGNATURES

I have read the consent form. The procedures have been explained to me and I was told which of them are experimental. I was told about the risks involved, as well as the possible benefits in this research. I voluntarily agree to participate in this study. I am free to withdraw my consent at any time. I was informed that if I withdraw, any previously collected information about my knee will not be used in the study.

By signing this form, I do not give up my legal rights. A copy of this form will be given to me.

_____

Subject's Name (print)

_____ _____

Signature of Subject **Date**

_____ _____

Investigator's Signature **Date**

VITA

Matthew Young received a BS in Mechanical Engineering from the University of Florida in 2002. From his graduation until 2005 he worked as a production engineer at Matsushita Electronics (Panasonic) in Knoxville, where his principle duties included the design and installation of automation equipment on assembly lines. Mr. Young returned to academia in 2009 and received a MS in Mechanical Engineering from University of Tennessee in 2011. He currently works in the BioRobotics Lab on the Tracking Fluoroscope System under the wonderful and extraordinary supervision of Dr. William R. Hamel. Mr. Young has taught several courses on system dynamics, machine design and Computer Aided Design and plans to pursue a teaching position specializing in machine mechanics and controls.